A Strategy to Mitigate the Onset of Electromechanical Damage in Nb_3Sn Accelerator Magnet Cables

Zur Erlangung des akademischen Grades einer

DOKTORIN DER INGENIEURWISSENSCHAFTEN (Dr.-Ing.)

von der KIT-Fakultät für
Elektrotechnik und Informationstechnik des
Karlsruher Instituts für Technologie (KIT)

angenommene

DISSERTATION

von

M.Sc. Kirtana Puthran
geboren in: Dharwad, India

Tag der mündlichen Prüfung:	23.03.2026
Hauptreferentin:	Prof. Dr. Tabea Arndt
Korreferent:	Prof. Dr. Herman ten Kate

This document is licensed under a Creative Commons Attribution 4.0 International License
(CC BY 4.0): https://creativecommons.org/licenses/by/4.0/deed.en

Abstract

Next-generation particle accelerators require superconducting magnets capable of generating magnetic fields beyond 15 T with large apertures. Operating at these intensities, niobium-tin (Nb_3Sn) conductors reach the limits of their mechanical performance, which fundamentally constrains the peak magnetic flux density attainable in engineered systems. The brittle intermetallic Nb_3Sn is vulnerable to irreversible mechanical damage that subsequently compromises superconducting performance. Damage initiation occurs under two critical loading scenarios through transverse compressive stresses at coil midplanes during operation, and room-temperature assembly prestress applied to counteract electromagnetic Lorentz forces. This thesis presents a comprehensive investigation of the electromechanical behaviour of Rutherford-type cables. Through parallel but separated characterization of complementary phenomena, this work establishes quantitative relationships between processing parameters and electromechanical performance. The research specifically addresses the critical question: How can Nb_3Sn conductor performance be strategically enhanced within existing manufacturing constraints to enable reliable operation beyond current technological limits?

The experimental program integrates electrical characterization of wires and cables at cryogenic temperatures with systematic metallographic analysis of mechanical damage in the superconductor cables under transverse compressive stress applied at room temperature. A novel classification methodology quantifies crack formation in the superconducting phase of the conductor, transforming microscopic observations into statistical distributions. The investigation characterizes both the onset thresholds where mechanical damage initiates and the evolution rates governing subsequent crack propagation under increasing transverse compression.

Beginning with reference Rutherford-type cables processed using standard protocols, the work establishes baseline damage behavior and identifies the critical prestress requirement to prevent severe electromagnetic performance degradation. Notably, mechanical damage in the brittle superconductor phase initiates at stress levels substantially below those causing measurable electrical degradation, revealing a critical operational window where undetected damage accumulates despite stable electromagnetic performance. Systematic variations in the impregnation resin system demonstrate improved damage resistance through modified mechanical properties. An enhanced resin system elevates damage onset thresholds and reduces crack propagation rates while simultaneously improving current-carrying capacity through strain state optimization. Studies on the variation in heat treatment duration reveal fundamental trade-offs between electromagnetic performance and mechanical resilience governed by microstructural features of the conductor. Increased heat treatment duration yields progressively diminishing electromagnetic gains while substantially degrading mechanical resilience. The investigation culminates in a combined approach pairing abbreviated heat treatment with enhanced resin systems, demonstrating complementary mechanisms where microstructural refinement controls crack initiation while resin properties govern propagation resistance. This optimization strategy of abbreviated heat treatment with enhanced resin demonstrates superior overall mechanical performance, preserving the refined microstructure that resists crack initiation while providing the compliant resin matrix that suppresses crack propagation, thereby creating a hierarchical defense mechanism against electromechanical degradation at multiple structural scales. The study establishes a multidimensional performance framework quantifying the fundamental trade-offs in Nb_3Sn conductor optimization.

These findings enable evidence-based selection of processing parameters for next-generation accelerator magnets targeting reliable operation near $15\,\mathrm{T}$. The demonstrated combined optimization strategy addresses the challenge where mitigating electromechanical damage, rather than maximizing superconducting capacity alone, now determines the viability of high-field accelerator magnets. This approach establishes an effective framework for balancing competing performance requirements within existing manufacturing constraints.

Abstract (Deutsch)

Die Teilchenbeschleuniger der nächsten Generation erfordern supraleitende Magnete, welche magnetische Feldstärken jenseits von $15\,\mathrm{T}$ bei großen Aperturen erzeugen können. Bei diesen Feldstärken erreichen Niob-Zinn-Leiter (Nb_3Sn) die Grenzen ihrer mechanischen Leistungsfähigkeit, was die maximal erreichbare magnetische Flussdichte in technischen Systemen grundlegend beschränkt. Das spröde intermetallische Nb_3Sn ist anfällig für irreversible mechanische Schädigung, die nachfolgend die supraleitenden Eigenschaften beeinträchtigt. Der Schadensbeginn tritt unter zwei kritischen Belastungsszenarien auf: durch transversale Druckspannungen in den Spulenmittenebenen während des Betriebs und durch Vorspannung bei Raumtemperatur, die zur Kompensation der elektromagnetischen Lorentzkräfte aufgebracht wird. Die vorliegende Dissertation untersucht das elektromechanische Verhalten von Rutherford-Kabeln. Durch parallele, aber getrennte Charakterisierung komplementärer Phänomene etabliert diese Arbeit quantitative Zusammenhänge zwischen Prozessparametern und elektromechanischer Leistungsfähigkeit. Die Forschung befasst sich spezifisch mit dieser kritischen Frage: Wie kann die Leistungsfähigkeit von Nb_3Sn-Leitern strategisch innerhalb bestehender Fertigungsbeschränkungen verbessert werden, um einen zuverlässigen Betrieb jenseits aktueller technologischer Grenzen zu ermöglichen?

Das experimentelle Programm integriert elektrische Charakterisierung von Drähten und Kabeln bei kryogenen Temperaturen mit systematischer metallografischer Analyse mechanischer Schädigung in den supraleitenden Kabeln unter transversaler Druckbeanspruchung bei Raumtemperatur. Eine neuartige Klassifikationsmethodik quantifiziert die Rissbildung in der supraleitenden Phase des Leiters und transformiert mikroskopische Beobachtungen in statistische Verteilungen. Die Untersuchung charakterisiert sowohl die Schwellwerte, bei denen mechanische Schädigung beginnt, als auch die Entwicklungsraten, die die nachfolgende Rissausbreitung unter zunehmender transversaler Kompression bestimmen.

Ausgehend von Rutherford-Referenzkabeln, die nach Standardprotokollen hergestellt wurden, etabliert die Arbeit das Basis-Schädigungsverhalten und identifiziert die kritische Vorspannung zur Vermeidung erheblicher elektromagnetischer Leistungsverschlechterung. Bemerkenswert ist, dass mechanische Schädigung in der spröden Supraleiterphase bei Spannungsniveaus deutlich unterhalb jener beginnt, die messbare elektrische Beeinträchtigung verursachen, wodurch ein kritisches Betriebsfenster offenbart wird, in dem unerkannte Schädigungsakkumulation trotz stabiler elektromagnetischer Leistungsfähigkeit erfolgt. Systematische Variationen im Imprägnierungsharzsystem zeigen verbesserte Schädigungsresistenz durch geänderte mechanische Eigenschaften. Ein verbessertes Harzsystem erhöht die Schwellwerte für Schadensbeginn und reduziert Rissausbreitungsraten, während es gleichzeitig die Stromtragfähigkeit durch Optimierung des Dehnungszustands verbessert. Studien zur Variation der Wärmebehandlungsdauer offenbaren fundamentale Kompromisse zwischen elektromagnetischer Leistungsfähigkeit und mechanischer Widerstandsfähigkeit, die durch mikrostrukturelle Merkmale des Leiters bestimmt werden. Eine verlängerte Wärmebehandlungsdauer führt zu progressiv geringeren elektromagnetischen Gewinnen, während sie gleichzeitig die mechanische Widerstandsfähigkeit erheblich beeinträchtigt. Die Untersuchung mündet in einem kombinierten Ansatz, der die verkürzte Wärmebehandlung mit verbesserten Harzsystemen verbindet und komplementäre Mechanismen aufzeigt, wobei mikrostrukturelle Verfeinerung die Rissinitiierung kontrolliert, während Harzeigenschaften die Ausbreitungsresistenz bestimmen. Diese Optimierungsstrategie aus verkürzter Wärmebehandlung mit verbessertem Harz zeigt überlegene mechanische Gesamtleistung, da sie die verfeinerte Mikrostruktur bewahrt, die der Rissinitiierung widersteht, während sie gleichzeitig die nachgiebige Harzmatrix bereitstellt, die Rissausbreitung unterdrückt, wodurch ein hierarchischer Abwehrmechanismus gegen elektromechanische Beeinträchtigung auf mehreren strukturellen Skalen entsteht. Die Studie etabliert ein multidimensionales Leistungsrahmenwerk, das die fundamentalen Kompromisse in der Nb_3Sn-Leiteroptimierung quantifiziert.

Diese Erkenntnisse ermöglichen eine evidenzbasierte Auswahl von Prozessparametern für Beschleunigermagnete der nächsten Generation, die auf zuverlässigen Betrieb nahe 15 T abzielen. Die vorgestellte kombinierte Optimierungsstrategie behandelt die Herausforderung, dass die Minderung elektromechanischer Schädigung – und nicht die alleinige Maximierung der supraleitenden Kapazität – nunmehr die Realisierbarkeit von Hochfeld-Beschleunigermagneten bestimmt. Dieser Ansatz etabliert einen effektiven Rahmen zur Abwägung konkurrierender Leistungsanforderungen innerhalb bestehender Fertigungsbeschränkungen.

Acknowledgements

I spent over three rewarding years being a lab rat at the Laboratory for Characterisation of Low Temperature Superconductors at CERN. It has fostered my dreams of being an experimentalist and a mechanic. As I reflect on this journey, I am filled with gratitude. I had the good fortune of not only conducting my research work at the lab, but also to experience the humanity that carries it all and discover myself in that jungle.

My supervisors have been instrumental in shaping this work and my growth as a research engineer. Christian Barth has been an inspiring mentor, teaching me how to build while giving me the autonomy to direct my research. I am thankful to Amalia Ballarino, my co-supervisor, for her keen insights into my work that led to its major outcomes and her constant support and encouragement. I shall always fondly remember my sense of awe and clarity and feeling a little less dazed and confused following my discussions with them. Professor Tabea Arndt's continual guidance and patience were crucial in refining my thesis and seeing this work through to the end.

Bentejui Medina-Clavijo taught me microscopy and therefore contributed to the most important aspects of my work. His company and friendship have been invaluable to me. Florian Girardot worked with me building the samples, lifting and transporting equipment I could not manage by myself and importantly, waking and working with a moody giant for long odd hours that sometimes left us at our wit's end. Oleg Kalouguine kindly shared his knowledge and tricks of the trade, which I continue to use many years later to this day. Simone Morisi worked with me building electrical equipment while teaching me on the go and was just such a pleasure to work with. Alejandro Zurita's experience and input made a big difference to my work and I remain grateful for letting me play with Vega. Piotr Koziol's software was the backbone of many of my experiments, and his constant encouragement and friendship meant as much as his pro-active technical support. Norbert Gal was an awesome lab-mate, helping me in times of great need. Simon Hopkins provided technical insight and help that was crucial to my work. I am grateful to Anne Eychenne, whose presence in the lab was vital for my heart and soul. Marc Careil offered his time and advice that was essential for building working hardware. Pierre Jacquot's words of encouragement and support were crucial for my experiments. Marina Malabailla was a watchful guardian of the metallography lab and kept me on my toes to maintain a standard essential for efficient work. Angelo Bonasia willingly shared the hardware I needed to build a machine central to my work.

Beyond the main lab, I was fortunate to work with colleagues from other facilities at CERN. Ludovic Favier of the Large Magnet Facility took me under his giant wing and unconditionally trained me in some of the most crucial aspects of building superconducting magnets. I am forever indebted to him. The wonderful people of the Large Magnet Facility showed me kindness and provided invaluable support during my time there. Cedric Urscheler, Ahmed Benfkih, Sebastien Clement, Francois-Olivier Pincot of the Polymer Laboratory carried out two of the most important operations for my samples. Michael Crouvezier of the Material Characterisation Laboratory provided me with access to the microscope that significantly improved my work's throughput. I shall fondly remember all the people from the High Temperature Superconductors and Devices lab, specially Julien Hurte and Mickey Lee who helped me whenever I asked for it and always made me belly laugh. I am grateful to Rob van Weelderen for his cool mentorship during my time as a research fellow at CERN prior to my doctoral studies. I am thankful to my colleagues at the MagDev lab at the Paul Scherrer Institut for their support and encouragement during the long months I was writing my thesis.

I have been blessed with the best of friendships, Richa Khosla, Anagha Jadhav, Sandhya Seetharaman, Salma Shaikh, Surbhi Baghotia, Amit Nayak, and Qamer Saquib have sustained, encouraged and enriched me. I am thankful for Preeti Ramaraj, her lovely self and twenty years of close friendship and Dorothea Fonnesu, my corvine sister in every universe. Serge Roguet's wonderful friendship during these years has brought joy to my life. I am grateful to Ashutosh Chauhan, my brother and friend for his presence and support that he has given me and my family through both our brightest and darkest days. I have had the warm caring presence of my close friend and confidant, Matt Noy, a real gem throughout this journey.

My Indian family with all my uncles, aunts and cousins have always supported and cheered me on. Amma and Appa taught and influenced me a great deal during my formative years. I am thankful to Hemant for being my big brother, challenging, inspiring and encouraging me. My mother Sadhana's hard work, advice and sacrifices through the years have led me to where I am today. And my departed father, Mulki Jayantha, who taught me to tell the time remains in my heart and thoughts.

Introduction

The pursuit of fundamental discoveries in particle physics drives the requirement for higher collision energies in particle accelerators, yet this quest faces a crucial barrier. Achieving these energies demands superconducting magnets capable of generating progressively stronger magnetic fields to guide and focus particle beams within these machines. At the heart of the proposed magnets lies niobium-tin (Nb_3Sn), a superconductor capable of carrying large electric currents without resistance when cooled to below its critical temperature. While Nb_3Sn's electrical properties enable magnetic fields beyond what previous technologies could achieve, its brittle nature creates a critical engineering challenge; harnessing this material's superconducting capabilities without inducing mechanical damage that compromises performance.

This challenge becomes acute in the next generation of accelerator magnets targeting magnetic fields exceeding $15\,\mathrm{T}$. At these field intensities, the electromagnetic stresses within the magnet coils approach the mechanical limits of the Nb_3Sn conductor itself. The superconductor, a brittle intermetallic compound, experiences compressive stresses during assembly, differential thermal contraction during cooldown to cryogenic temperatures, and Lorentz forces during energization, any of which can initiate irreversible mechanical damage in the conductor. Once initiated, it can propagate under continued loading, leading to progressive and irreversible electrical performance degradation, potentially rendering the magnets inoperable. Understanding and mitigating this coupled electromechanical degradation represents a critical constraint to advancing accelerator technology.

Purpose and structure of this thesis

This thesis investigates the onset and evolution of mechanical damage in Nb_3Sn Rutherford-type cables under transverse compression stress. It aims to establish practical strategies to enhance the mechanical resilience without sacrificing electrical performance. The investigation addresses a critical gap in current understanding. While extensive research has characterized electrical degradation under stress, the actual mechanical damage that precedes irreversible electrical degradation remains largely unexplored. By establishing when and how cracks initiate in the superconducting phase, this work provides the quantitative foundation needed to optimize conductor processing parameters and establish safe operational limits for next-generation accelerator magnets.

The thesis follows a progression from theoretical framework through experimental methodology to findings and optimization strategies:

Chapter 1 - Electromechanical degradation in Nb_3Sn conductors for accelerator magnets establishes the theoretical framework by examining the strain sensitivity of Nb_3Sn superconductors within the broader context of accelerator magnet engineering. The balance between electrical performance and mechanical integrity is the central theme. The chapter traces the hierarchical scales involved from microscopic superconducting filaments to macroscopic magnet systems and analyzes how the reaction heat treatment process, epoxy impregnation, and transverse compressive stress interact to determine electrical performance. A comprehensive review of previous degradation studies reveals critical knowledge gaps, particularly regarding thresholds for onset of damage and the relationship between processing parameters and mechanical resilience.

Chapter 2 - Experimental Methods presents the methodologies developed to address these knowledge gaps. The chapter details protocols for electrical characterization of both individual wires and cable assemblies. The mechanical characterization methodology employs a specialized compression bench to apply controlled transverse compression loads on cable samples. It also describes the metallographic techniques to enable systematic damage quantification across multiple structural scales.

Chapter 3 - Measurements & Observations presents the experimental results through systematic case studies investigating electromechanical behavior in the Nb_3Sn wires and Rutherford-type cables under varying processing conditions. The chapter begins with comprehensive microstructural damage characterization, establishing fundamental crack morphologies and distribution patterns within the hierarchical cable structure under transverse compression. It quantifies the electromechanical behaviour of the reference cable processed with the standard protocols. Subsequent case studies examine the effects of processing parameter variations including prestress, impregnation resin systems, and reaction heat treatment durations on both electrical performance and mechanical resilience. Each study combines the electrical characterization with quantitative metallographic analysis to correlate processing choices with performance outcomes. The experimental findings are synthesized through a multidimensional figure of merit analysis that integrates the electrical and mechanical performance metrics, culminating with optimization strategies that demonstrate complementary benefits from combined parameter modifications.

Chapter 4 - Conclusion synthesizes the key findings and their implications for future magnet development. The chapter discusses how the established relationships between processing, microstructure, and performance can guide the design of next-generation accelerator magnets. It identifies remaining challenges in the context of this research subject to improve Nb_3Sn magnet technology toward its fundamental limits, and proposes directions for future research to address these challenges.

Key contributions presented in this thesis

This work makes the following contributions to the field of superconducting magnet technology:

Quantification of damage thresholds: Through a systematic metallographic analysis, this thesis establishes the threshold for onset of cracks in Nb_3Sn cables under transverse compression for the standard protocols. The identification of onset of damage at stress levels significantly below those causing electrical degradation has direct implications for magnet assembly procedures and has already influenced production specifications for the High-Luminosity Large Hadron Collider quadrupole magnets.

Validation of prestress requirements: The large performance degradation observed without adequate mechanical support validates fundamental design principles for Nb_3Sn magnets and quantifies the required prestress levels at which progressive failure mechanisms initiate.

Processing parameters - electromechanical performance relationships: The investigation reveals quantitative correlations between processing parameters and electromechanical performance of the cables. The heat treatment duration for the formation of the superconductor governs microstructural features which directly control electromagnetic performance while trading against mechanical resilience. Impregnation resin selection influences both the electrical performance in context of the training behaviour and current-carrying capacity, and the cable's resistance to progression in mechanical damage. These relationships enable predictive optimization of processing protocols for specific applications, balancing electrical performance against mechanical robustness within existing manufacturing constraints.

Demonstration of optimization pathways: This work identifies a combined optimization strategy of abbreviated heat treatment with an enhanced resin system by demonstrating the effect of complementary mechanisms on the mechanical performance. The refined microstructure from shortened heat treatment resists crack initiation, while a compliant resin matrix suppresses crack propagation. This approach establishes the possibility of an integrated design framework toward future magnets requiring operation near mechanical limits.

Contents

Acronyms and symbols

Acronyms

AC Alternating Current

ASTM American Society for Testing and Materials

CERN European Organization for Nuclear Research

CMM Cable Measuring Machine

CTE Coefficient of Thermal Expansion

DC Direct Current

DCCT DC Current Transformer

EDX Energy-Dispersive X-ray Spectroscopy

FEA Finite Element Analysis

FGC Function Generator/Controller

FRESCA Facility for Reception of Superconducting Cables

GHe Gaseous Helium

HL-LHC High Luminosity - Large Hadron Collider

KDE Kernel Density Estimation

LHC Large Hadron Collider

LHe Liquid Helium

MQ Main Quadrupole

MQXF Magnet Quadrupole eXtra Focal

MQXFA Fermilab variant of MQXF magnets

MQXFB CERN variant of MQXF magnets

MSUT MSUT-Twente alternative epoxy resin system

PID Piping and Instrumentation Diagram

PID Proportional-Integral-Derivative

PIT Powder-in-Tube conductor manufacturing process

POLAB POLAB Mix enhanced epoxy resin system

RHT Reaction Heat Treatment

RRP Restacked Rod Process

RRR Residual Resistance Ratio

RT Room Temperature

SEM Scanning Electron Microscopy

SSL Short Sample Limit

USL Unified Scaling Law

VAMAS Versailles Project on Advanced Materials and Standards

VPI Vacuum Pressure Impregnation

Symbols

Symbol	Description
Superconducting Critical Parameters	
T_c	Critical temperature
T_c^*	Effective critical temperature
B_{c2}	Upper critical field
B_{c2}^*	Effective upper critical field
J_c	Critical current density
I_c	Critical current
J_e	Engineering current density

Symbol	Description
n	n-value (V-I characteristic exponent)
Strain Parameters	
ε	Applied strain
ε_0	Intrinsic strain
ε_m	Strain at maximum current density
$\varepsilon_{0,\mathrm{irr}}$	Irreversible strain limit
Unified Scaling Law Parameters	
F_P	Flux pinning force
$K(t, \varepsilon_0)$	Scaling parameter (temperature and strain-dependent)
$f(b)$	Scaling function (field-dependent)
t	Reduced temperature
b	Reduced magnetic field
Temperature and Field	
T	Temperature
T_g	Glass transition temperature
B	Magnetic field
B_p	Peak magnetic field
Electromagnetic Design Parameters	
E	Beam energy
ρ	Bending radius
G	Magnetic field gradient
μ_0	Permeability of free space
j	Overall current density in coil
w	Coil width
r	Aperture radius
θ	Angle (for cos-θ configuration)
T_p	Transposition pitch
Electromagnetic Forces	
$\vec{f}_L$	Lorentz force density (vector)
F_L	Lorentz force
$\vec{j}$	Current density (vector)
$\vec{B}$	Magnetic field (vector)

Symbol	Description
Electrical Measurements	
E	Electric field
E_c	Electric field criterion
I	Transport current
a	Offset term in power law fit
b	Linear resistance coefficient
C	Pinning force strength parameter
p	Low-field exponent
q	High-field exponent
R	Radius / Resistance
R^*	Effective radius
$R(293\,\mathrm{K})$	Resistance at room temperature
$R(20\,\mathrm{K})$	Resistance at low temperature
Self-Field Parameters	
B_a	Applied background field
B_self	Self-field contribution
B_s	Sample self-field
k_1	Self-field coefficient
Stress Components	
σ_r	Radial stress component
σ_θ	Azimuthal stress component
$\sigma_\mathrm{prestress}$	Prestress
$\sigma_\mathrm{prestress,cold}$	Cold prestress
$\sigma_\mathrm{Lorentz,pole}$	Lorentz stress at pole
$\sigma_{\theta,\mathrm{Lorentz}}$	Azimuthal Lorentz stress
$\sigma_{\theta,\mathrm{midplane}}$	Midplane azimuthal stress
$\Delta\sigma_\mathrm{thermal}$	Thermal stress change
σ_margin	Stress margin
σ_y	Yield strength
σ_0	Friction stress
Pressure Parameters	
P_{hyd}	Hydraulic output pressure
P_{air}	Input compressed air pressure

Symbol	Description
A_{air}	Pneumatic piston area
A_{hyd}	Hydraulic piston area
Material Properties	
E	Young's modulus
K_{IC}	Fracture toughness (Mode I)
k	Hall-Petch coefficient
d	Average grain diameter
Statistical Parameters	
μ	Arithmetic mean
σ	Standard deviation
Microstructural Measurements	
$\bar{d}$	Average grain size
L	Total test line length
N	Grain boundary intersection count
M	Microscope magnification
Geometric Parameters	
r	Radial distance
$\varnothing$	Diameter
Greek Letters	
β	Beta (for β-tungsten structure)
Chemical Formulas	
Nb_3Sn	Niobium-tin superconductor
NbTi	Niobium-titanium superconductor
Cu	Copper
Sn	Tin
Cr_3Si	Trichromium silicide
SiC	Silicon Carbide
Units - Electrical	
A	Ampere
V	Volt

Symbol	Description
W	Watt
Hz	Hertz
Ω	Ohm
Units - Mechanical	
MPa	Megapascal
GPa	Gigapascal
Pa	Pascal
N	Newton
Units - Dimensional	
mm	Millimeter
cm	Centimeter
m	Meter
µm	Micrometer
nm	Nanometer
Units - Temperature	
K	Kelvin
°C	Degrees Celsius
Units - Magnetic	
T	Tesla
Units - Time	
s	Second
ms	Millisecond
μs	Microsecond
h	Hour
Mathematical Operators	
$\pm$	Plus/minus

1 Electromechanical degradation in Nb_3Sn cables for accelerator magnets

Superconductivity is a quantum phenomenon characterized by zero electric resistance to direct current and the ability to exclude or constrain magnetic flux penetration. It has evolved from a scientific curiosity into an enabling technology for some of humanity's most ambitious engineering endeavors. This includes the fields of high energy physics, quantum computing, medical imaging, controlled thermonuclear fusion, magnetohydrodynamic power generation, magnetic separation, magnetic levitation and energy applications such as power transmission systems, electric motors and energy storage systems.

Among the various superconducting materials discovered since Kamerlingh Onnes' pioneering work in 1911, niobium-tin (Nb_3Sn) stands as a technological cornerstone for applications requiring magnetic fields approaching $10\,\mathrm{T}$. The superconductor, Nb_3Sn was discovered in 1954 but only gained serious consideration for large-scale applications in the mid-1990s. It has a critical temperature of $18.3\,\mathrm{K}$ and an upper critical field approaching $30\,\mathrm{T}$, placing it at the forefront of advanced high-field particle accelerator magnet development. Despite its exceptional superconducting properties, the widespread adoption of Nb_3Sn for this type of magnet application has been constrained by the inherently brittle nature of the material, coupled with complex manufacturing requirements and specialised infrastructure needs. Addressing these challenges has necessitated the coordinated advancement and integration of multiple engineering disciplines: materials science for optimizing microstructure, phase formation and electrical performance, electrical engineering for quench protection and stability analysis, mechanical engineering for stress management, cryogenic engineering for cooling systems, and manufacturing engineering for precision fabrication. All these disciplines operate interdependently in the development of a highly specialized magnet technology.

1.1 Strain sensitivity of Nb_3Sn superconductor: A brief overview

All superconductors exhibit some degree of sensitivity to mechanical stress, resulting in modification of their superconducting properties [1–3]. This sensitivity arises from strain-induced changes to the crystal lattice, which alters the phonon spectrum and electron-phonon coupling that underpins the superconducting state [4,5]. Nb_3Sn is a brittle intermetallic compound, exhibiting a particularly pronounced sensitivity to strain. The atomic arrangement of its crystal structure, while responsible for the superconducting properties, also renders it vulnerable to strain-induced degradation.

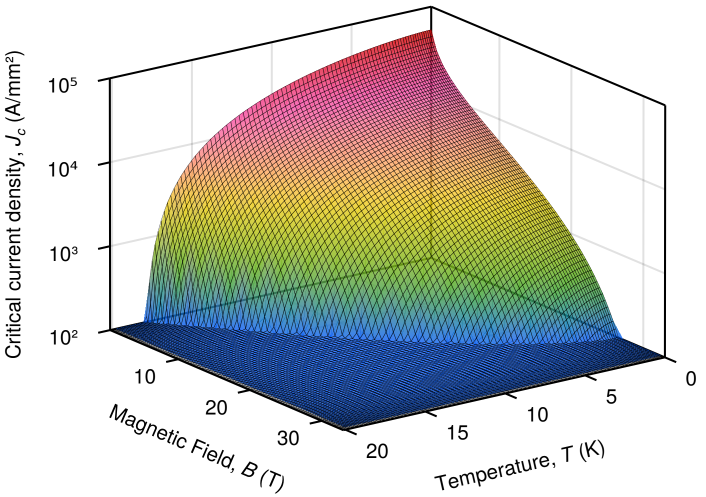

Figure 1.1: The critical surface of Nb_3Sn in temperature-field-current density space, as described by the Unified Scaling Law (Equation 1.1). The position and shape of this surface are strongly dependent on the strain state of the material.

1.1.1 Superconducting critical surface of Nb_3Sn

Nb_3Sn belongs to the class of A15 superconductors, characterized by a specific crystal structure (also known as the β-tungsten or Cr_3Si structure) in which niobium atoms form orthogonal chains along the three [100] directions [6]. This arrangement creates the framework of its superconducting behavior. The current-carrying performance of Nb_3Sn is characterized by the critical current density, J_c, operationally defined as the current density at which a critical electric field, E_c (typically $1\,\mu\mathrm{V/cm}$) develops across the superconductor. J_c is a function of the magnetic field, B, temperature, T, and strain, ε [3,7,8] in the material. Figure 1.1 illustrates this functional dependence as the three-dimensional critical surface of Nb_3Sn. Its extent is bounded by two thermodynamic limits:

- **Critical temperature**, $T_c \approx 18\,\mathrm{K}$ for stoichiometric Nb_3Sn above which superconductivity vanishes at zero field.
- **Upper critical field**, $B_{c2} \approx 27\,\mathrm{T}$ at $0\,\mathrm{K}$ above which superconductivity is destroyed.

The critical current density is determined by the material's ability to pin magnetic flux vortices that penetrate the superconductor in the mixed state. This flux pinning occurs at microstructural defects such as grain boundaries, precipitates, and compositional differences, which create local variations in the superconducting order parameter that trap vortices and prevent their motion under electromagnetic forces.

Several empirical scaling laws [9–11] have been developed in order to describe and predict conductor performance across the full operational parameter space. The critical surface behavior of Nb_3Sn is well described by the Unified Scaling Law (USL) [12–14], which parameterizes the flux pinning force[1] as a function of the critical current, I_c, magnetic field, B and strain, ε :

$$F_P \equiv I_c(B, T, \varepsilon)B = K(t, \varepsilon_0) \times f(b) \tag{1.1}$$

where:

- $\varepsilon_0 = \varepsilon - \varepsilon_m$ is the intrinsic strain, defined as zero at the strain where the current density is maximum at a given temperature, field and applied strain, ε_m
- $t = T/T_c^*(\varepsilon_0)$ is the reduced temperature scaling variable accounting for the strain-dependent *effective* [2] critical temperature, T_c^*
- $b = B/B_{c2}^*(t, \varepsilon_0)$ is the reduced magnetic field scaling variable normalized to the strain- and temperature-dependent *effective* upper critical field, B_{c2}^*

[1] For detailed parameterizations, scaling functions, and model comparisons, see references.
[2] The term *effective* distinguishes the operational critical parameters (T_c^*, B_{c2}^*) from the intrinsic material properties (T_c, B_{c2}). The effective values represent the apparent critical parameters measured in practical conductors where factors such as non-stoichiometry, inhomogeneous strain distribution, flux pinning effects, and current transfer resistance modify the observable transition behavior compared to ideal homogeneous samples.

- $K(t, \varepsilon_0)$ is the strain- and temperature-dependent prefactor that scales the maximum pinning force, incorporating the effects of $T_c(\varepsilon_0)$ and $B_{c2}(T, \varepsilon_0)$ variations
- $f(b)$ is the normalized field dependence function, typically represented as $b^p(1-b)^q$, describing the shape of the pinning force curve with the parameters p and q.

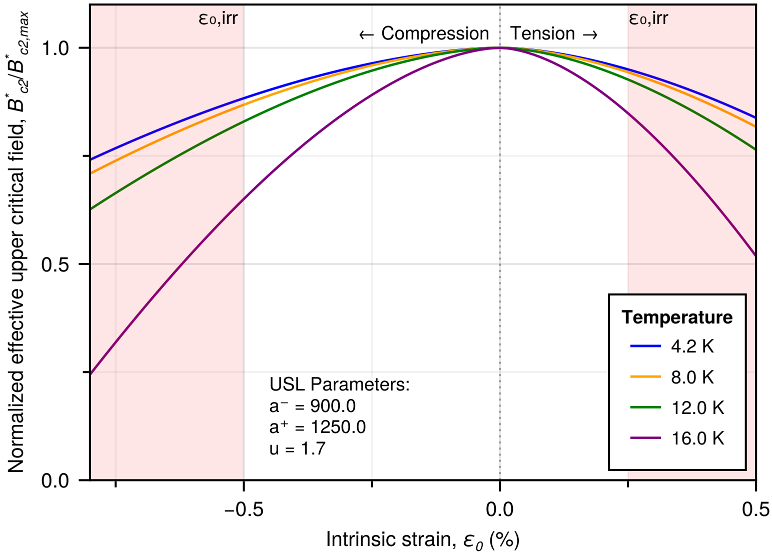

Figure 1.2: Normalized effective upper critical field, B^*_{c2} as a function of intrinsic axial strain, ε_0 for a modern Nb_3Sn conductor, illustrating the characteristic bell-shaped response and irreversible strain limits.

The strain dependence of Nb_3Sn manifests as a fundamental modification of its critical surface[10]. When a mechanical strain is applied to the conductor, the surface shifts in the three-dimensional (T, B, J_c) parameter space. Specifically, both the critical temperature and upper critical field decrease when the material experiences strain away from its optimal state, effectively shrinking the superconducting parameter space under mechanical load[9,15]. This is illustrated in Figure 1.2 which shows the characteristic bell-curve variation of *effective* upper critical field, B^*_{c2} with the intrinsic strain state, ε_0 of Nb_3Sn in a practical superconductor, using the Unified Scaling Law. The consequent impact on the critical surface is plotted in Figure 1.3, which shows how strain-induced degradation directly translates to a reduced current-carrying capacity, J_c.

A brief understanding of the strain sensitivity of Nb_3Sn requires the following key observations:

1. **Peak performance point**: In a practical superconductor wire, the Nb_3Sn phase exists in a state of compression after cooling from reaction temperature. The maximum performance

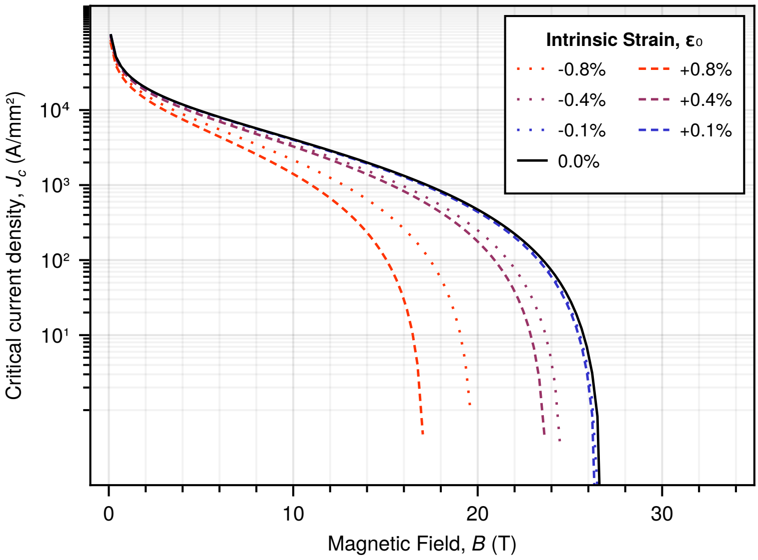

Figure 1.3: Critical current density versus magnetic field at 4.2 K for different strain states, illustrating the operational impact on accelerator magnet performance.

for J_c, which corresponds to a nearly strain-free intrinsic state ($\varepsilon = 0$) of the A15 phase, therefore, typically occurs at slight tensile strain ($\varepsilon \approx 0.2 - 0.4\%$) of the wire[16].

2. **Asymmetric response**: The shift in the critical surface is not symmetrical with respect to the direction in deviation of the strain state[16]. A tensile strain state is typically more detrimental. This is evident in the asymmteric shape of the bell-curves in Figure 1.2. The asymmetry is more pronounced at higher absolute strain states as seen in Figure 1.3.

3. **Reversible region**: Near the peak of the bell curves, small strain variations produce changes in critical current density that are fully recoverable when returning to the original strain state. This region essentially determines the operational windows for a magnet within which optimal electrical performance can be maintained.

4. **Irreversible boundaries**: There exists an irreversible strain limit, $\varepsilon_{0,\text{irr}}$ of typically $0.2 - 0.6\%$ in tension and $0.3 - 0.7\%$ in compression from the peak. Beyond these limits, depicted by shaded areas in Figure 1.2, permanent damage occurs and decrease in the current-carrying performance cannot be fully recovered. This is generally attributed to fracture in the brittle A15 phase[17–20], and corresponds to an upper limit on the working stress of about $250\,\text{MPa}$[1,21].

5. **Composition dependence**: The exact shape of the bell-curves and irreversible limits vary widely with conductor architecture, fabrication process, dopants, and heat treatment [4].

In summary, the critical surface of Nb_3Sn is highly sensitive to the strain state of the conductor, effectively creating a four-dimensional operational space where strain becomes an equally important parameter as temperature, magnetic field, and current density. This strain sensitivity emerges from the interplay of microstructural features, compositional variations, processing history, and the fundamental physics of the A15 crystal structure [4,22]. The result is a material that offers a high electromagnetic performance but demands careful mechanical stress management throughout its lifecycle, from fabrication through decades of operational service. This characteristic is a major defining constraint in high-field magnet design and operation, as briefly examined in the following section.

1.1.2 Consequences of strain sensitivity

Practical Nb_3Sn conductors are of a composite nature, consisting of extremely fine filaments of the superconductor (diameter of the order $10 - 100\,\mu\mathrm{m}$) embedded in a matrix of a normal conductor such as copper. The precursor components, Nb and Sn must be heat treated at elevated temperatures ($650 - 700\,^{\circ}\mathrm{C}$) to form the superconducting A15 phase through solid-state diffusion reactions. This heat treatment transforms the initial ductile precursor elements into the final brittle intermetallic phase of Nb_3Sn. The resulting conductor wire consists of multiple components each with distinct mechanical properties that collectively determine the conductor's response to applied strain.

Given the brittle nature of Nb_3Sn after reaction, specialized manufacturing approaches have had to be developed to address this limitation in the construction of large magnets. The predominant methodology is the *wind-and-react* technique. The conductor cables are first wound in an unreacted, ductile state into the desired shape of the magnet coil(s). The entire coil structure is then subject to the reaction heat treatment cycle. With this approach, the winding problem of a brittle material is circumvented. However, this requires the development of specialised infrastructure to handle the heat treatment of long coils in compatible moulds. The reacted coils require very careful handling post heat treatment. Subsequently, the coils are impregnated with a suitable material in order to provide mechanical stabilization to the conductor wires. The impregnation functions not only to provide mechanical support and prevent conductor motion, but also to maintain electrical insulation. Epoxy resins are the current popular choice of impregnating material for Nb_3Sn accelerator magnets. Nevertheless, epoxy-impregnated coils are susceptible to cracking [23] under the high thermal and electromagnetic stresses of an accelerator magnet, which can release energy sufficient to initiate quenches[3] in the superconductor.

From a larger perspective, a substantial compressive strain is induced in the Nb_3Sn phase as the conductor cools from reaction temperature to room temperature due to differential thermal contraction within the composite structure. This is exacerbated on cooling further down to cryogenic operation temperatures $(1.9 - 4.2\,\mathrm{K})$, as the different components with the magnet structure also contract at different coefficients of thermal expansion (CTE). To add to this finally at operating conditions, are the electromagnetic forces during operation. The forces tend to move and destabilise the coil components from within and separate the structure at its poles. While the application of *prestress* to magnet coils to retain mechanical integrity is a well proven technology, it requires careful optimization for Nb_3Sn coils so as not to damage the coils during the assembly procedure itself.

The consequence of the strain sensitivity of Nb_3Sn is thus a narrowly constrained window where the strain state must be maintained within approximately 0.3% throughout the entire construction and operation of the magnets. With the requirement to build larger particle accelerators for high energy physics, magnet field specifications are greater than $15\,\mathrm{T}$. Mitigation of strain-induced electromechanical degradation demands concurrent development across multiple scales, i.e. at conductor, coil and magnet levels. The successful construction of large-aperture quadrupoles, called Magnet Quadrupole eXtra Focal (MQXF) for the High Luminosity - Large Hadron Collider (HL-LHC) [24,25] at the European Organization for Nuclear Research (CERN) demonstrates that these challenges can be overcome for fields up to approximately $12\,\mathrm{T}$ [26–28], but higher fields will require continued advances on multiple fronts [29]. The following section examines the hierarchical scales, establishing the framework within which electromechanical optimization must occur.

[3] A rapid transition from superconducting to normal-conducting state that might induce permanent damage

1.2 Engineering a Nb_3Sn Accelerator Magnet

In high-energy particle circular colliders, the primary function of superconducting magnets is to guide and focus particle beams towards collision. For relativistic protons in circular accelerators, the relationship between beam energy, magnetic field and bending radius is given by [30–32]

$$E = 0.3 \times B \times \rho \tag{1.2}$$

where:

- E is the beam energy [GeV]
- B is the main bending dipole magnetic field strength [B]
- ρ is the bending radius [m]

This relationship establishes the direct proportionality between achievable beam energy and magnetic field strength for a given machine radius. Consequently, accelerator magnet development has been driven by systematic advancement toward higher field strengths to access increased particle beam energies. While dipole magnets guide the particle beams through uniform magnetic fields, quadrupole magnets focus beams through transverse field gradients. In a quadrupole, the magnetic field increases linearly with distance from the aperture center, creating restoring forces proportional to transverse displacement that maintain beam stability throughout the accelerator circulation.

Accelerator magnet coils typically use the cos-θ (dipoles) or cos-2θ (quadrupoles) configuration, where conductors are arranged following cosine function distributions to generate highly uniform fields [1,33]. This arrangement produces the desired multipole field while minimizing the amount of superconducting material required. The design of quadrupoles begins with the fundamental relationship between magnetic field gradient and coil parameters. For sector coil arrangements, the achievable gradient in a quadrupole follows [34]:

$$G = -\frac{\mu_0 j}{2\pi} \ln\left(1 + \frac{w}{r}\right) \tag{1.3}$$

where:

- G is the magnetic field gradient $[\mathrm{T/m}]$
- μ_0 is the permeability of free space $[4\pi \times 10^{-7}\ \mathrm{H/m}]$
- j is the overall current density in the coil $[\mathrm{A/mm^2}]$

- w is the coil width $[\mathrm{mm}]$
- r is the aperture radius $[\mathrm{mm}]$

This equation reveals three critical design levers[34]. The current density, j contributes linearly to the gradient, making it the most direct approach to achieve higher performance but limited by conductor technology. The coil width, w appears as a lograithmic variation, implying diminishing improvement with increasing conductor volume. The aperture radius, r appears inversely, creating a fundamental conflict between beam physics requirements for larger apertures and the need for higher gradients. For a typical design with $w/r \approx 0.5$, doubling the current density yields twice the gradient, while doubling the coil width increases gradient by only 60%. The theoretical gradient from electromagnetic design must thus be reconciled with the conductor capabilities.

Early accelerators utilized conventional copper-based electromagnets, typically limited to fields below $2\,\mathrm{T}$ due to resistive power dissipation constraints[4]. The introduction of NbTi superconductors in the 1970s enabled construction of accelerator magnets operating at $5-8\,\mathrm{T}$ while consuming minimal power[32,33]. The historical progression of NbTi technology through major accelerator projects tells a story of engineering advancement. The Tevatron at Fermilab pioneered the technology with $4.3\,\mathrm{T}$ dipoles, followed by Hadron-Electron Ring Accelerator (HERA) at Deutsches Elektronen-Synchrotron (DESY) with $4.6\,\mathrm{T}$ dipoles in the mid-1980s, and the ambitious Superconducting Super Collider (SSC) project which achieved $6.6\,\mathrm{T}$ in prototype dipoles before its cancellation in 1993[35]. This technology reached its culmination in the Large Hadron Collider (LHC) where $1,232$ main dipole magnets operating at $8.33\,\mathrm{T}$ enabled protons to reach energies of $7\,\mathrm{TeV}$ per beam.

The quest for higher collision energies has driven the need for magnetic fields beyond what NbTi magnets can provide. Nb_3Sn, with its superior critical field and current density characteristics, has emerged as its natural successor[31,32,36]. Figure 1.4 illustrates the difference in performance between these two superconductors. At $4.2\,\mathrm{K}$, NbTi conductors reach practical limits of approximately $1500\,\mathrm{A/mm^2}$ at $7.5\,\mathrm{T}$, while Nb_3Sn conductors can achieve current densities approaching $3000\,\mathrm{A/mm^2}$ at $12\,\mathrm{T}$[34,36,37]. For low magnetic field applications, NbTi remains the material of choice due to its superior mechanical properties, ease of manufacturing, and lower cost. However, its critical current density drops rapidly above $7\,\mathrm{T}$, as seen in Figure 1.4, where Nb_3Sn becomes essential despite its manufacturing challenges[38].

[4] Conventional electromagnets remain widely used across many accelerator facilities worldwide. Notable examples include most of the CERN Proton Synchrotron and Super Proton Synchrotron rings, the majority of beamlines at synchrotron light sources such as European Synchrotron Radiation Facility, Facility for Antiproton and Ion Research, and Diamond Light Source, as well as medical accelerators for cancer therapy. These conventional systems operate efficiently at lower fields where superconducting technology would not offer sufficient benefits to offset its higher complexity and cost.

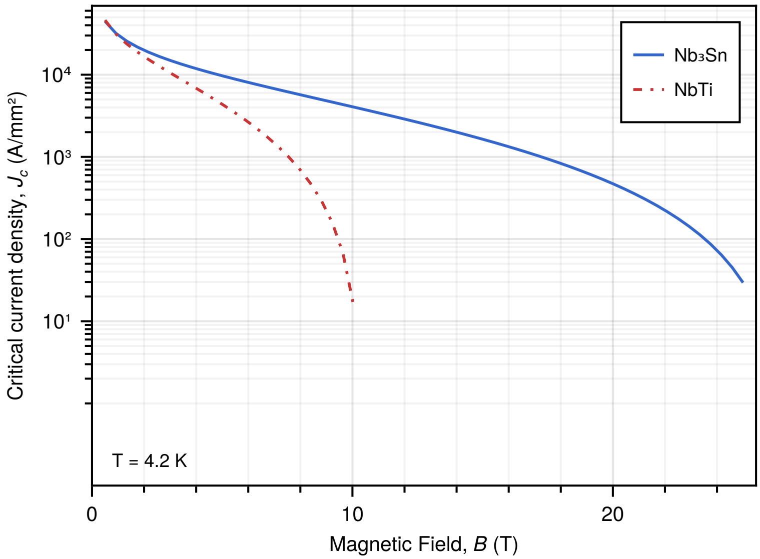

Figure 1.4: Comparison of critical current density as a function of magnetic field for NbTi and Nb_3Sn superconductors at $4.2\,\mathrm{K}$.

The operational margins of a superconducting magnet are determined through *loadline* calculations. The magnet loadline represents the linear relationship between magnetic field and current in the conductor for a given coil geometry. The intersection of the loadline with the critical surface curve of the selected superconductor is the *short-sample limit*. The difference between the operation point and the short-sample limit on the loadline is called the operating margin. Practical low temperature superconducting magnets are typically designed to operate at $75 - 85\%$ of the short sample limit to ensure stable performance[32].

The MQXF design[27,39] exemplifies how these theoretical relationships translate to engineering reality. Starting with beam physics requirements of aperture radius, r of $75\,\mathrm{mm}$ and target gradient, G of $132.2\,\mathrm{T/m}$, and choosing coil width, w of $36\,\mathrm{mm}$ to balance gradient capability against conductor volume, the design calculations yield an overall current density, $j = 469\,\mathrm{A/mm^2}$. This configuration results in a peak field of $11.3\,\mathrm{T}$ in the coil[28,40]. Shown in Figure 1.5, is the loadline calculation for this magnet with the selected Nb_3Sn conductor technology. At $4.2\,\mathrm{K}$, the magnet operates at a loadline fraction of 0.76, meaning it utilizes 76% of the conductor's theoretical maximum current capacity at the operating field. The 24% operating margin accounts for manufacturing variations, measurement uncertainties, degradation from mechanical stress, and provides operational stability against unexpected disturbances.

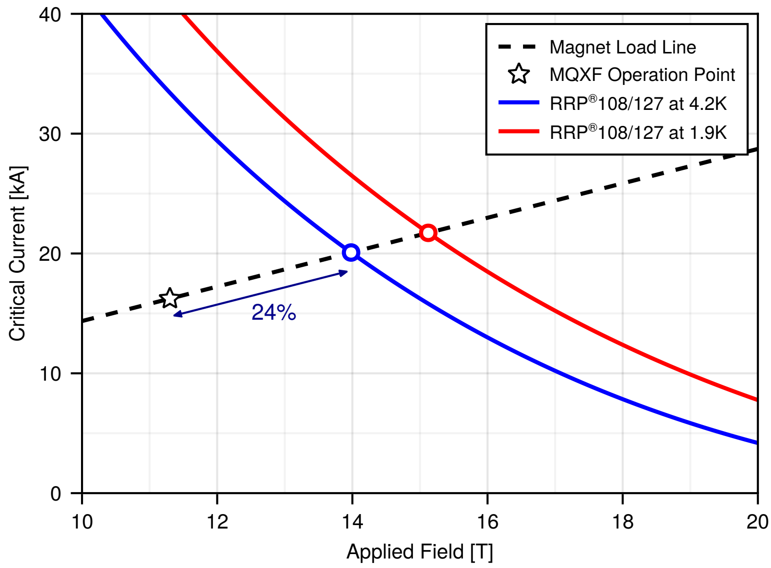

Figure 1.5: Loadline calculation for the MQXF quadrupole magnet showing the intersection of the magnet loadline with the critical surface of the chosen conductor technology (RRP® 108/127) at both 1.9 K and 4.2 K (scaled by a factor of 40 to account for number of wires in cable). The nominal operational point at 16.23 kA and 11.3 T represents 76% of the short sample limit, providing crucial margin against degradation. The temperature margin between operation at 1.9 K and the 4.2 K curve illustrates the additional stability achieved through cooling with superfluid helium.

In superconducting accelerator magnets, the very forces that enable beam manipulation can be detrimental to the structural integrity of the magnets themselves. These are the electromagnetic or Lorentz forces arising from their high current densities and the intense magnetic fields they generate. In the presence of a magnetic field, a conductor element carrying current experiences a force density given by

$$\vec{f}_L = \vec{j} \times \vec{B} \tag{1.4}$$

where:

- $\vec{f}_L$ is the Lorentz force density $[\mathrm{N/m^3}]$
- $\vec{j}$ is the current density vector $[\mathrm{A/m^2}]$
- $\vec{B}$ is the magnetic field vector [T]

For sector coil configurations employed in accelerator magnets, this force manifests primarily in three directions: radially outward - pushing the coil away from the aperture center, azimuthally toward the midplane - compressing the conductors, and longitudinally outward - elongating the coils[1,41]. A schematic of the magnetic lines of force and the electromagnetic forces within the sector coil configuration of the MQXF magnet in the transverse cross-section, is shown in Figure 1.6. The management of these electromagnetic stresses represents an important challenge in the construction of next-generation accelerator magnets.

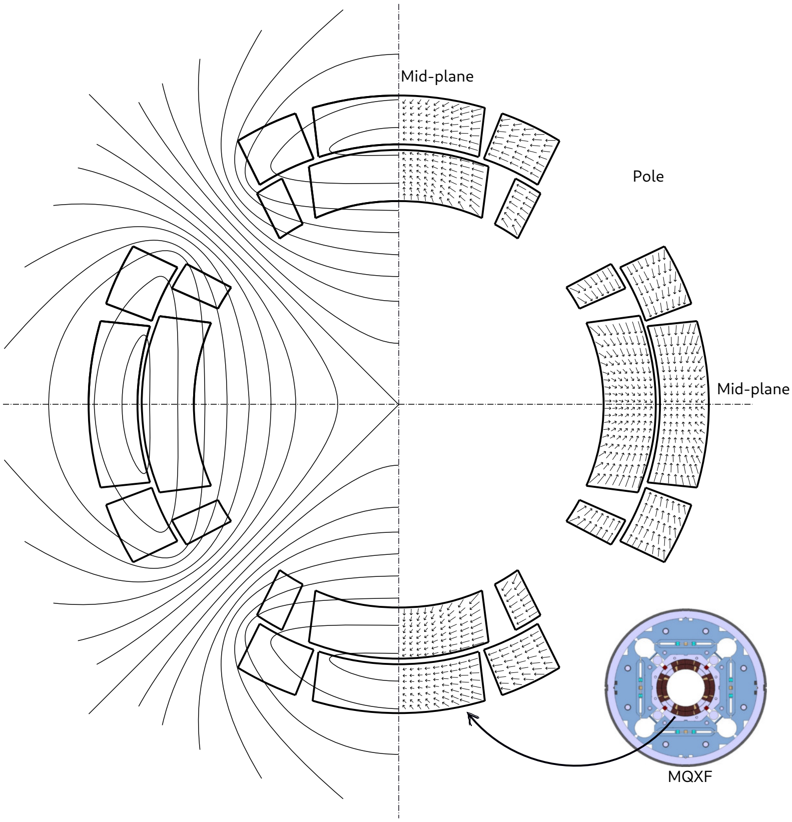

Figure 1.6: Schematic of the sector coil configuration of the MQXF quadrupole (cross-section at bottom-right[39]), showing the magnetic lines of force on the left-hand side and, vectors of electromagnetic force per unit volume, represented by arrows on the right. It illustrates the stresses tending to separate the coil from its structure at the poles, while accumulating at its mid-planes.

The magnetic and mechanical design and analysis of accelerator magnets is a computational task involving Finite-Element Analysis[42,43]. However, a first-order analytical derivation of electromagnetic stresses[34,41,44] provides insight into their scaling relationships and distribution patterns. Following the sector coil approximation for accelerator magnet configurations[45], the stress components in a quadrupole magnet can be expressed through their fundamental scaling relationships. The radial stress component derives from Maxwell stress tensor considerations, where the magnetic field energy density creates an isotropic pressure that acts to expand the field-containing volume with

$$\sigma_r = \frac{B^2}{2\mu_0} \tag{1.5}$$

where:

- σ_r is the radial stress component $[\mathrm{Pa}]$
- B is the magnetic field strength $[\mathrm{T}]$
- μ_0 is the permeability of free space $[4\pi \times 10^{-7}\,\mathrm{H/m}]$

The azimuthal stress distribution, which results from the accumulation of electromagnetic forces from the pole toward the midplane scales as:

$$\sigma_\theta \propto jGr^2 \tag{1.6}$$

where:

- σ_θ is the azimuthal stress component $[\mathrm{Pa}]$
- j is the overall current density $[\mathrm{A/m^2}]$
- G is the magnetic field gradient $[\mathrm{T/m}]$
- r is the radial distance from the aperture center $[\mathrm{m}]$

The main distinction between these stress components lies in their physical origins and spatial distribution. While radial stress represents uniform magnetic pressure acting outward on all surfaces, azimuthal stress results from the accumulation of electromagnetic forces along the angular coordinate, creating the characteristic stress concentration at the coil midplane. This quadratic dependence on aperture radius, r becomes particularly significant as future accelerator designs push toward larger beam apertures for increased luminosity.

To counteract the electromagnetic forces during operation, superconducting magnets are mechanically preloaded during assembly at room temperature[1,41,46–49]. This so-called *prestress* application serves a dual purpose. It aims to prevent the separation of the coil-structure at the poles where the electromagnetic forces act in opposition while maintaining the structural integrity of the full coil through controlled compression. The magnitude of the prestress must satisfy multiple constraints. At the pole regions, where electromagnetic forces oppose the applied compression, sufficient margin must be considered to prevent the coil-structure separation. Secondly, it should also account for the differential thermal contraction between coil components (CTE $\approx 3.5 - 3.9\,\mathrm{mm/m}$) and structural materials (stainless steel CTE $\approx 2.8\,\mathrm{mm/m}$) which results in a loss of the prestress by $30 - 40\,\mathrm{MPa}$ during cooldown from $293\,\mathrm{K}$ to $4.2\,\mathrm{K}$[50]. Moreover, additional losses can occur through epoxy creep and conductor settling during thermal cycles. The minimum prestress requirement thus follows:

$$\sigma_{\text{prestress}} > \sigma_{\text{Lorentz,pole}} + \Delta\sigma_{\text{thermal}} + \sigma_{\text{margin}} \tag{1.7}$$

Three primary structural approaches have evolved in superconducting magnet technology for prestress application. Traditional collared structures, pioneered for the Tevatron[46] and refined through generations of NbTi magnets, employ precision-machined laminations assembled under hydraulic pressure. Bladder-and-key systems[51], developed for Nb_3Sn applications, utilize temporary hydraulic bladders to create space for interference keys, enabling real-time stress monitoring during assembly. Shell-based design exploits differential thermal contraction, with aluminum or steel shells providing increasing compression during cooldown.

As described earlier, the azimuthal stress distribution in a sector coil design exhibits a strong angular dependence. It *accumulates* from the pole to a maximum compression value at the midplanes. Figure 1.6 demonstrates this stress concentration effect. Thus, at the mid-planes, electromagnetic and mechanical prestress combine additively:

$$\sigma_{\theta,\text{midplane}} = \sigma_{\text{prestress,cold}} + \sigma_{\theta,\text{Lorentz}} \tag{1.8}$$

This superposition produces the highest external mechanical loading in the coils at the midplanes. The asymmetric stress distribution therefore necessitates careful optimization of the prestress levels to simultaneously prevent pole separation and limit midplane compression.

The evolution of quadrupole magnets from early machines to modern high-luminosity upgrades reveals the escalating mechanical challenge. Table 1.1 quantifies this progression across four generations of accelerator technology. For the MQXF quadrupoles, an azimuthal stress of approximately $85\,\mathrm{MPa}$ at the coil radius and upto $110\,\mathrm{MPa}$ within the coil width is estimated[25]. Depending on the prestress compression, if the peak values reach $150\,\mathrm{MPa}$, and this may be sufficient to initiate irreversible mechanical damage in the Nb_3Sn conductor[31,53,55,56]. Despite

Table 1.1: Evolution of electromagnetic stress in accelerator quadrupoles showing the scaling challenge with increasing aperture and magnetic field requirements

Accelerator Quadrupole	**Gradient** [T/m]	**Aperture radius** [mm]	**Current density** [A/mm^2]	**Azimuthal stress** [MPa]
Tevatron low-β[52]	141	38	240	30
LHC MQ[25]	220	28	400	17
HL-LHC MQXF[53]	132.2	75	469	85
Future 15 T concepts[31,54]	~200	~90	~600	150–200

lower gradients, the MQXF quadrupoles experience significantly higher stresses than their LHC predecessors due to the r^2 scaling of azimuthal stress. This aperture dependence dominates the mechanical design space, with future 15 T magnets approaching stress levels of $150 - 200\,\mathrm{MPa}$, which is close to demonstrated irreversible electrical damage thresholds in Nb_3Sn cables[31,54].

The phenomena of a magnet quench, which is a sudden transition from superconducting to normal state, represents a significant challenge in high-field magnet engineering. A quench initiates when a localized disturbance generates sufficient heat to drive that region above its critical temperature, creating a normal-conducting zone with a finite resistance. The cascading nature arises when Joule heating exceeds local cooling capacity. This creates an expanding normal zone that can engulf the entire winding of the magnet within seconds. The sensitivity of superconducting magnets to quenches arises from four main factors[23], viz. the very low heat capacity of materials at cryogenic temperatures, nearly adiabatic winding conditions that prevent rapid heat dissipation, small temperature margins due to operation close to critical limits, and the high stored energy density (reaching $0.10\,\mathrm{J/mm^3}$ in HL-LHC magnets[25]). The primary causes include mechanical disturbances such as conductor motion, epoxy cracking, electromagnetic instabilities such as flux jumps, and thermal disturbances such as beam losses, radiation heating[1,57]. Even microscopic movements of less than $10\,\mu\mathrm{m}$ can generate sufficient frictional heating to trigger quenches[23].

Closely related to the quenching, is the phenomenon of *training* which is the tendency of magnets to quench at currents below their theoretical limits, gradually improving with successive quenches. This behavior is typically attributed to microscopic movements of conductors that eventually *settle* into stable positions after repeated electromagnetic cycling[23]. For a large collider with thousands of magnets, excessive training would render operation impractical, both economically and logistically. The energy released from mechanical events such as epoxy cracking or conductor microslips is sufficient to initiate quenches in high-field magnets[38]. Factors affecting training include epoxy impregnation quality, mechanical support structure design, prestress application, and microstructural variations in the conductor itself. Figure 1.7 presents the

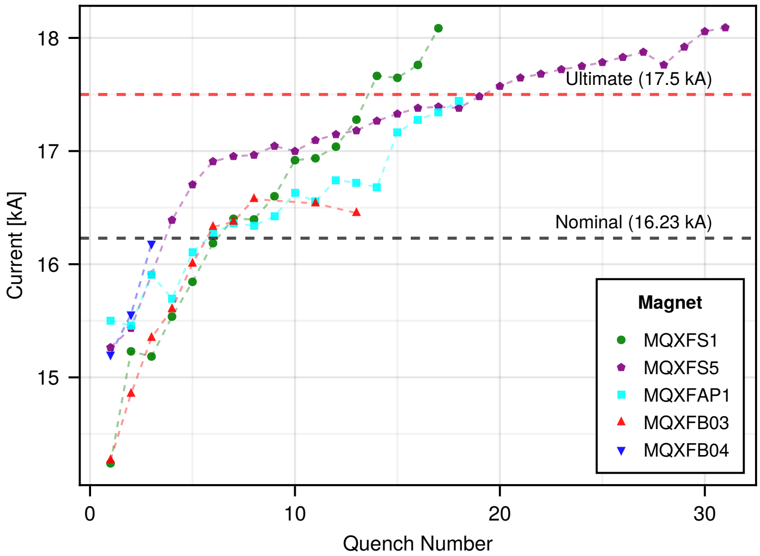

Figure 1.7: Training curves for MQXF quadrupole magnets showing quench current evolution with successive training cycles. Data includes short models (MQXFS1, MQXFS5), MQXFA prototype (MQXFAP1), and MQXFB prototypes (MQXFB03, MQXFB04). The horizontal lines indicate nominal current (16.23 kA) and ultimate current (17.5 kA) requirements for HL-LHC operation. MQXFB03 and MQXFB04 represent the latest generation magnets with improved coil fabrication procedures [27,28].

training behavior of selected quadrupole magnets in the development of the MQXF, demonstrating the progressive improvement in quench current with successive electromagnetic cycles across different magnet generations [27,28]. The data reveals variation in training requirements, with 4 m long coil prototypes MQXFAP2 requiring more training than the short models (MQXFS*). The latest generation magnets MQXFB03 and MQXFB04 achieve target performance with minimal training quenches [28].

Thus, mechanically-driven degradation pathways establishes transverse compressive stress as a primary performance-limiting factor in Nb_3Sn magnet technology. The convergence of multiple design constraints reinforces this. The inherent force accumulation in sector coils creates stress concentrations that cannot be eliminated through structural design modifications alone. The non-linear scaling with aperture size and field strength produces large increases in the resulting electromagnetic stresses even for modest parameter improvements. The demonstrated strain sensitivity of Nb_3Sn, particularly under compression [58], narrows the operational window. These constraints manifest as reduced maximum current carrying capacity due to superconductor damage, while insufficient prestress requires extended training periods before achieving nominal field. The correlation between prestress levels and electrical performance, also documented in MQXF development, underscores the connection between mechanical integrity and electromagnetic performance [56,59].

The selection of transverse compressive stress as the primary loading condition for investigation in this thesis follows directly from this analysis. The midplane stress represents the worst-case loading scenario, combining mechanical compression with electromagnetic forces additively. Furthermore, this loading mode correlates directly with practical prestress limits, where excessive compression risks immediate conductor damage while insufficient prestress risks destructive motion during operation. Thus, the construction of a Nb_3Sn accelerator magnet requires navigating interrelated factors while operating within narrow mechanical constraints established by the brittle superconducting phase. The selection of conductor architecture, optimization of heat treatment parameters, choice of impregnation material, and design of mechanical support structures must all be carefully balanced. The combined electromechanical behaviour emerges as the common thread linking processing decisions to operational reliability, creating an interesting engineering optimization problem where electromagnetic targets must be achieved within stringent mechanical boundaries.

1.2.1 Multiscale hierarchy in magnet construction

The engineering of Nb_3Sn accelerator magnets encompasses multiple scales from microscopic superconducting filaments to the accelerator magnet spanning several meters, illustrated in Figure 1.8. A multiscale perspective, presented in this section aims to provide a framework for understanding how microscopic material properties determine the performance of large-scale magnet systems.

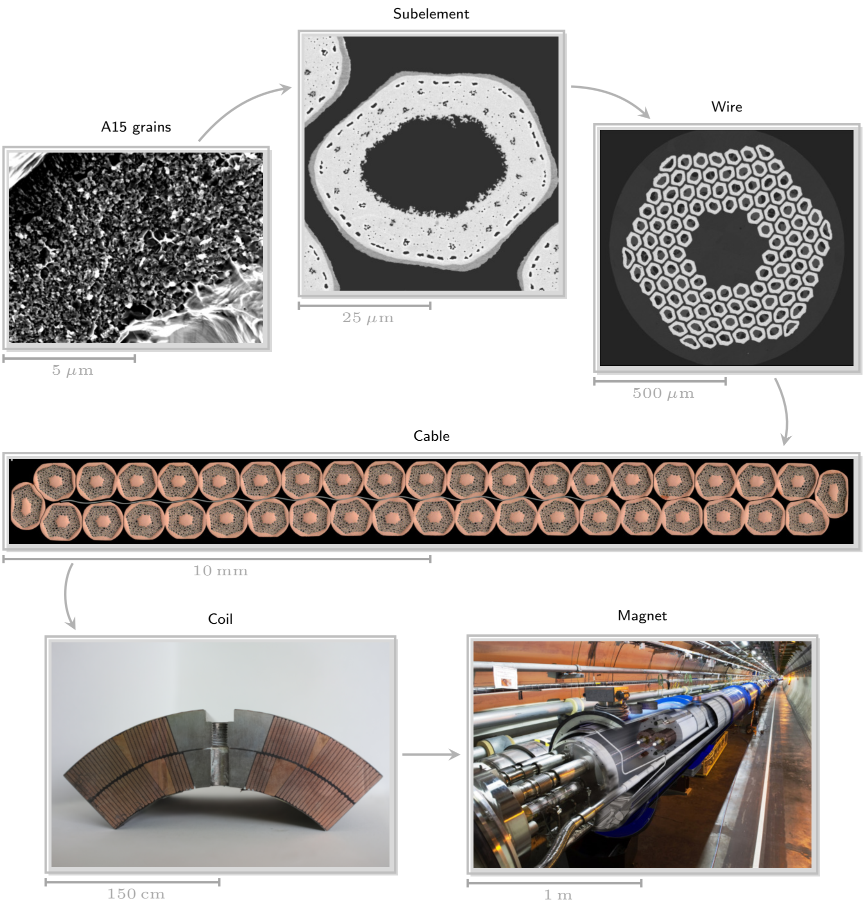

Figure 1.8: The multiscale hierarchy in Nb_3Sn accelerator magnets: from superconducting filaments (μm) to individual strands (mm), Rutherford cables (cm), individual magnet coils (m), and complete accelerator magnets (m). Each scale presents unique engineering challenges that must be addressed with compatible solutions.

1.2.1.1 Multifilamentary wire architectures

Type-II superconductors experience magnetic instabilities known as flux jumps when operated in their mixed state between the lower and upper critical fields [1,2]. In this regime, magnetic flux penetrates the material as quantized vortices while maintaining superconductivity in the regions between vortices. The magnetic instabilities occur when the electromagnetic forces on flux vortices overcome the pinning forces. This causes vortex motion that may generate heat faster than it can be dissipated, potentially triggering a transition to the normal state. The solution to this fundamental limitation emerged through the development of multifilamentary conductor architectures [60,61]. Such a wire is typically a composite structure consisting of numerous filaments, typically ranging from tens to thousands in number, with individual diameters of $10 - 100\,\mu\mathrm{m}$. These filaments are embedded in a normal conducting copper matrix that serves multiple functions; providing thermal stabilization through enhanced heat capacity and thermal conductivity, offering electrical stabilization via current sharing during transient events, and maintaining mechanical integrity. The filament size constraint emerges from stability considerations, with maximum dimensions limited to approximately $30 - 50\,\mu\mathrm{m}$ to ensure complete flux jump suppression under typical operating conditions [32].

The multifilamentary approach fundamentally alters the electromagnetic and thermal behavior of the conductor. By increasing the superconductor-to-normal metal interface area, heat generated by flux motion can be rapidly extracted to the copper matrix, which acts as a thermal reservoir. During a quench event, the copper provides an alternative current path with typical current sharing temperatures of $6 - 8\,\mathrm{K}$ for Nb_3Sn conductors, preventing voltage development that could lead to a quench. The conductor architecture must balance competing requirements of high current density, thermal stability, mechanical robustness, and acceptable AC losses [38].

The development of high-performance Nb_3Sn superconductor wires progressed through multiple technological generations, each addressing specific limitations while building upon previous achievements. Bronze-route conductors, embedded niobium filaments in a Cu-Sn bronze matrix and achieved critical current densities of approximately $1900\,\mathrm{A/mm^2}$ at $5\,\mathrm{T}$ and $4.2\,\mathrm{K}$ [60]. However, the fundamental constraint of tin solubility in copper (maximum 15.8 at.%) limited the achievable Nb_3Sn phase fraction [62,63]. Internal tin processes overcame this limitation by incorporating pure tin cores within the conductor structure, enabling critical current densities exceeding $2100\,\mathrm{A/mm^2}$ at $10\,\mathrm{T}$ [64–68]. The Powder-in-Tube (PIT) process, achieved critical current densities of approximately $2700\,\mathrm{A/mm^2}$ at $12\,\mathrm{T}$ and $4.2\,\mathrm{K}$ [36,69]. The Modified Jelly Roll (MJR) approach, a variant of the internal tin process utilizing an expanded niobium mesh wrapped around tin cores, achieved performance with critical current densities reaching $3300\,\mathrm{A/mm^2}$ at $12\,\mathrm{T}$ and $4.2\,\mathrm{K}$ [62,70,71].

Table 1.2: Performance comparison of Nb_3Sn wire architectures based on systematic characterization studies

Architecture	**Current density** $J_c(4.2\,\mathrm{K})$ $[\mathrm{A/mm^2}]$	**Irreversible damage**[a] [MPa]
Bronze route [72]	1900	100
Internal Tin [73]	2100	140
PIT [74,75]	2480	60–170
MJR [73]	2800	140–150
RRP® [76,77]	3000	110–175

[a] Transverse pressure at room temperature causing irreversible I_c degradation

The Restacked Rod Process (RRP®) architecture, currently represents the optimal technology for high-field accelerator magnet applications [37,71,78–80]. The internal architecture of the RRP® wire consists of multiple *subelements* of grouped niobium filaments assembled in a high-purity copper matrix. The RRP® architecture, its microstructural evolution during reaction heat treatment, particularly grain morphology development and barrier consumption, is examined in Section 1.2.2 and illustrated in Figure 1.14. The evolution of RRP® technology has involved systematic optimization of multiple parameters. For example, increasing the Nb:Sn atomic ratio from $3.4 : 1$ to $3.6 : 1$ and the diffusion barrier thickness by $\approx 30\%$ ensures the preservation of the purity of the copper matrix with minimal sacrifice in critical current density. The transition from tantalum [81] to titanium doping, introduced through Nb-47wt.%Ti rod additions, provided enhanced strain tolerance while enabling reaction at lower temperatures ($665\,^{\circ}\mathrm{C}$ versus $695\,^{\circ}\mathrm{C}$), reducing the risk of barrier degradation [21,37,79,82].

Systematic studies of irreversible damage limits in Nb_3Sn wires under transverse compression have established critical operational boundaries for magnet design [17]. Barzi et al. [73] demonstrated that irreversible critical current degradation thresholds vary significantly among conductor architectures when individual wires are tested within dummy cable configurations. Internal Tin conductors showed no permanent damage up to $140\,\mathrm{MPa}$, MJR wires exhibited irreversible degradation beginning at $140 - 150\,\mathrm{MPa}$, while PIT conductors demonstrated enhanced sensitivity with permanent damage initiating at $60\,\mathrm{MPa}$ [74,75]. For RRP® wires, investigations [76,77] have revealed that irreversible critical current degradation under transverse compression initiates at approximately $110 - 175\,\mathrm{MPa}$ when tested at room temperature, with the exact threshold strongly dependent on heat treatment parameters and strand diameter. Studies by Wolf et al. [83,84] using neutron diffraction revealed that under transverse loading, RRP® conductors experience a triaxial stress states with strain magnification factors of $1.3 - 1.5$ in the Nb_3Sn phase relative to the applied macroscopic stress.

Table 1.2 summarizes the key performance parameters that guided the selection of conductor architecture for the MQXF quadrupoles. The chosen RRP® conductor achieves the following specifications: effective filament diameter of $50 - 55\,\mu\mathrm{m}$, critical current density approaching $3000\,\mathrm{A/mm^2}$ at $12\,\mathrm{T}$ and $4.2\,\mathrm{K}$, residual resistivity ratio exceeding 150 after cabling, and n-values[5] greater than 30 at operating fields[37,79]. The high critical current density of RRP® wires, combined with acceptable mechanical properties and proven manufacturability at the multi-ton scale, has established it as the state-of-art technology for accelerator projects.

1.2.1.2 Rutherford-type cables: the building blocks of accelerator magnets

Accelerator magnet design requires conductors capable of carrying $10 - 20\,\mathrm{kA}$ to generate the necessary magnetic fields. Since individual (low-temperature) superconducting wires are limited to several hundred amperes, cable configurations comprising multiple wires are necessary to achieve the required current capacity while maintaining mechanical stability and magnetic field quality[38]. The selection between round and flat cable geometries depends on several technical parameters. These include current-carrying capacity, mechanical robustness, manufacturing feasibility, and magnetic field quality requirements. High-field accelerator magnets preferentially utilize flat cables due to their superior packing factor in coil windings, enhanced mechanical stability under electromagnetic forces, and capacity for precise conductor positioning essential for achieving stringent field quality specifications[33].

The Rutherford-type cable was initially developed at the Rutherford Appleton Laboratory[85] using NbTi superconducting wires. It has emerged as the standard configuration for accelerator magnets and has subsequently been adapted for Nb_3Sn wires[1,38]. This type of cable consists of multiple wires or strands, typically $20 - 40$ in number, which are arranged in a flat transposed pattern. The transposition pattern reduces coupling currents during field changes, improving the dynamic performance and lowering AC losses during magnet ramping. The cable is given a trapezoidal shape with a *keystone* angle to facilitate winding into the circular coil geometries for an accelerator magnet. This configuration also provides mechanical stability under the substantial electromagnetic forces experienced during operation, which is crucial for maintaining magnetic field quality and preventing quenches. Rutherford-type cables exhibit improved stability against mechanical disturbances compared to braided conductors, requiring approximately 60 times more energy to induce a quench[86].

The manufacturing of Rutherford-type cables demands specialized machinery capable of maintaining precise control over strand arrangement and cable dimensions. Figure 1.9[87] shows the

5 Parameter characterising the current-voltage characteristics in transition region of a superconductor.

cabling process where the initially round superconducting strands are progressively formed into the flat cable geometry. Asymmetric roller configurations are used to create the trapezoidal cross-section. Throughout this process, precise tension control on individual strands must be maintained to ensure dimensional accuracy and prevent excessive damage to the conductor[38,88].

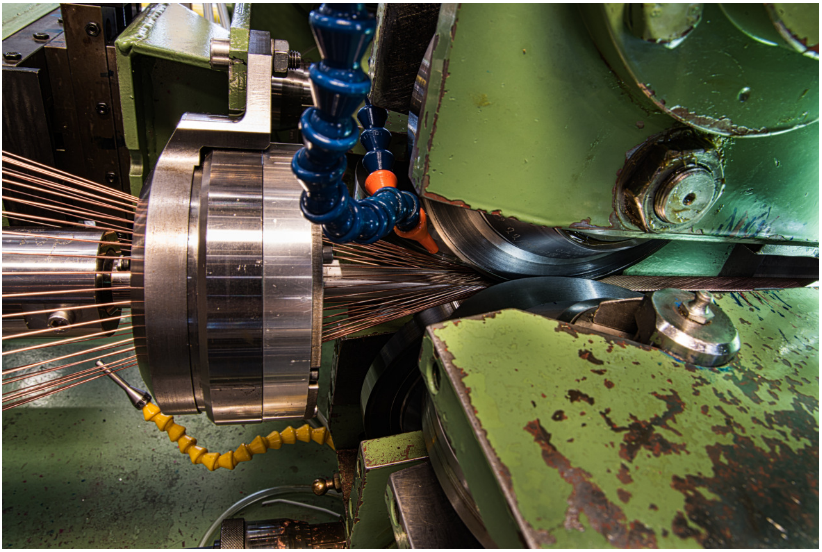

Figure 1.9: Picture of the Rutherford cabling process showing the transformation of round superconducting strands into a flat cable configuration[87]. The specialized cabling machine maintains precise control over strand positioning and tension during the forming operation.

An image of a Nb_3Sn Rutherford-type cable with S2-glass insulation prior to heat treatment is shown in Figure 1.10. A schematic of the transverse cross-section of the cable used for the MQXF quadrupoles is shown in Figure 1.11. The cable is composed of 40 RRP® strands with $0.85\,\mathrm{mm}$ diameter. It has a width of $18.15\,\mathrm{mm}$, mid-thickness of $1.525\,\mathrm{mm}$, and a keystone angle of 0.4^{o}. The cables also features a $12\,\mathrm{mm}$ wide, $25\,\mu\mathrm{m}$ thick stainless steel *core* positioned within the two layers of strands. A primary purpose of the core is to limit inter-strand coupling currents, thus effectively increasing inter-strand resistance[79].

During the cabling process, the (ductile) strands are *flattened* and thereby undergo significant mechanical deformation that inevitably impacts their electromagnetic performance after reaction[90], compared to virgin unflattened stands. This deformation typically reaches approximately 15% of the original strand geometry. It manifests most severely at the cable edges where the strands are *kinked*, as illustrated in Figure 1.11. These kinked edges experience combined effects of compaction and bending around the cable edges, which create localized stress concentrations that can damage the niobium diffusion barriers within the subelements. During the reaction heat

Figure 1.10: Photograph of a Nb_3Sn Rutherford-type cable with S2-glass insulation [89]. The image exhibits the characteristic flat geometry of the cable with multiple strands arranged in a transposed pattern. The S2-glass insulation provides electrical isolation between turns and creates channels for subsequent epoxy impregnation.

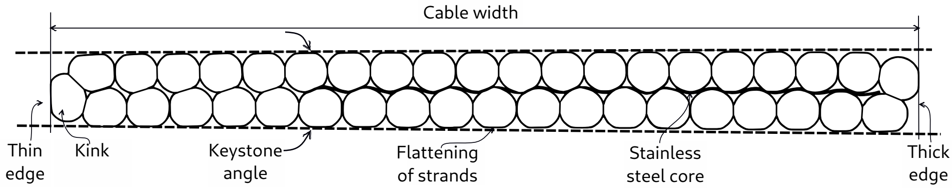

Figure 1.11: Cross-sectional geometry of a Rutherford-type cable showing the trapezoidal shape with key dimensional parameters including width, mid-thickness, keystone angle and the stainless steel core placement between the two strand layers. Also shown is the deformed strands within the cable structure, highlighting the non-circular, flattened strand shapes resulting from the cabling process. The strands experience approximately 15% shape deformation during the cabling process, with kinked strands at the edges experiencing the greatest deformation.

treatment of the strands, such barrier damage potentially leads to tin leakage and reduced purity of the copper matrix.

The quality assurance protocols for the cabling process include extracting strands from the cables and measuring their critical current properties in comparison to virgin wires. The *cabling degradation* is quantified as the percentage difference between critical currents of virgin and extracted strands. It must typically remain below 5% to meet performance requirements for high-field magnet applications [79,80]. The cabling degradation follows a clear relationship with compaction parameters, particularly the *thin edge compaction* in keystoned cables. Conductor sensitivity to cabling deformation varies substantially among architectures. Studies have demonstrated that reducing keystone angle from 0.55° to 0.4° for the RRP® cables results in significantly lowered cabling degradation [88].

The Rutherford-type cable configuration thus represents an engineering solution that balances electrical performance, mechanical stability, and manufacturability requirements, establishing the fundamental building block for high-field Nb_3Sn accelerator magnets. Beyond cabling deformation, the complexity of the configuration further influences the mechanical behavior of cables through inter-strand contact and insulation systems in addition to the microstructure within the component strands.

1.2.1.3 From cables to magnets : wind and react methodology

For Nb_3Sn magnets, the wind-and-react approach [91] is the prevailing technique used to construct the coils. In this process, the superconductor cables are wound in their unreacted, ductile state into the precise coil geometry and then subjected to the reaction heat treatment cycle. This technique addresses the inherent brittleness of Nb_3Sn by performing the most severe mechanical manipulations while the material remains in its ductile precursor state[6]. The MQXF coils represent substantial assemblies, with 50 turns wound in 2 layers. The magnetic lengths reach $4.2\,\mathrm{m}$ for Fermilab variant of MQXF magnets (MQXFA) and $7.15\,\mathrm{m}$ for CERN variant of MQXF magnets (MQXFB) configurations, requiring precise dimensional control throughout the manufacturing process [27,28,92].

Prior to winding, the cables are insulated with S2-glass fiber, as seen in Figure 1.10. This insulation (typically $145 - 165\,\mu\mathrm{m}$ thick) serves multiple functions. It provides electrical isolation between turns, creates channels for epoxy impregnation, and offers mechanical support to the brittle Nb_3Sn phase after reaction [93]. Recent innovations include braided insulation systems that achieve more uniform coverage compared to traditional wrapped approaches [94]. The coil winding process employs custom-designed tooling with adjustable mandrels and tension control systems [95]. For large accelerator magnets, semi-automated winding tables maintain precise tension (typically $10 - 30\,\mathrm{N}$) throughout the winding process to ensure dimensional accuracy. The cable path must be carefully controlled to avoid excessive strain, particularly at the coil ends where three-dimensional bending occurs. End spacers, precisely machined from materials compatible with high-temperature heat treatment, provide support at these critical regions and ensure conductor positioning.

The wound coil assembly is then secured with temporary binders and tooling before being transferred to reaction fixtures [96]. The fixtures are manufactured from stainless steel or Inconel with controlled thermal expansion properties. These fixtures must maintain the coil geometry

[6] Alternative react-and-wind approaches are sought for specific applications where mechanical strains can be maintained below critical thresholds, such as certain fusion devices or applications using specialized strain-tolerant designs.

while accommodating the dimensional changes that occur within the superconductor wires during heat treatment [97–103]. The wound coils undergo reaction heat treatment in specialized furnaces under controlled argon atmosphere conditions. The specific temperature profiles and durations critically influence both electromagnetic and mechanical properties of the resulting conductor, detailed in Section 1.2.2. Following the reaction, the brittle Nb_3Sn coils must be stabilized against mechanical movement through vacuum pressure impregnation with epoxy resin, further elaborated in Section 1.2.3. This process fills all void spaces with epoxy to provide mechanical support, prevent conductor motion, and maintain electrical insulation. The impregnation process for large accelerator magnets typically requires careful control of temperature, vacuum level, and pressure to ensure complete infiltration without introducing voids or other defects [27,95].

After impregnation, the coils undergo final assembly into the cold mass structure (bottom-right in Figure 1.6). This includes the application of the prestress compression to the coils, explained earlier in Section 1.2. While these assembly procedures are beyond the scope of this thesis work, they represent the final stage in transforming the coils into functional magnet systems. At each stage, specialized tooling and careful, precise control is essential to avoid damaging the brittle conductor [27], thus being highly critical stages in the construction of the magnets.

In this section, an overview of the multiscale nature in the construction of a Nb_3Sn accelerator magnet has been presented. It aims to highlight the distinctive requirements at each level of the structural hierarchy, with a focus on the composite nature of the superconductor wires and Rutherford-type cables. At the transition from cables to magnets, mechanical integrity becomes increasingly critical, with the increase in potential for stress concentration that can lead to degradation of the brittle Nb_3Sn phase. The reaction heat treatment and vacuum impregnation processes are further discussed in the following sections. Both processes represent critical design choices in magnet construction with implications for both electromagnetic performance and mechanical resilience against degradation in operating conditions.

1.2.2 Reaction heat treatment

During the Reaction Heat Treatment (RHT) process, dramatic changes occur within the superconductor wire as a result of the solid-state diffusion reactions of the precursor components. The fundamental electromagnetic and mechanical properties of the conductor are determined by the final microstructure of the wire after the heat treatment. This section details the three-stage RHT protocol used for the RRP® conductor of the MQXF quadrupoles. It also briefly examines the microstructural evolution within the wire during the RHT cycle. Finally, it discusses the microstructural basis of the relationships between the key processing parameters of the final stage and the electromechnical performance of the conductor. This provides the motivation for the investigation pathway of RHT optimization in this thesis work within the constraints of established manufacturing processes of the Nb_3Sn accelerator magnets.

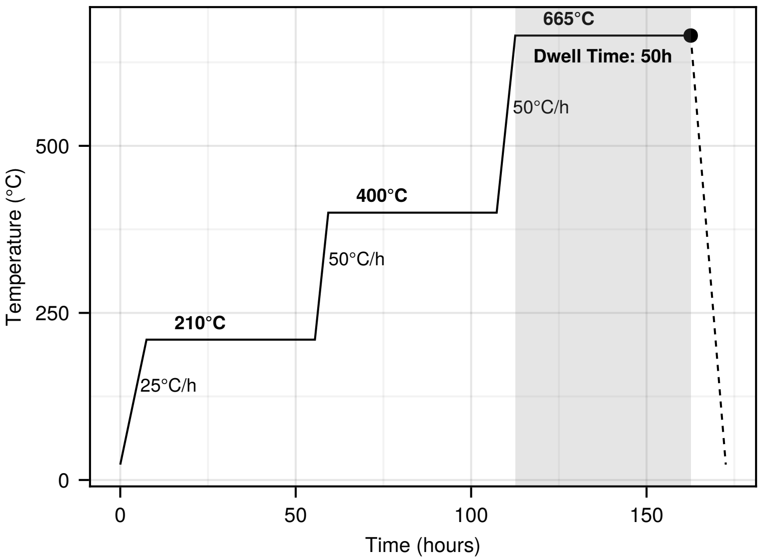

Figure 1.12: Standard three-stage reaction heat treatment protocol for MQXF magnets of RRP® cables showing temperature plateaus and ramp rates. The total heat treatment duration is approximately 8 days, with heating rates typically 25° C/h for the first ramp and 50° C/h for subsequent ramps.

The RHT cycle for RRP® conductors involves three distinct stages, each serving a specific purpose in the microstructural evolution. Figure 1.12 shows the standard three-stage RHT protocol adopted for the MQXF magnets, as follows :

1. **Initial low-temperature plateau** at $210\,^{\circ}\mathrm{C}$ for 48 hours that initiates Cu-Sn mixing and bronze formation

2. **Intermediate temperature plateau** at $400\,^{\circ}\mathrm{C}$ for 48 hours that promotes formation of Cu-Sn intermetallic compounds

3. **High-temperature plateau** at $665\,^{\circ}\mathrm{C}$ for 50 hours that facilitates the final Nb_3Sn or A15 phase formation

The total cycle is approximately 8 days long, with heating rates typically run at $25^{\circ}\ \mathrm{C/h}$ for the first ramp and $50^{\circ}\ \mathrm{C/h}$ for the two subsequent ramps.

1.2.2.1 Microstructural evolution during heat treatment

Cross-sectional micrographs of a RRP® Nb_3Sn wire before and after the complete heat treatment cycle are shown in Figure 1.13. In this type of wire architecture, the subelements are arranged in a hexagonal pattern (typically $108/127$ or $132/169$ configurations[7]) around the central copper core. A subelement refers to a discrete unit within the wire cross-section containing a tin-rich core surrounded by niobium filaments, all enclosed within a niobium diffusion barrier. As aforementioned, the purpose of the barrier is to control or prevent migration of tin into the surrounding copper matrix during reaction. This arrangement facilitates a controlled interdiffusion during heat treatment. Within each subelement, the transformation of Nb filaments surrounding Sn-rich cores to a connected Nb_3Sn or A15 phase structure surrounding the Cu-Sn core (which may contain voids) is clearly visible in the figure.

The reaction sequence during heat treatment follows a progression of phase transformations, which has been studied widely and is well documented[37,71,104–109]. Each stage has significant implications for both electromagnetic and mechanical properties. Drawing from comprehensive reviews[6,70,108,110], the microstructural evolution[8] can be described through the following stages:

- During the first stage ($210 - 215\,^{\circ}\mathrm{C}$), Sn and the surrounding Cu within the subelements interdiffuse to produce mainly η-Cu_6Sn_5 and partly ϵ-Cu_3Sn. This step primarily prevents tin leakage ("Sn bursts") during subsequent heating[107]. A protective layer of approximately $4 - 5\,\mu\mathrm{m}$ thickness forms at the interface. The formation of Cu-Sn alloys serves a dual

[7] The X/Y notation designates X subelements within a Y-position stack array, with non-populated positions typically filled with copper rods for stabilization.

[8] The phase transformations during heat treatment follow the Nb-Sn and Cu-Sn binary phase diagrams, which govern the formation sequence of intermetallic compounds and bronze phase are in Appendix A.1.

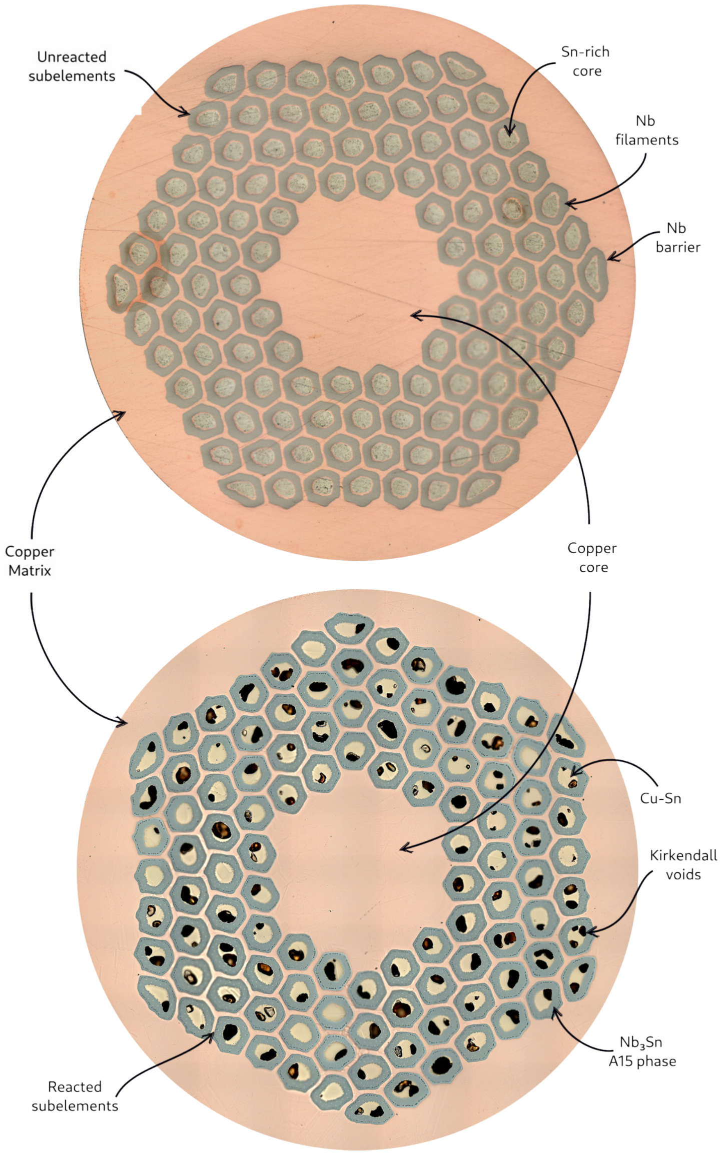

Figure 1.13: Cross-sectional micrographs of RRP® Nb_3Sn wire 108/127 before heat treatment (top) and after complete reaction heat treatment (bottom). The unreacted precursor elements, Nb filaments surrounding Sn-rich cores are transformed into a connected Nb_3Sn A15 phase within the subelements during the reaction.

purpose. It prevents tin redistribution and sets the stage for controlled chemical potential gradients in later phases.

- As temperatures rise to $215 - 300\,^{\circ}\mathrm{C}$, a critical ternary Cu-Nb-Sn phase called Nausite forms at the inner surface of the Nb filamentary area. With nominal composition of $(Nb_{0.75}Cu_{0.25})Sn_2$, Nausite functions as an "osmotic membrane" regulating diffusion kinetics[6,111]. It inhibits Sn diffusion into the filament pack while permitting Cu counter-diffusion into the Sn core[112]. This phase plays a crucial role in determining the uniformity of the final Nb_3Sn layer.

- In the second stage, at approximately $400\,^{\circ}\mathrm{C}$, the decomposition of η-Cu_6Sn_5 into ϵ-Cu_3Sn is initiated[80,108]. This transformation generates Kirkendall voids at the reaction front due to differential diffusion rates between Cu and Sn, with Cu diffusing significantly faster than Sn[113]. The volume reduction during ϵ-Cu_3Sn formation further contributes to void formation. During this stage, Nb begins to corrode on the core side as Nausite grows at the reaction interface.

- During the final third stage of the cycle, at temperatures above $586\,^{\circ}\mathrm{C}$, Nausite decomposition into $NbSn_2$ is triggered[80,108]. As temperatures approach $650\,^{\circ}\mathrm{C}$, Nb_6Sn_5 forms at the reaction front, followed by generation of Nb_3Sn at the interface between Nb_6Sn_5 and Nb filaments. Eventually, the Nb_3Sn filaments become substantially connected, forming into a single structure. An important advantage of RRP® conductors is their reduced Nb_6Sn_5 formation compared to other methods. This results in lower concentrations of coarse Nb_3Sn with poor intergranular connections[6,109].

Figure 1.14 illustrates the evolution of a subelement during the final stage of the standard heat treatment protocol. The first micrograph is of an unreacted subelement, showing the Nb filaments (in grey) and Ti doping rods (in black) surrounding the Sn-rich Cu core (in white). They are enclosed within the external Nb barrier (in grey) in a hexagonal shape to form the subelement. The second micrograph shows the subelement at the beginning of the third stage. The ϵ-Cu_3Sn phase (in dark grey) has formed at the core, and includes a void (in black). The Nb_6Sn_5 phase is visible (in light grey) at the interface of the core and the Nb filaments. As the duration of the stage increases, the reaction front progresses radially outward through the subelement forming the A15 phase (in white). The micrograph of the subelement, after 30 hours at this temperature (circled in green), shows the fully formed A15 phase. At this point, the niobium barrier is already begun to be reacted (possibly starting before 15 hours reaction time - shown in the fifth micrograph) and is depleted as the reaction front moves outward. The micrographs at 50 hours (circled in blue) and 75 hours (circled in red) show regions of highly thinned barrier at the edges, with some remnants at the vertices of the hexagonal subelements. The final micrograph at 200 hours shows no signs of any barrier left, and the tin has completely diffused into the copper matrix.

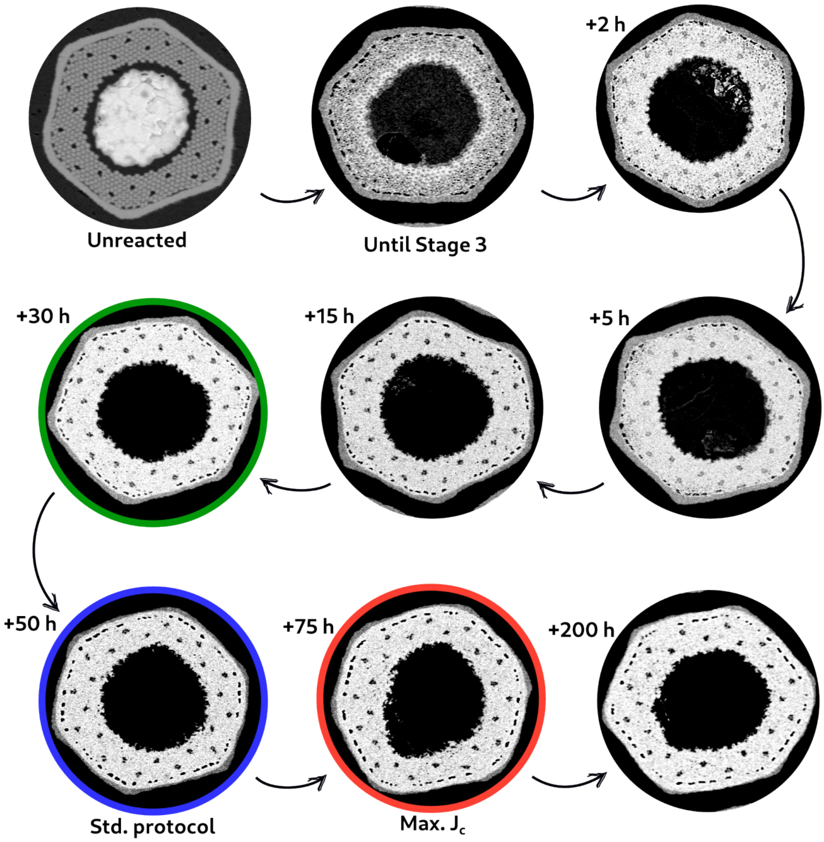

Figure 1.14: Evolution of the microstructure a RRP® 108/127 subelement during the final stage (665 °C) of reaction heat treatment, showing cross-sections at various durations starting from the virgin unreacted state, and at the beginning of the final stage in the first two micrographs respectively. The subsequent micrographs demonstrate the initial Nb_3Sn formation at the Nb-Sn interface (2 h), radial growth of the A15 phase consuming Nb filaments ($5 - 30$ h), and near-complete transformation with progressive Nb barrier consumption ($50 - 200$ h). The three highlighted cases - 30 h (green), 50 h (blue, standard protocol), and 75 h (red, maximum J_c) - represent the heat treatment durations investigated in this thesis for their distinct electrical and mechanical properties.

1.2.2.2 Impact of final RHT stage on electromechanical properties

The aspects of the final microstructure of the superconductor inevitably determine its electrical and mechanical properties. Specifically, the temperature and duration of the final stage of the RHT governs the A15 phase grain morphology and niobium barrier thickness of the subelements. Thus, both these parameters theoretically present opportunities to tune the electromechanical behaviour of the conductor wire. The effect of these are explored as follows:

1. **A15 Phase Formation**

   The volumetric fraction of A15 phase within conductor subelements evolves as a function of both temperature and time during the final heat treatment stage. Systematic investigations demonstrate that phase fraction increases from 57.1% to 62.0% (for a constant duration of $48\,\mathrm{h}$) if the temperature is raised from $642\,^{\circ}\mathrm{C}$ to $678\,^{\circ}\mathrm{C}$ for Ta-doped wire[114]. The 8.6% expansion of superconducting cross-section represents a direct enhancement of current-carrying capacity, though it accounts for only approximately one-third of the observed 25.3% increase in critical current. This indicates concurrent microstructural modifications contribute substantially to performance gains. From an electrical perspective, an increased A15 fraction correlates positively with enhanced critical current density through increased superconducting pathways. However, mechanical considerations might reveal competing effects. The rapid phase growth occurring at higher temperatures also generates internal stresses from volumetric mismatches between reacted and unreacted regions. This is critical due to the brittle nature of the A15 structure, as stress concentrators at phase boundaries serve as preferential crack initiation sites.

2. **Grain Size Evolution**

   Concurrent with phase formation, the Nb_3Sn grain morphology undergoes a systematic evolution characterized by progressive coarsening at elevated temperatures. The process initiates with the formation of fine crystallites with dimensions below $50\,\mathrm{nm}$ at reaction interfaces. This is followed by development of columnar structures extending radially through the A15 layer. These columnar grains subsequently decompose into equiaxed morphologies as heat treatment progresses, though columnar regions typically persist in portions of the Nb_3Sn layer until reaction completion[115]. A microstructural analysis reveals that the linear grain boundary density decreases from 1.99×10^7 to $1.66 \times 10^7\,\mathrm{m}^{-1}$ as heat treatment temperature increases from $680\,^{\circ}\mathrm{C}$ to $695\,^{\circ}\mathrm{C}$[109], representing a 16.5% reduction. For equiaxed grains, this corresponds to a grain size of approximately $150 - 200\,\mathrm{nm}$. This microstructural aspect directly impacts the electrical performance. Grain boundaries with thickness of approximately $3 - 4\,\mathrm{nm}$ are comparable to the coherence length of Nb_3Sn. They function as the effective flux pinning centers essential for maintaining high critical current density under magnetic fields. The maximum pinning force exhibits monotonic increase as grain size decreases down to $35\,\mathrm{nm}$[4]. Thus, grain refinement is encouraged[4,105,109] as it enhances electromagnetic performance through increased pinning site density. The mechanical integrity is also expected to deteriorate with grain coarsening according to Hall-Petch behavior[116], where fracture resistance decreases with increasing grain size given by:

$$\sigma_y = \sigma_0 + kd^{-1/2} \tag{1.9}$$

where:

- σ_y is the yield strength [MPa]
- σ_0 is the friction stress representing the intrinsic resistance to dislocation motion [MPa]
- k is the Hall-Petch coefficient [$\mathrm{MPa} \cdot \mu\mathrm{m}^{1/2}$]
- d is the average grain diameter [μm]

Thus, an extended RHT duration would result in a material increasingly susceptible to crack propagation.

3. **Niobium Barrier Consumption**

   The niobium diffusion barrier undergoes progressive consumption during the final heat treatment stage, with thickness reduction rates strongly dependent on temperature and duration. Studies[114] on Ta-doped RRP® wires reveal that for a duration of $48\,\mathrm{h}$ at $642\,^{\circ}\mathrm{C}$, average unreacted barrier thickness measures $1.22 \pm 0.35\,\mu\mathrm{m}$ with no subelements exhibiting completely reacted-through barriers, while for the same duration at $678\,^{\circ}\mathrm{C}$, average thickness decreases to $0.70 \pm 0.36\,\mu\mathrm{m}$ with 4.9% of subelements showing complete barrier consumption and 32.7% maintaining thickness below $0.5\,\mu\mathrm{m}$. The major electrical implication centers on the purity of the copper matrix[63]. A barrier breach enables tin contamination of the copper matrix. This substantially reduces the Residual Resistance Ratio (RRR) of the conductor wires compromising its stability during quench events[117]. A progressive barrier consumption removes critical reinforcement at locations of peak stress concentration along phase interfaces, though quantitative correlations between barrier thickness and mechanical strength remain insufficiently characterized in existing literature.

Beyond these primary mechanisms, Kirkendall voids formed through differential diffusion rates during solid-state reactions constitute significant stress concentrators that compromise mechanical integrity of superconductor wires[118,119]. However, void formation occurs predominantly during intermediate temperature stages ($200 - 400\,^{\circ}\mathrm{C}$) through Cu-Sn interdiffusion processes[120], thereby falling outside the scope of final-stage optimization strategies of this thesis work.

A sufficiently high reaction temperature and duration is thus necessary to allow the development of the grain morphology of the A15 phase to generate a high throughput electrical performance of the wire[9]. Higher temperatures or extended durations improve current-carrying capacity, but also simultaneously degrades the electrical stability and mechanical resilience of the superconductor. While a temperature adjustment of the final stage of the RHT cycle appears attractive for optimizing the trade-off between electrical and mechanical performance, two constraints limit this approach. The existence of a *strain irreversibility cliff* [114,121,122] confines viable processing temperature to an exceptionally narrow window. If reacted below $645\,^{\circ}\mathrm{C}$, RRP® conductors exhibit extreme brittleness with irreversible strain limits ($\varepsilon_{\mathrm{irr}}$) below 0.1%, rendering them unsuitable for magnet applications. Secondly, as described earlier, above $675\,^{\circ}\mathrm{C}$, the accelerated grain growth and barrier consumption rapidly degrade both electrical stability and mechanical integrity. This $20\,^{\circ}\mathrm{C}$ window is a tight buffer in a furnace for production-scale equipment where an achievable temperature uniformity across the volume is $\pm 3\,^{\circ}\mathrm{C}$ [123], thus effectively eliminating temperature as a practical optimization parameter.

The duration of the final heat treatment stage thus emerges as a primary feasible variable for improving the electromechanical behaviour of the conductor within the established coil construction technology. This thesis work investigates three strategically selected heat treatment durations at the standard $665\,^{\circ}\mathrm{C}$ temperature. A 50-hour duration constitutes the current standard protocol for the MQXF quadrupoles providing baseline performance characteristics. A duration of 75 hours approaches the upper practical limit for maximizing critical current density while maintaining acceptable mechanical properties before excessive microstructural degradation occurs. A lower limit of 30 hours is chosen where the mechanical properties is expected to improve through limited grain growth and barrier consumption, although with a lower current-carrying capacity. In the Figure 1.14, the respective subelement micrographs at these three chosen durations are marked. The progressive transformation of the A15 phase and consumption of the niobium barrier underpins this selection. Importantly, the selection spans the practical extremes implementable without modifications to existing production methods and infrastructure for the reaction heat treatment of accelerator magnet coils.

1.2.3 Impregnation in epoxy resin

The Vacuum Pressure Impregnation (VPI) process is a current state-of-art technology with which magnet coils are impregnated with epoxy resin after the reaction heat treatment cycle. The primary purpose is mechanical stabilization of the superconductor wires to prevent any movement that could trigger quenches. It also serves as an electrical insulation between the cables. Epoxy resins are thermosetting polymers that consist of two primary components: a base resin (typically containing epoxide groups) and a hardener (also called a curing agent). When these components are mixed at the molecular level, they undergo a chemical reaction known as cross-linking, forming a rigid three-dimensional network that provides mechanical strength and stability.

An epoxy resin system for superconducting magnet applications must satisfy an array of competing technical requirements [124–128] as follows:

1. A long pot life ($> 3\mathrm{h}$) to enable complete impregnation of large coil assemblies.
2. A low viscosity ($< 300\,\mathrm{mPa}\cdot\mathrm{s}$ at processing temperature) to ensure void-free infiltration through complex cable architectures.
3. Sufficiently low processing temperatures ($< 150\,^\circ\mathrm{C}$) to prevent microstructural degradation of the reacted Nb_3Sn phase or thermal damage to the S2-glass insulation system during the curing cycle.
4. Sufficient mechanical integrity and interface adhesion with the superconductor at cryogenic temperatures to withstand electromagnetic forces during operation without debonding or cracking.
5. High radiation resistance critical for operating magnets in accelerator environments, where accumulated doses can reach $10 - 100\,\mathrm{MGy}$ over operational lifetimes.

The VPI process represents a critical manufacturing step where the process parameters such as vacuum level, resin degassing, injection pressure, and curing temperature profile directly influence the mechanical properties of the final composite structure[9]. The impregnation must penetrate through all the components of coil structure, providing mechanical support to prevent conductor motion and maintaining integrity of the electrical insulation. However, achieving complete void-free impregnation through extremely small volumes is particularly challenging for large accelerator magnets [35], over distances exceeding several meters. The quality of the impregnation is generally

[9] A detailed description of the three-stage VPI process, including specific parameters and timelines for MQXF magnet production, is provided in Appendix A.2

characterized by the void content and resin distribution uniformity. These aspects collectively determine the mechanical behavior and reliability of the magnet under operational stresses.

1.2.3.1 Impact of epoxy systems on electromechanical properties

The impregnation-derived properties manifest in the superconducting magnet performance through two primary aspects: the training behavior and current carrying capacity influenced by the strain state of the superconductor. The following epoxy properties critically influence these performance mechanisms:

- **Curing temperature**: The curing temperature constrains the processing protocols and influences residual stress development. Resins with lower curing temperatures of $85 - 110\,^{\circ}\mathrm{C}$ minimize thermal stress but may compromise the final mechanical properties of the assemblies. Systems which cure at $110 - 125\,^{\circ}\mathrm{C}$ are generally chosen to balance processability with performance requirements.

- **Glass transition temperature** : During the VPI process, stress begins to accumulate on cooldown at the glass transition temperature, T_g. Thus, it consequently governs the strain state on further cooldown from ambient to operating conditions. Lower values of T_g reduces the strain state of the superconductor but potentially compromises the room-temperature mechanical integrity. Systems with T_g near room temperature experience plastic deformation during cooling, while higher T_g systems ($> 100\,^{\circ}\mathrm{C}$) accumulate substantial thermal stress that shifts the strain state of Nb_3Sn in the conductor further into compression[129]. On the other hand, a higher T_g is preferable in the case of local hot-spots developed during a quench, in which case the integrity of the resin itself is more likely to be maintained.

- **Thermal expansion coefficient**: The thermal expansion coefficient creates differential strain through its mismatch with metallic components. Epoxy systems exhibit $44 - 68 \times 10^{-6}\,\mathrm{K}^{-1}$ compared to $5 - 20 \times 10^{-6}\,\mathrm{K}^{-1}$ for conductors[101,130,131], generating compressive pre-strain in the Nb_3Sn filaments during cooldown.

- **Fracture toughness at cryogenic temperatures**: The fracture toughness of the epoxy system controls its resistance to crack initiation and propagation under mechanical disturbances. Higher fracture toughness reduces crack propagation rates and consequently, training quenches occurring through the Kaiser effect[57,132], wherein irreversible structural modifications stabilize with successive cycles .

- **Young's modulus**: The Young's modulus, E, of the epoxy resin controls the efficiency of stress transfer between the epoxy matrix and conductor components. Higher moduli improve load distribution but concentrate stresses at material interfaces where damage preferentially initiates. Epoxy-impregnated Nb_3Sn coils exhibit moduli of $33\,\mathrm{GPa}$ at room temperature and $45\,\mathrm{GPa}$ at $4.2\,\mathrm{K}$, substantially exceeding that of polyimide-insulated NbTi systems with $6-7\,\mathrm{GPa}$ and $11-12\,\mathrm{GPa}$ respectively[93].

- **Interface bond strength**: The interface adhesion affects the contact area between the epoxy and conductor surfaces during operational conditions. It ranges from $4\,\mathrm{MPa}$ for lacquer-coated conductors to over $10\,\mathrm{MPa}$ for direct epoxy-conductor interfaces[57,133]. Inadequate adhesion creates preferential failure paths and reduces the effective stress transfer, concentrating loads in the remaining bonded regions.

Research spanning fundamental resin characterization to applied studies in strands and cables demonstrates these property interdependencies. Investigations range from molecular-scale crosslink density optimization to full-scale magnet training behavior, establishing direct correlations between material properties and electromagnetic performance. The geometric constraints of actual magnets prove critical. Operational assemblies feature extremely thin resin layers ($100-200\,\mu\mathrm{m}$) surrounding cables, different from thick test specimens ($10-50\,\mathrm{mm}$) used in laboratory characterization[72,73]. Evidence from Van Oort et al.[134], Wolf et al.[84], Lenoir et al.[135] confirms that strands at cable edges with thicker resin accumulations exhibit lesser degradation compared to interior strands compressed by thin layers, highlighting the importance of representative test geometries.

The following section discusses the epoxy resin systems addressing competing requirements for accelerator magnets, focusing on three formulations selected for systematic investigation in this thesis. These selections represent both current technology baselines and enhanced systems targeting improved fracture toughness of the resin system while maintaining manufacturing feasibility for large-scale magnet production.

1.2.3.2 Epoxy material systems and selection for Nb_3Sn magnets

Material selection for impregnation of a Nb_3Sn accelerator magnet represents a critical optimization parameter with direct implications for damage thresholds, training behavior, and fatigue life under cyclic loading. No single formulation delivers optimal performance across all requirements, viz. fracture toughness at cryogenic temperatures, radiation hardness for accelerator environments, processability for large-scale manufacturing, and thermal properties that minimize stress accumulation during cooldown[124]. In recent years, substantial efforts have been dedicated to developing specialized epoxy resins tailored for Nb_3Sn superconducting accelerator magnet applications[125,127–130]. These collaborative programs systematically characterize the material properties at cryogenic temperatures, radiation tolerance, and processing compatibility to establish formulations meeting the stringent requirements of high-field magnet technology. This kind of research and development is further complemented by characterising the electrical performance of impregnated conductors [74], cables [126,136] and subscale magnets [27,137].

For a systematic investigation of the effect of the impregnation resin on the electrical performance of cables in this thesis, the following three epoxy systems have been selected:

1. **CTD-101K®** is a DGEBA (Diglycidyl Ether of Bisphenol A)-based resin with anhydride hardener that serves as the workhorse for Nb_3Sn accelerator applications including the HL-LHC upgrade [95]. This system establishes the performance baseline against which enhanced formulations are evaluated. It has a well-developed processability and its viscosity remains below $200\,\mathrm{cP}$ for more than 24 hours at $60\,^{\circ}\mathrm{C}$ processing temperature. This enables void-free impregnation of complex coil geometries exceeding several cubic meters [130]. The system achieves a glass transition temperature of $140\,^{\circ}\mathrm{C}$, providing mechanical stability during room-temperature assembly operation [129]. It has a high radiation resistance, maintaining properties up to $38\,\mathrm{MGy}$ proton irradiation, ensures reliability throughout operational lifetimes in accelerator environments [130]. However, its fracture toughness, K_{IC} at 77 K is $1.52\,\mathrm{MPa}\sqrt{\mathrm{m}}$, which renders it susceptible to cracking under moderate stress conditions [130]. This limitation has been implicated in the long training behavior of Nb_3Sn accelerator magnets under development [28].

2. **POLAB Mix** is a modified CTD-101K® formulation, developed at the Polymer Laboratory at CERN, incorporating 10 wt% DY040 flexibilizer. This modification achieves K_{IC} of $2.33\,\mathrm{MPa}\sqrt{\mathrm{m}}$ at 77 K, which is a 53% improvement in fracture toughness at 77 K compared to the baseline (parent) resin. The strategic placement of flexibilizer molecules comprising polyethylene glycol chains, increases spacing between crosslink points by approximately $15 - 20\%$ [130]. The molecular-scale modification enables localized deformation that dissipates stress concentrations before critical stress intensity for crack initiation. With this resin system, the effects of fracture toughness can be isolated while maintaining identical processing protocols. Its glass transition temperature remains unchanged at $140\,^{\circ}\mathrm{C}$. Its viscosity also stays below 200 cP for more than 24 hours at 60 °C, preserving the processability of the parent system. The Young's modulus decreases to $3.07\,\mathrm{GPa}$ from CTD-101K®'s $3.53\,\mathrm{GPa}$, potentially enhancing compliant stress redistribution, while strain at break increases from 1.3% to 1.6% at room temperature, indicating enhanced ductility beneficial during assembly operations.

3. **MSUT-Twente** resin system has an alternative chemistry composed of Araldite MY740 resin with Aradur HY906 hardener and DY062 accelerator. It demonstrates 61% enhanced fracture toughness at 77 K relative to CTD-101K®. With $K_{IC} = 2.44\,\mathrm{MPa}\sqrt{\mathrm{m}}$ at 77 K, it represents the highest fracture toughness among the processable systems [129]. This formulation exhibits slightly higher ball indentation hardness ($245 \pm 12\,\mathrm{MPa}$) and lower

glass transition temperature, $107\,^\circ\mathrm{C}$ compared to CTD-101K® indicating different network structure that may benefit specific stress distributions [129]. However, its pot life is $4-6$ hours and viscosity approaches $500\,\mathrm{mPa\cdot s}$ at processing temperature, constraining impregnation of very large assemblies. Its radiation tolerance comparable to CTD-101K® has been demonstrated, though comprehensive testing beyond $10\,\mathrm{MGy}$ remains ongoing.

Table 1.3: Comparison of relevant properties of the selected epoxy resin systems [95,127,129,130,136]

Property	**Unit**	**CTD-101K**	**POLAB Mix**	**MSUT-Twente**
Fracture toughness, K_{IC} at $77\,\mathrm{K}$	$\mathrm{MPa}\sqrt{\mathrm{m}}$	1.52	2.33	2.44
Fracture toughness, K_{IC} at RT	$\mathrm{MPa}\sqrt{\mathrm{m}}$	0.82	1.17	1.52
Pot life at $60\,^\circ\mathrm{C}$	h	> 24	> 24	4–6
Viscosity at $60\,^\circ\mathrm{C}$	$\mathrm{mPa\cdot s}$	< 200	< 200	< 500
Glass transition temp.	$^\circ\mathrm{C}$	140	140	107
Young’s modulus at RT	GPa	3.53	3.07	3.2–3.8
Strain at break at RT	%	1.3	1.6	1.8–2.1
Thermal expansion	$\times 10^{-6}\,\mathrm{K}^{-1}$	44 ± 4	—	44 ± 4
Radiation dose limit	MGy	> 38	> 38	> 10
Bond strength at RT	MPa	15–20	18–25	12–18
Curing temperature	$^\circ\mathrm{C}$	110–125	110–125	85–110

Several alternative systems were evaluated but ultimately not selected for this investigation due to some fundamental limitations as follows:

- Filled resin systems have the promise of enhanced mechanical performance but face limitations in processability. Alumina-filled resins such as Stycast 2850FT can achieve remarkable training improvements, reaching 80% of critical current in $2-3$ quenches versus $10 - 16$ for unfilled systems [126]. Initial quench currents reach 88% of critical current compared to $57 - 59\%$ for unfilled CTD-101K®. However, particulate fillers are known to increase viscosity beyond vacuum impregnation limits. Moreover, standard glass braid insulation are incompatible for large filler sizes, necessitating alternate insulation techniques [126]. Another critical consideration would be the proof of achieving uniform filler distribution across meter-scale assemblies.

- Two resin formulations with high fracture toughness at low temperatures have been disqualified due to processing and performance limitations. The resin MY750 achieves high fracture toughness ($K_{IC} = 4.7\,\mathrm{MPa}\sqrt{\mathrm{m}}$ at $77\,\mathrm{K}$), which is a threefold improvement over CTD-101K® [129,130]. Yet, its pot life is below 4 hours which would preclude large coil impregnation. Morover, its radiation resistance degrades precipitously below $1\,\mathrm{MGy}$[127]. Its glass transition at $45\,^{\circ}\mathrm{C}$ risks mechanical instability during warm assembly, and risks property change in case of a local hot spots during quenches. The resin system Mix61 demonstrates $2.4\,\mathrm{MPa}\sqrt{\mathrm{m}}$ fracture toughness but exhibits severe bubble formation at doses below $1\,\mathrm{MGy}$, eliminating accelerator applications despite excellent initial properties[127].

- The use of paraffin wax as impregnation for accelerator magnets presents a new alternative to epoxy resins. It has been recently shown that wax impregnation enables Nb_3Sn Rutherford cables to achieve critical current without training[136]. Its low shear modulus, minimal bonding, and low-friction characteristics enable controlled movement during electromagnetic loading rather than an energy release. However, its radiation hardness remains uncharacterized as of date. In the case of wax, conventional pre-compression strategies become inapplicable, necessitating entirely different stress-management infrastructure compared to the current methods.

Impregnation resins serve as the critical interface mediating load transfer, crack arrest, and strain redistribution throughout the composite structure of a Nb_3Sn superconducting magnet. The choice of impregnation system thus influences both its structural integrity and electromechanical performance boundaries. This manifests through competing mechanisms where optimization of one parameter invariably compromises another, constraining the available options for high-field applications.

Under mechanical load, a complex stress distribution occurs within an impregnated Rutherford-type cable geomtery. Stress concentrations are inevitably introduced at locations such as the strand crossover points, material interfaces and resin-void regions - if any. The damage accumulation in the brittle phases follow an irreversible progression where microcracks, once initiated may propagate under subsequent loading cycles. The mechanical environment is fundamentally altered by the hierarchichal multi-scale nature of the structure compared to that of a bulk material. Thus, mechanical characterization of only the latter provides insufficient information of the net influence of impregnation on the integrity of the A15 phase. Similarly, electrical performance metrics mask subsurface damage until degradation reaches irreversible levels, creating false confidence in operational boundaries established through transport current measurements. This disconnect between mechanical damage onset and its manifestation on the electrical behaviour necessitates direct structural evaluation to establish true safety margins for magnet construction and operation.

A systematic quantification of the onset of damage via microcracks and its evolution in the A15 phase of impregnated Nb_3Sn cables under tranverse compressive stress is a primary motivation of this thesis work. Based on their viability as potential candidates for impregnation of large-scale Nb_3Sn accelerator magnets, the three aforementioned epoxy resin systems are chosen to compare the differences of their effect on the onset threshold and evolution of damage in the

A15 phase. For the first two systems (CTD-101K® and POLAB Mix), an additional correlation with electrical measurements is carried out. This qualifies the effect of the resin on the training behaviour and strain state of the superconductor via the current carrying capacity. The findings provide a combined empirical foundation for optimizing impregnation systems for next-generation accelerator magnets.

1.2.4 Electromechanical performance of Nb_3Sn cables subject to transverse compression

The strain-dependent critical current of Nb_3Sn conductors exhibits the characteristic bell-shaped response (described in Section 1.1) under transverse compression, with performance initially improving due to relief in the strain-state before degrading at higher loads through irreversible damage mechanisms. While single-strand characterization provides fundamental understanding of this behavior[77,138,139], cable geometries introduce additional complexity through inter-strand mechanical interactions and non-uniform stress distributions. Moreover, the presence of impregnation materials between strands also further modifies the load transfer pathways. This results in the increase in the presence of stress amplification factors that can initiate damage at nominal stress levels substantially below single-wire thresholds, necessitating dedicated investigation of the electromechanical performance of impregnated cables.

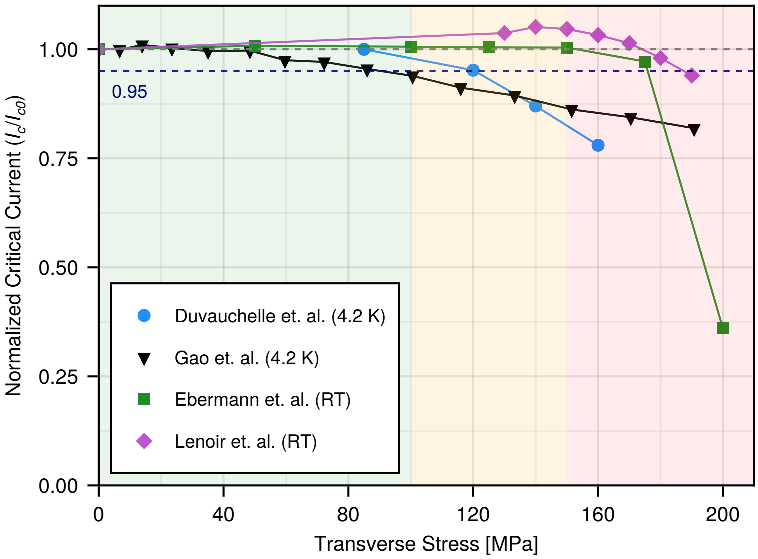

Figure 1.15: Evolution of normalized critical current with applied transverse compression for RRP® Nb_3Sn Rutherford-type cables. Data compiled from studies of different cable layouts with in-situ compression at 4.2 K (Duvauchelle et al.[140], Gao et al.[75]) and room-temperature compression with 50 MPa prestress during cold measurement (Ebermann et al.[141], Lenoir et al.[135]). The shaded regions indicate reversible behavior (green, $< 100\,\mathrm{MPa}$), transition zone with damage onset (orange, $100 - 150\,\mathrm{MPa}$), and irreversible degradation (red, $> 150\,\mathrm{MPa}$).

Table 1.4: Summary of RRP® Nb_3Sn cable studies under transverse compression

Authors	Sample Details	RHT & Impregnation Resin	Irreversible Damage Limit (MPa)	Key Findings on Damage Mechanism
Duvauchelle et al.[140]	18-strand Rutherford cable with 1.0 mm ∅ RRP® 132/169 wires	210 °C/72 h, 400 °C/72 h, 665 °C/50 h; CTD-101K®	∼160	• 4.8 % reversible degradation at 120 MPa upto 13 % degradation at 140 MPa • Degradation primarily associated with B_{c2} reduction • n-value significantly reduced after 160 MPa loading
Gao et al.[75]	Various Rutherford cables with 0.7–1.0 mm ∅ RRP®/PIT wires	Various; CTD-101K®	RRP®: ∼190 PIT: ∼150	• B_{c2} reduced by 7 % (RRP®) and 10 % (PIT) under 150 MPa • Interface alignment critical • No significant degradation after thermal cycling
Ebermann et al.[83,84,141,142]	40-strand double stack with 0.7 mm ∅ RRP® 144/169 wires	210 °C/48 h, 400 °C/50 h, 650 °C/50 h; CTD-101K®	∼175	• Non-monotonic behavior with improvement up to 75 MPa • Longitudinal cracks parallel to applied stress (Mode I fracture) • Damage along 45 ° planes to load
Lenoir et al.[135]	40-strand double stack with 0.7 mm ∅ RRP® 108/127 wires	210 °C/48 h, 400 °C/50 h, 650 °C/50 h; CTD-101K®	∼170	• Mechanical damage appears before electrical degradation • I_c max at 140 MPa with cracks already present • Cumulative loading more damaging than monotonic

Systematic investigations of transverse compression effects on Nb_3Sn cables have employed diverse experimental methodologies[72,74,143–148]. A comprehensive compilation of these studies across different conductor architectures is provided in Appendix A.3. This section discusses specifically the reported findings on the electromechanical behaviour of RRP® architecture Rutherford-type cables from four selected studies. Figure 1.15 presents the evolution of normalized critical current with applied transverse stress for these studies, with key experimental parameters summarized in Table 1.4.

- **Duvauchelle et al.[140]**: The study applied in-situ transverse loads from $85 - 160\,\mathrm{MPa}$ at $4.2\,\mathrm{K}$ with critical current measurements performed at each pressure level, followed by return to $80\,\mathrm{MPa}$ after each increment to distinguish between reversible and irreversible degradation. The measurements revealed reversible degradation of 4.8% at $120\,\mathrm{MPa}$ increasing to 13% at $140\,\mathrm{MPa}$, with the degradation mechanism attributed primarily to strain-induced reduction of B_{c2} rather than filament breakage. Irreversible degradation of

$1.8 - 2.4\%$ is measured up to $140\,\mathrm{MPa}$, which increased to 11.5% after $160\,\mathrm{MPa}$ loading, accompanied by a significant reduction in n-value that indicated irreversible damage to the conductor.

- **Gao et al.**[75]: The study applied in-situ transverse loads from $0 - 250\,\mathrm{MPa}$ at $4.2\,\mathrm{K}$ with critical current measurements at multiple pressure levels, determining reversibility by unloading completely to assess permanent degradation after each loading cycle. The cables showed initial critical current improvement starting from approximately $20\,\mathrm{MPa}$ and reaching a maximum around $50\,\mathrm{MPa}$, followed by gradual degradation at higher pressures, with the critical current decreasing by about 10% of its peak value at $130\,\mathrm{MPa}$. The defined irreversible degradation threshold where a permanent critical current reduction of about 2% was observed after unloading was measured to occur at $190 \pm 3\,\mathrm{MPa}$.

- **Ebermann et al.**[83,84,141]: The study successively applied transverse compression at room temperature from $50 - 200\,\mathrm{MPa}$ on the sample followed by critical current measurements at $4.2\,\mathrm{K}$ (with $50\,\mathrm{MPa}$ prestress) after each applied load. No critical current degradation was detectable after loading up to $150\,\mathrm{MPa}$. A degradation of about 4% was observed after applying $175\,\mathrm{MPa}$, while subsequent loading to $200\,\mathrm{MPa}$ resulted in severe degradation. Metallographic studies identified the onset of cracks in the superconductor between $150\,\mathrm{MPa}$ and $175\,\mathrm{MPa}$.

- **Lenoir et al.**[135]: Similar to the previous, this study also applied room-temperature transverse compression successively from $130 - 190\,\mathrm{MPa}$ on the sample followed by critical current measurements at $4.2\,\mathrm{K}$ (under $50\,\mathrm{MPa}$ prestress). A critical current degradation of $\approx 5\%$ from the intial virgin sample is measured at $\approx 170\,\mathrm{MPa}$, however the performance reduction from the peak value begins at $140\,\mathrm{MPa}$ while n-value reduction begins at $160\,\mathrm{MPa}$ indicating the damage within the conductor. A metallographic examination on a separate set of specimens revealed that micro-cracks were already present at $140\,\mathrm{MPa}$ in 36% of examined strands, demonstrating that mechanical damage precedes detectable electrical degradation by at least $30\,\mathrm{MPa}$.

These investigations of RRP® Nb_3Sn cables under transverse compression reveal consistent degradation behavior progressing through three distinct stages. In general, an improvement in performance of about $3 - 5\%$ is measured with increasing load from the virgin state, attributed to relief of compressive strain state in the A15 phase. Below $\approx 150\,\mathrm{MPa}$, cables exhibit reversible performance changes generally attributed to strain-induced modifications of the superconducting critical parameters, particularly B_{c2} [74,149–151]. The transition region between $150 - 170\,\mathrm{MPa}$ marks the onset of irreversible phenomena, where mechanical damage impacts the electrical performance. Critically, Lenoir et al. demonstrated that this mechanical damage precedes detectable electrical degradation by $30 - 40\,\mathrm{MPa}$, with cracks observed at $140\,\mathrm{MPa}$ despite maximum I_c

performance, challenging conventional reliance on transport measurements alone for establishing operational limits. This study also showed the enhanced sensitivity under cumulative loading compared to monotonic stress, has profound implications for magnet assembly and operation where cyclic thermo-mechanical loads are inherent. These findings establish that while electrical measurements provide essential performance verification, metallographic characterization is indispensable for determining true mechanical integrity limits, suggesting operational stress limits of $150 - 180\,\mathrm{MPa}$ may already permit subcritical damage accumulation with potential long-term reliability consequences.

1.3 Motivation

Next-generation accelerator magnets are targeted to operate with magnetic fields beyond $15\,\mathrm{T}$. In this regime, transverse stresses approach the electromechanical limits of Nb_3Sn. Recent investigations reveal that mechanical damage accumulation precedes electrical detection by a significant margin. While transport current measurements indicate irreversibility in the electrical performance of RRP® Rutherford-type cables due to transverse compression in the range of $150 - 200\,\mathrm{MPa}$, mechanical damage in the form of microcracks initiate in the A15 phase at substantially lower stresses and accumulates irreversibly without corresponding electrical signatures. The offset between damage onset and electrical manifestation implies that manufacturing and operational limits derived solely from critical current measurements may permit subcritical damage accumulation with implications for long term magnet reliability.

Although the strain sensitivity of Nb_3Sn has been extensively characterised, the relationship between processing parameters and mechanical damage under transverse compression remains inadequately understood. Current literature documents limited systematic data on crack initiation thresholds and microstructural features controlling propagation or processing strategies that enhance electromechanical behaviour. This knowledge gap constrains both the optimization of conductor processing protocols and the definition of operational boundaries for magnets approaching material limits. Systematic quantification of the onset and evolution of mechanical damage therefore provides an additional metric for optimizing the electromagnetic performance.

Rather than pursuing radical conductor redesign, this thesis proposes identifying incremental modifications to existing technologies that can yield significant performance improvements. Two specific opportunities emerge from the literature:

1. **Reaction heat treatment optimization**: The temperature and duration of the final stage of the RHT cycle for A15 formation significantly influences electromechanical properties of the conductor through its effects on the microstructure as discussed in Section 1.2.2. Given the narrow window of the temperature for optimal phase formation, the duration of heat treatment is proposed as a primary adjustable parameter.

2. **Impregnation resin selection**: Enhanced resin systems with improved fracture toughness, described in Section 1.2.3, offer potential for better stress distribution and damage mitigation without requiring changes to established impregnation processes.

This thesis addresses the following specific research questions:

1. What are the true thresholds for the onset of mechanical damage in Nb_3Sn Rutherford-type cables under transverse compression, and how do these thresholds correlate with electrical performance degradation?
2. Can the minimal prestress limit to ensure electromechanical integrity of an impregnated cable under operational conditions be quantified?
3. Can modification of reaction heat treatment duration improve mechanical resilience without unacceptable sacrifice of critical current density?
4. To what extent can advanced impregnation resin systems enhance resistance to damage in Nb_3Sn cables?
5. Does a combination of the two processing parameters exhibit effects that exceed any benefits of individual optimizations?

By systematically investigating these questions through the experimental methodologies detailed in Chapter 2, this thesis aims to establish quantitative relationships between processing parameters, microstructural features, and electromechanical performance. The findings, presented in Chapter 3, provide practical guidelines for optimizing conductor processing to achieve maximum electrical performance while maintaining mechanical integrity under the demanding conditions of next-generation accelerator magnets.

2 Experimental Methods

The electromechanical behaviour of a Nb_3Sn high-field accelerator magnets is crucially determined by several operational procedures in constructing the magnet such as reaction heat treatment cycle, impregnation and applied prestress on the magnet itself. The aim of this work is to show that the behaviour may be improved by optimising one or more of these procedures if the lower limit of damage onset and evolution characteristics are known.

This chapter presents the experimental methods used to characterize the electrical behaviour and quantify the onset and evolution of damage in the A15 phase. The experimental program comprises two separated complementary tracks via electrical and mechanical characterization. Both tracks employ conductor configurations (wires or cables) appropriate to specific objectives. The sample preparation and testing methodology are detailed through the following sections:

- **Section 2.1 - Electrical Characterization**: This section presents the electrical testing methods employing both wire-level and cable-level measurements to establish superconducting performance.
- **Section 2.2 - Mechanical Characterization**: This section details the development of a specialized compression bench for precise application of transverse compressive stress on Nb_3Sn cables. It also describes the novel damage mapping approach developed to quantify crack density at multiple structural scales from individual subelements through complete cable assemblies.

These methodologies aim to address the critical knowledge gaps identified in Chapter 1 by enabling direct correlation between processing choices and performance limits. The parallel characterization of electrical and mechanical properties on identical conductor batches establishes causal relationships that separated individual studies may not reveal. Significantly, the damage mapping methodology provides the first quantitative framework for establishing mechanical thresholds based on microstructural evidence rather than electrical degradation alone, a capability essential for defining and improving true operational limits in next-generation high-field magnets.

2.1 Electrical characterisation

The goal of the electrical measurements in this work is to characterise the critical superconducting properties that define conductor performance under varying processing parameters. This section describes the experimental methods for this type of characterization through the following subsections:

- **Section 2.1.1 - Measurements on wires**: Wire-level measurements are used to establish intrinsic superconducting properties, viz. critical current density, field dependence, and residual resistance ratio following standardized protocols. The virgin wire data provides manufacturing quality benchmarks, while extracted wire (after cabling) data quantify cabling degradation through direct performance comparison. The wire-level characterization is the primary method used for the studies on effect of variation of RHT cycle on electrical behaviour.
- **Section 2.1.2 - Measurements on cables**: Cable-level testing is employed to investigate electrical performance of the Rutherford-type cables capturing effects inaccessible through wire measurements including training behavior and the influence of impregnation resin systems. The cable-level characterization serves as the primary benchmark for the electrical performance of the cables used in this work. It is further used to study the effect of insufficient prestress and variation of impregnation resin on its electrical behaviour.

2.1.1 Measurements on wires

The electrical characterization of Nb_3Sn wires follows standardized protocols established by the Versailles Project on Advanced Materials and Standards (VAMAS)[152,153] consortium. This approach ensures consistent methodology across different testing facilities and reliable comparison of results obtained at different laboratories.

2.1.1.1 Critical current measurements

The critical current measurements are performed in liquid helium at $4.2\,\mathrm{K}$ using a cryogenic test station capable of generating background magnetic fields up to $15\,\mathrm{T}$. A schematic of the measurement setup is in Figure 2.1. Its configuration accommodates two VAMAS barrels, each incorporating a wound wire sample, within a single sample insert. This enables simultaneous testing of two samples during each cooldown. The current leads at the top of the cryostat allow switching between samples using automated changeover switches, with a maximum power supply capacity of 2500 A. The samples are wound helically on the VAMAS barrels, as seen in the figure. The applied background magnetic field is parallel to the barrel axis, resulting in an angle of approximately 88.2° between the strand and the applied magnetic field direction [154].

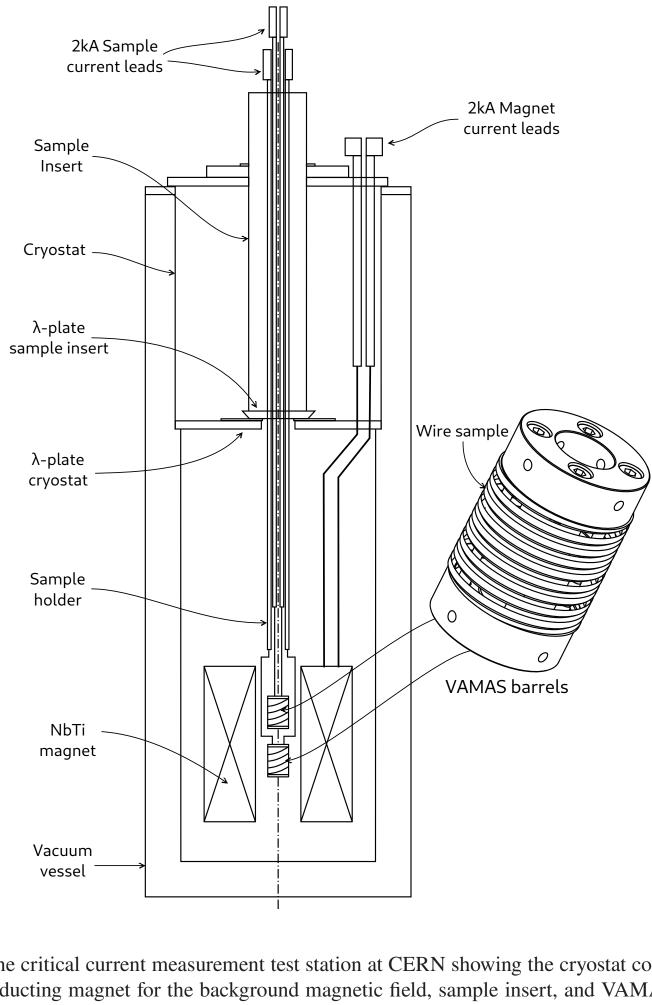

Figure 2.1: Schematic of the critical current measurement test station at CERN showing the cryostat configuration with NbTi superconducting magnet for the background magnetic field, sample insert, and VAMAS barrels. The system accommodates two VAMAS barrels within a single sample insert, with 2 kA current leads for both magnet and sample circuits. The λ-plates separate the superfluid helium bath from the normal liquid helium reservoir in both the main cryostat and sample insert.

The specifications of the RRP® Nb_3Sn wires used in this study are presented in Table 2.1. Wire samples were selected from MQXF quadrupole production inventory to ensure representative performance distribution.

Table 2.1: Specifications of Nb_3Sn wire used for electrical characterization [27,79].

Parameter	Unit	Value
Wire diameter	mm	0.85
Number of subelements	(-)	108
Stack configuration	(-)	127
Cu/non-Cu ratio	(-)	1.2 ± 0.1
Effective filament diameter	μm	50-55
Superconductor fraction	(-)	0.55
Nb:Sn mass ratio	(-)	3.6 : 1
Ti doping concentration	at.%	0.7-1.0
Manufacturer	-	Bruker OST

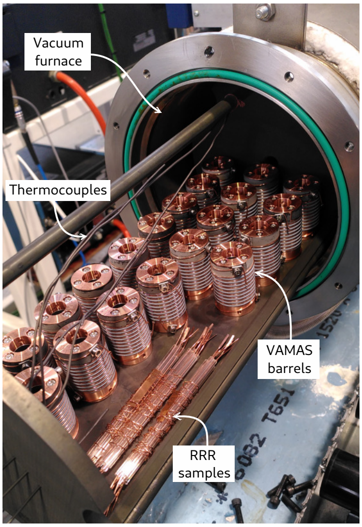

Figure 2.2: Picture of the vacuum furnace insert for reaction heat treatment of Nb_3Sn wire samples at CERN. Multiple VAMAS barrels containing wound wire samples and RRR measurement specimens are positioned within the furnace chamber. Thermocouples ensure temperature uniformity across all samples during the heat treatment cycle.

For the sample preparation, wire segments of approximately $2\,\mathrm{m}$ length are carefully wound onto Ti-6Al-4V (Ti-6-4) alloy VAMAS barrels. The titanium alloy provides a thermal expansion coefficient that closely matches the Nb_3Sn wires, minimizing strain effects during thermal cycling. The winding is performed under controlled tension of $20\,\mathrm{N}$ to ensure uniform contact with the barrel surface. As a standard practice, two pairs of voltage taps are attached to the wire approximately $60\,\mathrm{mm}$ and $90\,\mathrm{mm}$ apart, allowing for redundancy in measurements. The $60\,\mathrm{mm}$

voltage tap lengths are usually sufficient to obtain a reliable I_c measurements while the latter is used in case of abnormal measurement signals. For the RRR measurements described in the following section, shorter wire segments (10-15 cm) are cut from the same billets.

Several samples are reacted simultaneously in the same furnace, as seen in Figure 2.2 under high vacuum ($< 10^{-5}\,\mathrm{mbar}$) to prevent oxidation during the reaction process. The furnace used for heat treatments is equipped with multiple thermocouples positioned such that temperature uniformity is ensured across all samples. The ramp rates, dwell temperatures, and hold durations for the defined RHT cycle are programmed using a PID controller system that maintains temperature stability of better than $\pm 2\,^{\circ}\mathrm{C}$ during the cycle.

The electrical characterization measurements for each sample are conducted at multiple background fields, ranging from 12 to $14.5\,\mathrm{T}$ in $0.5\,\mathrm{T}$ increments, establishing the magnetic field dependence of critical current of the conductor. The supplied current is ramped at $10\,\mathrm{A/s}$ while the voltages across the sample are continuously monitored. The Figure 2.3a presents an example of the typical raw voltage-current characteristics after offset correction. The electric field characteristics for these measurements are then extracted from the voltage measurements by using the effective distance between the voltage taps ($60\,\mathrm{mm}$), shown for the corresponding exemplary measurement in Figure 2.3b.

The I_c and n-value are extracted from the electric field-current characteristic using a power law fit, described in Equation 2.1 applied for $I > 0.6\, I_{E_c}$:

$$E = a + bI + E_c \left(\frac{I}{I_c} \right)^n \tag{2.1}$$

where:

- E is the measured electric field across the voltage taps [$\mu\mathrm{V/cm}$]
- a is the offset term accounting for residual voltages in the measurement circuit [$\mu\mathrm{V/cm}$]
- b is the linear resistance coefficient from ohmic contributions [$\mu\mathrm{V/(cm \cdot A)}$]
- I is the transport current ramped at $10\,\mathrm{A/s}$ during measurement [A]
- $E_c = 0.1\,\mu\mathrm{V/cm}$ is the electric field criterion defining the transition threshold
- I_c is the critical current where the electric field reaches E_c [A]
- n is the transition index characterizing the steepness of the V-I curve

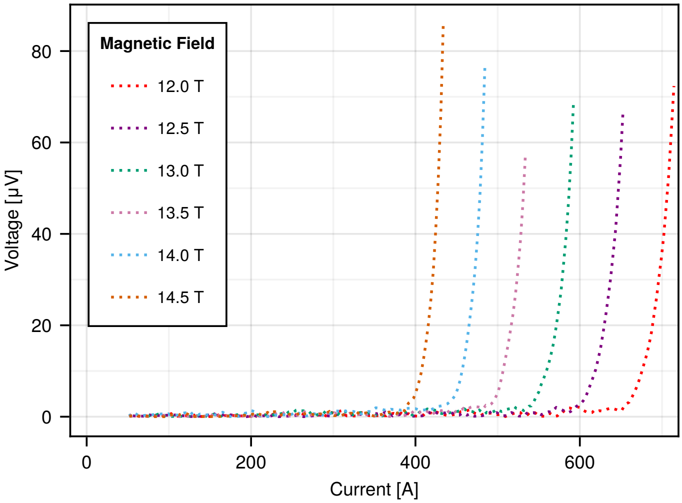

(a) Typical raw voltage-current characteristics at various magnetic fields from $12.0\ \mathrm{T}$ to $14.5\ \mathrm{T}$. The offset voltage has been corrected to align the baseline voltages.

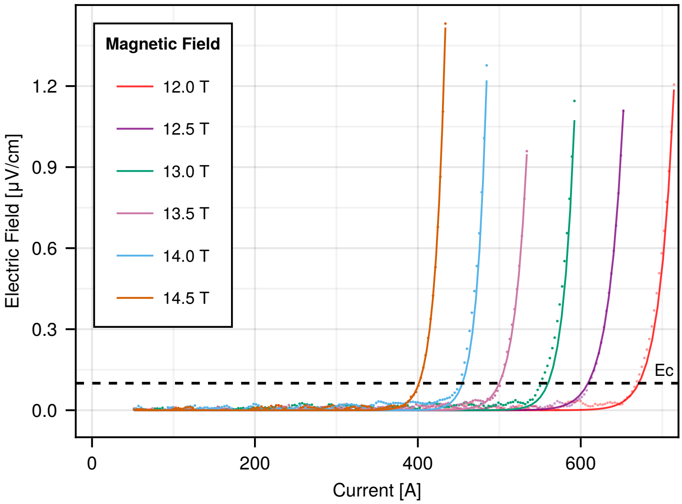

(b) Electric field versus current characteristics derived from the voltage data shown in Figure 2.3a. The solid lines represent power law fits to the experimental data, from which both I_c and n-value are extracted using Equation 2.1. The horizontal dashed line indicates the $E_c = 0.1\ \mu\mathrm{V/cm}$ criterion used for the power law fits.

Figure 2.3: Representative critical current measurements for a Nb_3Sn wire (CERN sample Idn: AO08S00196A01UY) with 50-hour heat treatment at $4.2\ \mathrm{K}$. The measurements span magnetic fields from $12.0\ \mathrm{T}$ to $14.5\ \mathrm{T}$, demonstrating the systematic decrease in critical current with increasing field strength.

As is seen in the Figure 2.3, the voltage remains negligible while the wire is fully superconducting, then rises sharply as dissipation begins due to flux flow at critical current. At higher magnetic fields, flux pinning becomes less effective resulting in a more gradual onset of dissipation (lower n-values) and reduced critical currents as the increased flux density and reduced pinning force density facilitate earlier vortex motion.

The electromagnetic characterization requires correction for the self-field generated in the wire. The peak magnetic field experienced by the conductor is given by:

$$B_{p,wire} = B_{\text{a}} + B_{\text{self}} \tag{2.2}$$

where:

- B_p is the peak magnetic field at the location of maximum field intensity [T]
- B_{a} is the applied background field from the test station magnet [T]
- B_{self} is the self-field contribution from the transport current in the wire [T]

For Nb_3Sn wires wound on VAMAS barrels, the self-field component is given by [154]:

$$B_{\text{self}} = \left[\frac{2}{R^*} - 0.9\right] I_c \times 10^{-4} \tag{2.3}$$

where:

- I_c is the critical current [A]
- $R^* = 0.84R$ is the effective radius accounting for current distribution, with $R = 0.425\,\text{mm}$
- The term $\frac{2}{R^*}$ represents the straight wire self-field coefficient
- The factor 0.9 corrects for the helical winding geometry on the barrel

The critical current density in Nb_3Sn follows the USL described in Section 1.1:

$$I_c = \frac{C}{B_p} b^p (1-b)^q \tag{2.4}$$

where:

- C is the pinning force strength parameter [$\text{A} \cdot \text{T}$]

- B_p is the peak field including applied and self-field contributions [T]
- $b = B_p/B_{c2}$ is the reduced field, with $B_{c2} \approx 25\,\mathrm{T}$ at $4.2\,\mathrm{K}$
- $p = 0.5$ is the low-field exponent from the Kramer flux shear model and $q = 2$ is the high-field exponent for collective flux-lattice shearing [10]

Figure 2.4 demonstrates the scaling law fit for the measurements shown in Figure 2.3 over the measured field range $12.0 - 14.5\,\mathrm{T}$, demonstrating agreement between the model and experimental values. The extracted parameters, B_{c2} and C, fully characterize the electromagnetic behavior, enabling performance predictions for magnet design beyond the measured range.

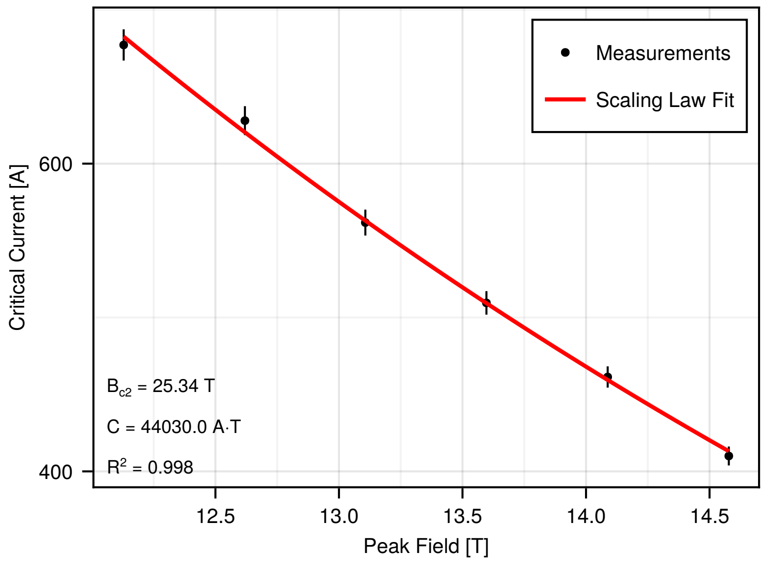

Figure 2.4: Critical current versus peak field for Nb_3Sn wire after 50-hour heat treatment at $4.2\,\mathrm{K}$. The solid line shows the fit to Equation 2.4 with extracted parameters $B_{c2} = 25.3\,\mathrm{T}$ and $C = 44030.0\,\mathrm{A \cdot T}$.

2.1.1.2 Residual resistance ratio measurements

The residual resistance ratio quantifies the purity of copper by comparing its electrical resistance at room temperature ($293\,\mathrm{K}$) to that at cryogenic temperature ($20\,\mathrm{K}$) just above the superconducting transition):

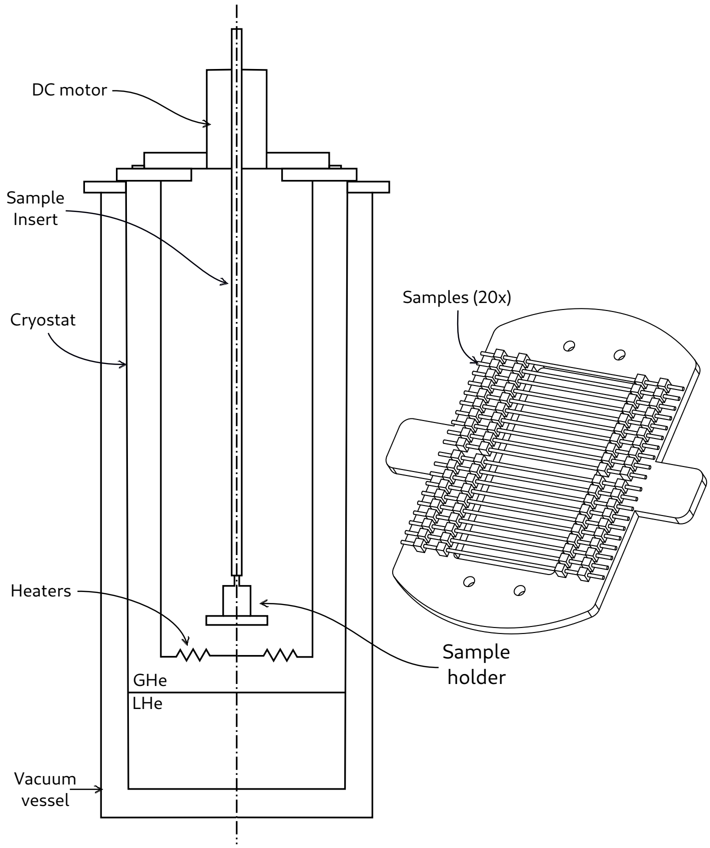

Figure 2.5: Schematic of the RRR measurement setup at CERN showing the cryostat configuration with sample insert, vacuum vessel, and Direct Current (DC) motor for sample positioning. Resistive heaters within the setup enable controlled temperature regulation, while PT100 sensors distributed along the depth monitor temperature gradients during the measurement cycle. The sample holder accommodates upto 20 wires specimens mounted for four-point resistance measurements.

$$\mathrm{RRR} = \frac{R(293\,\mathrm{K})}{R(20\,\mathrm{K})} \tag{2.5}$$

where:

- $R(293\,\mathrm{K})$ is the resistance at room temperature where phonon scattering dominates [Ω]
- $R(20\,\mathrm{K})$ is the resistance just above T_c where impurity scattering dominates [Ω]

For a Nb_3Sn conductor, the RRR represents a critical stability parameter, with specifications requiring values exceeding 100 for MQXF magnets after cabling [28]. The RRR directly impacts thermal and electrical stability during operation, providing essential margin for quench protection. As described in Section 1.2.2, this metric experiences systematic degradation during the cabling process. Environmental control during reaction heat treatment similarly affects RRR values, with contamination or oxidation significantly reducing the electrical conductivity of the copper matrix. These characteristics make RRR measurements valuable for quality control, providing rapid first-order assessment of both cabling and reaction heat treatment procedures. The advantage of quicker measurements also enables efficient batch screening and process optimization.

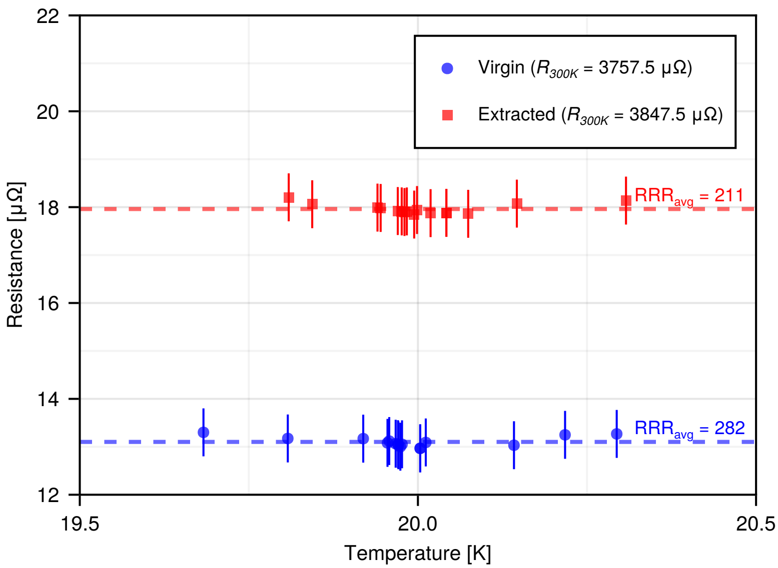

Figure 2.6: Temperature-dependent resistance measurements near the superconducting transition for virgin and extracted Nb_3Sn wires. The virgin wire (blue) exhibits an RRR of 282, while the extracted wire (orange) shows a reduced RRR of 211, representing a 25% reduction due to the cabling process.

The measurement setup, illustrated in Figure 2.5, consists of a cryostat equipped with a sample holder that accommodates up to 20 wire samples for simultaneous testing. The system incorporates a motorized sample insertion mechanism with PID-controlled positioning, vacuum vessel for thermal isolation, and a bipolar Peltier element with PID regulation for the warm reference measurement. For temperature monitoring, calibrated Cernox® and Pt100 resistive temperature sensors are positioned on the sample holder, with automatic switching between sensors depending on the temperature range. The measurements are conducted during controlled warm-up from liquid helium temperature. The warming rate and sample position are regulated by PID controllers to achieve temperature stability better than $\pm 0.25\,\mathrm{K}$ during the critical measurement region at $20\,\mathrm{K}$. A measurement current of $2.5\,\mathrm{mA}$ is applied with both positive and negative polarity, with resistance calculated by averaging the two measurements to eliminate thermal offsets. The current source maintains stability $\pm 0.01\%$, while voltage measurement uses a nanovoltmeter with $10\,\mathrm{nV}$ resolution.

As aforementioned, RRR measurements have been performed on both virgin wires and wires extracted from cables after the cabling process. The virgin wires represent the baseline condition directly from the manufacturer, while extracted wires have undergone the mechanical deformation associated with Rutherford cable fabrication. Figure 2.6 shows typical measurement results for RRP® wires comparing virgin and extracted conditions, demonstrating the systematic reduction in RRR values due to cabling degradation.

2.1.2 Measurements on cables

The cable measurements employ an *inverted double-stack cable* sample configuration consisting of two Rutherford-type cables positioned with opposing keystone orientation so as to produce a net rectangular cross-section assembly. The sample is prepared following the standard wind-and-react protocol and vacuum resin impregnation process. These type of measurements have been used in this work to qualify the baseline performance of the cables, the effect of loss of prestress on the cables and influence of varying the impregnation resin on the electrical behaviour.

2.1.2.1 Description of the test station

The Facility for Reception of Superconducting Cables (FRESCA) at CERN has originally been designed for quality control testing of NbTi Rutherford cables for the LHC magnets[155]. It has been integral to the qualification of superconducting cables for major projects, including the original LHC NbTi cables and subsequently has accumulated extensive experience in cable testing for large-scale accelerator projects[135,141,149,156,157]. The facility has undergone systematic modifications and upgrades to accommodate the specific requirements of Nb_3Sn technology[158], including enhanced cryogenic control, data acquisition, magnet protection systems and modified sample holder configurations.

A schematic overview of the FRESCA test station with its main components is shown in Figure 2.7. It is of a double-cryostat design consisting of an outer cryostat which houses a $1.3\,\mathrm{m}$ long NbTi dipole magnet capable of generating background fields up to $9.6\,\mathrm{T}$. The design of the dipole magnet provides a usable aperture of $88\,\mathrm{mm}$ diameter for accommodating the inner cryostat. The inner cryostat has a $72\,\mathrm{mm}$ diameter aperture for the sample insert. With this configuration, the sample can be changed by warming up only the inner cryostat. This configuration reduces helium consumption and turnaround time between measurements, allowing for high-throughput testing capabilities essential for comprehensive cable characterization campaigns.

Both the cryostats operate with a two-bath design, using λ-plates to separate the $1.9\,\mathrm{K}$ (superfluid helium) lower bath from the $4.2\,\mathrm{K}$ (normal liquid helium) upper bath, maintained at atmospheric pressure. Two independent sub-cooled superfluid refrigeration systems provide approximately $15\,\mathrm{W}$ cooling capacity at $1.9\,\mathrm{K}$ for each cryostat. The magnetic field in the central region of the dipole magnet exhibits homogeneity of 3% over approximately $600\,\mathrm{mm}$ along the sample axis. The magnet is energized by a dedicated $16\,\mathrm{kA}$ power supply with $6\,\mathrm{V}$ output and 1 quadrant operation, utilizing $16\,\mathrm{kA}$ power converters equipped with DC Current Transformer (DCCT) and Function Generator/Controller (FGC) systems. The orientation of the background field can be adjusted relative to the sample by rotating the sample holder, allowing for measurements with the

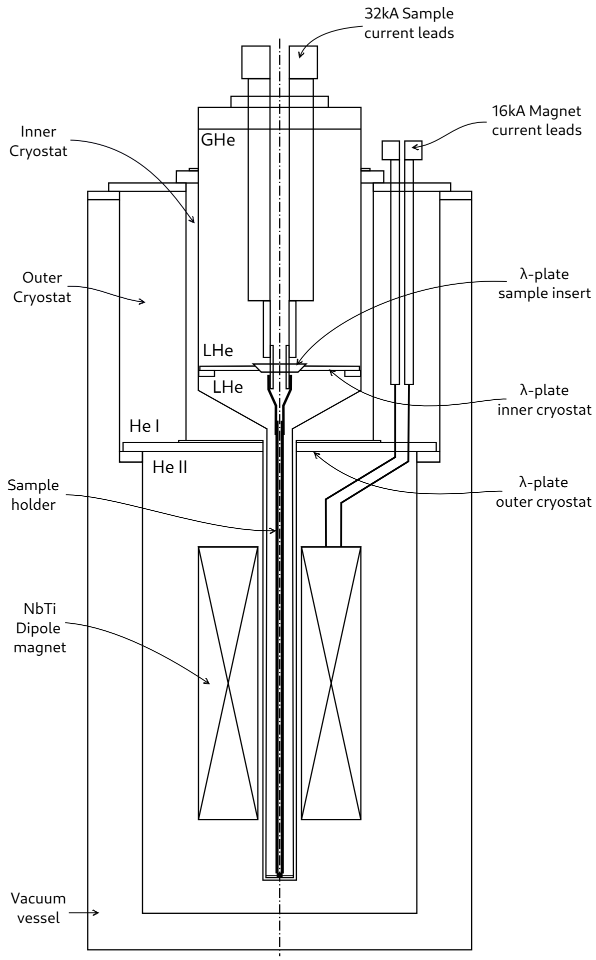

Figure 2.7: Schematic overview of the FRESCA test facility at CERN showing the main components: outer cryostat with background dipole magnet, inner cryostat with sample insert, cryogenic systems, power supplies, and data acquisition and control systems. The double-cryostat configuration allows for efficient sample exchange while maintaining the background magnet at cryogenic temperatures.

peak magnetic field perpendicular or parallel to the cable width. The field direction can also be switched by changing the polarity of the current injection to the magnet. Only the latter is used in this thesis work. The FRESCA test station is integrated within the test infrastructure at the laboratory that includes a $2\,\mathrm{g/s}$ LHe cold box, $6\,\mathrm{kL}$ He buffer, and GHe recovery system.

The **sample current circuit** consists of a $32\,\mathrm{kA}$ power supply, also equipped with DCCT and FGC systems and providing current stability within $\pm 0.1\%$ of the operating value. The current is delivered to the sample through water-cooled copper current leads that connect the room temperature power terminals to the cryostat. Below that, the current leads are cooled with gaseous helium until the superconducting parts of the circuit inside the cryostat, which are maintained at liquid helium temperature. The current path in the sample follows a *hairpin* configuration, with the current flowing in opposite directions in the two cable sections. This arrangement creates an anti-parallel current flow as the current enters through one leg of the sample, traverses the bottom connection, and returns through the other leg. Current uniformity among the strands is ensured by the low-resistance connections at the sample ends, with resistances below $1\,\mathrm{n\Omega}$ at cryogenic temperatures. The integrity of the current path is continuously monitored during testing, with multiple voltage taps allowing for detection of localized transitions.

The **data acquisition system** of the test-station provides high-resolution, real-time monitoring of sample performance under varying test conditions. The primary measurement system consists of eight Keithley $2182\mathrm{A}$ nanovoltmeters for precision low-voltage measurements, with input channel selection managed through a National Instruments PXIe matrix switching system (2×32 input channels, 16 output channels). The nanovoltmeters achieve sampling rates of approximately $10\,\mathrm{Hz}$ with appropriate filtering and electromagnetic shielding to minimize interference, which is particularly critical during high-current and high-field operation. A high-speed transient recorder (18-bit resolution, $200\,\mathrm{mV}$ range, $100\,\mathrm{kHz}$ sampling rate) provides time-resolved voltage measurements that enable precise identification of quench initiation sites within the sample.

The protection of the background magnet during a quench event is ensured by the universal Quench Detection System (uQDS)[159], a **quench detection system** developed at CERN. The station employs a redundant mechanical switch configuration consisting of four $7\,\mathrm{kA}$ switches arranged with two switches in parallel (providing $14\,\mathrm{kA}$ capacity) and two such parallel pairs in series for enhanced reliability. The switches achieve opening times of less than $20\,\mathrm{ms}$, with total response time (including discrimination and reaction delays) not exceeding $40\,\mathrm{ms}$. The circuit incorporates a $40\,\mathrm{m\Omega}$ dump resistor and a comprehensive interlock system that continuously monitors various safety signals across the entire installation, including cryogenic levels, magnet temperature, vacuum integrity, and sample conditions. This integrated safety system prevents operation if any monitored parameter falls outside acceptable ranges. The sample-specific quench detection is implemented through continuous monitoring of voltage signals across different sections of the sample and current leads, by comparison to predetermined threshold values via the so-called POTAIM[1] protection system. When any threshold is exceeded for a given discrimination time, the protection system initiates a rapid discharge sequence that includes immediate trigger signal to the power supply for a current ramp-down and activation of energy extraction resistors

[1] Potection-Amaint: An older generation of quench detection system used at the major test facilities at CERN

to accelerate current decay. The voltage-based protection for both the sample and current leads is carefully tuned and checked prior to every measurement run.

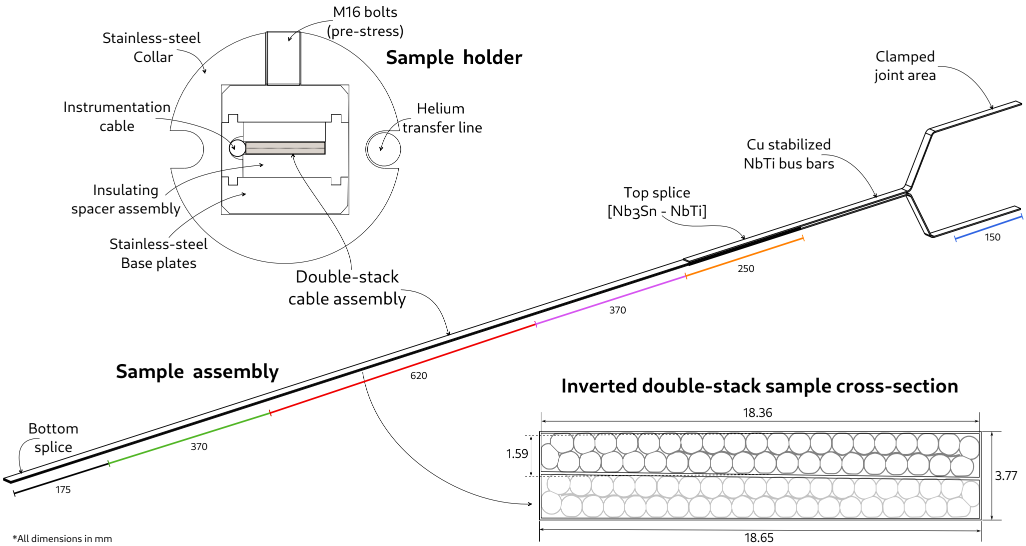

Figure 2.8: Cross-sectional schematics of the sample holder assembly (top-left) of FRESCA at CERN showing the structural configuration with stainless steel collar, M16 prestress bolts, and the baseplates and insulating spacer assembly containing the sample and instrumentation cable; (center) the sample assembly showing the complete current path from Cu-stabilized NbTi bus bars through the top splice to the Nb_3Sn double-stack cable and bottom splice, the lengths of regions of high field, top and bottom low fields and splices are marked; (right) the rectangular cross-section of the inverted double-stack configuration with nominal dimensions of a single cable and fully impregnated assembly.

The sample holder for FRESCA, shown in Figure 2.7, is designed as a cylindrical structure with outer diameter of $69\,\mathrm{mm}$ that fits within the aperture of the inner cryostat. The overall length of the sample holder is approximately $2\,\mathrm{m}$, accommodating the entire sample assembly. A schematic of its cross-section in the sample area is shown in Figure 2.8. The sample holder consists of two main components: the structural stainless-steel collar that provides mechanical support and the inner assembly comprising the stainless steel base plates and the intermediate insulating spacer assembly that contain the double-stack cable sample assembly. The collar is a welded stainless steel tube structure with an inner cavity of $35 \times 35\,\mathrm{mm}$ and prestress application capability via M16 screws. It is mechanically connected to the sample insert underneath the λ-plate, as shown in Figure 2.7. On insertion in the test station, it is additionaly secured within the inner cryostat using a locking pin at the bottom, which ensures precise positioning and prevents movement during testing. The design also accommodates the instrumentation wiring for the sample, which further exits through dedicated feedthroughs at the top of the sample insert.

2.1.2.2 Description of sample preparation

The complete sample assembly comprises two Nb_3Sn cables arranged in an inverted double-stack configuration connected at the bottom to form the hairpin current path. Each cable leg is terminated at the top with a soldered connection to Cu-stabilized NbTi bus bars, creating a continuous electrical circuit with anti-parallel current flow. A schematic of the assembly with a cross-section is shown in Figure 2.8. The NbTi bus bars of the sample are connected to the power supply bus bars of the sample insert via clamped connections.

All cables used for this study are second-generation RRP® technology used for the MQXF magnets [160]. The specifications of the cable are detailed in Table 2.2. The cables (pre-insulated with in-situ S2-glass braiding) are sourced from excess inventory produced for the MQXFB quadrupole magnets at CERN.

Table 2.2: Main specifications of the MQXFB Nb_3Sn Rutherford cable. [160]

Parameter	**Unit**	**MQXFB**
Number of strands	(-)	40
Strand diameter	mm	0.85
Strand architecture	-	RRP® 108/127
Bare cable width	mm	18.15 ± 0.05
Bare cable mid-thickness	mm	1.525 ± 0.01
Keystone angle	°	0.40 ± 0.1
Transposition pitch (T_p)	mm	109 ± 3
Stainless steel core width	mm	12.0 ± 0.1
Stainless steel core thickness	μm	25.0 ± 1.5
S2 - glass insulation thickness (nominal)	mm	0.145
After reaction and insulation:		
Reacted cable width (nominal)	mm	18.65
Reacted cable thickness (nominal)	mm	1.88

The sample preparation produces the hairpin-type assembly through a sequential wind-and-react process followed by vacuum pressure impregnation. The key steps of the sample preparation procedure are summarized below:

1. **Cable selection and initial stacking**: Two $2\,\mathrm{m}$ lengths of cable are selected from the qualified inventory for the MQXF magnets of the HL-LHC. They are stacked with opposing

keystone angles, as shown in Figure 2.8 within the reaction heat treatment mold, creating a net rectangular cross-section from the individual trapezoidal geometries.

2. **Reaction heat treatment**: The stacked cables undergo the chosen RHT protocol cycle (refer Figure 1.12) in a circulated argon atmosphere protection to prevent oxidation, transforming the ductile precursor wires into the final brittle form.

3. **Voltage tap installation**: Following heat treatment, thin copper sheet voltage taps are inserted through the S2-glass insulation at predetermined locations, with longitudinal offsets between the taps on the two cables in order to prevent electrical shorts and maintain uniform sample thickness. Figure 2.9a shows a picture of the (impregnated) sample with voltage taps.

4. **Pre-tinning and bottom splice**: The top area of each cable designated for connection with the NbTi bus bar undergoes pre-tinning with Sn-Pb solder. This is followed by the splicing operation joining the two cables at the bottom. A micrograph of the cross section of the bottom splice is shown in Figure 2.10.

5. **Vacuum pressure impregnation**: The assembly is transferred to a VPI mold for impregnation with the resin systems under investigation, following the three-stage protocol of evacuation, resin introduction, and controlled curing.

6. **Top splice connection**: Post-impregnation, the NbTi bus bars are connected to each cable with an insulation sheet placed between the Nb_3Sn cables in the splice region. A picture of the splicing operation is shown in Figure 2.9b. This ensures permanent electrical insulation while maintaining mechanical integrity. A micrograph of the cross section of the top splice is shown in Figure 2.11.

7. **Instrumentation Cable**: The voltage taps are soldered to the instrumentation cable which is laid next to the sample prior to final assembly. A continuity check is carried out at this stage, ensuring the connection of the voltage taps essential for quench detection.

8. **Final assembly and prestress application**: The instrumented sample is placed within the intermediate insulating spacer assembly which is further enclosed within stainless-steel base plates (refer Figure 2.7). This assembly is integrated into the sample holder collar assembly, with which a prestress of approximately $50\,\mathrm{MPa}$ is applied on the transverse cross-section of the sample. The sample holder is mounted on the sample insert and the final electrical connection of the sample is made via the clamped connectors to the current delivery system.

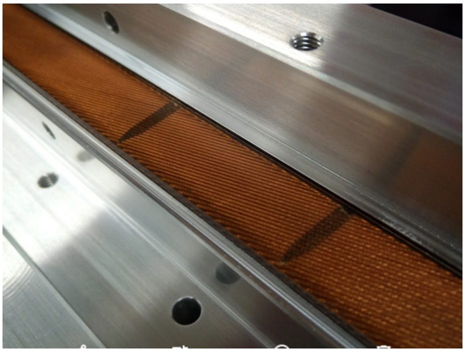

(a) Voltage tap placement showing thin copper sheets inserted through S2-glass insulation

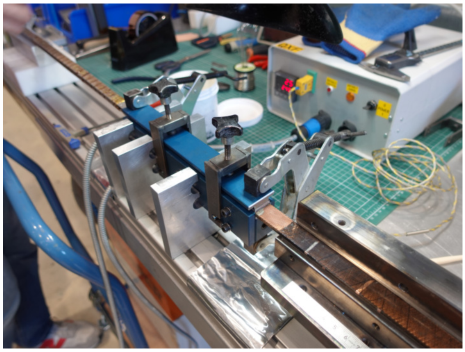

(b) Operation creating the top splice connection between the cable ends and NbTi bus bars

Figure 2.9: Critical assembly operations during FRESCA sample preparation.

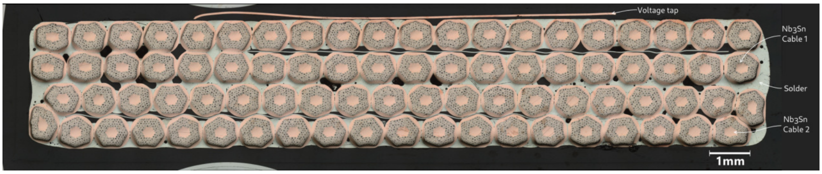

Figure 2.10: Bottom splice connection: Micrograph showing the cross-section of the soldered connection between the reacted Nb_3Sn cables at the bottom end of the sample.

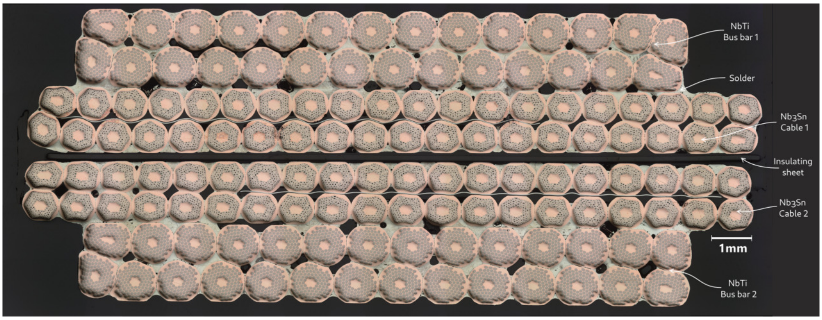

Figure 2.11: Top splice connection: Micrograph showing the cross-section of the soldered connection between the top end of the reacted Nb_3Sn cables and the NbTi bus bars with the insulation sheet separating the cable pairs.

The complete preparation sequence requires $8 - 12$ weeks per sample, with the developed procedure providing reproducible samples that faithfully represent the geometrical dimensions of cables in actual MQXF quadrupole coils.

2.1.2.3 Description of a measurement run

Each measurement campaign for the electrical characterization of a cable sample consists of a complete cooldown cycle during which systematic current ramp tests are performed across multiple background magnetic fields. The test protocol evaluates cable performance under progressively varying electromagnetic loading conditions to establish training behavior and stable current-carrying capacity.

The test facility operates in a dual-temperature configuration: the background dipole magnet is maintained at $1.9\,\mathrm{K}$ in superfluid helium to maximize its current density and field generation capability, while the sample is maintained at $4.2\,\mathrm{K}$ in normal liquid helium. The temperature stability is maintained within $\pm 0.1\,\mathrm{K}$ throughout the measurement campaign, monitored continuously by calibrated temperature sensors positioned at multiple locations along the sample insert.

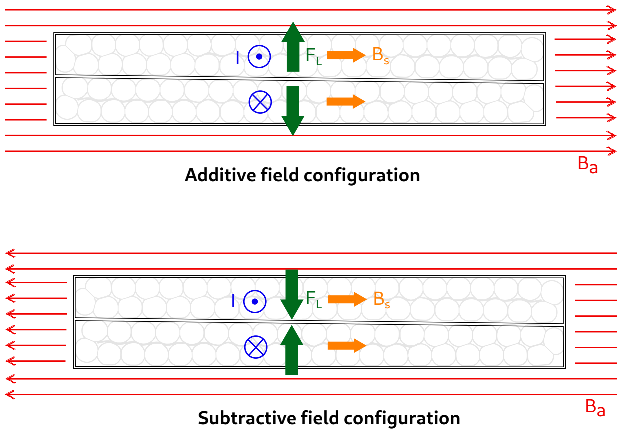

Figure 2.12: Schematic representation of the two magnetic field configurations used in the cable measurements: (top) Additive configuration where the sample's self-field, B_s adds to the applied background field, B_a from the dipole magnet, and (bottom) subtractive configuration where the self-field opposes the background field. The anti-parallel current, I flow in the double-stack cable creates opposing Lorentz forces, F_L in each leg, with the net field and load determined by the relative orientation to the external field.

The sequence of tests for each measurement campaign is as follows:

- **Initial conditions**: Measurements commence at the maximum available background field ($9.6\,\mathrm{T}$) in the additive configuration, where the cable's self-field adds to the applied field, as shown in Figure 2.12. This approach immediately identifies performance at the most electromagnetically demanding conditions.

- **Field stepping sequence**: The background field is decreased in $0.5\,\mathrm{T}$ increments from $9.6\,\mathrm{T}$ to the lowest field of interest[2] or until reaching the power supply limit of $32\,\mathrm{kA}$.
- **Current ramp protocols**: A two-stage approach is used with fast current ramp rates of $250\,\mathrm{A/s}$ for initial identification of the range of current carrying capacity. This is followed by slower ramp rates of $10\,\mathrm{A/s}$ for precise determination of the quench currents.

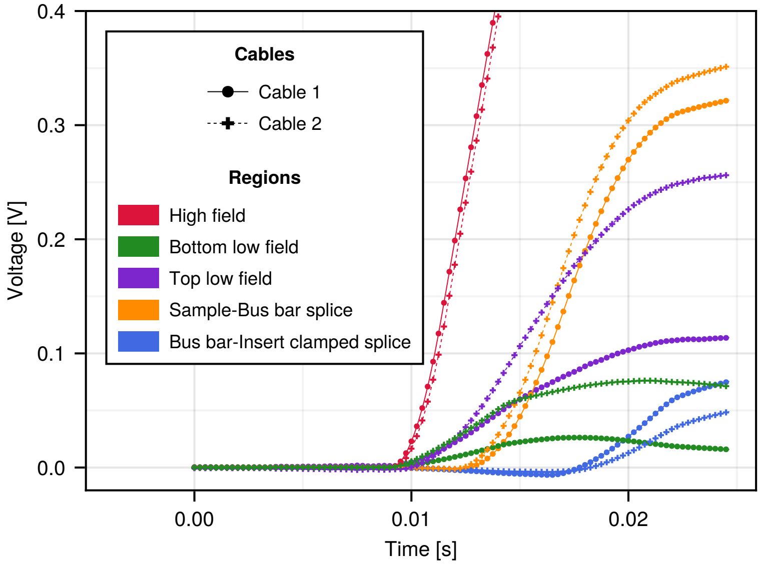

Figure 2.13: Representative voltage signals during a quench event showing sequential normal zone development across the sample regions (see Figure 2.8 for color-coded region identification). The rapid voltage rise initiates in the high-field region (red), confirming proper quench localization, followed by propagation through the low-field regions and splices as the normal zone expands.

- **Quench detection and localization**: The voltage thresholds for quench detection are set at $100\,\mathrm{mV}$ across each cable length with a $20\,\mathrm{ms}$ discrimination time. The protection sequence initiates an immediate ramp-down of the power supply at $450\,\mathrm{A/s}$ if a quench is detected. The high-frequency transient recording at $100\,\mathrm{kHz}$ is also analyzed to localise the quench within the sample, as exemplified in Figure 2.13. This verification that quenches originate in the high-field region (and not at any other location in the sample current circuit) is essential for a valid performance assessment of the sample.

[2] This systematic progression is visible in the measurement data presented in Figures 3.6, 3.10, and 3.15 of Chapter 3

- **Field reversal**: The measurement sequence is repeated in subtractive configuration, shown in Figure 2.12(b). The polarity of the power supply to the background magnet is reversed while maintaining direction of the supplied current to the sample.

The data analysis to extract quantitative performance metrics is carried out as follows:

- **Performance estimation**: The probability density function of quench current distributions at each applied field is estimated using kernel density estimation (KDE) with a Gaussian kernel, as detailed in Appendix A.5. The stable performance region is defined by currents exceeding the 95th percentile of the cumulative distribution, as illustrated in Figure 2.14. Only quench currents within this stable region are used to calculate the mean and standard deviation reported as the cable's current carrying capacity at each field level.

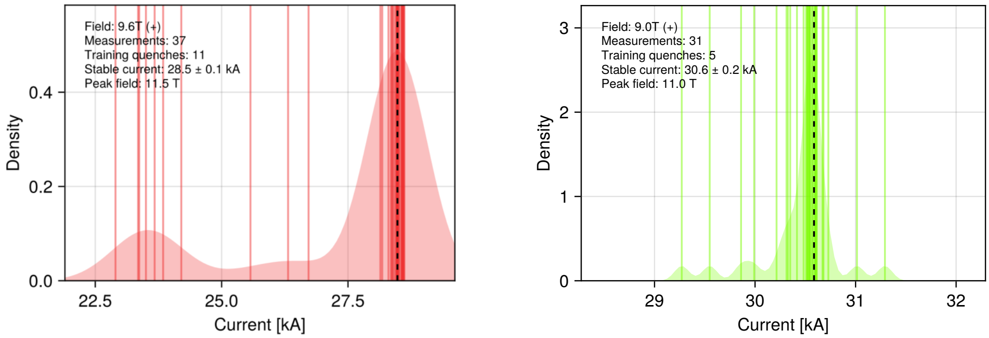

(a) KDE analysis at 9.6 T showing stable region threshold

(b) KDE analysis at 9.0 T showing stable region threshold

Figure 2.14: Kernel density estimation analysis of quench current distributions for the reference cable at 9.6 T and 9.0 T applied fields. The shaded regions indicate current values above the 95% stability threshold, with the mean of these values used to determine stable performance.

- **Self-field correction**: To account for the magnetic field generated by the transport current in the anti-parallel cable configuration, a self-field correction is applied as follows:

$$B_{\text{p,cable}} = B_{\text{a}} + k_1 I \tag{2.6}$$

where:

  - $B_{\text{p,cable}}$ is the peak field in the cable determining performance limits [T]
  - B_{a} is the applied field from the background dipole magnet [T]

– $k_1 = 63.4\,\mathrm{mT/kA}$ is the self-field coefficient from finite element analysis, shown for $1\,\mathrm{kA}$ in Figure 2.15

– I is the transport current in kA with opposite polarity in the two cable layers [A]

This correction becomes particularly significant at lower applied fields where the self-field contribution represents a significant fraction of the peak field in the sample.

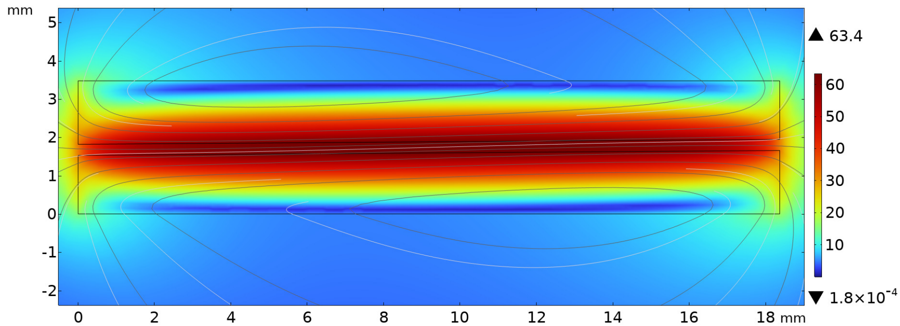

Figure 2.15: Finite element analysis of the self-field distribution in the double-stack cable configuration at $I = 1\,\mathrm{kA}$. The color scale indicates the magnetic flux density magnitude, showing field enhancement at the cable edges and the anti-parallel current effect between the two cable layers.

- **Scaling law analysis**: The critical current versus peak magnetic field behaviour is determined using Equation 2.4 for further analysis.

For this thesis work, four cable samples have been prepared and measured. The comprehensive electrical characterization results of three samples are presented in Chapter 3. The sample processed with a 75-hour duration of the final stage of RHT is not reported, since its current carrying capacity exceeded the maximum deliverable $32\,\mathrm{kA}$ of the test-station at even the highest fields.

2.2 Mechanical characterisation of damage due to transverse compression

The aim of the mechanical characterization measurements is to quantify the stress thresholds at which damage initiates and propagates in Nb_3Sn cables under transverse compression. Unlike electrical degradation, which manifests as a continuous performance decline, mechanical damage occurs through discrete crack formation events at the microstructural level. For this thesis work, a systematic methodology for correlating applied macroscopic stress with microscopic damage evolution across the hierarchical structure of Rutherford cables, from individual A15 grains through subelements to complete cable assemblies has been developed. This quantitative framework employs statistical analysis of cracks observed across thousands of subelements, thus establishing evidence-based quantification of the onset and evolution of damage due to transverse compression.

The mechanical characterization employs the same inverted double-stack cable configuration identical in construction to those used for electrical characterisation measurements in cables, but prepared without voltage taps or electrical connections. This configuration enables application of a uniform unilateral transverse compression, while permitting destructive metallographic examination at locations of interest identified by mapping the pressure distribution on the surface.

The methodology for mechanical characterization comprising two sequential steps is described as follows:

- **Section 2.2.1 - Controlled stress application and characterization**: This section describes the application of transverse compression using a specialized bench that has been adapted from Rutherford cabling machine technology specifically for this work. This step employs the use of pressure-sensitive films to measure the stress distribution at the contact surfaces.
- **Section 2.2.2 - Metallography and damage mapping methodology**: This section presents the systematic metallographic examination procedure, which employs a novel classification scheme developed for this investigation. The scheme assigns damage levels based on crack counts per subelement, thereby enabling statistical correlation between applied stress and microstructural degradation.

For clarity in terminology, in context of the mechanical characterization, the term *sample* refers to the double-stack cable assembly subjected to transverse compression, while *specimen* designates the metallographically prepared cross-section used for microscopic examination.

2.2.1 Application of transverse compression on samples

The application of uniform transverse compression on superconducting cables presents significant experimental challenges. Unlike homogeneous materials with uniform geometries, Rutherford-type cables feature complex cross-sectional profiles with alternating strand positions, voids, and material interfaces that create highly non-uniform stress distributions even under seemingly uniform external loading [73,83,134,161]. To address these challenges, a specialized compression bench was developed by adapting an existing Cable Measuring Machine (CMM) originally designed for dimensional measurements of Rutherford-type cables.

The following sections detail the development of the compression bench for application of tranverse compression stress and the methodology for characterizing the resulting stress distributions.

2.2.1.1 System overview and working principle

Figure 2.16 shows the Piping and Instrumentation Diagram (P&ID) of the upgraded compression bench. The system's core operating principle relies on pneumatic-to-hydraulic force amplification. The pneumatic circuit incorporates standard air treatment components, filter, lubricator, and pressure regulator to condition the compressed air supply. A $5/2$ directional solenoid valve provides electronic control of pneumatic pressure delivery to the hydraulic amplifier. The compressed air at relatively low pressure acts on a large-diameter piston within the hydraulic amplifier. This pneumatic pressure is converted to significantly higher hydraulic pressure through the ratio of the areas between the pneumatic and hydraulic pistons:

$$P_{hyd} = P_{air} \cdot \frac{A_{air}}{A_{hyd}} \tag{2.7}$$

where:

- P_{hyd} is the output pressure to compression cylinders
- P_{air} is the input compressed air pressure
- $\frac{A_{air}}{A_{hyd}} \approx 25$ is the mechanical amplification ratio

The amplifier design enables generation of hydraulic pressures up to $200\,\mathrm{bar}$ using standard laboratory compressed air supply of $\approx 8\,\mathrm{bar}$. This high-pressure hydraulic output drives the cylinders mounted on a compression gauge assembly. Beyond the pressure amplification, this pneumatic-hydraulic configuration provides inherent mechanical filtering that dampens pressure fluctuations, resulting in stable loading profiles. The system maintains force stability better than $\pm 0.5\%$ target pressure during the compression cycle.

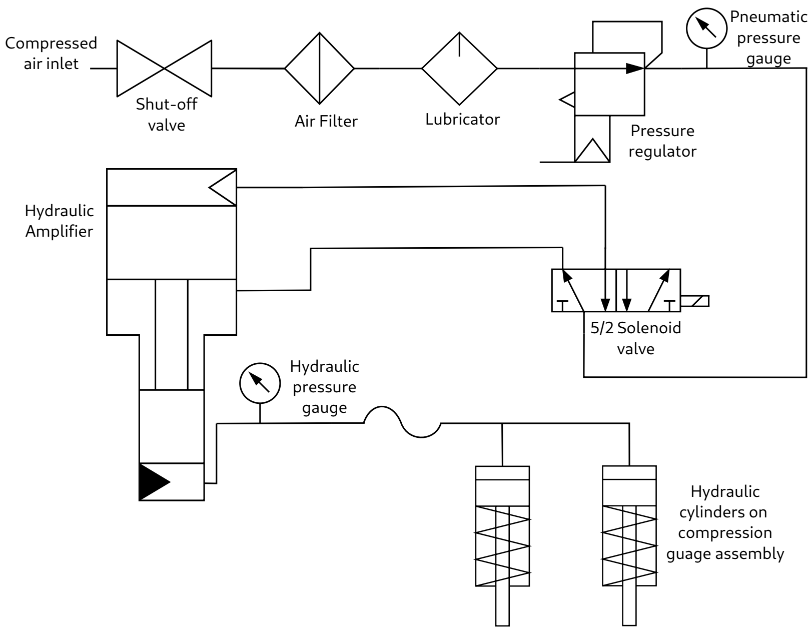

Figure 2.16: P&ID of the upgraded compression bench control system showing the pneumatic-to-hydraulic amplification principle. Compressed air flows through the treatment unit before the $5/2$ solenoid valve directs it to the hydraulic amplifier, which generates high-pressure output for the hydraulic cylinders on the compression gauge assembly.

2.2.1.2 Development of the compression bench

The compression bench was developed through extensive modification of an existing CMM platform. The CMM provided an ideal foundation due to its robust mechanical design, inherent dimensional stability, and precision-machined components, which are critical requirements for applying controlled transverse stress to superconducting cables.

The key engineering modifications implemented in developing the compression bench include:

1. **Implementation of digital control architecture**: The original manual control system was completely replaced with a National Instruments CompactRIO (cRIO) controller running LabVIEW Real-Time operating system, providing deterministic real-time control capabilities and high-speed data acquisition through a reconfigurable FPGA module. All data

processing and PID control algorithms execute within the FPGA at rates exceeding 1 kHz. The control strategy employs a closed-loop configuration where the electronic pressure regulator adjusts the pneumatic pressure based on feedback from the hydraulic pressure measurement at the amplifier outlet, which serves as the process variable for the PID controller. A custom LabVIEW application manages continuous data acquisition from all sensors at 20 Hz and implements safety interlocks. This digital transformation has enabled reproducible loading profiles essential for systematic investigations.

2. **Integration of electronic pressure control system**: The manual needle valves were replaced with electronic pressure control valves, enabling programmable pressure profiles. These valves interface directly with the CompactRIO controller, allowing automated execution of the loading sequence.

3. **Design and fabrication of custom electrical cabinet**: A dedicated control cabinet was built to house all new instrumentation including signal conditioning modules for sensor integration, regulated power supplies for consistent operation, emergency stop circuits, and system health monitoring indicators. The cabinet provides a centralized interface for all control and safety systems.

4. **Integration of digital pressure monitoring**: A high-accuracy pressure transducer were installed at the hydraulic amplifier output to provide real-time measurement of actual system pressure. This direct measurement eliminates uncertainties associated with pneumatic-to-hydraulic conversion and enables closed-loop pressure control.

5. **Redesign of compression gauge lever mechanism**: The original lever system was redesigned to ensure purely vertical motion and eliminate lateral force components. The new mechanism incorporates the existing precision alignment guides and V-springs that maintain lateral stability without introducing parasitic loads on the sample, achieving parallelism better than $10\,\mu\mathrm{m}$ across the compression surfaces.

6. **Installation of high-accuracy displacement measurement**: Inductive sensors with ceramic sensing faces were mounted to provide $1\,\mu\mathrm{m}$ resolution displacement measurements. Two sensors positioned symmetrically detect any potential misalignment before compression testing, while continuously monitoring uniaxial deformation of the sample.

Figure 2.17 illustrates the compression gauge assembly of the bench, with the sample is placed on the fixed lower base plate. The hydraulic cylinders actuate the compression gauge lever through the central movable compression block. The alignment guides constrain its motion to a single vertical axis. The compression surfaces have precision-ground hardened steel plates with surface roughness of $0.4\,\mu\mathrm{m}$ Ra, minimizing friction effects and ensuring uniform load transmission.

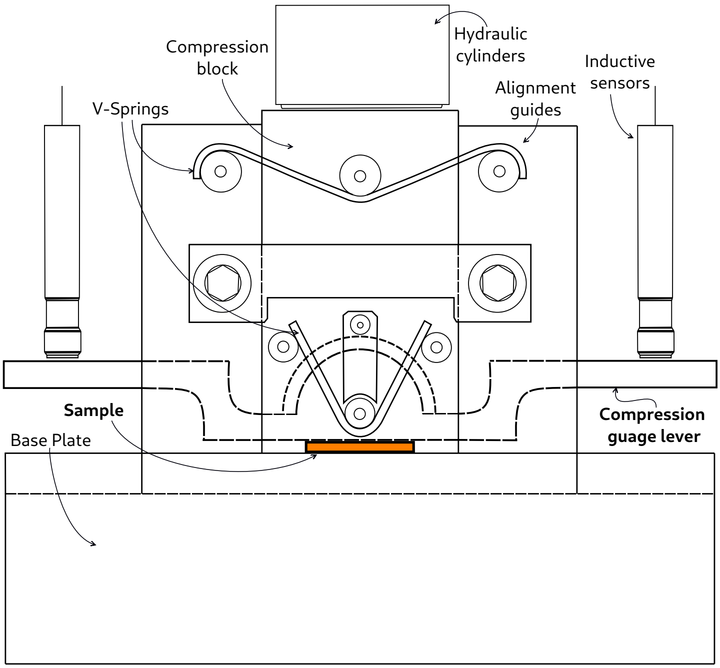

Figure 2.17: Cross-sectional schematic of the compression gauge assembly featuring the redesigned lever mechanism and integrated sensor configuration. Components include: (1) hydraulic cylinders providing vertical actuation force, (2) movable compression block with precision-ground contact surface, (3) double-stack cable sample position between compression surfaces, (4) precision alignment guides constraining motion to vertical axis, (5) inductive position sensors for displacement measurement, and (6) V-springs ensuring lateral stability. The assembly design eliminates lateral force components while maintaining parallelism better than $10\,\mu\mathrm{m}$ across the $25 \times 120\,\mathrm{mm}$ compression surfaces.

The plate dimensions ($25\,\mathrm{mm} \times 120\,\mathrm{mm}$) exceed the sample width to prevent edge effects on samples with nominal dimensions of $18.65\,\mathrm{mm} \times 3.8\,\mathrm{mm} \times 50\,\mathrm{mm}$.

All compression tests follow a standardized cycle consisting of three distinct phases: a 120-second linear ramp to the target pressure, a 120-second hold at constant pressure, and a rapid pressure release. This specific timing sequence has been established based on the specifications of the pressure-sensitive film[162], which is used to analyze the compression stress on sample and described in the following section. Figure 2.18 shows an example of the pressure and displacement evolution during a compression test, illustrating the control stability achieved with the system. The displacement curve provides valuable information about the mechanical response of the sample, with changes in slope indicating heavy internal damage events such as degradation of the impregnation resin. However, this data while potentially useful, is not used further for the damage analysis.

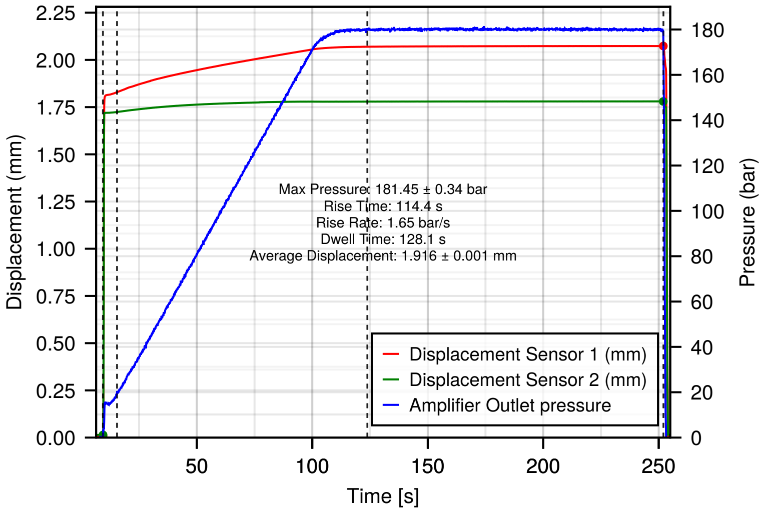

Figure 2.18: Representative pressure and displacement curves during a standard compression test on a double-stack cable sample. The hydraulic pressure at the amplifier outlet (blue) shows controlled ramp-up over 120 s to the target value of 180 bar, corresponding to approximately 170 MPa applied stress on the sample. The displacement measurements from two independent sensors (red and green) demonstrate symmetric sample deformation and stable control throughout the 120 s dwell period.

2.2.1.3 Analysis of applied compression stress

The translation from applied force to local stress depends critically on surface conditions at the sample-anvil interface. Surface roughness, parallelism deviations, edge effects, and contaminants can all create significant stress concentrations that deviate from the nominal pressure. Even microscopic surface irregularities ($\sim 1\,\mu$m) can generate localized force concentrations. These practical considerations necessitate precise sample preparation with tightly controlled dimensional tolerances, high surface finish quality, and careful handling to prevent contamination. Without such precautions, the stress field becomes dominated by surface artifacts rather than the mechanical response of the sample to uniform loading.

Thus, while the hydraulic pressure provides a measure of the total force or average stress applied to the sample, it does not reveal the actual stress distribution across the cable surface. To address this limitation, pressure-sensitive films [Fujifilm Prescale films[162]] are employed to map the stress distribution on the sample surfaces. These films are placed between the contact surfaces of the sample and the compression plates during testing. The specialized films contain microscopic color-forming capsules that rupture under pressure, creating a color pattern whose density corresponds to the magnitude of the local pressure. The pressure-sensitive films are selected with pressure ranges matching the expected stress levels in the cable samples. For this methodology, films rated for 50-130 MPa (Medium Pressure) and 130-300 MPa (High Pressure) are used simultaneously to capture the full range of stresses, including localized peak values that may significantly exceed the nominal applied pressure. The spatial resolution of these films (approximately $0.125\,\mathrm{mm}$) enables distinction of pressure variations between individual strands within the cable structure.

The analysis procedure for selecting specimens for metallographic examination involves the following steps:

1. The prescale films positioned on both surfaces of each sample during the standardized compression cycle are digitized using the FPD-8010E Pressure Distribution Mapping System[163]. A two-dimensional pressure distribution map is generated to visualize the complete stress field with $\pm 10\%$ absolute precision for each surface of the sample. A representative example is shown in Figure 2.19.

2. A suitable cross-sectional plane of interest is identified for subsequent metallographic examination, with edge effects being avoided. A peak detection algorithm is implemented to identify maxima in the local pressure. These peaks correspond to the positions of the individual strands. Statistical parameters are calculated from the extracted peak population: arithmetic mean, μ and standard deviation, σ for both surfaces. A typical 2D pressure profile, with the identified peaks is shown in Figure 2.20. The statistical descriptor, $\mu \pm \sigma$ is assigned as the characteristic stress state for each specimen.

For the $2\,\mathrm{D}$ pressure profile shown in Figure 2.20, the specimen is compressed at a nominal average pressure of $\approx 125\,\mathrm{MPa}$. The peak detection algorithm identifies the local maxima at strand centers, with values reaching approximately $160\,\mathrm{MPa}$ in this example. The extracted peak distribution yields the characteristic stress parameters that define the mechanical loading condition for subsequent damage correlation analysis. The pressure distribution also reveals a pattern in the stress localization. The metallic strands, with elastic moduli exceeding $100\,\mathrm{GPa}$, create preferential load paths compared to the surrounding epoxy resin of $3 - 5\,\mathrm{GPa}$. This stiffness mismatch generates the stress pattern where peak values at strand-to-strand contact points typically exceed nominal pressure by $10 - 30\%$. The methodology captures these variations through statistical analysis. The analysis protocol includes verification of loading symmetry through correlation of peak locations and magnitudes between surfaces. For the example shown in the figure, the analysis yields mean peak pressures of $139 \pm 12\,\mathrm{MPa}$ and $135 \pm 9\,\mathrm{MPa}$ for top and bottom surfaces respectively.

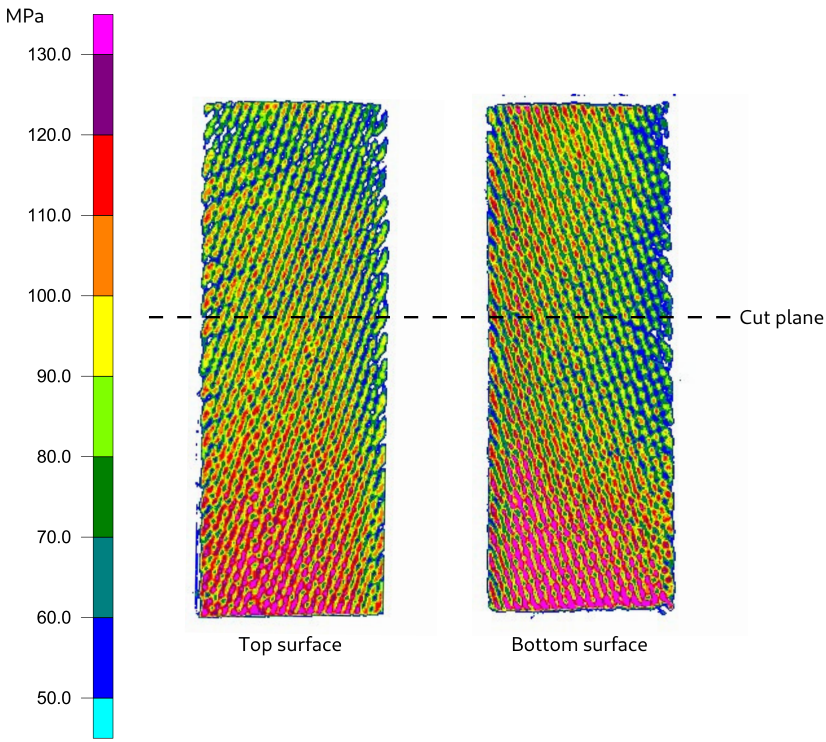

Figure 2.19: Two-dimensional pressure distribution map obtained from Prescale film analysis of a compressed double-stack cable sample. The color scale (left) indicates pressure magnitude in MPa. The pressure localization corresponds to the underlying strand structure, with higher stress (red-yellow) at strand centers and lower stress (blue-green) in interstitial regions. The non-uniform nature of the stress field demonstrates why average pressure values inadequately characterize the complex loading state within superconducting cables.

The observed stress localization also highlights the need to conduct studies where the thickness of the impregnation resin is well controlled and closely matches that of actual magnets. In final magnet assemblies, the filling factor is so crucial that the resin thicknesses are actually very small. A precursor investigation to this thesis work [135] has demonstrated that thicker resin areas provide better protection to the strands. This finding aligns with observations by Gao et al. [161], who show that the deviatoric strain component, which is primarily responsible for damage, decreases with increasing epoxy volume. The double-stack configuration used in this study reproduces the dimensional constraints of actual magnet assemblies, ensuring that the resin distribution closely approximates operational assemblies.

The pressure distribution maps provide a reasonable approximation of the macroscopic stress state applied to the cable structure. It should be noted, however, that the internal stress distribution within individual strands and subelements involves additional complexity not fully captured by

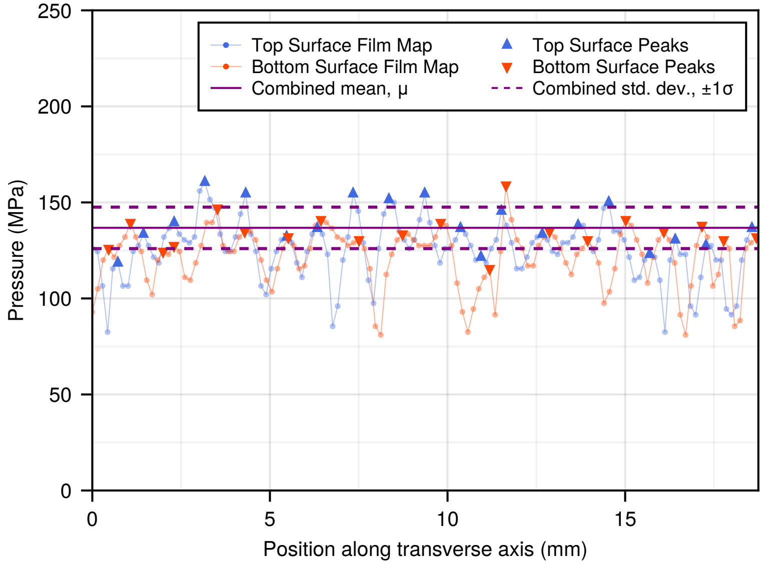

Figure 2.20: 2D Pressure distribution obtained from Prescale film analysis for a selected cross section compressed at a nominal average pressure of 124 MPa. Note the significant localization of stress at the strand centers, with peak values reaching approximately 161 MPa. The combined distribution of the peak values yields a stress descriptor of 137 ± 11 MPa applied stress for this specimen. These distribution maps guide the selection of transverse observational planes for metallographic inspection.

surface measurements and would require a comprehensive Finite Element Analysis (FEA)[164]. Factors such as interfacial friction, three-dimensional load transfer, and the complex composite microstructure create intricate local stress fields that ultimately govern damage initiation at the microscopic level. The measurements serve primarily to characterize the input loading condition and identify regions of interest for metallographic examination.

2.2.2 Metallography of specimens

Metallography has been instrumental in establishing microstructure-property relationships in Nb_3Sn conductors, quantifying composition gradients and their correlation with critical field variations[70,105], identifying void formation mechanisms that affect mechanical integrity[120], and optimizing heat treatment parameters through grain size and phase fraction analysis[109]. Post-mortem metallographic examination of large-scale magnets[165–167] has directly informed design modifications that improve performance in high-field accelerator applications.

The metallographic approach described in this section builds upon these established techniques, adapting them specifically to characterize evolution of damage in Nb_3Sn cables subjected to controlled transverse compression. The methodology has been optimized for the RRP® 108/127 architecture Rutherford-type cables used in this work, with particular attention to preserving and accurately identifying damage features while avoiding preparation-induced artifacts.

2.2.2.1 Specimen preparation procedure

The metallographic analysis of Nb_3Sn superconducting cables requires meticulous specimen preparation due to the brittle nature of the A15 phase. After selecting the cross-section to be observed, the double-stack cable samples are carefully sectioned using a low-speed diamond wire saw (Well 3242-4) with a wire diameter of $0.25\,\mathrm{mm}$. The cutting speed is maintained below $1\,\mathrm{mm/min}$ with constant cooling lubricant flow to minimize mechanical stresses and prevent overheating during sectioning.

Six specimens are prepared simultaneously in a single batch, including one control specimen in the virgin state. This virgin control serves as a critical reference, verifying that no damage is introduced during the specimen preparation process itself. The sectioned specimens are embedded in Buehler EpoxiCure 2[168] epoxy resin, selected for its low viscosity, minimal shrinkage during curing, and good edge retention. Each specimen is placed in a silicone mold with the cross-section of interest facing downward. After applying a release agent, the epoxy resin and hardener (mixed in a $100 : 23$ ratio by weight) are thoroughly stirred and carefully poured over the specimens. To minimize porosity, the specimens are transferred to a pressure vessel (Kulzer Technomat) and maintained at $2\,\mathrm{bar}$ pressure during the $24\,\mathrm{h}$ room temperature curing process.

Once embedded, the specimens undergo a systematic grinding sequence with progressively finer silicon carbide (SiC) abrasive papers on a Presi MechaTech 250 automatic polishing machine. The grinding sequence employs four grades of SiC papers: P180 ($82.0\,\mu\mathrm{m}$), P320 ($46.2\,\mu\mathrm{m}$), P600 ($25.8\,\mu\mathrm{m}$), and P1200 ($15.3\,\mu\mathrm{m}$). A force of $10\,\mathrm{N}$ per specimen is applied for 2 minutes at each grit size. Both the platen and specimen holder rotate at $150\,\mathrm{RPM}$, in alternated directions.

Figure 2.21: Sample preparation process showing six specimens mounted in epoxy resin after curing, including five test specimens and one virgin control specimen.

Water is used as a lubricant with continuous flow to remove debris and prevent overheating. This grinding process typically removes $1 - 1.5\,\mathrm{mm}$ of material, eliminating any damage that might have been introduced during the cutting process.

Following grinding, specimens undergo a multi-stage polishing procedure using diamond abrasives of decreasing particle sizes. The sequence begins with $9\,\mu\mathrm{m}$ diamond suspension on a TEXMET P cloth for 5 minutes. Next, specimens are polished with $3\,\mu\mathrm{m}$ diamond on VerduTex cloth for 4 minutes, then $1\,\mu\mathrm{m}$ diamond also on VerduTex for 3 minutes, and finally $0.25\,\mu\mathrm{m}$ diamond on MD-Chem cloth for 2 minutes. Throughout the polishing sequence, an increased force of $15\,\mathrm{N}$ per specimen is applied compared to the grinding sequence. The softer polishing cloths distribute the pressure more evenly across each specimen surface.

The final stage involves mechanical chemical polishing using colloidal silica suspension $(0.02\,\mu\mathrm{m})$ on a soft polishing cloth, carried out on a Presi Vibrotech 200 vibratory polisher. This critical step removes the final thin layer of mechanically deformed material, revealing the true microstructure at the surface. The quality of the final polished surface is assessed using optical microscopy. A properly prepared specimen shows no scratches, pull-outs, or other preparation artifacts, with the different phases in the conductor wires (copper matrix, Nb_3Sn layer, and Cu-Sn core) clearly distinguishable with good contrast. Figure 2.21 shows six specimens mounted in epoxy resin after the sample preparation procedure. A systematic examination is then conducted on each specimen using the damage classification methodology described in the following section.

2.2.2.2 Damage Classification methodology

In classical fracture mechanics, the analysis of damage typically involves the measurement of crack length or crack tip opening displacement to calculate the local stress intensity factor[116]. However, this approach becomes challenging when applied to complex composite structures like a Nb_3Sn cable[19]. The double-stack samples in this study, containing 80 wires with 108 subelements each, present a total of $8,640$ subelements per specimen. An optical micrograph of a single polished specimen is shown in Figure 2.22 illustrates this. Cracks initiate at various stress concentrators, which differ significantly in both type and size across the specimen. As transverse pressure increases, not only do existing cracks propagate, but new cracks also begin to nucleate at different locations. This results in the development of cracks with variable lengths throughout the observed specimen. As an example, an optical micrograph of a selected area of a single wire in a polished specimen is shown in Figure 2.23. It shows both undamaged and damaged subelements, with a few cracks of varying lengths (marked with black arrows for the latter). In the transverse cross-section, the observed crack lengths range from approximately 3 μm (the minimum detectable size using the optical microscope) to about 13 μm, which corresponds to the thickness of the A15 phase layer in the RRP® 108/127 strand architecture. In rare cases, some subelements exhibit cracks exceeding this typical maximum length.

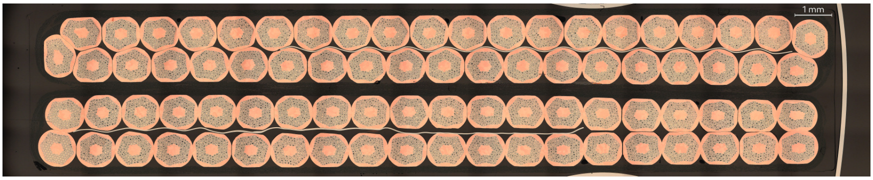

Figure 2.22: Low-magnification optical micrograph of a polished specimen showing the double-stack cable structure with its characteristic rectangular cross-section. Each specimen contains 80 individual strands (40 per cable), each comprising 108 subelements, totaling 8,640 subelements.

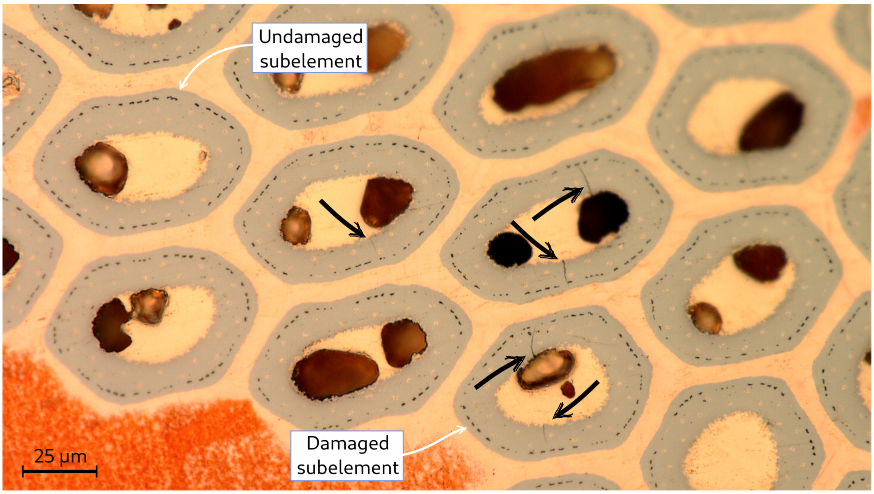

Figure 2.23: High-magnification optical micrograph showing examples of undamaged and damaged subelements. Cracks in the A15 phase are indicated by the black arrows. The visible cracks demonstrate varying lengths from approximately 3 μm to 13 μm, illustrating the brittle failure mode of the A15 phase under transverse loading.

To quantitatively characterize the extent and progression of damage across specimens subjected to different levels of transverse pressure, a damage mapping method has been developed. This approach allows for a systematic comparison of crack density distribution at the subelement, strand, and specimen levels. The methodology assigns a damage level to a subelement based on the total number of cracks observed in the plane of observation, with levels D1 through D5 corresponding to one through five or more cracks, respectively (as illustrated in Figure 3.1 of Chapter 3). For enhanced visualization and data analysis, each damage level is assigned a specific color code, creating damage maps of the specimens that allow rapid assessment of damage distribution and severity. Finally, a programmatic extraction of the damage statistics is carried out for each specimen.

The damage mapping approach provides several advantages over traditional fracture mechanics methods for these complex specimens:

1. It accounts for the multi-site nature of crack initiation in the heterogeneous composite specimens
2. It captures both the severity (damage level of each subelement) and extent (number of damaged subelements) of degradation within each specimen
3. It provides a statistical basis for establishing threshold stress values for the onset and progression of damage

This damage classification methodology thus provides a systematic statistical framework for quantifying and comparing mechanical degradation across specimens subjected to different stress levels. The application of this methodology to cable specimens and the resulting observations of crack morphology, damage patterns, and their correlation with processing parameters are presented in Chapter 3.

2.2.3 Measurement of microstructural features

As described in Section 1.2.2 of Chapter 1, the two key microstructural features which evolve during the final stage of the RHT cycle for the RRP® conductors are the A15 grain size and Nb barrier thickness. They govern both the electrical and mechanical performance of the wire. This section describes the methods used to quantify these features in the context of the parameteric variation of the duration of the final stage of RHT in this work.

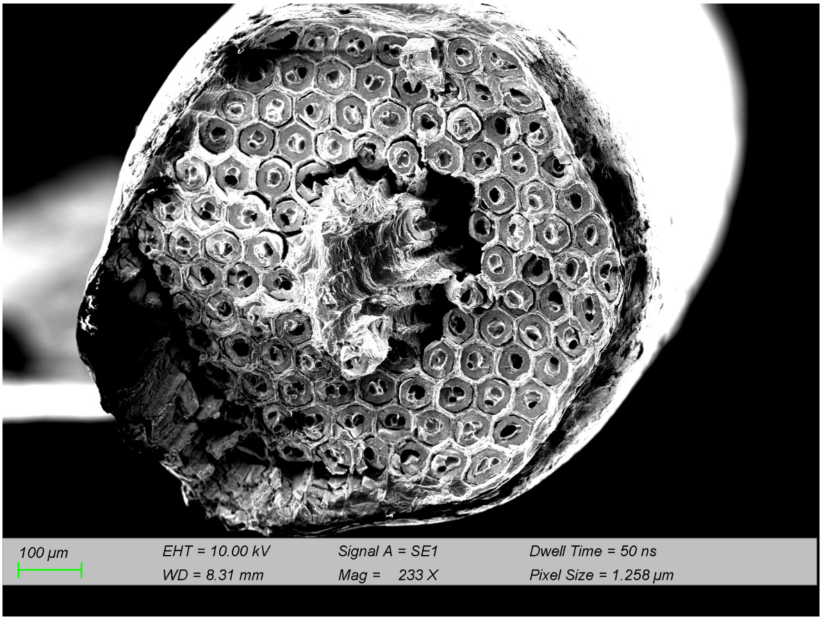

Figure 2.24: SEM micrograph of a cryogenic fracture surface of an RRP® $108/127$ Nb_3Sn strand showing the distribution of subelements around the Cu core. This overview shows the internal architecture with 108 subelements arranged in a hexagonal pattern. The fracture predominantly follows intergranular paths, providing a suitable surface for grain structure analysis in a subelement.

2.2.3.1 Measurement of A15 phase grain size

For the measurement of grain size, virgin strands used in the RRR characterization studies are subjected to a controlled fracture process. The extracted strands are immersed in liquid nitrogen (LN_2) for approximately 5 minutes to thoroughly cool the material below its ductile-to-brittle transition temperature. While still at cryogenic temperature, the strands are quickly fractured by applying a sudden bending force. This cryogenic fracture predominantly results in intergranular fracture paths in the Nb_3Sn layer, effectively revealing the three-dimensional grain structure as shown in Figure 2.24.

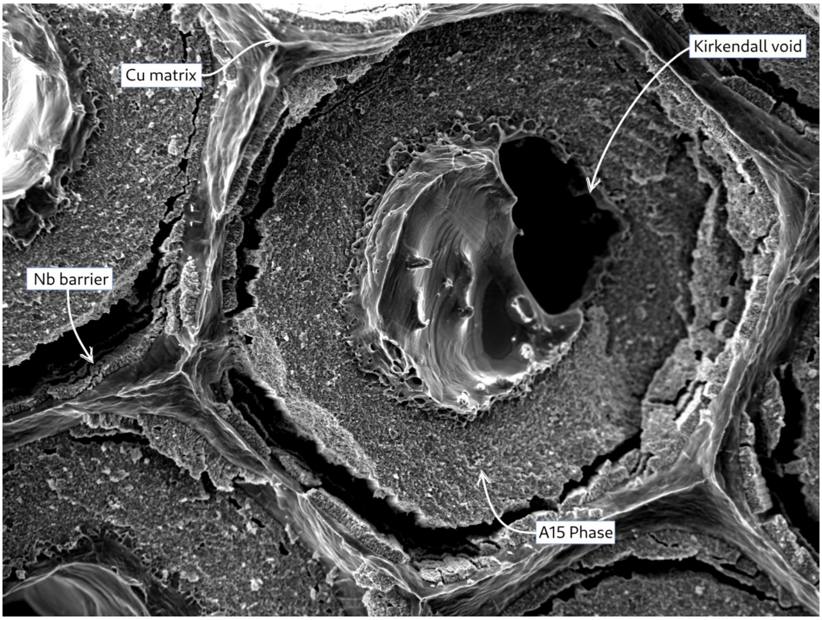

Figure 2.25: Higher magnification view of a single fractured subelement showing the distinct regions: Cu matrix surrounding the hexagonal subelement, Nb diffusion barrier (with columnar grain structure), Nb_3Sn A15 layer with visible grain structure, and the central Cu-Sn core region. The intergranular fracture path in the Nb_3Sn layer clearly reveals individual grains, enabling direct measurement of grain size distributions as a function of heat treatment parameters.

Secondary electron imaging of the fracture surfaces is performed using a Zeiss Merlin SEM at accelerating voltages of $10\,\mathrm{kV}$ with working distances of $8 - 9\,\mathrm{mm}$, providing optimal contrast for grain boundary observation. Figure 2.25 shows a higher magnification view of a single fractured subelement, revealing the distinct microstructural regions. The intergranular fracture path delineates the individual grains within the A15 phase layer, while the Nb diffusion barrier exhibits its characteristic columnar grain morphology in the outer periphery of the subelement. The presence of Kirkendall voids in the Cu-Sn core indicates the solid-state diffusion mechanism responsible for phase formation during the reaction heat treatment.

Figure 2.26 presents a magnification of a subelement in the previous figure. The equiaxed Nb_3Sn grains of the A15 phase are visible, along with the columnar grains of the Nb barrier. A distinct grain size gradient is evident within the A15 layer, with coarser grains adjacent to the Cu-Sn core interface where grain coarsening occurs preferentially with increasing heat treatment duration,

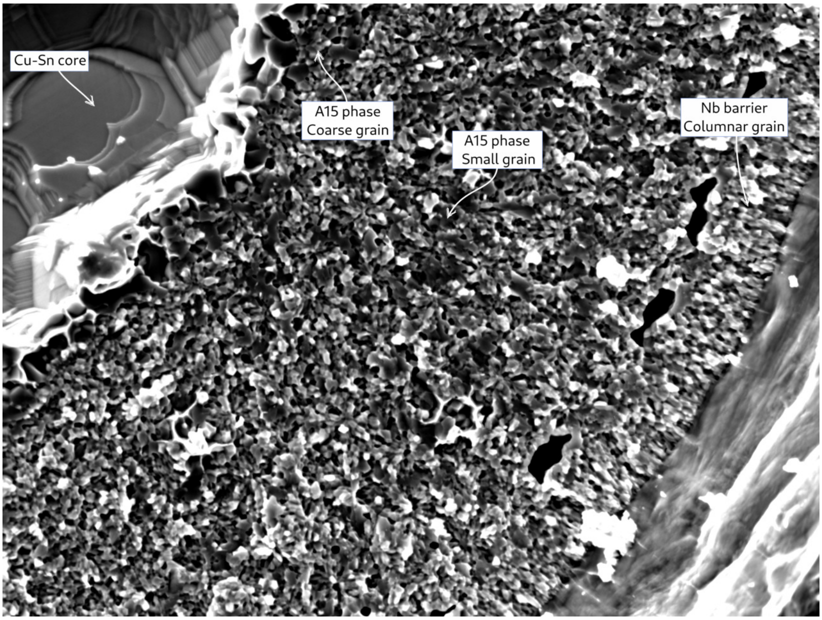

Figure 2.26: High-magnification SEM image showing the A15 phase grain structure and adjacent microstructural features. The image reveals both coarse-grained A15 regions near the Cu-Sn core interface and fine-grained regions in the center and closer to the Nb barrier, demonstrating the grain size gradient typical of RRP conductors. The columnar morphology of the Nb barrier grains is visible at the right edge, while Kirkendall voids (appearing as dark cavities) are distributed throughout the A15 microstructure.

and finer grains at the center and near the Nb barrier. This bimodal distribution reflects the temperature-dependent grain growth kinetics during the final heat treatment stage.

The grain size measurements are performed using the linear intercept method according to ASTM E112 standard at the central region of the A15 layer. For each heat treatment condition, a minimum of 10 representative micrographs are analyzed at this magnification. On each micrograph, a minimum of 5 random line traverses are made, with at least 50 grain boundary intersections counted per line to ensure statistical validity. The average grain size is calculated using:

$$\bar{d} = \frac{L}{N \cdot M} \tag{2.8}$$

where:

- $\bar{d}$ is the average grain size
- L is the total test line length

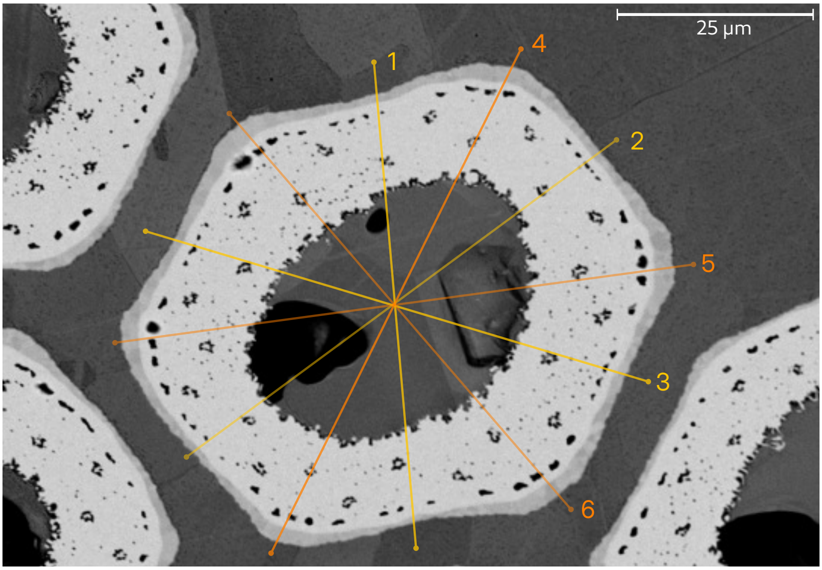

Figure 2.27: Schematic representation of EDX line scan positions across a hexagonal subelement. Lines 1-3 cross the flat edges where the barrier where maximum barrier thickness occurs. Lines 4-6 traverse the vertices experiencing maximum thinning.

- N is the grain boundary intersection count
- M is the microscope magnification

This grain size analysis has been conducted for samples subjected to different heat treatment durations at the final $665\,^{\circ}\mathrm{C}$ plateau of the RHT cycle. The results of this analysis provide insights into how grain size variations influence both the superconducting properties and mechanical behavior of the conductors.

2.2.3.2 Measurement of Niobium barrier thickness

In the subelement of the RRP® wire, the Niobium barrier serves as a critical diffusion barrier preventing Sn contamination of the Cu stabilizer matrix, thereby preserving the RRR essential for thermal stability (see Section 1.2.2). The quantitative characterization of barrier thickness provides essential data for understanding the electromechanical behaviour. Variations in barrier thickness could affect local stress concentrations at preferential crack initiation sites due to the abrupt modulus transitions between the different components of the conductor.

Energy Dispersive X-ray spectroscopy (EDX) line scans are used to provide precise compositional profiles across the radial dimension of individual subelements. This technique measures

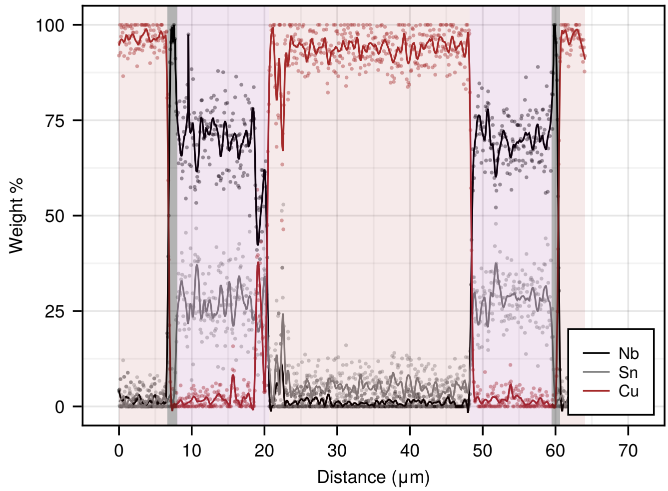

(a) EDX compositional profile across a flat edge (Line 2) showing the thinner Nb barrier regions with thickness of $1.8 \pm 0.2\,\mu\mathrm{m}$

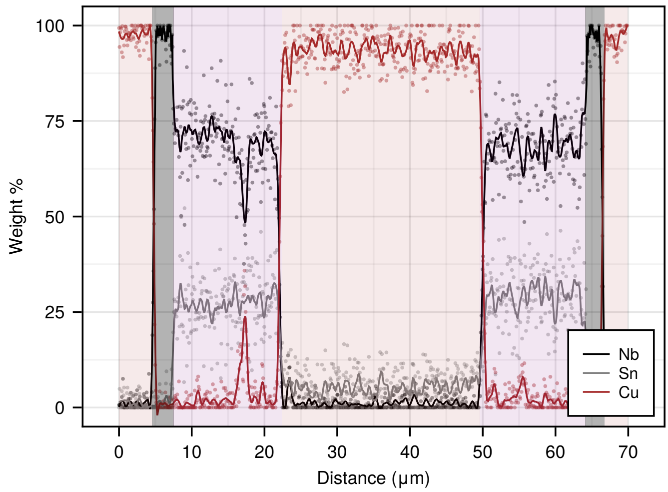

(b) EDX compositional profile across opposite vertices (Line 5) showing the thicker Nb barrier regions with thickness of $2.5 \pm 0.2\,\mu\mathrm{m}$ at vertices, representing a 40% increase compared to edge positions.

Figure 2.28: Representative EDX line scan results demonstrating spatial variation in Nb barrier thickness across a subelement after 50 h heat treatment at $665\,°\mathrm{C}$. The element distribution profiles show Nb (black), Sn (grey), and Cu (red) weight percentages. Pink shaded regions indicate the Nb_3Sn phase, while grey regions highlight the residual Nb barrier. The hexagonal shape of the subelements reflects in both the cumulative length of the profiles and the thickness of the barriers in the plots.

characteristic X-ray emission intensities proportional to elemental concentrations, enabling determination of phase boundaries with sub-micrometer resolution. The hexagonal geometry of RRP® subelements exhibits systematic variations in the barrier thicknesses at the vertices and flat edges due to the hexagonal shape itself. Six line scans are performed per analyzed subelement to capture this geometric dependence: three traversing the vertices and three crossing the flat edges, as illustrated in Figure 2.27.

The EDX measurements employ standardized acquisition parameters to ensure reproducibility across the specimen matrix. Line scans utilize a $15\,\mathrm{kV}$ accelerating voltage with beam current of $1.5\,\mathrm{nA}$, providing optimal excitation of the Nb Lα ($2.17\,\mathrm{keV}$), Sn Lα ($3.44\,\mathrm{keV}$), and Cu Kα ($8.05\,\mathrm{keV}$) characteristic X-ray lines while minimizing beam spreading in the interaction volume. Figure 2.28 presents representative compositional profiles, with the percentage by weight profiles of the three elements plot across the respective selected lines. A quantitative barrier thickness extraction employs a scripted peak analysis algorithm applied to the component intensity profiles. The figures show the areas of the Cu-Sn core, A15 phase and the Nb barrier in the respective shaded zones. The barrier boundaries are defined where the Nb concentration increases to 98% of its maximum value, corresponding to the interface between the pure Nb barrier and adjacent phases. The variation in the thickness at the edges and vertex positions is evident in this figure. The statistical analysis encompasses measurements from a minimum of 20 subelements per specimen, with equal sampling of edge and vertex positions. For the final barrier thickness characterization, both vertex and edge measurements are combined to provide a comprehensive thickness distribution representative of the complete subelement population. This averaged approach captures the effective barrier performance relevant to both electrical and mechanical properties.

2.3 Summary

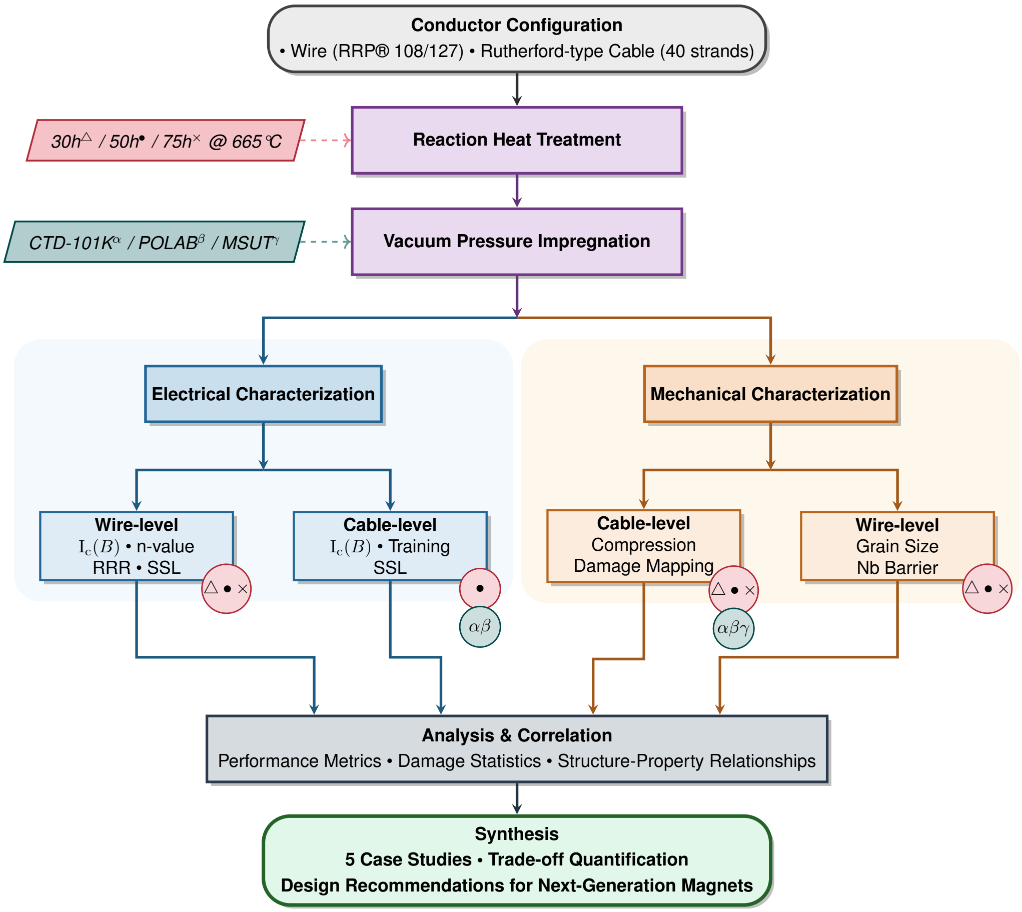

Figure 2.29: Overview of the experimental methodology framework employed in this thesis. The workflow illustrates the parallel characterization tracks from the initial conductor configuration through sample preparation, electrical and mechanical testing, to final synthesis. Processing parameters (RHT duration: $\triangle$ = 30h, $\bullet$ = 50h, $\times$ = 75h; Resin systems: α = CTD-101K, β = POLAB, γ = MSUT) are systematically varied to establish structure-property relationships.

This chapter has presented the experimental methodology integrating electrical and mechanical characterization to establish quantitative performance limits in Nb_3Sn Rutherford-type cables. The wire-level measurements provide intrinsic superconducting properties including critical current density $I_c(B)$, n-value, and RRR following standardized protocols. The cable-level testing characterizes electrical performance of impregnated cables under operational conditions. The development of a specialised compression bench has enabled application of controlled transverse compression stress on cable samples from 70 to $200\,\mathrm{MPa}$. The novel damage classification methodology transforms metallographic observations of cracks in $8,640$ subelements per specimen into statistical distributions. This establishes the quantification of mechanical damage thresholds via a microstructure-based framework rather than relying solely on electrical performance degradation metrics.

Figure 2.29 delineates the systematic workflow from the conductor configuration (wires or cables) through parallel characterization tracks to integrated analysis and synthesis. The processing parameters under investigation, viz. reaction heat treatment duration at $665^\circ\mathrm{C}$ and impregnation resin selection, serve as independent variables while maintaining all other manufacturing protocols constant. The methodology quantifies both immediate responses (critical current, training behavior) and latent sensitivities (crack initiation thresholds, damage evolution rates) across the operational parameter space. This dual-track approach reveals correlations through separated studies: electrical performance at $4.2\,\mathrm{K}$ under magnetic loading versus mechanical integrity at $293\,\mathrm{K}$ under assembly stresses. Chapter 3 demonstrates how the combined methodology exposes the fundamental trade-offs between electrical performance and mechanical resilience, providing quantitative relationships essential for extending Nb_3Sn technology toward $15\,\mathrm{T}$ class accelerator magnets.

3 Measurements & Observations

The research questions established in Chapter 1 regarding electromechanical limits in Nb_3Sn accelerator magnets have been systematically investigated through the experimental methodology detailed in Chapter 2. This chapter presents comprehensive results addressing dual objectives: quantifying the lower thresholds of transverse compression where mechanical damage initiates in the brittle A15 phase, and proposing strategies to elevate these thresholds through reaction heat treatment (RHT) optimization at the conductor level and resin selection at the process level.

The chapter begins with characterization of the microstructural damage occuring in the A15 phase due to transverse compression on Rutherford-type cables. This establishes the fundamental crack morphology and localization patterns. Following this foundation, the experimental program encompasses five case studies examining distinct configurations of Nb_3Sn Rutherford-type cables, and listed in Table 3.1:

Table 3.1: Experimental matrix of case studies investigating electromechanical behavior

Case Study	Configuration	Key Parameter	Primary Outcome
I	*RHT dwell:* 50 h *Resin:* CTD-101K®	Standard protocol	Baseline damage threshold established
II	*RHT dwell:* 50 h *Resin:* CTD-101K®	Prestress	Critical prestress requirement identified
III	*RHT dwell:* 50 h *Resin:* POLAB, MSUT	Impregnation resin	Enhanced mechanical tolerance achieved
IV	*RHT dwell:* 30 h, 50 h, 75 h *Resin:* CTD-101K®	Dwell time	Inverse correlation demonstrated & quantified
V	*RHT dwell:* 30 h *Resin:* POLAB	Dwell time, Impregnation resin	Complementary benefits confirmed

The chapter concludes with a comprehensive synthesis that consolidates all experimental findings into a quantitative optimization framework for Nb_3Sn cables. This framework employs a multidimensional figure of merit analysis to establish systematic design guidelines for balancing electromagnetic performance against mechanical resilience across the parameter space.

3.1 Microstructural Damage Characterisation

This section presents the characteristics of microstructural damage identified through systematic metallographic examination using the methodology described in Section 2.2. The analysis reveals consistent damage features across multiple specimens, including distinct crack morphologies within the subelements and characteristic localization patterns at the strand level. These observations form the foundation for interpreting the onset of cracks and damage evolution rates due to transverse compression on the double-stack specimens reported in the subsequent case studies.

3.1.0.1 Crack Morphology in a subelement

Through detailed optical and scanning electron microscopy analysis of the damaged specimens, two distinct types of cracks are consistently observed across all specimens under investigation, as illustrated in Figure 3.1:

1. **Primary cracks:** These cracks, indicated by 'P' in Fig. 3.1, are the first to appear in the subelements when transverse pressure is applied. They typically initiate either at voids present in the Cu-Sn core or at the Nb_3Sn/Cu-Sn core interface. Figure 3.1a shows a high-magnification SEM micrograph of a typical primary crack propagating through the Nb_3Sn layer, illustrating the sharp, clean fracture path characteristic of brittle failure in this intermetallic compound. Once initiated, these cracks propagate radially outward, oriented parallel to the loading direction, depicted by the white arrows in Figure 3.1b. The directional nature of these primary cracks indicates deformation by transverse elongation due to the Poisson effect, characteristic of Mode I (opening mode) type cracking [116].

2. **Secondary cracks:** These cracks, indicated by 'S' in Figure 3.1, initiate at a different location, specifically at the Nb_3Sn/Nb barrier interface. Importantly, these secondary cracks are only observed in subelements that already exhibit two or more primary cracks, suggesting a sequential damage mechanism. This observation suggests that the nucleation of secondary cracks results from the release of accumulated residual stress in the outer circumferential area of the subelements due to the primary cracks. Unlike primary cracks, secondary cracks propagate radially inwards with no specific orientation, indicating a different stress state driving their formation.

The damage classification system (D1-D5) based on crack count per subelement, illustrated in Figure 3.1, enables quantitative comparison across specimens and processing conditions. The

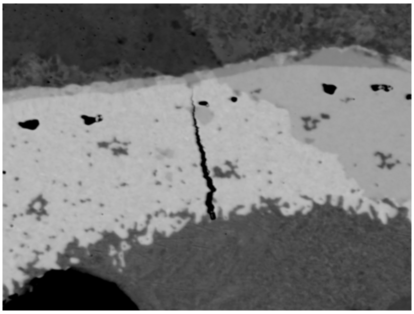

(a) High-magnification SEM micrograph showing a primary crack (P) propagating radially outward from the Cu-Sn core through the Nb_3Sn layer.

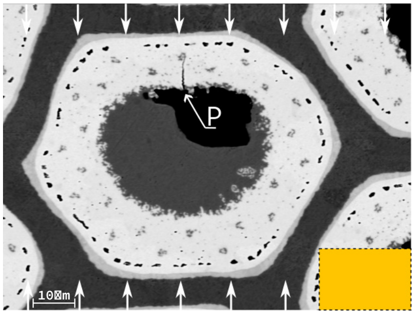

(b) D1 - Primary crack (P) initiates at the Cu-Sn core and propagates radially outward parallel to the loading direction. The compressive loading direction is shown.

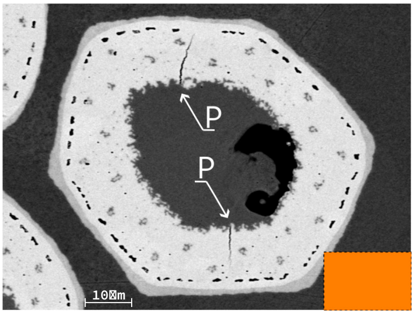

(c) D2 - Two cracks are visible within the subelement.

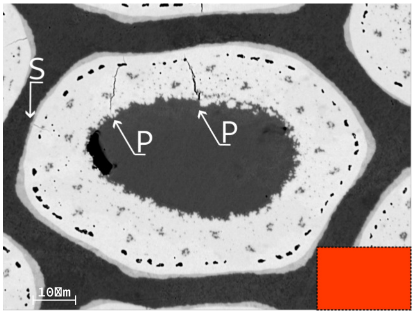

(d) D3 - Three cracks have formed, with secondary cracks (S) beginning to initiate at the Nb_3Sn/Nb barrier interface.

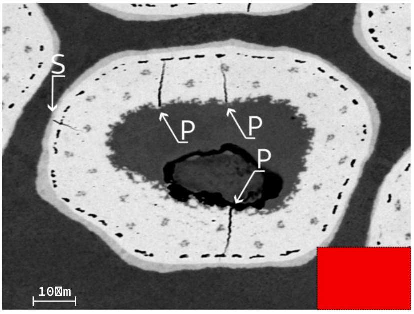

(e) D4 - Four cracks are present, showing further progression of damage.

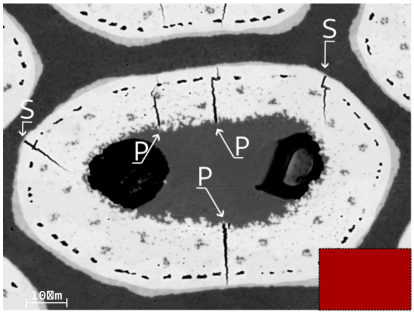

(f) D5 - Five or more cracks, representing severe damage with both primary and secondary crack types.

Figure 3.1: SEM micrographs showing the typical evolution of damage observed in the Nb_3Sn subelements. (a) High-magnification view of a primary crack propagating from the Cu-Sn core through the Nb_3Sn layer. (b-f) Damage levels (D1 to D5) are assigned to each subelement according to the total number of cracks observed. Primary cracks (P) initiate at the Cu-Sn core or at the Nb_3Sn/Cu-Sn core interface and propagate radially outward, parallel to the loading direction. Secondary cracks (S) initiate at the Nb_3Sn/Nb barrier interface in subelements with multiple primary cracks. All subelements shown are from a single wire in Specimen B.4.

sequential pattern of primary cracks at the inner interfaces followed by threshold-dependent secondary cracking remained consistent across all tested configurations.

3.1.0.2 Damage localization in a strand

A thorough analysis of damage distribution patterns within individual strands reveals distinct spatial organization characteristics of cracked subelements [169]. Three critical observations emerge from the examination of the double stack specimens as follows:

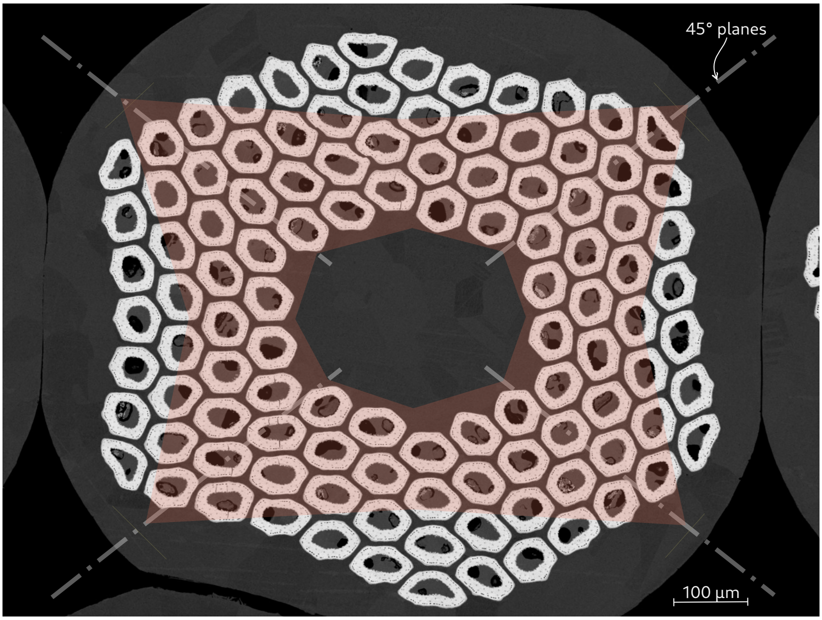

Figure 3.2: SEM micrograph of a single strand (circled in Figure 3.3) showing the characteristic damage zone localization along 45° planes (indicated by dashed gray lines). The orange shaded region delineates the damage zone boundaries where subelement cracking is concentrated. The damaged subelements are confined within this zone regardless of the local hexagonal packing arrangement.

1. **Preferential damage localization along maximum shear planes**

   The damaged subelements are concentrated along planes oriented at $45°$ relative to the axis of the applied load, as illustrated in Figure 3.2. These preferential failure planes correspond to the theoretical maximum shear stress orientation given by

$$\tau_{\text{max}} = \sigma/2 \tag{3.1}$$

where

- τ_{max} is the maximum shear stress
- σ is the applied normal uniaxial stress

The consistency of this angular relationship across all examined specimens confirms that the macroscopic stress state governs crack initiation sites in any given strand.

2. **Radial damage progression within localized zones**

   Crack development within the identified $45°$ zones exhibits systematic radial progression from subelements close to the Cu core towards the subelements in the periphery of the wire. Figure 3.3 illustrates this phenomenon through a comparison of multiple wires within a specimen. In the figure, some of the strands are categorized as exhibiting low damage **[L]** or high damage **[H]** based on the number and severity of cracked subelements within the damage zone. Initial damage manifests in central subelements adjacent to the copper core, as seen in the wires marked **[L]**. As the transverse stress increases, the damage front

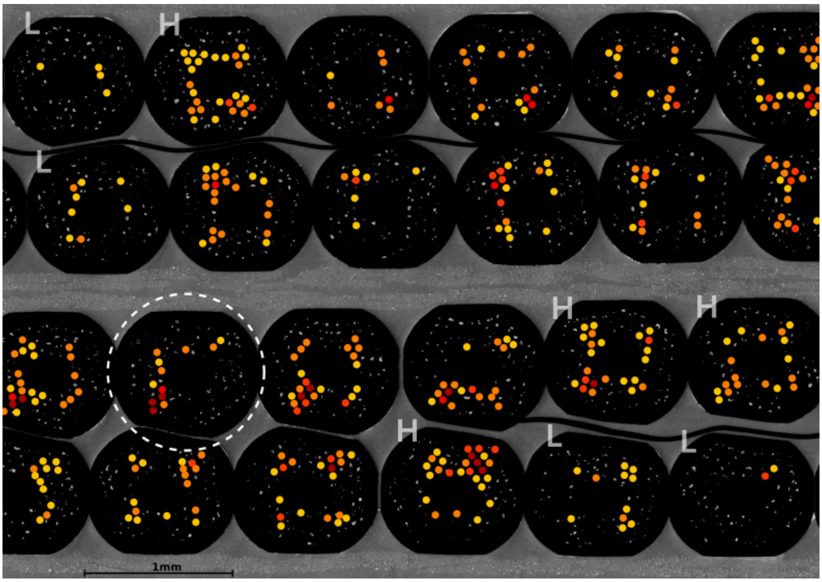

Figure 3.3: Damage map for a section of Specimen B.4 showing multiple strands with varying levels of damage. Each subelement with cracks is color-coded according to its damage level (D1-D5). To illustrate the systematic damage progression within a wire, some are marked 'L' [Low damage] - exhibiting fewer affected subelements concentrated in the central region. The strands marked 'H'[High damage] display greater number of cracked subelements. A comparison of the two types shows that the damage progresses from inner subelements outward within a strand, while maintaining concentration along the 45° planes consistent across all strands. A magnification of the circled wire is shown in Figure 3.2.

propagates outward while remaining confined within the established 45° zones, as seen in the wires marked **[H]**.

3. **Independence from subelement packing geometry**

   The close-packed hexagonal arrangement of subelements within each wire exerts negligible influence on macroscopic damage localization patterns. The damage zones maintain strict adherence to the 45° orientation regardless of the local packing direction or subelement orientation. This observation holds even when the hexagonal lattice axes are misaligned with the principal stress directions. Overall, the dominance of continuum-level stress fields over discrete microstructural features validates the application of homogenized material models for predicting damage initiation thresholds in the RRP conductor architectures.

A mechanistic explanation for the observed onset and evolution of damage may be reflected as follows:

1. **Hierarchical composite under transverse loading**: The impregnated cable integrates materials spanning two orders of magnitude in stiffness[170], from a compliant epoxy resin (E $\approx 3-4\,\mathrm{GPa}$) to the stiff metallic components: copper matrix ($110\,\mathrm{GPa}$), niobium barriers ($105\,\mathrm{GPa}$), Cu-Sn cores ($90\,\mathrm{GPa}$), and Nb_3Sn filaments ($70-100\,\mathrm{GPa}$). As described in Section 1.2, each component serves a distinct function. The A15 phase provides superconductivity, copper enables thermal and electrical stabilization, niobium barriers protect the copper matrix from tin contamination, and epoxy impregnation prevents conductor motion while bridging the $150\,\mu\mathrm{m}$ gaps between cables. This stiffness ratio between epoxy and metals creates stress concentration factors of $2.0-2.5$ at interfaces[164].

2. **Sequential thermal stress accumulation**: The cable develops residual stresses through two distinct thermal cycles. First, cooldown from the reaction heat treatment at $665\,^{\circ}\mathrm{C}$ induces differential contraction within each strand. The copper contracts $3.25\,\mathrm{mm/m}$ while Nb_3Sn contracts $2.5\,\mathrm{mm/m}$, creating $0.2-0.4\%$ compressive strain within the A15 phase. Second, epoxy impregnation at $110-120\,^{\circ}\mathrm{C}$ introduces additional stresses during curing and subsequent cooldown, as the resin ($\alpha = 44-68\times10^{-6}\mathrm{K}^{-1}$) contracts far more than metals ($\alpha = 5-20\times10^{-6}\mathrm{K}^{-1}$), further modifying the strain states of the components.

3. **Crack initiation at critical interfaces**: Above a critical applied transverse compression, cracks initiate where stress concentrations exceed material limits, specifically at Nb_3Sn/Cu-Sn interfaces where the brittle-ductile transition creates stress singularities. At these interfaces, Kirkendall voids act as preferential nucleation sites, with local stresses reaching $200-250\,\mathrm{MPa}$. Since the damage consistently localizes along 45° planes corresponding to maximum shear stress, macroscopic stress fields control fracture patterns regardless of local microstructural orientation.

4. **Progressive failure through mechanical hierarchy**: The damage advances predictably based on component strength. The copper matrix yields first (at $\sim 50\,\mathrm{MPa}$), transferring load to stiffer constituents until Nb_3Sn fractures at interface stress concentrations. The niobium barriers (yield strength $275 - 390\,\mathrm{MPa}$) provide resistance against crack propagation. Secondary cracks form only after multiple primary cracks compromise the subelements, indicating structural degradation must accumulate locally before spreading.

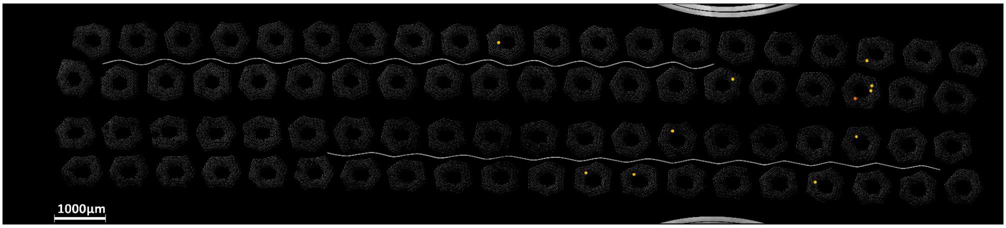

(a) Specimen A.3 (50h - CTD-101K); $106 \pm 15\,\mathrm{MPa}$

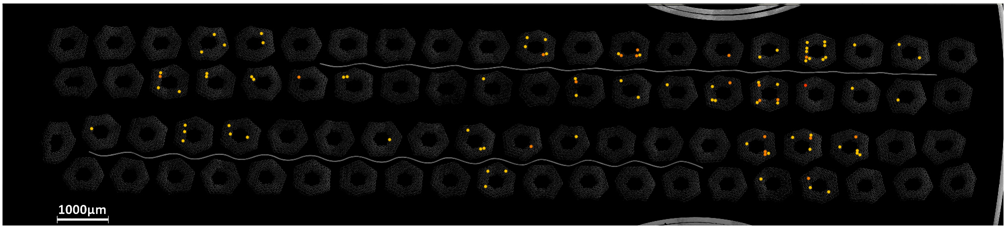

(b) Specimen A.6 (50h - CTD-101K); $142 \pm 13\,\mathrm{MPa}$

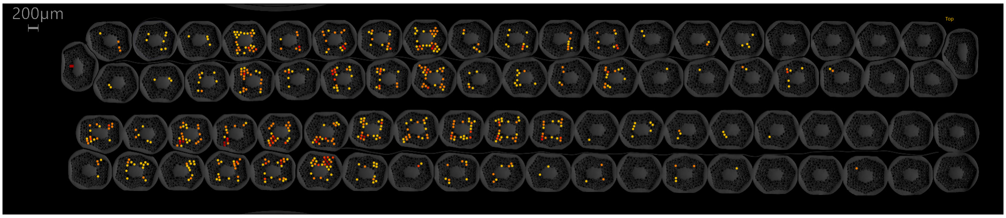

(c) Specimen B.4 (75h - CTD-101K); $104 \pm 16\,\mathrm{MPa}$

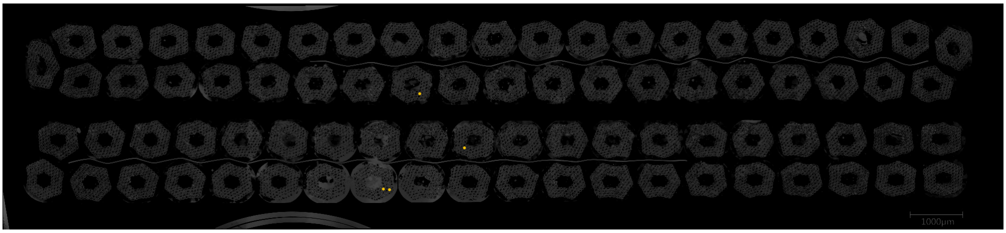

(d) Specimen D.3 (50h - MSUT-Twente); $109 \pm 10\,\mathrm{MPa}$

Figure 3.4: Optical micrographs of transverse cross-sections with damage visualization overlay. Colored dots indicate damaged subelements classified according to the D1-D5 scheme defined in Figure 3.1, while gray structures represent intact subelements.

3.1.0.3 Examples of crack maps

This section aims to present the workflow with examples using four selected specimens. In the Figure 3.4, optical micrographs with damage visualization overlays for these specimens is shown. The corresponding damage level distributions with percentages of damaged subelements are plot on a logarithmic scale for each of these specimens in Figure 3.5. The number and percentage of affected strands is also listed in each graph.

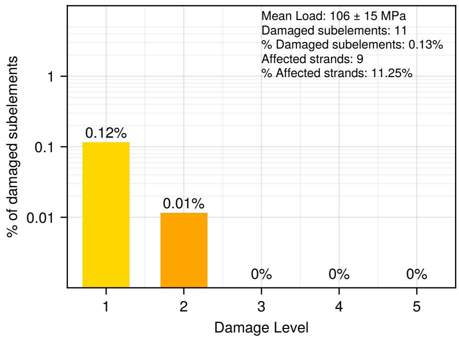

(a) Specimen A.3 (50 h - CTD-101K®); 106 ± 15 MPa

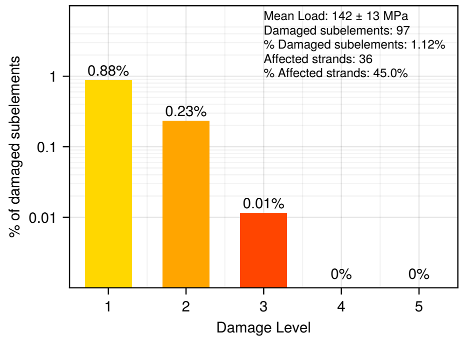

(b) Specimen A.6 (50 h - CTD-101K®); 142 ± 13 MPa

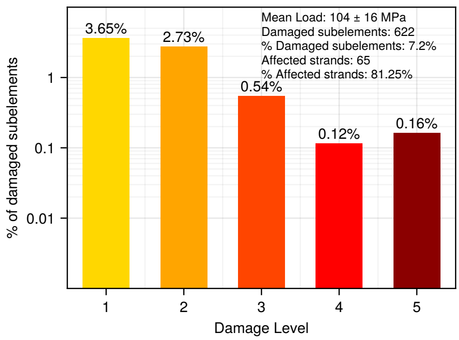

(c) Specimen B.4 (75 h - CTD-101K®); 104 ± 16 MPa

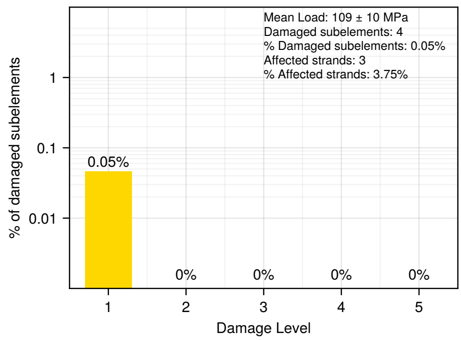

(d) Specimen D.3 (50 h - MSUT-Twente); 109 ± 10 MPa

Figure 3.5: Quantitative damage level distributions corresponding to specimens in Figure 3.4. Vertical axis uses logarithmic scale to capture the wide range of damage percentages. The distributions reveal damage variations spanning two orders of magnitude between processing conditions.

The methodology demonstrates several key capabilities:

- **Load response characterization**: Specimens A.3 and A.6, both with identical processing (50 h final RHT stage & CTD-101K® impregnation resin) but different applied mean loads

(106 MPa vs 142 MPa), show damage progression from 0.13% to 1.12% of total number of subelements in the double-stack specimens. This demonstrates the quantification of load-dependent damage evolution for a processing parameter.

- **Processing parameter differentiation**: Specimens A.3, B.4 and D.3, all with similar applied mean loads of $\approx 105 \pm 15$ MPa exhibit total subelement damage of 0.13%, 7.2% and 0.05% respectively, demonstrating the comparison of damage states for different processing parameters at the same load.

By quantifying the microscopic damage into statistical data, the relationships between heat treatment duration, impregnation material selection, and mechanical resilience are analysed in this work. The methodology thus enables a systematic investigation of processing-structure-property relationships in Nb_3Sn cables samples on a macroscopic scale.

3.2 Case Study I: Reference Cable

The reference cable establishes the performance baseline for Nb_3Sn Rutherford-type cables manufactured according to standard HL-LHC quadrupole magnet protocols. This reference case employs a $50\,\mathrm{h}$ dwell at $665\,°\mathrm{C}$ during the third stage of the reaction heat treatment cycle, followed by vacuum pressure impregnation with CTD-101K® epoxy resin. The investigation addresses three critical questions:

1. What electromagnetic performance can be reliably achieved with established manufacturing procedures?
2. At what transverse pressure does mechanical damage initiate in the brittle Nb_3Sn phase during room-temperature assembly?
3. How does this damage evolve with increasing pressure, and what are the implications for magnet design limits?

For the electrical characterization, one double-stack sample (Cable Id: H16OC0367A) has been tested in the FRESCA facility, establishing maximum current-carrying capacity across magnetic fields in both additive and subtractive configurations. Virgin and extracted wire measurements have been used for direct comparison of cabling and processing degradation. Further, a load line analysis to determine the operational margins for the MQXF coils constructed with this cable is described.

A second double-stack cable sample (Cable Id: H16OC0370A) is used for the systematic metallographic examination under controlled transverse compression from $70 - 150\,\mathrm{MPa}$. The level of transverse compression stress at which cracking in the A15 phase of the subelements is initiated and propagates has been identified and presented.

Key Findings

- **Electrical performance**: $28.5 \pm 0.1\,\mathrm{kA}$ in a peak field of $11.45\,\mathrm{T}$ with 10 training quenches, resulting in a 18% loadline margin above nominal operation of MQXF magnets
- **Damage onset**: $105 \pm 15\,\mathrm{MPa}$ transverse compression stress at room temperature
- **Damage characteristics**: At $140\,\mathrm{MPa}$, $\approx 1\%$ of subelements and $\approx 45\%$ of strands are affected

3.2.1 Electrical Performance

Figure 3.6 presents the data from a series of current ramp tests performed at various background magnetic fields. The measurement procedure is detailed in Section 2.1.2.3. The horizontal axis represents consecutive current ramp runs, while the vertical axis shows the maximum current achieved in each measurement. The colors indicate varying background field magnitudes ranging from $0-9.6\,\mathrm{T}$, with triangular markers distinguishing between additive (+) and subtractive (-) applied field directions relative to the cable's self-field .

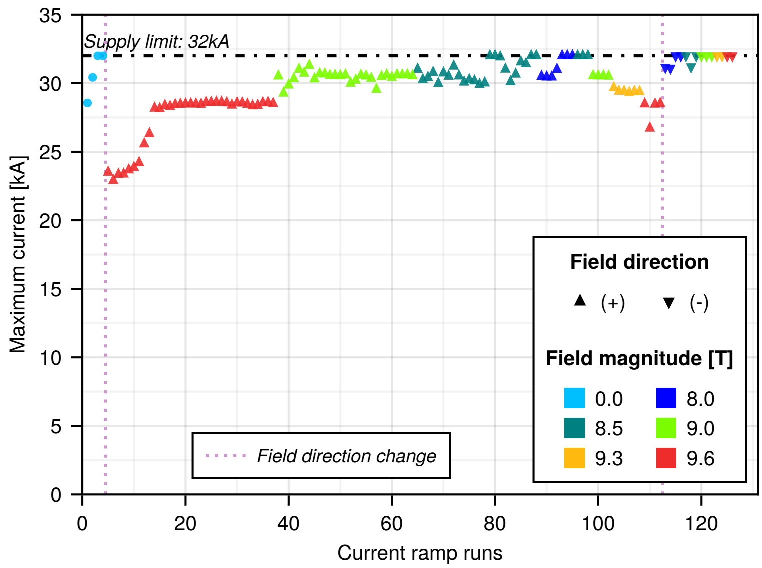

Figure 3.6: Electrical measurement data for the reference cable [H16OC0367A]. The data shows the training behavior and stability across different magnetic field strengths and polarities. The colors identify the different applied background fields from $0-9.6\,\mathrm{T}$, with triangular markers distinguishing between additive(+) and subtractive(-) field configurations.

Table 3.2 summarizes the stable current values from the measurements identified through KDE analysis at different background fields. It includes the calculated peak field, Lorentz forces and an estimation of the local transverse stress in the cable (refer Section 2.1.2).

Key observations from the electrical measurements include:

1. **Training behavior**: The sample underwent 10 training quenches to reach stable currents in the maximum background field of $9.6\,\mathrm{T}$, with $3-4$ additional quenches for the subsequent lower applied fields until $8\,\mathrm{T}$.

Table 3.2: Electrical performance and calculated electromagnetic loads for the reference cable with50 h heat treatment and CTD-101K® impregnation resin across background field configurations

Applied Field (Direction) [T]	**Quench Current** (Mean ± Std. Dev.) [kA]	**Peak Field** (Mean) [T]	**Lorentz Force** (Mean) [kN/m]	**Transverse Stress** (Mean) [MPa]
9.6 (+)	28.5 ± 0.1	11.5	326	17.8
9.3 (+)	29.4 ± 0.1	11.2	330	18.0
9.0 (+)	30.5 ± 0.4	10.9	334	18.2
8.5 (+)	> 32*	10.6	339	18.5
8.0 (+)	> 32*	10.1	323	17.6
9.6 (-)	> 32*	7.5	241	13.1

* Limited by maximum power supply

2. **Highest field performance**: At $9.6\,\mathrm{T}$ background field in the additive direction, the cable demonstrated a stable performance of $28.5 \pm 0.1\,\mathrm{kA}$ corresponding to a peak field of $11.5\,\mathrm{T}$ in the sample.

3. **Lower field performance**: At applied field of $9.0\,\mathrm{T}$, the cable achieved $30.5 \pm 0.4\,\mathrm{kA}$ with a calculated peak field of $10.9\,\mathrm{T}$. At field values of $8.5\,\mathrm{T}$ and below in the additive orientation, and for all subtractive field polarities, performance was consistently limited by the power supply maximum of $32\,\mathrm{kA}$, indicating that the cable's true electrical performance limit at these magnetic fields could not be determined.

4. **Lorentz force estimation**: At the highest measured performance of $32\,\mathrm{kA}$ in $10.6\,\mathrm{T}$ peak field, the cable experiences a Lorentz force of $339\,\mathrm{kN/m}$, corresponding to a transverse stress of $18.5\,\mathrm{MPa}$ in each cable. This quantified stress for the reference cable configuration confirms that the applied $50\,\mathrm{MPa}$ prestress ensures the cable remains in compression throughout operation.

5. **Electrical stability**: After the inital quenches at each applied field, the sample maintained reproducible performance with no evidence of cumulative degradation. This suggests that the electromagnetic forces were effectively counteracted by the applied prestress and the impregnation resin after an inital *settling* of the strands during training. The cable also successfully maintained peak current of $32\,\mathrm{kA}$ for extended periods ($>$ 30 seconds) over numerous current ramp cycles.

The overall electromagnetic performance evaluation of the cable sample is conducted by analysing the I_c versus B_p behaviour, shown in Figure 3.7. Using the measured stable currents and estimated peak fields from the measurement run, the critical current variation with magnetic field is derived using the scaling law described by Equation 2.4. The green points represent the measured cable data, while the dashed line shows the fitted critical current curve. The shaded green area indicates the confidence interval of the fit. Additional data points from virgin (in yellow) and extracted (in gray) wire measurements are included for calculation of the cabling and processing degradation. The scaling law fit for the cable sample utilizes only three measured data points, yet provides useful estimates for performance comparison across the operational field range. Table 3.3 presents a comparative analysis at key field values between cable measurements and model predictions based on virgin and extracted strand data. These values are derived from the scaling law fits applied to both cable and strand measurements. In the figure, the black solid line represents the load line for the MQXF quadrupole magnet design, with the intersection of this line and the critical current curve of the reference cable, marked by the circle symbol defining the Short Sample Limit (SSL) of the magnet. The nominal operational point for this magnet is marked by the star symbol. Table 3.4 summarizes the key parameters obtained from the scaling law fit and loadline analysis for both cable and strand measurements.

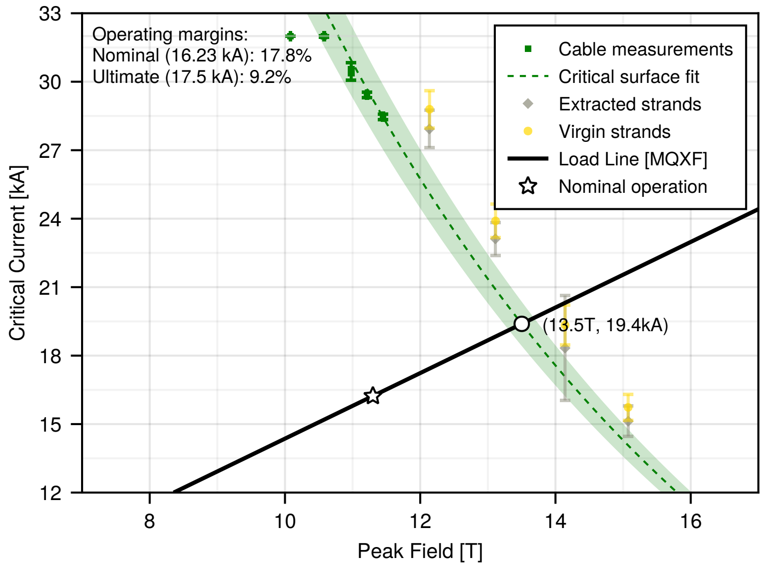

Figure 3.7: Short sample limit (SSL) and operating margin analysis for the reference cable, processed with the standard heat treatment and impregnation resin. The green points represent cable measurements, with the dashed line showing the scaling law fit of the critical current as a function of peak field. The shaded area indicates the confidence interval of the fit. Yellow points show data from virgin strands, while gray points represent extracted strands of this cable. The black line represents the load line for the MQXF magnet design, with the white circle marking the intersection point (SSL) at 13.5 T and 19.4 kA. The operating margin for nominal operation of the magnets at 16.23 kA at 11.3 T with the reference cable is about 18%.

Table 3.3: Critical current values derived from scaling law fits applied to cable and strand measurements, showing magnetic field-dependent cabling degradation and cable-to-strand performance deviation at 4.2 K

Field	Cable Sample	Virgin Strand Model	Extracted Strand Model	Cabling Degradation Virgin/Extracted	Cable Performance vs. Extracted
[T]	[kA]	[kA]	[kA]	[%]	[%]
10.0	36.7	42.7	41.7	2.3	12.0
11.0	30.8	35.7	34.7	2.8	11.2
12.0	25.7	29.6	28.7	3.0	10.5
13.0	21.4	24.4	23.5	3.7	8.9
14.0	17.6	19.9	19.1	4.0	7.9

Key findings from the electromagnetic performance evaluation include:

1. **Comparison with single strands**: The comparison between virgin and extracted strand data reveals minimal cabling degradation of $2-4\%$, with this effect becoming slightly more pronounced at higher magnetic fields. A more significant difference is observed between the cable sample and extracted strands, ranging from $8-12\%$ reduction. This arises from multiple factors including residual strain effects within the impregnated Rutherford cable configuration, current distribution non-uniformities among the multi-strand assembly, and electromagnetic coupling effects between adjacent strands. The B_{c2} value derived for the cable (26.1 T) exceeds both virgin (25.2 T) and extracted (25.5 T) strand values. This apparent enhancement lacks physical justification and indicates limitations in the cable scaling law fit [171], particularly due to insufficient measurement points at fields above 12 T where the critical surface behavior becomes most apparent. The scaling parameter, C shows a successive reduction in the cable ($1558\,\mathrm{kA}\cdot\mathrm{T}$) compared to strand values ($1844\,\mathrm{kA}\cdot\mathrm{T}$ for virgin, $1823\,\mathrm{kA}\cdot\mathrm{T}$ for extracted), reflecting approximately 15% reduction in the effective pinning force within the cable configuration.

2. **Short sample limit analysis**: A short sample limit of 19.4 kA at 13.5 T is estimated from the cable sample measurements, representing a $5-6\%$ reduction compared to strand limit predictions (virgin: 20.1 kA at 13.9 T, extracted: 19.8 kA at 13.8 T). The operational margins for the MQXF magnets is then 18% at nominal operating conditions and 9% at ultimate conditions. While the load line margins falls below the 20% typically targeted for high-field accelerator magnets, the stability and reproducibility after initial training with no evidence of cumulative degradation over numerous current ramp cycles validate the mechanical design approach and confirm effective management of electromagnetic forces during operation.

Table 3.4: Scaling law parameters and short sample limit analysis for the reference cable (50-hour heat treatment, CTD-101K® resin) compared with virgin and extracted strand measurements at 4.2 K

Parameter	Unit	Cable	Virgin Strand	Extracted Strand
Upper critical field (B_{c2})	[T]	26.1	25.2	25.5
Scaling parameter (C)	[kA·T]	1558 ± 78	1844	1823
Short sample limit	[kA at T]	19.4 at 13.5	20.1 at 14.0	19.8 at 13.8
Nominal operating margin (16.23 kA)	[%]	17.8	23.6	22.3
Ultimate operating margin (17.5 kA)	[%]	9.2	14.6	13.4

3.2.2 Damage Onset and Evolution

For the metallographic investigation to characterise the onset and evolution of damage, six specimens were subjected to mean transverse compression stresses varying from $80 - 150\,\mathrm{MPa}$. Table 3.5 quantifies the crack density distribution obtained across these specimens. Figure 3.8 illustrates the evolution of damage with increasing transverse pressure for these specimens, showing both the percentage of damaged subelements and their classification by severity level. Figure 3.9 presents the corresponding distribution of affected strands across the double-stack cable specimen cross-sections. For all the specimens, crack morphology and distribution follows patterns established in Section 3.1.

Table 3.5: Statistical distribution of damage across specimens subjected to varying transverse compression stress with 50-hour heat treatment duration and CTD-101K® impregnation resin.

Specimen	Applied Stress		Number of damaged subelements							Strands with damaged subelements	
Id.	Mean, μ (MPa)	Std. Dev., σ (MPa)	D1	D2	D3	D4	D5	Net	[% of 8640]	Net	[% of 80]
A.1	90	19	0	0	0	0	0	0	0	0	0
A.2	96	13	0	0	0	0	0	0	0	0	0
A.3	106	15	10	1	0	0	0	11	0.13	9	11.25
A.4	118	18	29	4	0	0	0	33	0.38	18	22.5
A.6	142	13	76	20	1	0	0	97	1.12	36	45.0
A.5	147	8	67	18	0	0	0	85	0.98	34	42.5

Key observations from the metallographic analysis include:

1. **Damage onset threshold**: No cracks were observed in specimens A.1 and A.2, subjected to mean compressive stresses of $90\,\mathrm{MPa}$ and $96\,\mathrm{MPa}$ respectively. Initial damage appeared in specimen A.3 at $106 \pm 15\,\mathrm{MPa}$, with 0.13% of subelements showing cracks.

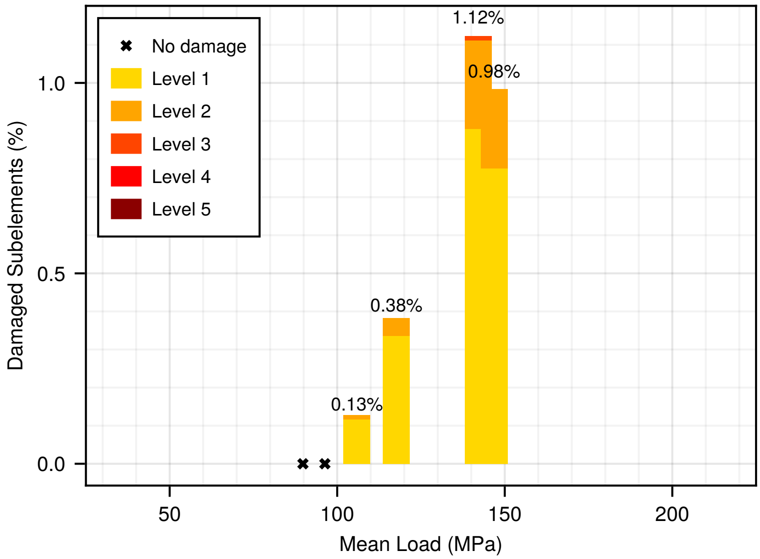

Figure 3.8: Percentage of damaged subelements categorized by damage level (D1-D5) as a function of applied mean transverse pressure for the reference cable specimens, with 50-hour heat treatment duration and CTD-101K® impregnation resin. The predominance of D1 and D2 damage levels indicates resistance to crack propagation in this range.

This establishes the damage onset threshold at $\approx 105 \pm 15\,\mathrm{MPa}$ for the reference cable configuration.

2. **Damage evolution with pressure**: The progression of damage with increasing transverse stress reveals a non-linear relationship. At a mean applied stress of $118\,\mathrm{MPa}$ (specimen A.4), damage remained minimal with 0.4% of subelements affected. The damage increased to ≈1% at a mean stress of $140\,\mathrm{MPa}$ in specimens A.5 & A.6. Between the onset threshold and $140\,\mathrm{MPa}$, the average damage gradient measures approximately $0.025\%/\mathrm{MPa}$. In context of the distribution across the affected strands, at mean stress of $142\,\mathrm{MPa}$, the 1.12% of damaged subelements are distributed across 45% of the strands. The predominance of low-level damage (D1 and D2) across all tested pressures indicates that crack initiation occurs readily between $100 - 140\,\mathrm{MPa}$, but propagation requires higher loads. Only specimen A.6 showed any D3 damage, and no specimens exhibited D4 or D5 damage levels.

A discussion on the observed severity and distribution of damage can be made as follows:

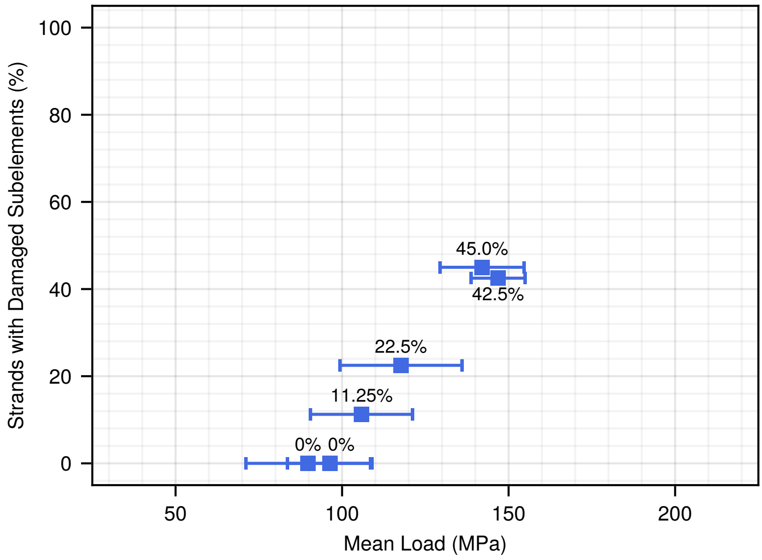

Figure 3.9: Percentage of strands containing at least one damaged subelement as a function of applied mean transverse compression stress for the reference cable specimens, with 50-hour heat treatment duration and CTD-101K® impregnation resin. The ratio between affected strands and damaged subelements demonstrates the distributed nature of damage throughout the cable cross-section.

1. **Damage localization and matrix accommodation**: The predominance of low-level damage (D1-D2) with only 1% of subelements affected at $140\,\mathrm{MPa}$ indicates that the copper matrix still effectively accommodates deformation after initial crack formation. Once a crack initiates, the surrounding copper undergoes local plastic flow, relieving stress concentrations and preventing immediate crack propagation. This suggests that the damage remains limited despite pressures well above the onset threshold.

2. **Mechanical-electrical performance offset**: A critical finding emerges from comparing the onset of mechanical damage at $105\,\mathrm{MPa}$ with electrical performance expectations. Previous studies on RRP® cables (described in Section 1.2.4) suggest that irreversible electrical degradation of $> 2\%$ occurs in the range of $150 - 190\,\mathrm{MPa}$. The data presented here indicate that the onset of cracking the A15 phase may also contribute to the onset of irreversible electrical degradation, alongwith the plasticization of the copper matrix as is currently theorized. Importantly, this offset between mechanical and electrical thresholds implies a substantial operational window exists where mechanical damage exists but electrical performance remains largely unaffected. The copper matrix's current-sharing

capability and the redundancy inherent in the multifilamentary design enable the conductor to maintain performance despite localized damage.

3.2.3 Implications for Magnet Design

The reference case study establishes critical performance benchmarks and design constraints for Nb_3Sn accelerator magnets, using the standard RHT protocol and CTD-101K® resin. The cable sample underwent 10 training quenches, and demonstrates stable electrical performance resulting in a loadline margin of 18% for nominal operating conditions of the magnet. This is a sufficient performance headroom for reliable operation. The damage onset threshold of $105 \pm 15\,\mathrm{MPa}$ establishes a fundamental constraint for magnet assembly procedures, if cracking in the A15 phase is to be avoided. Based on this finding, a maximum transverse pressure limit of $100\,\mathrm{MPa}$ is recommended for room-temperature prestress application. This recommendation, more conservative than some previous studies suggest, accounts for the observation that mechanical damage precedes measurable electrical degradation. The specification has been adopted for MQXF quadrupole magnets currently being fabricated at CERN[172].

The quantified damage thresholds and operating margins, obtained by characterising impregnated cables thus provide essential data for optimizing assembly procedures and establishing realistic performance expectations. This baseline performance serves as the reference against which subsequent processing variations will be evaluated, enabling systematic assessment of potential improvements in both electromagnetic capability and mechanical resilience.

3.3 Case Study II: Insufficient Prestress

Following the analysis of the reference cable, this case study examines the consequences of insufficient external mechanical support during operation. This configuration attempts to simulate conditions where insufficient prestress, manufacturing variations, assembly defects or stress relaxation compromise the structural integrity of the Nb_3Sn cables. The investigation employed identical processing protocols to Case Study I, i.e. the standard $50\,\mathrm{h}$ duration for the final stage of RHT at $665\,^\circ\mathrm{C}$ and impregnation with CTD-101K® epoxy resin. Only a single modification is made to the sample holder configuration, such that a few pre-determined regions of the double-stack cable sample were deliberately left without the $50\,\mathrm{MPa}$ prestress transfer through the insulating spacer assembly (refer Figure 2.8).

This investigation addresses a critical operational scenario:

- What is the behavior of Nb_3Sn cables when the electromagnetic forces are not adequately counteracted by the external prestress?
- What is the minimum local prestress load required for stable electrical performance of the cable at $4.3\,\mathrm{K}$?

For this study, the electrical performance of a double-stack cable sample (Cable Id: H16OC0290A) in the modified sample holder is measured to quantify the impact on current-carrying capacity and operational stability. Next, a metallographic analysis is carried out on the quench localization site to document the microstructural damage mechanisms.

Key Findings

- **Electrical performance**: 38% capacity loss demonstrates severe degradation without adequate mechanical support
- **Critical failure threshold**: $11 \pm 2\,\mathrm{MPa}$ interfacial debonding establishes minimum operational prestress requirement
- **Operating margin**: Less than 1% margin eliminates safety factor, confirming prestress as fundamental design requirement

3.3.1 Electrical Performance

Figure 3.10 presents the electrical test data for the cable sample in this case-study. The measurement protocol replicated that of the reference case, with current ramp tests at background fields from $0 - 9.6\,\mathrm{T}$ in both additive(+) and subtractive(-) configurations (refer Figure 2.12). The Table 3.6 summarizes the electrical performance determined from the measurement run for each applied background field, along with the calculated corresponding peak field, Lorentz forces and the equivalent local transverse stress in the cables.

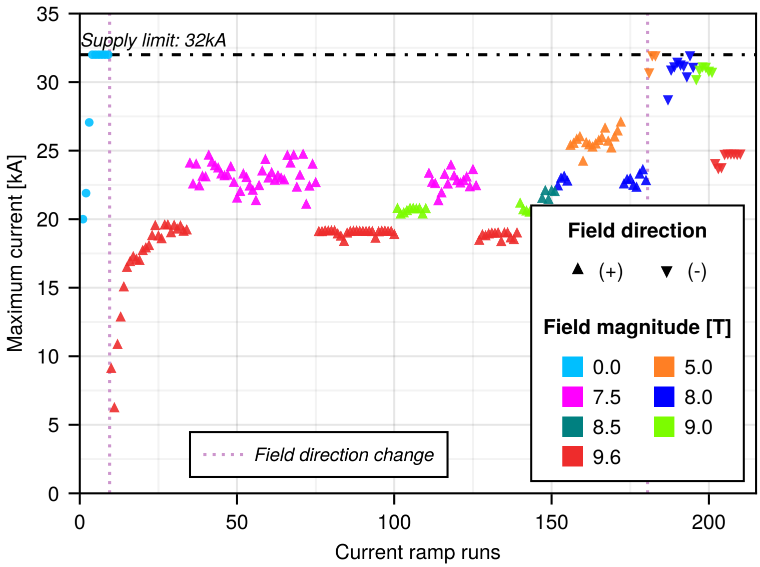

Figure 3.10: Electrical measurement data for double-stack cable sample (Id: H16OC0290A). Extended training behavior and current oscillations indicate mechanical instability in regions without adequate pre-compression. The colors differentiate the applied background field strengths from $0 - 9.6\,\mathrm{T}$, with the triangular markers distinguishing additive (+) and subtractive (-) field directions

The analysis of the electrical measurements reveal deviations from the reference sample behavior:

1. **Extended training period**: The number of training quenches extended beyond 30 ramp cycles compared to approximately 10 cycles for the reference sample. The training also began at much lower quench currents, around $6\,\mathrm{kA}$ compared to $23\,\mathrm{kA}$ for the former.

2. **Reduced current-carrying capacity and stability**: In $9.6\,\mathrm{T}$ background field, the sample reaches a stable $18.9 \pm 0.3\,\mathrm{kA}$, with an estimated peak field of $10.8\,\mathrm{T}$ in the cables. This represents a 38% reduction from the reference sample's $30.5 \pm 0.4\,\mathrm{kA}$ for the same peak field. The increased standard deviation reflects the mechanical state within the sample. Moreover, the sample exhibited substantial oscillations in quench currents as the applied magnetic field is lowered, and the current carrying capacity increases. These fluctuations,

which are not observed in the reference case suggest mechanical instability due to regions without prestress stabilization.

3. **Local transverse stress estimation**: Analysis of the estimated stress due to Lorentz forces at quench conditions reveals that quenches occur when the force reached approximately $175 - 216\,\mathrm{kN/m}$, corresponding to transverse stresses of $9.5 - 11.8\,\mathrm{MPa}$ on the cable surface.

4. **Repeatable degraded performance**: The cable demonstrated repeatable quench behaviour or current-carrying capacity on cycling between field levels, indicating a stable but severely degraded mechanical configuration rather than progressive deterioration.

Table 3.6: Electrical performance and calculated electromagnetic loads for the cable with inadequate prestress, 50-hour heat treatment duration and CTD-101K® impregnation resin across background field configurations

Applied Field (Direction) [T]	**Quench Current** (Mean ± Std. Dev.) [kA]	**Peak Field** (Mean) [T]	**Lorentz Force** (Mean) [kN/m]	**Transverse Stress** (Mean) [MPa]
9.6 (+)	18.9 ± 0.3	10.8	205	11.2
9.0 (+)	20.6 ± 0.2	10.3	213	11.6
8.5 (+)	21.8 ± 0.3	9.9	216	11.8
8.0 (+)	22.8 ± 0.4	9.5	216	11.8
7.5 (+)	23.2 ± 1.0	9.0	209	11.4
5.0 (+)	26.2 ± 1.3	6.7	175	9.5
9.6 (-)	24.5 ± 0.5	8.0	196	10.7
9.0 (-)	30.8 ± 0.3	7.0	216	11.8

The comparison of cable measurements with virgin and extracted strand data, with a loadline analysis is shown in Figure 3.11. The red points represent measured cable performance data, dramatically shifted to lower currents compared to the extrapolation based on extracted (gray) strand measurements. The fitted critical current curve intersects the MQXF load line at $16.7\,\mathrm{kA}$ and $11.6\,\mathrm{T}$, which corresponds to the short sample limit with this cable. The Table 3.7 presents the field-dependent performance comparison using the scaling law fits from the cable and strand transport-current measurements. The systematic degradation across all field values quantifies the severity of performance loss in a case of inadequate mechanical support. Table 3.8 summarizes the scaling law parameters and operational margins estimated using these fits.

Key findings from the electromagnetic performance evaluation include:

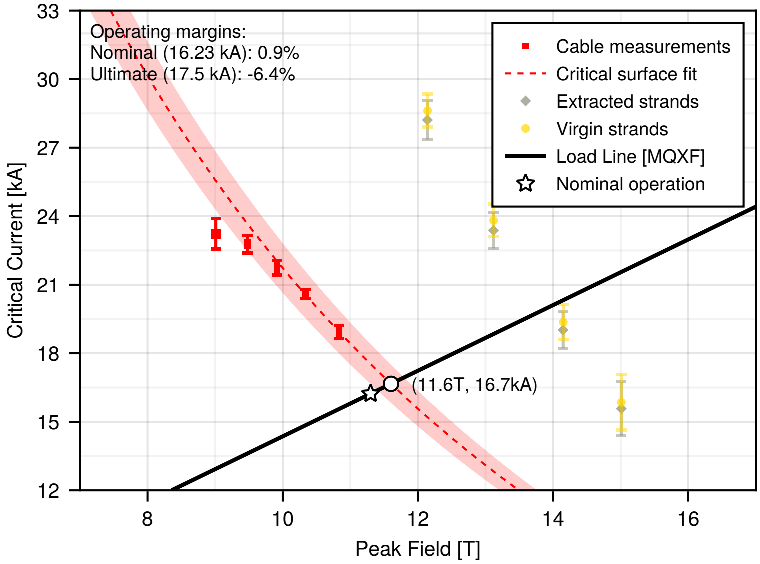

Figure 3.11: Short sample limit and operational limit analysis for the cable sample with inadequate pre-compression. Red points represent cable measurements, with the dashed line showing the critical current fit. Yellow and gray points indicate virgin and extracted strand data respectively. The MQXF load line intersects the fit curve at 11.6 T and 16.7 kA resulting in operating margin of 0.9% at nominal conditions.

Table 3.7: Field-dependent critical current comparison between cable sample with inadequate prestress, 50-hour heat treatment duration, and CTD-101K® impregnation resin versus strand measurements at 4.2 K

Field	**Cable Sample**	**Virgin Strand**	**Extracted Strand**	**Cabling Degradation**	**Cable Sample**
		Model	Model	Virgin/Extracted	Degradation
[T]	[kA]	[kA]	[kA]	[%]	[%]
10.0	21.7	42.5	41.9	1.4	48
11.0	18.4	35.5	35.0	1.4	47
12.0	15.6	29.5	29.0	1.7	46
13.0	13.1	24.3	23.9	1.6	45
14.0	11.0	19.9	19.5	2.0	44

1. **Severe performance degradation without prestress**: The cable demonstrates 44 - 48% degradation compared to extracted strand model predictions across the operational field range. The scaling parameter, C reduces to $889 \pm 44\,\mathrm{kA} \cdot \mathrm{T}$, which is 50% of extracted strand value. This degradation cannot be attributed to cabling effects, which is measured to be $1 - 2\%$ difference between virgin and extracted strands, but directly results from

Table 3.8: Scaling law parameters and short sample limit analysis for cable sample with inadequate prestress, 50-hour heat treatment duration, CTD-101K® impregnation resin compared with virgin and extracted strand measurements at $4.2\,\mathrm{K}$

Parameter	Unit	Cable	Virgin Strand	Extracted Strand
Upper critical field (B_{c2})	[T]	26.6	25.6	25.5
Scaling parameter (C)	[kA·T]	889 ± 44	1831	1810
Short sample limit	[kA at T]	16.7 at 11.6	20.1 at 14.0	20.0 at 13.9
Nominal operating margin (15.23 kA)	[%]	0.9	23.5	22.9
Ultimate operating margin (16.5 kA)	[%]	-6.4	14.5	14.0

mechanical instability under electromagnetic loading without adequate external constraint. Similar to the previous case, the apparent B_{c2} enhancement compared to the strands represents an unphysical artifact arising from lack of sufficient data points at higher fields.

2. **Short sample limit analysis**: The short sample limit for this cable sample is estimated from the scaling law fit to be $16.7\,\mathrm{kA}$ at $11.6\,\mathrm{T}$, compared to $19.4\,\mathrm{kA}$ at $13.5\,\mathrm{T}$ for the reference case. For this value, the operating margins becomes critically low under 1% for nominal conditions and -6% at ultimate conditions.

3. **Critical prestress threshold identified**: The consistent quench initiation at $11 \pm 2\,\mathrm{MPa}$ stress estimated from the Lorentz forces in the cable establishes the minimum mechanical support requirement during operation, to avoid this critical failure mode.

3.3.2 Post-Test Examination and Damage Assessment

Visual inspection and metallographic examination of the cable sample following the measurement campaign revealed the physical manifestations of electromagnetic failure in regions without prestress. Figure 3.12 presents the macroscopic structural changes, while Figure 3.13 shows the transverse cross-section at the quench localization site. Figure 3.14 illustrates the microscopic damage mechanisms through higher magnification imaging.

Key observations from the post-test examination include:

1. **Macroscopic cable deformation and delamination**: The sample exhibited pronounced bulging of $0.5 - 1\,\mathrm{mm}$ beyond original thickness, at the locations where prestress was not applied. This equates to a $7 - 8\%$ dimensional increase in the uncompressed regions. At the location where quench initiation was localised, a clear delamination occurred at the resin interface between the two cables forming the double-stack sample, as shown in

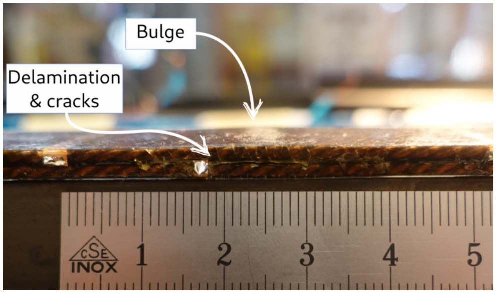

(a) External view showing bulging deformation and visible delamination between the two cables.

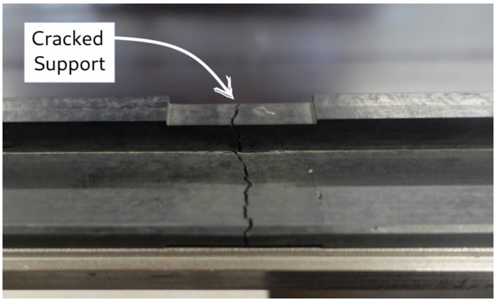

(b) Crack in the insulating sample holder assembly, where prestress is not transfered.

Figure 3.12: Macroscopic damage in the region where quenches are localised during electromagnetic loading. The visible delamination between cables (a) and structural failure of the sample holder (b) indicate severe mechanical instability under Lorentz forces in the region with inadequate prestress.

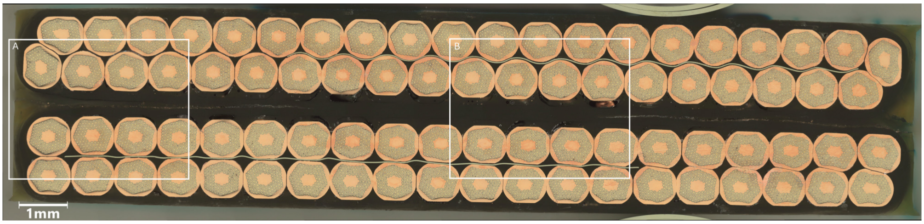

Figure 3.13: Transverse cross-section at the quench localization site showing extensive damage. Cracks in the impregnationresin delaminating the cables (A) is shown in Figure 3.14a. Debonding of the wires from the impregnation resin (B) is shown in Figure 3.14b.

Figure 3.12a. The structural failure extended beyond the sample itself, with well-defined cracks propagating through the sample holder structure at the undercompressed locations, as seen in Figure 3.12b. This points to the cable's inability to contain the electromagnetic stresses without external mechanical constraint.

2. **Symmetric crack initiation and propagation patterns**: A micrograph of the metallographed cross-section of the sample at the quench site highlighting the two types of damage observed, is shown in Figure 3.13. Major cracks in the impregnation resin initiated from both thin edges of the double-stack sample and propagating symmetrically inward between the two cables, shown in Figure 3.14a. This corresponds to the macroscopic bulging and delamination observed. The crack morphology exhibited characteristic brittle fracture through the impregnation resin. In Figure 3.14b, debonding occurred at the strand-resin interfaces, particularly pronounced at the inner strand locations where peak stresses are expected (refer Figure 2.15).

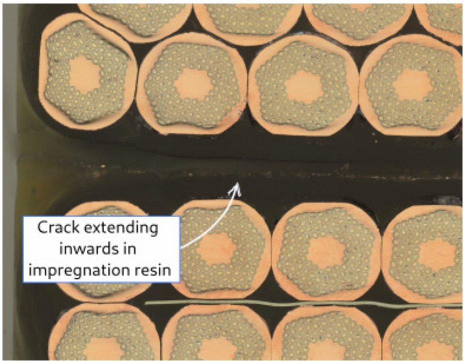

(a) Crack propagation through impregnation resin between adjacent strands showing characteristic brittle fracture morphology.

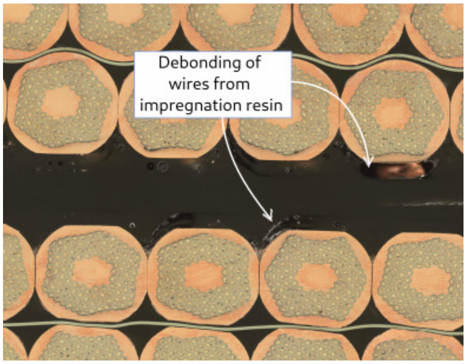

(b) Interfacial debonding between strands and impregnation resin, with separation occuring predominantly at the strand/resin interface.

Figure 3.14: Microstructural damage mechanisms in the under-compressed region. Resin cracking (a) and interfacial debonding (b) dominate the damage pattern while Nb_3Sn subelements within strands remain intact.

3. **Preserved Nb_3Sn microstructure despite composite failure**: No visible cracking was observed within Nb_3Sn subelements despite extensive resin damage and interfacial debonding. The superconducting subelements maintained structural integrity while the supporting resin underwent progressive degradation. This selective damage pattern explains the degraded but non-zero current-carrying capacity observed during electrical testing.

A mechanistic interpretation of the observed damage can be explained by:

1. **Interfacial failure at critical stress threshold**: The calculated transverse stress of $11 \pm 2\,\mathrm{MPa}$ at quench initiation closely matches reported epoxy-copper interfacial bond strength[133]. CTD-101K® demonstrates adhesion strength of $8.5\,\mathrm{MPa}$ on a copper substrate at room temperature, increasing to $13.5\,\mathrm{MPa}$ at $77\,\mathrm{K}$. The observed failure indicates that interfacial debonding represents the primary failure mechanism rather than bulk resin fracture, which would require exceeding the fracture toughness of $0.82\,\mathrm{MPa}\sqrt{\mathrm{m}}$.

2. **Progressive degradation through cyclic loading**: Each current ramp subjected the under-compressed cable to Lorentz forces inducing cyclic bending moments. Once initial debonding occurred at the strand-resin interface, freed surfaces deflected under electromagnetic loading, inducing tensile stress in the surrounding resin and driving crack propagation. This mechanism explains the extended training behavior and oscillating electrical performance attributed to movement quenches.

3.3.3 Implications for Magnet Design and Operation

The severe performance reduction observed without adequate prestress demonstrates the critical importance of uniform mechanical support throughout the magnet structure. Operating margins decreased from approximately 18% to less than 1% at nominal conditions for the MQXF magnet, eliminating the safety factor required for reliable operation. This reduction in margin leaves no capacity for environmental variations, manufacturing tolerances, or degradation over operational lifetime.

This case study thus establishes the minimum prestress requirement during magnet operation, and consequent effects of the lack of it. The local prestress must remain above $11 \pm 2\,\mathrm{MPa}$ throughout operational lifetime accounting for prestress relaxation or creep. Regions experiencing insufficient support, whether from assembly tolerances, structural discontinuities, or differential thermal contraction would undergo resin-strand interfacial debonding. Once debonding initiates, cyclic electromagnetic forces drive progressive mechanical degradation in the impregnation resin through crack propagation, manifesting as extended training, current instabilities, and ultimately negative operating margins as demonstrated in this investigation.

3.4 Case Study III: Variation in Impregnation Resin

Building on the theoretical framework presented in Section 1.2.3, this investigation evaluates two alternative resin systems proposed for future accelerator magnets with superior fracture toughness, viz. POLAB Mix and MSUT-Twente. These resin systems promise improved material properties compared to the standard CTD-101K® resin, potentially improving the strain state of the A15 phase, and/or reducing both crack initiation and the energy release that triggers training quenches.

This investigation addresses three critical questions:

1. What impact do alternative resin systems have on electrical performance, training behavior, and operational stability?
2. Can alternative resin systems significantly elevate the transverse compressive stress threshold for mechanical damage in Nb_3Sn cables?
3. How do they differ in damage evolution rate under increasing transverse compression?

For electrical characterization, one double-stack sample (Cable Id: H16OC0366A) impregnated with POLAB Mix underwent testing. The mechanical damage assessment was conducted on both the resin systems on double-stack cable specimens (Cables Ids: H16OC0367A for POLAB Mix, H16OC0290A for MSUT-Twente). Samples of $50\,\mathrm{mm}$ length were subjected to controlled transverse compression from $70 - 180\,\mathrm{MPa}$, followed by metallographic analysis to quantify damage onset and evolution patterns. All the samples in this case study are processed for the reference $50\,\mathrm{h}$ during the final stage of the RHT cycle.

Key Findings

- **Electrical performance**: 5% I_c enhancement with POLAB Mix, with a 50% reduction in training quenches compared to CTD-101K® impregnated sample
- **Damage onset**: Improved threshold for POLAB Mix: $121 \pm 15\,\mathrm{MPa}$, no improvement in threshold for MSUT-Twente: $109 \pm 10\,\mathrm{MPa}$
- **Damage characteristics**: At $140\,\mathrm{MPa}$, POLAB Mix shows $\approx 0.15\%$ and MSUT-Twente $\approx 0.43\%$ damaged subelements, compared to $\approx 1\%$ for reference CTD-101K® case.

3.4.1 Electrical Performance with POLAB Mix Resin

Figure 3.15 presents the data from the electrical characterization performed at various background magnetic fields for the cable sample impregnated with POLAB Mix resin. The horizontal axis represents consecutive current ramp runs, while the vertical axis shows the maximum current achieved in each measurement. The different colors indicate varying background field magnitudes ranging from $0 - 9.6\,\mathrm{T}$, with triangular markers distinguishing between additive (+) and subtractive (-) applied field directions relative to the cable's self-field.

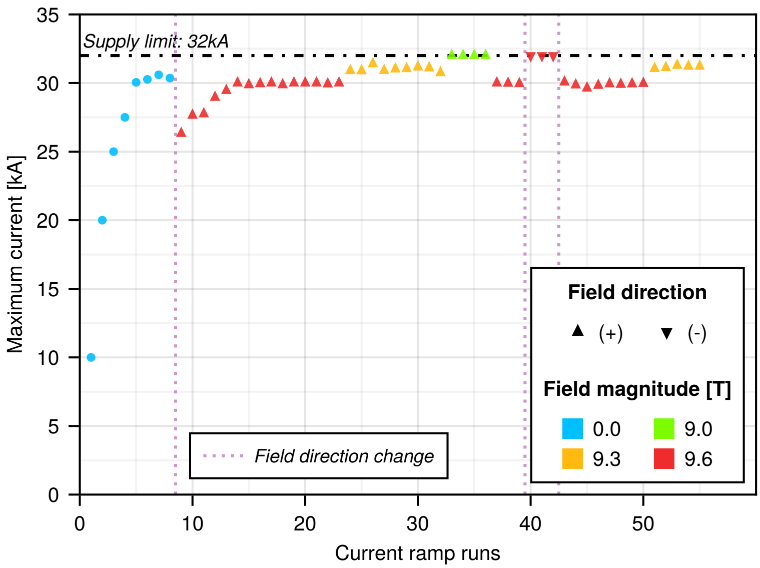

Figure 3.15: Electrical measurement data for the POLAB Mix resin cable sample [H16OC0366A]. The data shows the training behavior and stability across different magnetic field strengths and polarities. The colors identify the different applied background fields from $0 - 9.6\,\mathrm{T}$, with triangular markers distinguishing between additive (+) and subtractive (-) field directions.

Table 3.9 summarizes the stable current values from the measurement run identified through KDE analysis at different background fields. It also includes the calculated peak field, Lorentz forces and an estimation of the local transverse stress in the cable respectively.

Key observations from the electrical measurements include:

1. **Training behavior**: The sample reached stable performance after 5 current ramp cycles, compared to approximately 10 cycles required for the reference CTD-101K® sample. This

Table 3.9: Electrical performance and calculated electromagnetic loads for the cable with POLAB Mix resin and 50-hour heat treatment duration across background field configurations

Applied Field (Direction) [T]	**Quench Current** (Mean ± Std. Dev.) [kA]	**Peak Field** (Mean) [T]	**Lorentz Force** (Mean) [kN/m]	**Transverse Stress** (Mean) [MPa]
9.6 (+)	29.9 ± 0.2	11.5	345	18.8
9.3 (+)	31.1 ± 0.2	11.3	352	19.2
9.0 (+)	> 32*	11.1	355	19.3
9.6 (-)	> 32*	7.5	241	13.1

* Limited by power supply maximum

50% reduction in training requirements indicates a more rapid mechanical stabilization with the enhanced resin system.

2. **Highest field performance**: At $9.6\,\mathrm{T}$ background field in the additive direction, the cable demonstrated a stable performance of $29.8 \pm 0.2\,\mathrm{kA}$ corresponding to a peak field of $11.5\,\mathrm{T}$. This represents approximately 5% improvement over the reference CTD-101K® sample which achieved $28.5 \pm 0.1\,\mathrm{kA}$ in the same background field.

3. **Lower field performance**: In a background field of $9.3\,\mathrm{T}$, the cable achieved $31.1 \pm 0.2\,\mathrm{kA}$ with a calculated peak field of $11.3\,\mathrm{T}$. At field values of $9.0\,\mathrm{T}$ and below in the additive orientation, and for all subtractive field polarities, performance was consistently limited by the power supply maximum of $32\,\mathrm{kA}$.

4. **Lorentz force estimation**: At the highest measured current of $32\,\mathrm{kA}$ and $11.1\,\mathrm{T}$ field, the cable experienced an estimated Lorentz force of $345\,\mathrm{kN/m}$, corresponding to a transverse stress of $19.3\,\mathrm{MPa}$, much lower than the applied prestress of $50\,\mathrm{MPa}$. This represents a slightly higher operational stress compared to that calculated for the reference case ($18.5\,\mathrm{MPa}$), due to the enhanced current capacity.

5. **Electrical stability**: After initial training, the sample maintained reproducible performance with standard deviations of $0.25\,\mathrm{kA}$ or less across all field levels. The cable successfully maintained peak current of $32\,\mathrm{kA}$ for extended periods (> 30 seconds) over numerous current ramp cycles at $9.0\,\mathrm{T}$ and below, with no evidence of progressive degradation through the measurement campaign.

The overall electromagnetic performance evaluation of the cable sample is conducted by analysing the I_c versus B_p behaviour, shown in Figure 3.16. Using the measured stable currents and estimated peak fields from the measurement run, the critical current variation with magnetic field is derived using the scaling law. The blue points represent the measured cable data, while the dashed line shows the fitted critical current curve. The shaded blue area indicates the confidence interval of the fit. Additional data points from virgin (yellow) and extracted (gray) strand measurements are included for comparison of the cabling and processing degradation respectively. The black solid line represents the load line for the MQXF quadrupole magnet design, with the intersection of this line and the critical current curve, marked by the circle symbol defining the short sample limit of this cable. The nominal operational point for this magnet is marked by the star symbol.

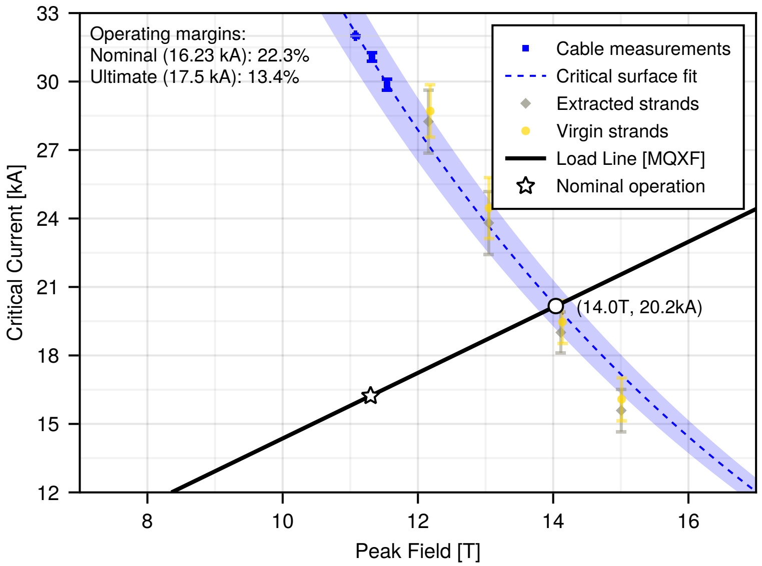

Figure 3.16: Short sample limit (SSL) and loadline analysis for the cable sample impregnated with POLAB Mix resin. The blue points represent cable measurements, with the dashed line showing the fitted critical current curve as a function of peak field. The shaded area indicates the confidence interval of the fit. Yellow points show data from virgin strands, while gray points represent extracted strands. The black line represents the load line for the MQXF magnet design, with the white circle marking the SSL at 14.0 T and 20.2 kA. Operating margins for nominal (16.23 kA) conditions with this processing protocol measures about 22% at 4.2 K
.

Table 3.10 presents a comparative analysis at key field values between cable measurements and model predictions based on virgin and extracted strand data. These values are derived from the scaling law fits applied to both cable and strand measurements. Table 3.11 summarizes the key parameters obtained from the scaling law fit and SSL analysis for both cable and strand measurements.

Key findings from the electromagnetic performance evaluation include:

Table 3.10: Critical current values derived from scaling law fits applied to cable and strand measurements, showing magnetic field-dependent cabling degradation and cable-to-strand performance deviation at 4.2 K

Field	Cable Sample	Virgin Strand Model	Extracted Strand Model	Cabling Degradation Virgin/Extracted	Cable Performance vs. Extracted
[T]	[kA]	[kA]	[kA]	[%]	[%]
10.0	37.9	43.0	42.3	1.7	10.4
11.0	32.5	35.9	35.2	2.0	7.7
12.0	27.9	29.8	29.2	2.1	4.5
13.0	23.8	24.6	24.0	2.4	0.8
14.0	20.3	20.1	19.5	3.1	–

Table 3.11: Scaling law parameters and short sample limit analysis for the cable with POLAB Mix resin and 50-hour heat treatment duration compared with virgin and extracted strand measurements at 4.2 K

Parameter	Unit	Cable	Virgin Strand	Extracted Strand
Upper critical field (B_{c2})	[T]	29.6	25.6	25.3
Scaling parameter (C)	[kA·T]	1784 ± 74	1854	1839
Short sample limit	[kA at T]	20.2 at 14.0	20.1 at 14.0	19.9 at 13.9
Nominal operating margin (16.23 kA)	[%]	22.3	23.8	22.9
Ultimate operating margin (17.5 kA)	[%]	13.4	14.8	14.0

1. **Comparison with single strands**: The cable measurements show 10% degradation at $10\,\mathrm{T}$ decreasing to values within the confidence interval of the fit. Similar to the reference case, the B_{c2} value derived for the cable ($29.6\,\mathrm{T}$) exceeds both virgin ($25.6\,\mathrm{T}$) and extracted ($25.3\,\mathrm{T}$) strand values, indicating limitations in the cable scaling law fit at high fields.

2. **Short sample limit analysis**: Using the scaling law fit and MQXF loadline, a short sample limit of $20.2\,\mathrm{kA}$ at $14.0\,\mathrm{T}$ is estimated for this cable, representing a 4% improvement compared to the reference case limit of $19.4\,\mathrm{kA}$ at $13.5\,\mathrm{T}$. This provides operational margins of approximately 22% at nominal conditions and 13% at ultimate conditions. Both margins exceed those achieved with CTD-101K impregnation (18% and 9% respectively), with the nominal margin now surpassing the 20% typically targeted for high-field accelerator magnets. The scaling parameter, C of $1784 \pm 74\,\mathrm{kA}\cdot\mathrm{T}$ represents 98% of the extracted strand value ($1821\,\mathrm{kA}\cdot\mathrm{T}$), indicating reduced degradation compared to the reference CTD-101K® sample which retained only 85% of strand performance.

A mechanistic interpretation of the enhanced electromagnetic performance reveals two complementary effects:

1. **Enhanced strain state through compliant matrix**: The POLAB Mix resin's reduced elastic modulus ($3.07\,\mathrm{GPa}$ versus $3.53\,\mathrm{GPa}$ for CTD-101K® at room temperature) enables more effective stress redistribution within the cable structure. When transverse electromagnetic forces induce Poisson expansion perpendicular to the loading direction, the more compliant resin accommodates this deformation with reduced reaction stresses on the Nb_3Sn phase. Since both resins share identical glass transition temperatures ($140\,^{\circ}\mathrm{C}$), thermal stress accumulation during cooldown remains unchanged, isolating the mechanical compliance as the differentiating factor. This enhanced compliance may shift the A15 phase closer to its optimal strain state under operational loading, explaining the improvement in the critical current of the impregnated cable.

2. **Fracture toughness preventing microcrack-induced quenches**: The 43% enhancement in fracture toughness at room temperature (1.17 versus $0.82\,\mathrm{MPa}\sqrt{\mathrm{m}}$) alters the mechanical energy dissipation during electromagnetic cycling. The molecular-scale modification with the flexibilizer in the Polab Mix enables localized plastic deformation that dissipates stress concentrations before reaching the critical intensity required for crack propagation. During training, each electromagnetic cycle generates mechanical disturbances from differential thermal expansion and electromagnetic force variations. The enhanced fracture toughness prevents these disturbances from accumulating as microcracks, which would otherwise release energy sufficient to trigger training quenches. This mechanism could directly explain the 50% reduction in training cycles, as the sample achieves mechanical equilibrium more rapidly than that observed with the CTD-101K® impregnation.

3.4.2 Damage Onset and Evolution

For the metallographic investigation to characterize the onset and evolution of damage, specimens were subjected to mean transverse compression stresses varying from 70 to 180 MPa. Tables 3.12 and 3.13 quantify the crack density distributions obtained across these specimens for both resin systems. Figure 3.17 and Figure 3.18 illustrate the evolution of damage with increasing transverse pressure for POLAB Mix specimens, showing both the percentage of damaged subelements and the distribution of affected strands. Figure 3.19 and Figure 3.20 present the corresponding data for MSUT-Twente specimens.

Key observations from the metallographic analysis include:

1. **Damage onset threshold**: The onset of damage appeared in POLAB Mix specimens E.2 at mean stress of $121 \pm 15\,\mathrm{MPa}$, affecting 0.2% of subelements distributed across 12.5% of strands. This represents a $\approx 15\,\mathrm{MPa}$ improvement over the reference CTD-101K® system which showed damage onset at $106 \pm 15\,\mathrm{MPa}$. MSUT-Twente specimens

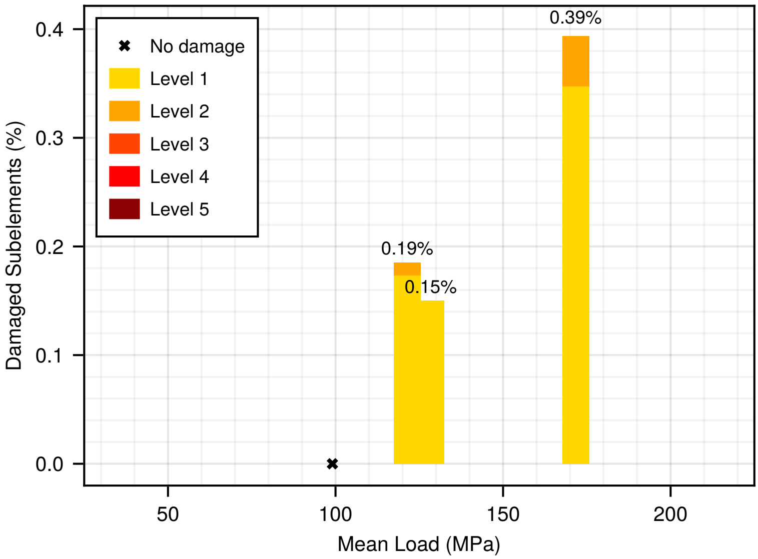

Figure 3.17: Percentage of damaged subelements categorized by damage level (D1-D5) as a function of applied transverse pressure for cables with 50-hour heat treatment duration and POLAB Mix impregnation resin.

Table 3.12: Statistical distribution of damage across specimens subjected to varying transverse compression stress, with 50-hour heat treatment duration and POLAB Mix impregnation resin

Specimen	**Applied Stress**		**Number of damaged subelements**							**Strands with damaged subelements**	
Id.	Mean, μ (MPa)	Std. Dev., σ (MPa)	D1	D2	D3	D4	D5	Net	[% of 8640]	Net	[% of 80]
E.1	100	10	0	0	0	0	0	0	0	0	0
E.2	121	15	15	1	0	0	0	16	0.19	10	12.50
E.4	128	8	13	0	0	0	0	13	0.15	9	11.25
E.3	172	19	30	4	0	0	0	34	0.39	18	22.50

exhibited initial damage at $110 \pm 10\,\mathrm{MPa}$ (specimen D.1) with minimal impact of only 0.05% of subelements across 3.75% of strands. The MSUT onset threshold falls within the uncertainty range of the reference system, indicating no significant improvement in crack initiation resistance despite the enhanced fracture toughness.

2. **Damage evolution with pressure**: The progression of damage reveals distinct behaviors between resin systems. In the $100 - 140\,\mathrm{MPa}$ range, damage gradients measured $0.025\%/\mathrm{MPa}$ for CTD-101K (from Case Study I), $0.005\%/\mathrm{MPa}$ for POLAB Mix, and $0.012\%/\mathrm{MPa}$ for MSUT-Twente. Above $140\,\mathrm{MPa}$, both resins demonstrate a lowered

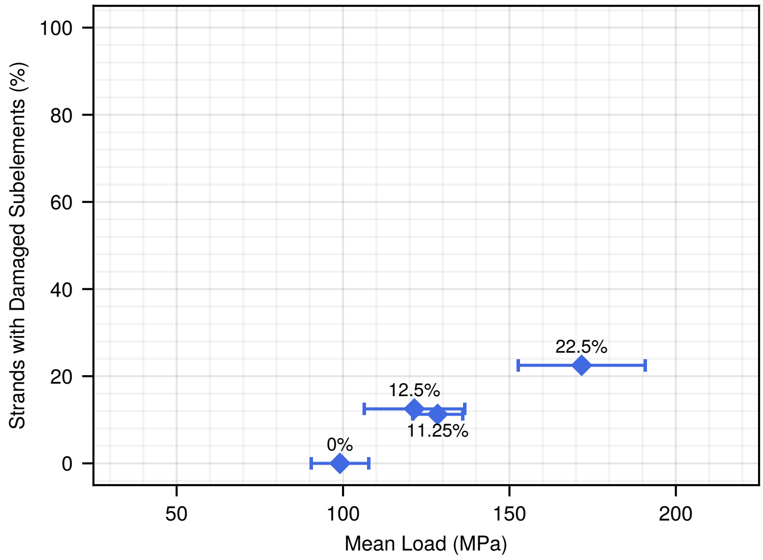

Figure 3.18: Percentage of strands containing at least one damaged subelement as a function of applied transverse pressure for cables with 50-hour heat treatment duration and POLAB Mix resin.

Table 3.13: Statistical distribution of damage across specimens subjected to varying transverse compression stress, with 50-hour heat treatment duration and MSUT-Twente impregnation resin

Specimen	**Applied Stress**		**Number of damaged subelements**							**Strands with damaged subelements**	
Id.	Mean, μ (MPa)	Std. Dev., σ (MPa)	D1	D2	D3	D4	D5	Net	[% of 8640]	Net	[% of 80]
D.5	90	8.5	0	0	0	0	0	0	0	0	0
D.1	110	10	4	0	0	0	0	4	0.05	3	3.75
D.2	114	11	36	1	0	0	0	37	0.43	17	21.25
D.4	169	34	52	8	0	0	0	60	0.69	33	41.25
D.3	183	40	55	6	0	0	0	61	0.71	34	42.50

$0.006\%/\mathrm{MPa}$, achieving $20-50\%$ improvement in damage progression rates compared to the reference system. Neither of the enhanced resin system samples exhibited severe damage levels (D3-D5) even at maximum tested pressures exceeding $170\,\mathrm{MPa}$, with all observed cracks remaining at D1 or D2 damage levels.

A mechanistic interpretation of the enhanced damage resistance reveals:

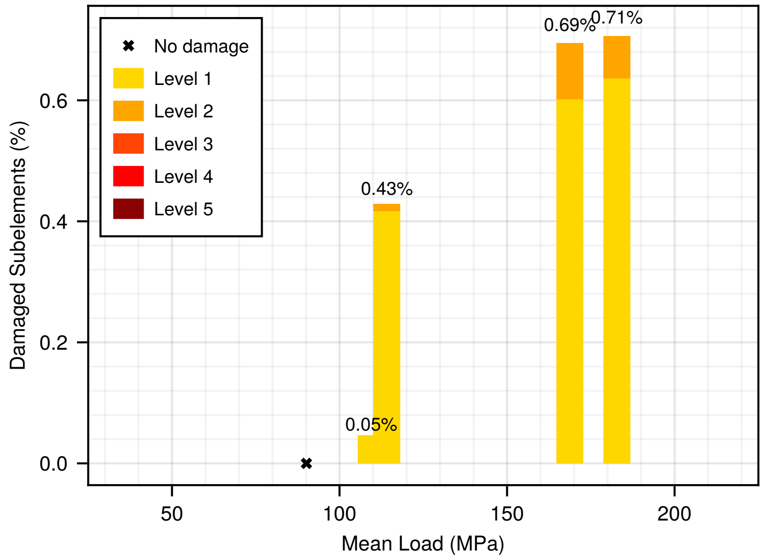

Figure 3.19: Percentage of damaged subelements categorized by damage level (D1-D5) as a function of applied transverse pressure for cables with 50-hour heat treatment duration and MSUT-Twente impregnation resin.

1. **Role of elastic modulus**: The $15\,\mathrm{MPa}$ improvement in damage onset for POLAB Mix correlates with its reduced elastic modulus of $3.07\,\mathrm{GPa}$ compared to $3.53\,\mathrm{GPa}$ for CTD-101K® at room temperature. This 13% reduction in stiffness enables more compliant stress redistribution at strand crossover points, delaying the critical stress intensity required for crack initiation at Nb_3Sn/Cu-Sn interfaces. MSUT-Twente, with elastic modulus of $3.59\,\mathrm{GPa}$ similar to CTD-101K®, experiences comparable stress concentrations at material interfaces, explaining the similar range of damage onset threshold.

2. **Effect of improved fracture toughness**: The reduced damage progression in both alternative resins may result from improved mechanical coupling between the epoxy matrix and conductor. Enhanced fracture toughness prevents microcracking in the resin that would otherwise create local stress amplification at interfaces. The tougher resin matrix maintains more uniform load distribution across the cable cross-section, limiting the propagation of damage from initially cracked subelements to neighboring regions. The absence of D3-D5 damage levels suggests that even though crack initiation occurs in the Nb_3Sn, the surrounding tougher matrix prevents the stress intensification that drives crack propagation in the reference system.

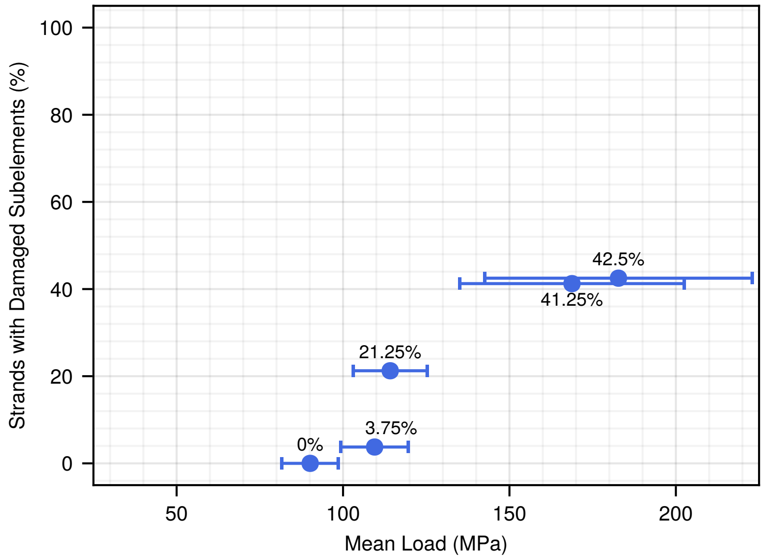

Figure 3.20: Percentage of strands containing at least one damaged subelement as a function of applied transverse pressure for cables with 50-hour heat treatment duration and MSUT-Twente impregnation resin.

3.4.3 Implications for Magnet Design

The alternative resin systems evaluated in this study offer performance improvements while maintaining compatibility with existing manufacturing processes. POLAB Mix demonstrates a 5% increase in critical current at $9.6\,\mathrm{T}$ and requires approximately half the training quenches compared to the reference CTD-101K system. The damage onset threshold of $121 \pm 15\,\mathrm{MPa}$ represents approximately $10 - 15\,\mathrm{MPa}$ improvement over the baseline, providing a small additional margin for assembly procedures. These improvements result from the enhanced fracture toughness and reduced elastic modulus, which affect both the strain state of the Nb_3Sn phase and the energy dissipation during mechanical disturbances. No significant improvement in the damage onset threshold was shown for the specimens impregnated with MSUT-Twente resin, however its enhanced fracture toughness suggests reduced number of training quenches in the electrical performance as well.

The reduced damage progression rates observed with both alternative resins suggest potential benefits for magnets experiencing higher operational stresses. At $140\,\mathrm{MPa}$, POLAB Mix and MSUT-Twente show 0.15% and 0.4% damaged subelements respectively, compared to 1% for the reference system. The predominance of lower damage levels in the subelements across all tested pressures indicates improved resistance to crack propagation. While these resins demonstrate clear mechanical advantages, implementation requires validation of long-term stability and processing reproducibility at production scale. The results support continued investigation of resin formulations optimized for the specific requirements of high-field superconducting magnets, where incremental improvements in damage tolerance can extend operational capabilities.

3.5 Case Study IV: Variation in RHT Dwell Time

Following the establishment of performance baselines and resin variation experiments, this case study examines the effect of reaction heat treatment duration of the A15 phase formation in the RRP® conductor as the primary control parameter. In this investigation, three durations for the final stage of RHT cycle are studied, as justified in Section 1.2.2. The $50\,\mathrm{h}$ protocol, which represents the baseline adopted for the Nb_3Sn MQXF magnets at CERN is established in Case Study I. The extended $75\,\mathrm{h}$ treatment is the manufacturer recommendation for maximizing critical current density obtained from this conductor. An abbreviated $30\,\mathrm{h}$ treatment explores potential retainment of mechanical properties through preservation of features which enhance mechanical performance. All protocols maintain identical ramp rates, and initial ($210\,^{\circ}\mathrm{C}/48\,\mathrm{h}$) and intermediate ($400\,^{\circ}\mathrm{C}/48\,\mathrm{h}$) plateaus.

This investigation addresses critical questions regarding the heat treatment optimization:

1. How does the RHT time of the A15 phase affect the balance between critical current density and mechanical resilience?
2. Can the relationship between RHT duration and the onset and evolution of mechanical damage be quantified?

For electrical characterization, wires from multiple billets spanning the production performance spectrum underwent virgin strand testing at $4.2\,\mathrm{K}$ across $12-15\,\mathrm{T}$ applied fields. Mechanical damage assessment utilized the same double-stack cable sample configuration (Cable Ids: H16OC0370A for $75\,\mathrm{h}$ and H16OC0364A for $30\,\mathrm{h}$) subjected to controlled transverse compression from $80-190\,\mathrm{MPa}$. Microstructural analysis is used to quantify the A15 grain size variation through cryogenic fracture surfaces and Nb barrier thickness via energy-dispersive X-ray spectroscopy for each heat treatment duration.

Key Findings

- **Electrical performance**: Modest 3% I_c enhancement at $12\,\mathrm{T}$ from $30\,\mathrm{h}$ to $75\,\mathrm{h}$, offset by severe 48% RRR degradation compromising thermal stability
- **Damage onset**: Progressive redution from $138\,\mathrm{MPa}$ at $30\,\mathrm{h}$ through $105\,\mathrm{MPa}$ at $50\,\mathrm{h}$ to less than $78\,\mathrm{MPa}$ at $75\,\mathrm{h}$ with extended treatment showing reduced mechanical resilience
- **Trade-off quantified**: $60\,\mathrm{MPa}$ mechanical improvement costs only 3% in J_c implying the mechanical resilience degrades $16\times$ faster than electromagnetic performance improvement

3.5.1 Electrical Performance

The electrical measurement test program included 23 unique wires for the 30 h treatment , 11 wires for the 50 h treatment , and 18 wires for the 75 h treatment at 4.2 K across applied background fields of 12 – 15 T. Residual resistance ratio (RRR) measurements were performed on 24, 39, and 21 samples for the 30 h, 50 h, and 75 h treatments respectively. Figures 3.21, 3.22 and 3.23 present box plots[1] showing the statistical distribution of critical current, n-values and RRR respectively across the measured wire populations. Table 3.14 summarizes the mean and standard deviation of the measurement data. The overlapping standard deviations indicate that while mean trends are consistent, individual wire populations show considerable variation that reflects inherent heterogeneity in the wire populations. These represent statistical tendencies rather than deterministic effects.

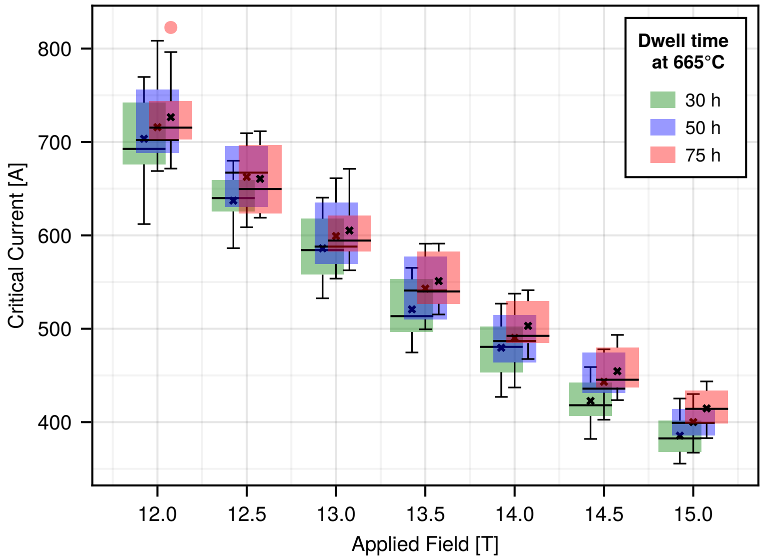

Figure 3.21: Effect of applied magnetic field and reaction heat treatment duration on critical current at 4.2 K. Critical current systematically decreases with increasing field strength, with extended treatment duration showing enhanced electrical performance.

Key observations from the electrical measurements include:

[1] Box plots display the distribution of data through quartiles. The box extends from the first quartile (Q1) to the third quartile (Q3), with a line at the median, and a cross at the respective mean. Whiskers extend to show the range of the data within 1.5 times the interquartile range, with outliers plotted as individual points.

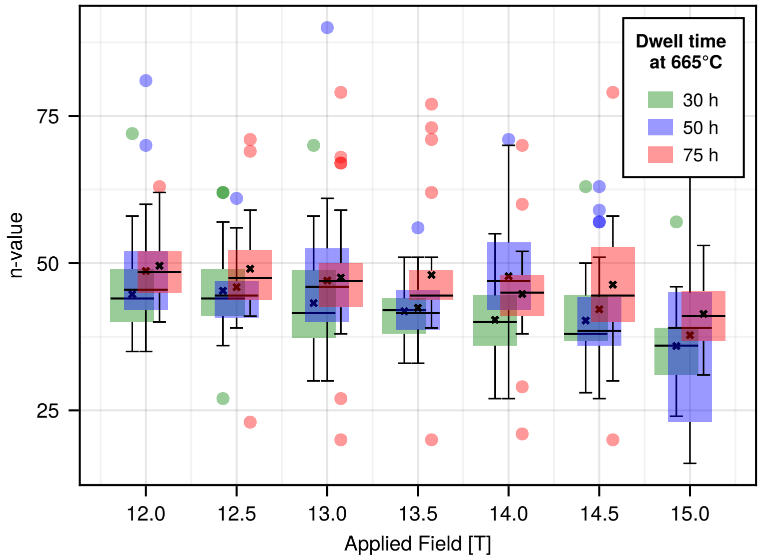

Figure 3.22: Effect of the heat treatment duration and applied magnetic field on the steepness of superconducting transitions (n-value), where higher values indicate more uniform current distribution.

Table 3.14: Electrical performance parameters for Nb_3Sn wires as a functions of applied field and reaction heat treatment durations at 4.2 K. Mean ± standard deviation values from $n = 23$ for 30 h, $n = 11$ for 50 h, $n = 18$ for 75 h wire measurements.

Applied	**30 hours**		**50 hours**		**75 hours**	
Field [T]	$\mathbf{I_c}$ [A]	**n-value**	$\mathbf{I_c}$ [A]	**n-value**	$\mathbf{I_c}$ [A]	**n-value**
12.0	703 ± 42	45 ± 7	716 ± 40	49 ± 10	727 ± 39	50 ± 6
12.5	637 ± 30	45 ± 8	663 ± 36	46 ± 7	661 ± 34	49 ± 10
13.0	586 ± 33	43 ± 8	599 ± 37	47 ± 12	605 ± 31	48 ± 11
13.5	521 ± 30	42 ± 5	543 ± 34	42 ± 7	551 ± 27	48 ± 12
14.0	480 ± 28	40 ± 5	490 ± 29	48 ± 11	503 ± 23	45 ± 8
14.5	423 ± 23	40 ± 7	443 ± 26	42 ± 10	455 ± 21	46 ± 10
15.0	386 ± 19	36 ± 7	400 ± 20	38 ± 15	415 ± 19	41 ± 6
RRR	517 ± 42		360 ± 31		270 ± 50	

1. **Variation of current-carrying capacity**: Critical current values systematically increased with extended processing time across all field levels. At 12 T, mean critical currents measured 703 A for 30 h, 716 A for 50 h, and 727 A for 75 h, representing difference of -1.8% and $+1.5\%$ relative to the 50 h baseline. This is already known to be directly

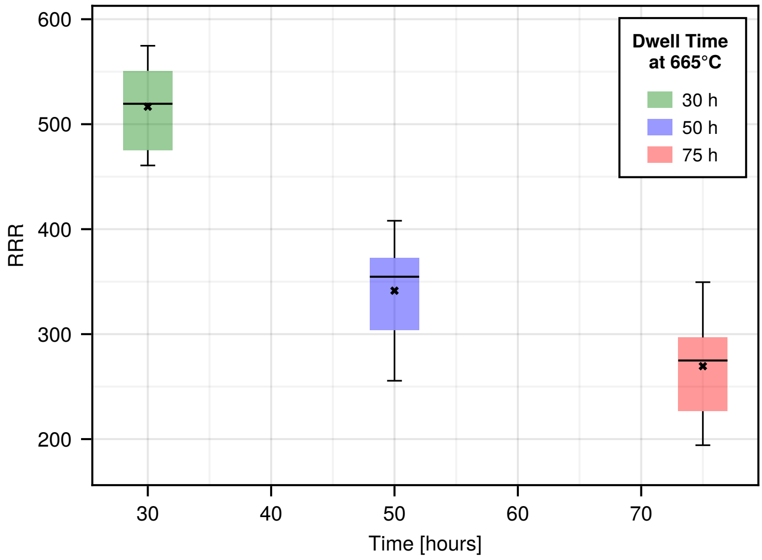

Figure 3.23: Residual resistivity ratio evolution as a function of reaction heat treatment duration at $665°$C. The non-linear decrease reflects progressive copper matrix contamination from niobium barrier dissolution of the subelements.

correlated to the increase in the A15 phase area. The relative benefit of extended heat treatment increases with applied field magnitude. At $15\,\mathrm{T}$, mean critical currents of $386\,\mathrm{A}$ for $30\,\mathrm{h}$, $400\,\mathrm{A}$ for $50\,\mathrm{h}$, and $415\,\mathrm{A}$ for $75\,\mathrm{h}$ demonstrating a difference of -3.6% and $+3.75\%$ from the $50\,\mathrm{h}$ baseline, respectively. This field-dependent difference shows that extended heat treatment also enhances the phase connectivity and stoichiometry.

2. **Homogeneity of current path**: The power law exponent (n-value), characterizes the steepness of the power-law fit of the current-voltage curve. Higher n-values indicate more uniform critical current distribution across the multifilamentary wire. Extended heat treatment showed systematic improvement with RHT duration. Mean n-values at $12\,\mathrm{T}$ increased from 45 for $30\,\mathrm{h}$ to 49 for $50\,\mathrm{h}$ to 50 for $75\,\mathrm{h}$. The marginal gain from $50\,\mathrm{h}$ to $75\,\mathrm{h}$ suggests an approach toward saturation in transition uniformity.

3. **Purity of copper matrix**: Residual resistance ratio measurements show non-linear decrease with extended heat treament, as shown in Figure 3.23. The mean RRR values of 517 for $30\,\mathrm{h}$, 360 for $50\,\mathrm{h}$, and 270 for $75\,\mathrm{h}$ represent a 48% reduction from shortest to longest treatment. The degradation rate is non-linear, with 7.8 RRR units per hour decrease between $30\,\mathrm{h}$ and $50\,\mathrm{h}$, and 3.6 RRR units per hour between $50\,\mathrm{h}$ and $75\,\mathrm{h}$. This degradation

is a direct reflection of the purity of the copper matrix of the superconducting wire, which decreases on the diffusion of tin from the subelement cores into the matrix. The coarsening of copper grains during prolonged heating may further affect the tin diffusion kinetics by reducing grain boundary density, though this remains to be confirmed through microstructural analysis.

Figure 3.24 presents the scaling law fits for the three heat treatment durations intersecting with the MQXF quadrupole magnet load line[2]. The green, blue and red lines are the fits for the $30\,\mathrm{h}$, $50, \mathrm{h}$ and $75\,\mathrm{h}$ measurement data with the confidence intervals are the respective shaded areas. The short sample limits for each fit is marked by circles at the intersection points on the plot. Table 3.15 summarizes the key parameters derived from the scaling law fits and their implications for magnet design.

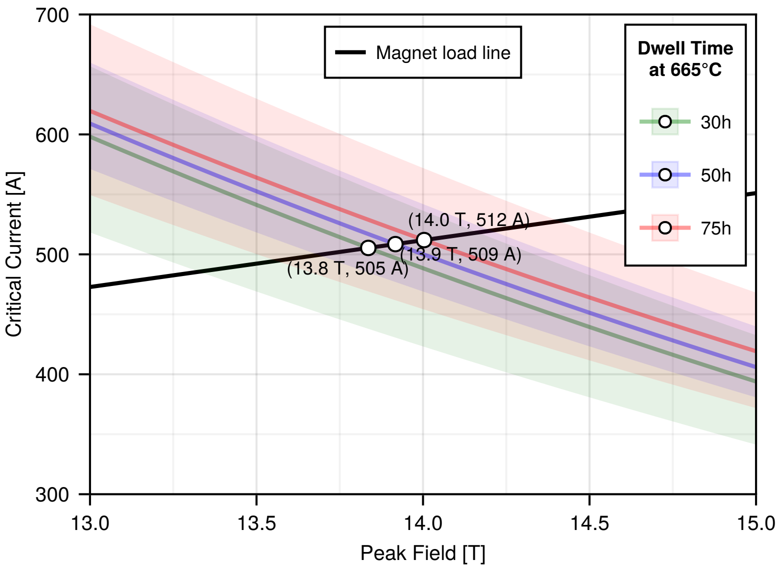

Figure 3.24: Critical current scaling curves for three heat treatment durations intersecting with MQXF quadrupole load line. Short sample limits occur at the intersection points, showing minimal variation despite extended processing times.

The electromagnetic performance evaluation reveals critical trade-offs inherent to reaction heat treatment duration parameter:

[2] The Y axis for the load-line in this plot is scaled for a single wire by dividing by number of strands in a cable (40)

Table 3.15: Scaling law parameters and short sample limit analysis derived from statistical data of transport current measurements across heat treatment durations.

Parameter	**Unit**	**30 hours**	**50 hours**	**75 hours**
Upper critical field (B_{c2})	[T]	25.5	25.9	26.6
Scaling parameter (C)	[kA·T]	45.2	44.9	44.1
Short sample limit	[A at T]	505 at 13.0	509 at 13.9	512 at 14.0
Operating margin at $4.2\,\mathrm{K}$	[%]	24.4	25.4	26.1

- **Scaling law parameters**: The upper critical field, B_{c2} values showed progressive improvement from $25.5\,\mathrm{T}$ for $30\,\mathrm{h}$ to $25.9\,\mathrm{T}$ for the $50\,\mathrm{h}$ baseline to $26.6\,\mathrm{T}$ for $75\,\mathrm{h}$, representing -1.9% and $+2.5\%$ variation relative to the $50\,\mathrm{h}$ standard protocol, respectively. The systematic enhancement with extended processing suggests improved A15 phase stoichiometry and tin distribution. Conversely, the scaling parameter, C exhibited a marginal decrease with the increasing duration, showing $+0.4\%$ for $30\,\mathrm{h}$ and -2.0% for $75\,\mathrm{h}$ variation from the $50\,\mathrm{h}$ baseline. This trend reveals that bulk pinning force density actually decreases with extended treatment, indicating a decrease in the grain boundary pinning sites.
- **Short sample limit analysis**: The SSL values demonstrate a minimal variation across the heat treatment range, with the $30\,\mathrm{h}$ treatment achieving $505\,\mathrm{A}$ at $13.8\,\mathrm{T}$ and the $75\,\mathrm{h}$ treatment reaching $512\,\mathrm{A}$ at $14.0\,\mathrm{T}$. This corresponds to a decrease of 1% and an increase of 0.7% in the loadline margin for operating conditions for the respective RHT durations compared to the current standard protocol.

The opposing trends of increasing critical current, I_c ($+3.4\%$ from $30\,\mathrm{h}$ to $75\,\mathrm{h}$ at $12\,\mathrm{T}$) and decreasing scaling parameter, C (-2.4% from $30\,\mathrm{h}$ to $75\,\mathrm{h}$) indicate that while the total A15 phase volume increases with extended heat treatment, the flux pinning effectiveness per unit volume decreases due to grain boundary density reduction. This competition between enhanced superconducting phase fraction and degraded pinning site density results in near-constant short sample limits ($< 2\%$ variation), suggesting that electromagnetic performance has reached fundamental material limits regardless of heat treatment duration within the investigated range.

3.5.2 Damage Onset and Evolution

For the metallographic investigation to characterize the onset and evolution of damage with varying heat treatment duration, specimens were subjected to mean transverse compression stresses ranging from $70 - 200\,\mathrm{MPa}$. Tables 3.16 and 3.17 quantify the crack density distributions for the $30\,\mathrm{h}$ and $75\,\mathrm{h}$ heat treatments respectively, with the $50\,\mathrm{h}$ reference data previously presented in

Table 3.5 Case Study I. Figures 3.25 and 3.26 and Figures 3.27 and 3.28 present the corresponding data for the 30 h and 75 h specimens.

Table 3.16: Statistical distribution of damage across specimens subjected to varying transverse compression stress with 30-hour heat treatment and CTD-101K® impregnation resin.

Specimen	Applied Stress		Number of damaged subelements							Strands with damaged subelements	
Id.	Mean, μ (MPa)	Std. Dev., σ (MPa)	D1	D2	D3	D4	D5	Net	[% of 8640]	Net	[% of 80]
C.3	107	10	0	0	0	0	0	0	0	0	0
C.1	137	11	0	0	0	0	0	0	0	0	0
C.2	138	18	1	0	0	0	0	1	0.01	1	1.25
C.4	158	20	20	2	0	0	0	22	0.25	16	20.00
C.5	197	48	96	20	1	0	0	117	1.35	26	32.50

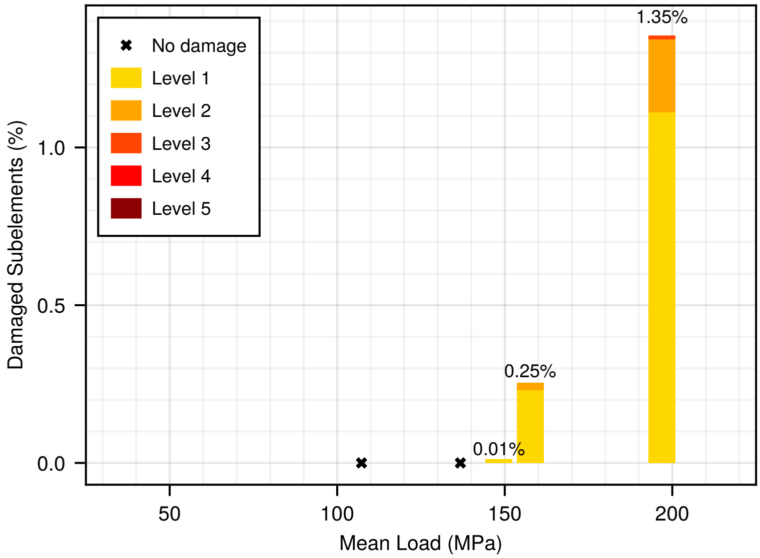

Figure 3.25: Percentage of damaged subelements categorized by damage level (D1-D5) as a function of applied transverse pressure for 30-hour heat treatment duration. The absence of damage up to 137 ± 11 MPa and minimal progression at higher compression stress demonstrates better mechanical resilience than extended RHT duration.

Key observations from the metallographic analysis include:

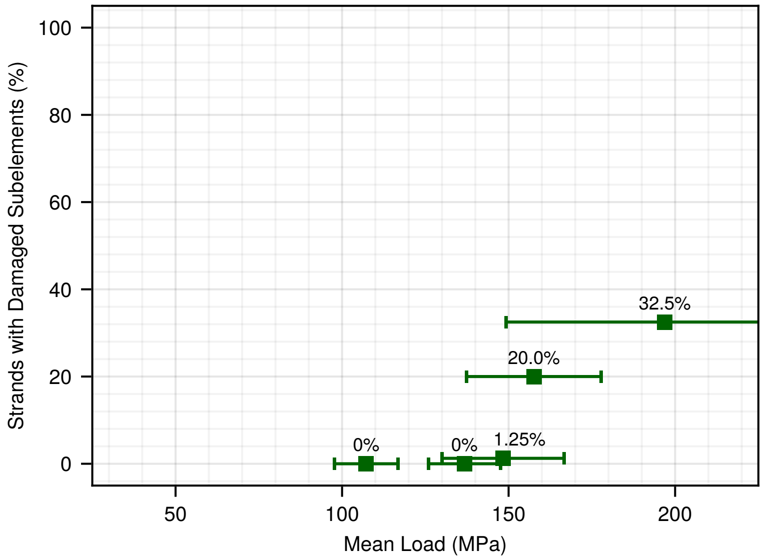

Figure 3.26: Percentage of strands containing at least one damaged subelement as a function of applied transverse compressive stress for 30-hour heat treatment duration. Even at higher loading of 197 ± 48MPa, only 32.5% of strands are affected.

Table 3.17: Statistical distribution of damage across specimens subjected to varying transverse compression stress, with 75-hour heat treatment duration and CTD-101K® impregnation resin.

Specimen	Applied Stress		Number of damaged subelements							Strands with damaged subelements	
Id.	Mean, μ (MPa)	Std. Dev., σ (MPa)	D1	D2	D3	D4	D5	Net	[% of 8640]	Net	[% of 80]
B.1	78	13	24	3	0	0	0	27	0.31	20	25.0
B.2	93	15	74	11	3	0	0	88	1.02	37	46.25
B.3	93	13	71	13	0	1	0	85	0.98	34	42.5
B.4	104	16	315	236	47	10	14	622	7.20	65	81.25
B.5	165	27	514	523	136	60	133	1366	15.81	69	86.25

1. **Damage onset thresholds**: The specimens C.3 and C.1 of 30 h heat treatment exhibited no damage at pressures up to $137 \pm 11\,\mathrm{MPa}$, with initial cracking observed in specimen C.2 at $138 \pm 18\,\mathrm{MPa}$. This represents an approximately $30\,\mathrm{MPa}$ improvement over the 50 h reference treatment which showed damage onset at $106 \pm 15\,\mathrm{MPa}$ in Case Study I. In contrast, specimen B.1 of the 75 h treatment, with a mean stress of $78 \pm 13\,\mathrm{MPa}$ presented 0.3% subelement damage, establishing the damage onset for this heat treatment duration below this stress value. It represents a reduction of $> 30\,\mathrm{MPa}$ compared to the reference configuration.

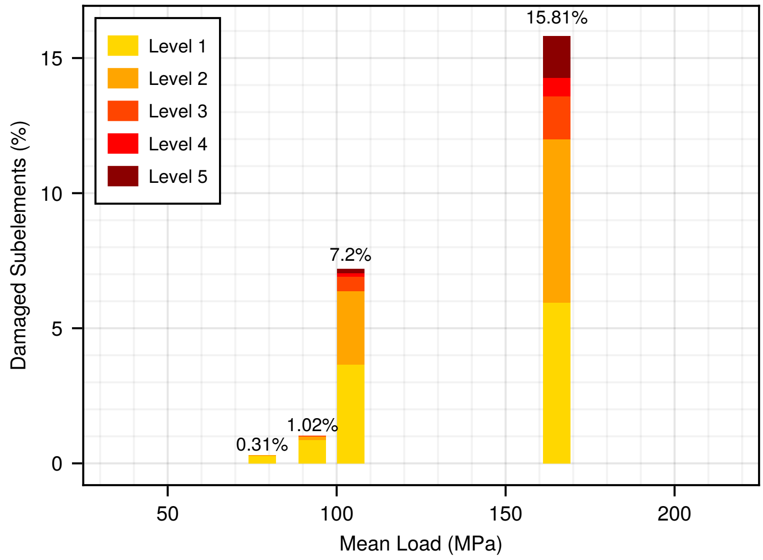

Figure 3.27: Percentage of damaged subelements categorized by damage level (D1-D5) as a function of applied transverse pressure for 75-hour heat treatment. The rapid progression to severe damage levels (D3-D5) at moderate pressures indicates compromised mechanical integrity.

2. **Damage evolution with pressure**: The progression of damage varies significantly between heat treatment durations across pressure ranges. In the $70-100\,\mathrm{MPa}$ range, only the $75\,\mathrm{h}$ treatment exhibits damage with gradient of $0.035\%/\mathrm{MPa}$, while $30\,\mathrm{h}$ and $50\,\mathrm{h}$ treatments show no damage. In the $100-150\,\mathrm{MPa}$ operational range, damage gradients measure $0.001\%/\mathrm{MPa}$ for $30\,\mathrm{h}$, $0.025\%/\mathrm{MPa}$ for $50\,\mathrm{h}$, and $0.14\%/\mathrm{MPa}$ for $75\,\mathrm{h}$. At $140\,\mathrm{MPa}$ specifically, damaged subelements comprise 0.01% for $30\,\mathrm{h}$ (interpolated), 1.0% for ($50\,\mathrm{h}$), and 8.5% for $75\,\mathrm{h}$ (interpolated). Above $150\,\mathrm{MPa}$, the $30\,\mathrm{h}$ treatment maintains a gradient of $0.024\%/\mathrm{MPa}$, while the $75\,\mathrm{h}$ treatment shows $0.17\%/\mathrm{MPa}$. The $75\,\mathrm{h}$ treatment demonstrates a 140-fold increase in damage rate compared to the $30\,\mathrm{h}$ treatment in the operational pressure range, indicating that extended heat treatment not only reduces damage thresholds but increases damage accumulation rates at all stress levels.

A microstructural characterization has been carried out to understand its role in the observed electrical and mechanical performance. Figure 3.29 presents the niobium barrier thickness distributions measured through Energy-Dispersive X-ray Spectroscopy (EDX) spectroscopy for each heat treatment duration, as described in Section 2.2.3. The mean barrier thickness decreased from $3.2 \pm 1.4\,\mu\mathrm{m}$ for $30\,\mathrm{h}$ treatment to $2.1 \pm 1.3\,\mu\mathrm{m}$ for $50\,\mathrm{h}$ treatment and $1.8 \pm 0.6\,\mu\mathrm{m}$ for $75\,\mathrm{h}$ treatment, representing a 45% reduction across the investigated range. Figure 3.30 illustrates the

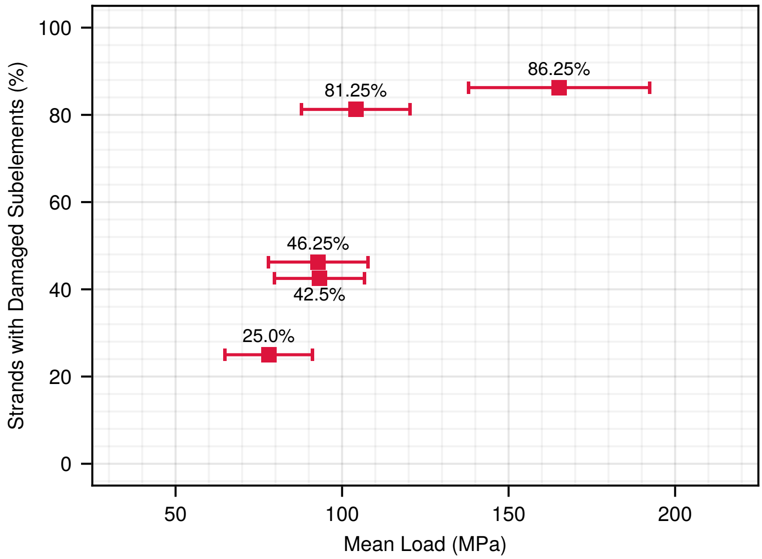

Figure 3.28: Percentage of strands containing at least one damaged subelement as a function of applied transverse pressure for 75-hour heat treatment. At a mean of 104 MPa, typical of assembly operations for MQXF magnets, 81.25% of strands already exhibit damage.

A15 grain size evolution determined from cryogenic fracture surface analysis (refer Section 2.2.3). The mean grain size increased systematically from $128 \pm 2\,\mathrm{nm}$ for $30\,\mathrm{h}$ treatment to $139 \pm 7\,\mathrm{nm}$ for $50\,\mathrm{h}$ treatment and $159 \pm 4\,\mathrm{nm}$ for $75\,\mathrm{h}$ treatment, demonstrating a 24% coarsening across the heat treatment range.

A mechanistic interpretation of the observed damage evolution reveals two microstructural features that control both damage onset thresholds and evolution rates:

1. **Niobium barrier degradation**: Assuming a circular subelement of outer radius, r_o containing a Nb_3Sn core with radius, r_c surrounded by a Nb matrix. The force equilibrium in the subelement - prior to the onset of cracking requires:

$$F_{total} = \sigma_{Nb_3Sn} \cdot \pi r_c^2 + \sigma_{Nb} \cdot \pi (r_o^2 - r_c^2) \tag{3.2}$$

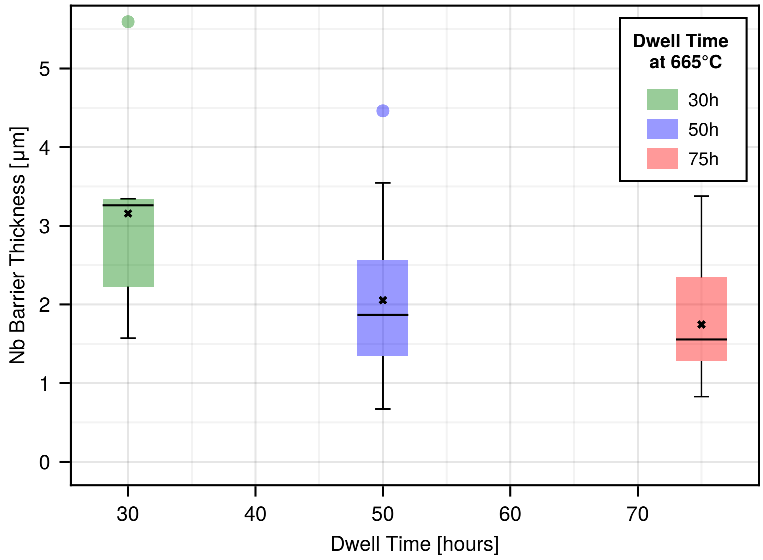

Figure 3.29: Niobium barrier thickness distributions showing progressive consumption with extended heat treatment duration. Measurements represent averages from six line scans per subelement taken at both vertex and edge positions of the hexagonal geometry.

Compared to the brittle Nb_3Sn phase with elastic modulus of $125 - 150$ GPa[173,174], Nb is a ductile material with elastic modulus of ~ 105 GPa[175]. Considering strain compatibility ($\varepsilon_{Nb_3Sn} = \varepsilon_{Nb}$), the stress ratio is approximately:

$$\frac{\sigma_{Nb_3Sn}}{\sigma_{Nb}} = \frac{E_{Nb_3Sn}}{E_{Nb}} = \frac{135}{105} = 1.3 \tag{3.3}$$

The stress in the brittle Nb_3Sn core is:

$$\sigma_{Nb_3Sn} = \frac{F_{total}}{\pi r_c^2 + \pi(r_o^2 - r_c^2) \cdot \frac{E_{Nb_3Sn}}{E_{Nb}}} = \frac{F_{total}}{1.3\pi r_o^2 - 0.3\pi r_c^2} \tag{3.4}$$

For fixed subelement size of $r_o \approx 30\,\mu$m, the barrier reduction from $3.2\,\mu$m to $1.7\,\mu$m increases r_c from $26.8\,\mu$m to $28.2\,\mu$m, increasing stress in the brittle Nb_3Sn phase by approximately 2.5% according to the force equilibrium analysis.

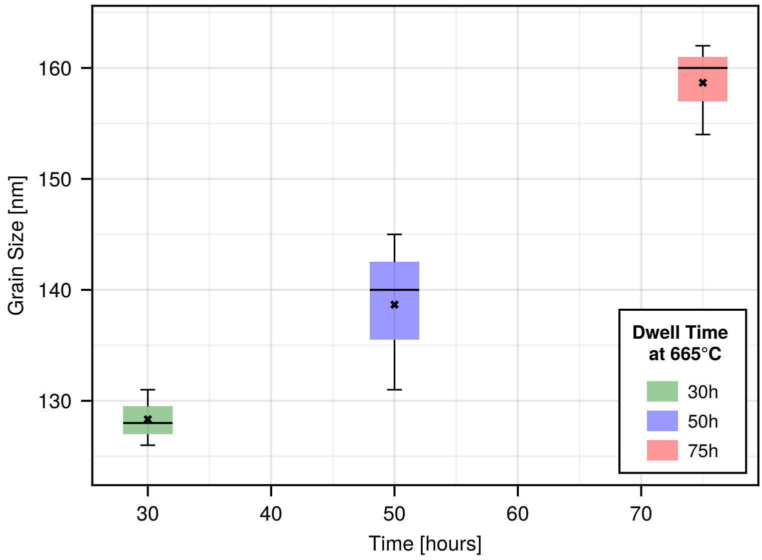

Figure 3.30: A15 grain size distributions for three heat treatment durations showing progressive coarsening with extended processing time. Measurements are obtained from cryogenic fracture surfaces at multiple locations within the Nb_3Sn layer.

2. **Grain size effects**: According to the Hall-Petch relationship (Equation 1.9), the grain boundary contribution to strength scales inversely with the square root of grain size. For the observed coarsening:

$$\frac{\sigma_{30h}}{\sigma_{75h}} \propto \sqrt{\frac{d_{75h}}{d_{30h}}} = \sqrt{\frac{158.7}{128.3}} = 1.11 \tag{3.5}$$

The 24% grain coarsening from $128\,\mathrm{nm}$ to $159\,\mathrm{nm}$ reduces the grain boundary strengthening contribution by approximately 10%. The grain boundaries act as crack deflection and arrest sites in polycrystalline materials[116,176]. The non-linear relationship between grain size and damage accumulation suggests that a critical grain size threshold may exist below which crack propagation is effectively impeded by the increased density of grain boundary obstacles.

The investigation of heat treatment duration reveals a fundamental trade-off between electromagnetic performance and mechanical resilience. Extended processing from 30 to 75 hours yields modest critical current enhancement of 3.4% at $12\,\mathrm{T}$, while precipitating a $60\,\mathrm{MPa}$ reduction in damage onset threshold (from $138\,\mathrm{MPa}$ to $< 78\,\mathrm{MPa}$). This quantified relationship is approximately 18 MPa mechanical degradation per 1% J_c improvement at 12 T. It provides critical guidance for optimizing Nb_3Sn conductors where mechanical constraints increasingly limit achievable magnetic field levels.

Table 3.18: Summary of electrical, mechanical, and microstructural properties measured across reaction heat treatment durations for Nb_3Sn wire populations at 4.2 K. Performance ratios normalized to the 50 h baseline treatment quantify relative variations.

Parameter	**Unit**	**30 hours**	**50 hours**	**75 hours**
Electrical Properties at 4.2 K				
Critical current, I_c at 12 T	[A]	703 ± 42	716 ± 40	727 ± 39
Critical current, I_c at 15 T	[A]	386 ± 19	400 ± 20	415 ± 19
n-value at 12 T	–	45 ± 7	49 ± 10	50 ± 6
Upper critical field, B_{c2}	[T]	25.5 ± 0.8	25.9 ± 0.6	26.6 ± 0.6
Scaling parameter, C	[kA·T]	44.2	44.7	45.1
Short sample limit	[A at T]	505 at 13.8	508 at 13.9	512 at 14.0
Residual resistance ratio (RRR)	–	517 ± 42	360 ± 31	270 ± 50
Mechanical Properties				
Damage onset threshold	[MPa]	138 ± 18	105 ± 10	78 ± 13
Damage at 110 MPa	[% subelements]	0	0.38	7.20
Microstructural Features				
Nb barrier thickness (average)	[μm]	3.2 ± 1.4	2.1 ± 1.3	1.8 ± 0.6
A15 grain size	[nm]	128 ± 2	139 ± 7	159 ± 4
Performance Ratios (normalized to 50 h**)**				
Critical current, I_c at 12 T		0.98	1.00	1.02
Critical current, I_c at 15 T		0.96	1.00	1.04
RRR		1.44	1.00	0.75
Damage threshold		1.31	1.00	0.74
Nb barrier thickness		1.54	1.00	0.85
A15 grain size		0.92	1.00	1.14

3.5.3 Implications for Magnet Design

Table 3.18 consolidates the comprehensive characterization data across the studied heat treatment conditions, revealing the interdependencies between the processing parameter and performance metrics.

The investigation definitively quantifies the relationship between RHT duration of the A15 phase and electromechanical properties: each additional hour of heat treatment beyond 30 hours costs approximately 0.08% in critical current at $12\,\mathrm{T}$ and costs approximately $1.3\,\mathrm{MPa}$ in damage onset threshold. This establishes that mechanical resilience degrades 16 times faster than the improvement in electromagnetic performance, demonstrating why extended heat treatments might prove counterproductive for mechanically-constrained applications. Moreover, the thermal stability affected by RRR also experiences a non-linear decrease above $30\,\mathrm{h}$ dwell times. The microstructural evolution through grain coarsening and barrier consumption creates this asymmetric response by simultaneously diminishing the grain boundary barriers that deflect crack paths and removing the ductile niobium phase that provides the primary mechanical constraint. For magnets targeting $150 - 200\,\mathrm{MPa}$ operational stresses, the 30-hour treatment's $138\,\mathrm{MPa}$ threshold provides essential margins while the $75\,\mathrm{h}$ treatment's threshold of less than $78\,\mathrm{MPa}$ ensures failure during assembly.

This quantified relationship transforms heat treatment selection from empirical optimization to engineering calculation: applications can now balance the J_c penalty against mechanical requirements. Current HL-LHC magnets operating below $100\,\mathrm{MPa}$ justify the $50\,\mathrm{h}$ baseline, achieving optimal electromagnetic performance within mechanical constraints. Solenoid configurations with predominantly hoop stress distributions may accommodate the $75\,\mathrm{h}$ treatment's enhanced J_c despite its $78\,\mathrm{MPa}$ threshold, provided design features limit peak stresses below $70\,\mathrm{MPa}$. Next-generation accelerator magnets could instead implement shorter treatments, accepting the modest J_c reduction to gain the correlated improvement in mechanical resilience essential for reliable operation at elevated stresses.

3.6 Case Study V: Combined Optimization

The systematic investigations of individual processing parameters revealed distinct pathways for improving the electromechanical performance of the Nb_3Sn cable, with enhanced resin systems offering improved crack propagation resistance, and reduced training requirements (Case Study III) and shortened heat treatment providing higher thresholds of damage onset (Case Study IV). This case study examines the outcome on combining these parameters using a $30\,\mathrm{h}$ duration for the final stage of RHT and impregnation with POLAB Mix resin. The quantified onset of damage thresholds are $138 \pm 18\,\mathrm{MPa}$ and $121 \pm 15\,\mathrm{MPa}$ for the $30\,\mathrm{h}$ treatment and POLAB Mix respectively, while the damage evolution rates in the $140 - 190\,\mathrm{MPa}$ range are approximately 0.024%/MPa and 0.006%/MPa respectively.

This investigation aims to address a critical question regarding the combined parameter optimization:

1. Does the combination of a shortened heat treatment and enhanced resin provide additive benefits, synergistic enhancement, or complementary control over different aspects of mechanical damage?

For this investigation, double-stack cable samples (Cable Id: H16OC0364A) underwent the abbreviated $30\,\mathrm{h}$ reaction heat treatment at $665°\mathrm{C}$ followed by vacuum pressure impregnation with POLAB Mix resin. Electrical characterization was not performed in this case study; however, the electrical performance can be inferred from the systematic relationships established in Case Studies III and IV. The assessment of mechanical damage involved application of transverse compression stress from $80 - 190\,\mathrm{MPa}$, with subsequent metallographic analysis to quantify onset and evolution of damage.

Key Findings

- **Damage onset**: Approximately $135\,\mathrm{MPa}$ transverse compression stress at room temperature, representing a 30% improvement over standard protocol
- **Damage evolution rate**: $0.005\%/\mathrm{MPa}$ per MPa in the $140 - 180\,\mathrm{MPa}$ range, a $5\times$ reduction compared to standard protocol
- **Damage characteristics**: Demonstration of complementary control where heat treatment governs crack initiation while resin suppresses crack propagation

3.6.1 Damage Onset and Evolution

Table 3.19 quantifies the crack density distribution obtained across the specimens in this case study. Figure 3.31 illustrates the evolution of damage with increasing transverse pressure, showing both the percentage of damaged subelements and their classification by severity level. Figure 3.32 presents the corresponding distribution of affected strands across the double-stack cable specimen cross-sections. The crack morphology and distribution patterns follow those established in Section 3.1.

Table 3.19: Statistical distribution of damage across specimens subjected to varying transverse compression stress, with 30-hour heat treatment duration and POLAB Mix impregnation resin

Specimen	Applied Stress		Number of damaged subelements							Strands with damaged subelements	
Id.	Mean, μ (MPa)	Std. Dev., σ (MPa)	D1	D2	D3	D4	D5	Net	[% of 8640]	Net	[% of 80]
F.7	84	6	0	0	0	0	0	0	0	0	0
F.1	129	10	0	0	0	0	0	0	0	0	0
F.2	137	9	1	0	0	0	0	1	0.01	1	1.25
F.5	167	22	12	0	0	0	0	12	0.14	12	15.00
F.3	184	39	22	3	0	0	0	25	0.29	18	22.50

Key observations from the metallographic analysis include:

1. **Damage onset threshold**: No cracks were observed in specimens F.7 and F.1, subjected to mean compressive stresses of $84\,\mathrm{MPa}$ and $129\,\mathrm{MPa}$ respectively. Initial damage appeared in specimen F.2 at $137 \pm 8\,\mathrm{MPa}$, with only a single cracked subelement in one strand. This establishes the damage onset threshold at approximately $137 \pm 8\,\mathrm{MPa}$ for the combined optimization. Comparing with individual optimizations, this threshold falls within the uncertainty range of the $30\,\mathrm{h}$ treatment alone ($138 \pm 18\,\mathrm{MPa}$) but represents a $15\,\mathrm{MPa}$ improvement over POLAB Mix with standard heat treatment ($121 \pm 15\,\mathrm{MPa}$). The combined configuration also thus achieves a $31\,\mathrm{MPa}$ improvement over the reference in Case Study I ($106 \pm 15\,\mathrm{MPa}$).

2. **Damage evolution with pressure**: The progression of damage with increasing transverse compressive stress reveals higher resistance to crack propagation. At $167\,\mathrm{MPa}$ (specimen F.5), damage remained minimal with only 0.14% of subelements affected, all exhibiting D1-level damage. This represents a 44% reduction compared to the $30\,\mathrm{h}$ treatment with standard resin (0.25% at $158\,\mathrm{MPa}$) and a 64% reduction compared to POLAB Mix with standard heat treatment (0.39% at $172\,\mathrm{MPa}$), noting the differences in applied mean stress.

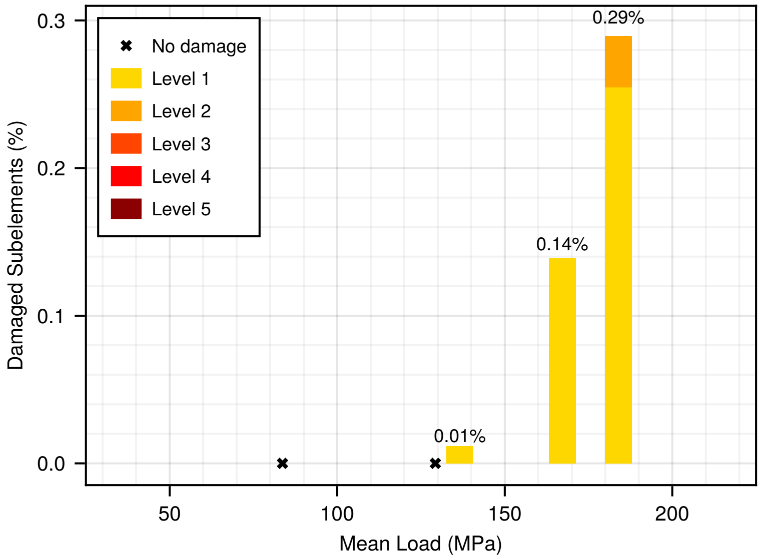

Figure 3.31: Percentage of damaged subelements categorized by damage level (D1-D5) as a function of applied transverse compression stress for the combined optimization: 30 h heat treatment with POLAB Mix resin. The absence of D3-D5 damage levels demonstrates exceptional crack propagation resistance.

At higher mean stress of $184\,\mathrm{MPa}$ (specimen F.3), damage affected only 0.29% of subelements distributed across 22.5% of strands. The damage gradient in the $140-180\,\mathrm{MPa}$ range measures approximately $0.006\%/\mathrm{MPa}$ in the subelements. Critically, no specimens exhibited severe damage levels (D3-D5) even at the maximum tested pressure, with 88% of damaged subelements showing only single cracks, D1 and the remainder limited to D2 level.

The mechanistic interpretation of the combined optimization reveals complementary rather than additive or synergistic effects, with each processing parameter independently controlling distinct stages of the failure process:

1. **Microstructure-controlled crack initiation**: The onset of damage at $137 \pm 9\,\mathrm{MPa}$ corresponds to the threshold measured for the single parameter variation of $30\,\mathrm{h}$ RHT duration, indicating that crack nucleation is governed by the refined grain structure and preserved niobium barriers. These microstructural features establish the critical stress intensity required for initial crack formation at the Nb_3Sn/Cu-Sn interfaces in this case, rather than the impregnation resin.

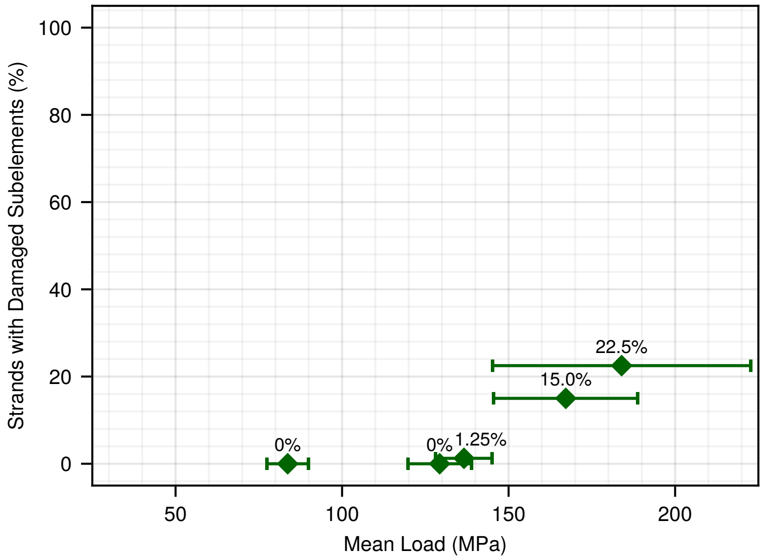

Figure 3.32: Percentage of strands containing at least one damaged subelement as a function of applied transverse compression stress for the combined optimization.

2. **Resin-controlled crack propagation**: The damage evolution rate of $0.006\%/\mathrm{MPa}$ matches that observed for POLAB Mix alone, confirming that crack propagation in the A15 phase is governed by the resin's enhanced fracture toughness. The resin matrix reduces the stress concentration in the A15 phase through viscoelastic energy dissipation and localized plastic deformation. This mechanism maintains the stress intensity factor below the critical threshold for unstable propagation, confining damage to isolated D1-D2 levels even at $190\,\mathrm{MPa}$ loading.

The expected electromagnetic performance based on established correlations can be discussed as follows:

1. **Critical current characteristics and thermal stability**: The configuration would retain the base properties of $30\,\mathrm{h}$ treatment with potential enhancement from improved strain state due to the modified resin. Results from Case Study IV indicate a penalty of less than 2% on the current-carrying capacity at operational fields. However, the compliant matrix would partially recover performance (upto 5% as measured in Case Study III) through a lowered compressive strain state of the A15 phase. The short sample limit and consequently operational margins are expected to be similar to that of the standard reference

case. The RRR characteristics of > 500 would be inherited from the heat treatment duration parameter.

2. **Training behavior**: The combined configuration is expected to require no more than the number of training quenches measured for the case of modified resin alone of Case Study III. The enhanced fracture toughness of the resin would dissipate mechanical disturbances before they accumulate into crack-induced energy releases, reducing peak stresses at strand crossovers where movement typically initiates.

The combined optimization of reaction heat treatment and impregnation resin demonstrates complementary benefits in addressing the competing demands of electromagnetic performance and mechanical integrity. With damage onset at approximately $135\,\mathrm{MPa}$ and higher crack propagation resistance maintaining subelement damage below 0.3% upto $190\,\mathrm{MPa}$, this approach enables reliable operation in the stress regimes required for $15\,\mathrm{T}$ class accelerator magnets. The hierarchical defense mechanisms, from A15 phase grain-level to cable-level, provide a pathway for extending Nb_3Sn technology beyond current mechanical limitations.

3.7 Synthesis and Summary

The investigation across the five case studies has enabled the development of a quantitative framework for optimizing processing parameters of impregnated Nb_3Sn cables. Figure 3.33 shows the onset and progression of damage via affected strands as a function of applied transverse pressure for all configurations. Figures comparing the onset and progression via damaged subelements are in Appendix A.6. The Table 3.20 consolidates the key findings across all case studies, enabling direct comparison of electrical performance and mechanical resilience under various processing conditions.

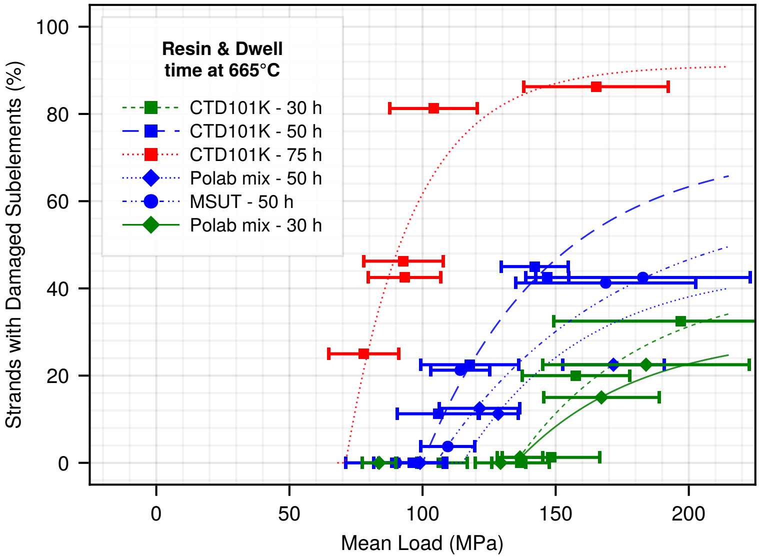

Figure 3.33: Evolution of the damage as a function of processing parameters. Heat treatment duration demonstrates the strongest influence on mechanical resilience, with a 66 MPa variation on the onset between 30h and 75h treatments. Enhanced resin systems provide incremental improvements, while combined optimization achieves complementary benefits exceeding individual contributions.

The duration of the final stage of the RHT cycle, denoted by color in Figure 3.33 exerts the strongest influence on mechanical resilience. Decreasing the heat treatment duration from the standard protocol enhances mechanical properties significantly, with the abbreviated 30 h treatment exhibiting no damage until substantially higher stress levels and minimal progression thereafter. Conversely, extending the treatment to 75 h dramatically reduces the damage threshold and accelerates damage evolution, with noticeable degradation occurring at relatively modest compression stress. This mechanical behavior correlates inversely with electromagnetic performance, where longer heat treatments yield marginally improved critical current density but at significant cost to structural integrity. Alternative resin systems, distinguished by marker shape in Figure 3.33, provide distinct mechanical enhancements without compromising electrical performance. The POLAB Mix formulation elevates the damage threshold and substantially reduces the damage evolution rate compared to the reference CTD-101K®, while simultaneously enhancing current-carrying capacity. The MSUT-Twente system similarly improves damage resistance, though to a lesser extent. The combined optimization approach achieves complementary benefits from both parameter adjustments, maintaining the high threshold characteristic of abbreviated heat treatment while exhibiting the lowest damage evolution rate of all configurations. The minimum prestress essential during operation to prevent resin-strand interfacial debonding is also quantified, as this failure mode causes rapid reduction in current-carrying capacity.

Table 3.20: Synthesis of electrical and mechanical performance across all investigated configurations. The reference case establishes baseline performance from which all comparisons are derived. Alternative resin systems enhance mechanical properties with improvement in the current-carrying capacity. Heat treatment duration (30–75 h) demonstrates inverse correlation between electrical performance and mechanical resilience. Combined optimization achieves complementary benefits from both parameter adjustments.

Configuration	**Electrical Properties**		**Mechanical Properties**		
	Margin at I_{nom} [%]	**RRR** (Mean)	**Onset** [MPa]	**Damage** at $110\,\mathrm{MPa}$ [%]	**Damage** at $170\,\mathrm{MPa}$ [%]
Reference Case					
$50\,\mathrm{h}$ + CTD-101K®	$25^w/18^c$	360	105 ± 15	0.20^i	1.12
Resin Variations ($50\,\mathrm{h}$ **heat treatment)**					
POLAB Mix	22^c	360	121 ± 15	0	0.39
MSUT-Twente	N/M	360	110 ± 10	0.05	0.69
Heat Treatment Variations (CTD-101K® resin)					
$30\,\mathrm{h}$	24^w	517	138 ± 18	0	0.25
$75\,\mathrm{h}$	26^w	270	78 ± 13	7.20	15.81
Combined Optimization					
$30\,\mathrm{h}$ + POLAB Mix	N/M	517	137 ± 9	0	0.14
Inadequate Prestress					
$50\,\mathrm{h}$ + CTD-101K®	1	517	11 ± 2^b	–	–

^{w}Wire-level measurements; ^{c}Cable-level measurements; ^{i}Interpolated value;
N/M - Not Measured; ^{b}Interfacial debonding threshold

A multidimensional figure of merit can be constructed that transforms the discrete experimental data into a continuous, differentiable function. A composite performance index (CPI) that integrates the key performance metrics identified throughout this investigation may be defined as:

$$\text{CPI}(\tau, r) = w_1 \cdot \frac{J_c(\tau, r, B_{op})}{J_{c,max}} + w_2 \cdot \frac{\sigma_{th}(\tau, r)}{\sigma_{th,max}} + w_3 \cdot \frac{\text{RRR}(\tau)}{\text{RRR}_{max}} + w_4 \cdot \frac{N_{train,ref}}{N_{train}(r)} \tag{3.6}$$

where:

- τ is the reaction heat treatment dwell time in hours
- r is the resin type (CTD-101K®, POLAB Mix, or MSUT)
- B_{op} is the operational magnetic field for the specific application
- w_i are the application-specific weighting factors with $\sum_{i=1}^{4} w_i = 1$
- $J_{c,max}$ is the maximum observed critical current at B_{op} ($75\,\text{h}$ treatment)
- $\sigma_{th,max}$ is the maximum observed damage threshold ($30\,\text{h}$ treatment)
- RRR_{max} is the maximum measured RRR ($30\,\text{h}$ treatment)
- $N_{train,ref}$ are the number of training cycles of the reference system (CTD-101K®)
- $N_{train}(r)$ are the experimentally measured training cycles for resin r

This formulation normalizes each performance metric relative to the maximum achieved with the standard CTD-101K® resin. For heat treatment variations, normalized terms range between $0.5 - 1.0$, establishing a bounded comparison framework. Enhanced resin systems produce values exceeding unity in specific metrics, quantifying performance improvements relative to the standard. Thus, this approach differentiates between parameter optimization within the standard resin system (≤ 1.0) and performance enhancement through alternative material systems (> 1.0). The formulation remains valid across the investigated heat treatment range of $30 - 75$ hours for all three investigated resin systems. Each performance function is modeled on experimental observations through physically-motivated functional forms.

The critical current density function must capture the observed gradual enhancement with extended heat treatment. The power law form naturally represents this behavior based on the kinetics of A15 phase formation:

$$J_c(\tau, r, B_{op}) = J_{c,max}(B_{op}) \cdot \left(\frac{\tau}{\tau_{ref}}\right)^n \cdot \eta_r \tag{3.7}$$

where:

- $J_{c,max}(B_{op})$ is the maximum critical current achieved at field B_{op} (corresponding to the $75\,\mathrm{h}$ treatment)
- $\tau_{ref} = 75\,\mathrm{h}$ is the reference heat treatment duration
- $n = 0.035$ is the power law exponent calibrated from experimental data at $12\,\mathrm{T}$
- η_r is the resin enhancement factor for J_c, e.g. 1.05 for POLAB Mix, 1.00 for CTD-101K

This power law formulation reproduces the mean critical current values obtained from the experimental Case Study IV with $704\,\mathrm{A}$ at $30\,\mathrm{h}$, $716\,\mathrm{A}$ at $50\,\mathrm{h}$, and $727\,\mathrm{A}$ at $75\,\mathrm{h}$ at $12\,\mathrm{T}$.

The damage onset threshold function requires separate treatment of the two dominant microstructural effects. The multiplicative form reflects the independent contributions of barrier thickness and grain size to mechanical strength:

$$\sigma_{th}(\tau, r) = \sigma_{th,max} \cdot f_{Nb}(\tau) \cdot g_{gr}(\tau) \cdot \xi_r \tag{3.8}$$

where:

- $\sigma_{th,max} = 140\,\mathrm{MPa}$ represents the mean threshold measured at $\tau_0 = 30\,\mathrm{h}$
- $f_{Nb}(\tau)$ is the barrier reinforcement contribution
- $g_{gr}(\tau)$ is the grain size strengthening contribution
- ξ_r is the resin enhancement factor, e.g.: 1.15 for POLAB Mix, 1.04 for MSUT-Twente, 1.00 for CTD-101K

The niobium barrier consumption follows a power law decay that better captures the non-linear dissolution kinetics observed experimentally. The power law form reflects the physical reality that barrier dissolution accelerates as the remaining barrier becomes thinner and more susceptible to interdiffusion. This acceleration occurs because thinner barriers provide less resistance to tin diffusion from the bronze core, leading to faster consumption rates at longer heat treatment times. The barrier function is expressed as:

$$f_{Nb}(\tau) = \left(\frac{\tau_0}{\tau}\right)^{\alpha} \tag{3.9}$$

where:

- $\alpha = 0.4$ is the power-law exponent calibrated from the experimental damage threshold data.

The grain size contribution incorporates the Hall-Petch relationship, where mechanical strength scales inversely with the square root of grain size:

$$g_{gr}(\tau) = \sqrt{\frac{d_0}{d_0 \cdot e^{(\tau-\tau_0)/\tau_{gr}}}} = e^{-\frac{\tau-\tau_0}{2\tau_{gr}}} \tag{3.10}$$

where:

- d_0 is the inital grain size at $\tau_0 = 30\,\mathrm{h}$
- $\tau_{gr} = 135\,\mathrm{h}$ is the estimated characteristic grain coarsening time
- Factor of 2 in denominator from square root of Hall-Petch relationship

This combined formulation closely reproduces the experimentally measured damage thresholds of $140\,\mathrm{MPa}$ at $30\,\mathrm{h}$, $105\,\mathrm{MPa}$ at $50\,\mathrm{h}$, and $82\,\mathrm{MPa}$ at $75\,\mathrm{h}$, demonstrating the validity of this microstructurally-informed approach to predicting mechanical resilience across the heat treatment parameter space.

The residual resistance ratio degradation follows exponential decay due to progressive tin contamination of the copper matrix through barrier dissolution:

$$\mathrm{RRR}(\tau) = \mathrm{RRR}_0 \cdot e^{-\frac{\tau-\tau_0}{\tau_{RRR}}} \tag{3.11}$$

where:

- $\mathrm{RRR}_0 = 517$ is the mean RRR obtained through statistical measurements at $\tau_0 = 30$ h
- $\tau_{RRR} \approx 60\,\mathrm{h}$ is the characteristic time for copper contamination

This combined formulation results in RRR values: 517 at $30\,\mathrm{h}$, 370 at $50\,\mathrm{h}$, and 244 at $75\,\mathrm{h}$ (compared to 517 ± 42, 360 ± 31, and 270 ± 50 experimental data respectively), closely approximating the decrease in the RRR across the heat treatment parameter space.

The training behavior demonstrates resin-dependent performance, with enhanced fracture toughness reducing the number of quenches required to reach stable operation:

$$N_{train}(r) = \begin{cases} 10 & \text{for CTD-101K} \\ 5 & \text{for POLAB Mix} \\ 5-10 & \text{for MSUT-Twente (estimated)} \end{cases} \tag{3.12}$$

Table 3.21: Calculated performance function values for all investigated configurations

Configuration	$J_c/J_{c,max}$ at 12 T	$\sigma_{th}/\sigma_{th,max}$	$\mathrm{RRR}/\mathrm{RRR}_{max}$	$N_{train,ref}/N_{train}$	CPI[a]
Heat Treatment Variations (CTD-101K resin)					
30 h at 665°C	0.97	1.00	1.00	1.00	0.99
50 h at 665°C (ref.)	0.98	0.75	0.72	1.00	0.86
75 h at 665°C	1.00	0.56	0.47	1.00	0.77
Resin Variations (50 h heat treatment)					
POLAB Mix	1.04	0.87	0.72[d]	2.00	1.15
MSUT-Twente	0.98-1.04[e]	0.79	0.72[d]	1.0-2.0[e]	0.87-1.13
Combined Optimization					
30 h + POLAB Mix	1.02[b]	1.15	1.00	2.00	**1.29**

[a]Using equal weights $w_i = 0.25$ for illustrative purposes; [d]Assumed similar to 50 h with CTD-101K®; [e]Estimated value based on enhanced fracture toughness

Table 3.21 consolidates the calculated performance metrics across all investigated configurations, demonstrating the systematic trade-offs between electrical and mechanical properties. The combined performance index reveals that the complementary optimization through abbreviated heat treatment (30 h) with POLAB Mix resin achieves the highest overall performance (CPI $= 1.29$), surpassing individual parameter optimizations.

From the established performance functions, the individual component derivatives can be derived for a sensitivity analysis. The derivative of current carrying capacity is:

$$\frac{\partial J_c}{\partial \tau} = J_{c,max}(B) \cdot \eta_r \cdot \frac{n}{\tau_{ref}} \cdot \left(\frac{\tau}{\tau_{ref}}\right)^{n-1} \tag{3.13}$$

For the damage threshold function,

$$\frac{\partial \sigma_{th}}{\partial \tau} = \sigma_0 \cdot \xi_r \cdot \left[\frac{\partial f_{Nb}}{\partial \tau} \cdot g_{gr}(\tau) + f_{Nb}(\tau) \cdot \frac{\partial g_{gr}}{\partial \tau}\right] \tag{3.14}$$

The individual derivatives of the component functions are:

$$\frac{\partial f_{Nb}}{\partial \tau} = -\alpha \cdot \left(\frac{\tau_0}{\tau}\right)^{\alpha} \cdot \frac{1}{\tau} \tag{3.15}$$

$$\frac{\partial g_{gr}}{\partial \tau} = -\frac{1}{2\tau_{gr}} \cdot e^{-\frac{\tau-\tau_0}{2\tau_{gr}}} \tag{3.16}$$

Substituting the individual derivatives:

$$\frac{\partial \sigma_{th}}{\partial \tau} = \sigma_0 \cdot \xi_r \cdot \left[-\alpha \cdot \left(\frac{\tau_0}{\tau}\right)^{\alpha} \cdot \frac{1}{\tau} \cdot g_{gr}(\tau) - \frac{1}{2\tau_{gr}} \cdot f_{Nb}(\tau) \cdot g_{gr}(\tau)\right] \tag{3.17}$$

Similarly, for the variation of RRR,

$$\frac{\partial \text{RRR}}{\partial \tau} = -\frac{\text{RRR}_0}{\tau_{RRR}} \cdot e^{-\frac{\tau-\tau_0}{\tau_{RRR}}} \tag{3.18}$$

The mechanical-electromagnetic trade-off can be quantified through the ratio of sensitivities:

$$\Lambda(\tau) = \frac{\partial \sigma_{th}/\partial \tau}{\partial J_c/\partial \tau} \tag{3.19}$$

where Λ represents the mechanical threshold change (in MPa) per unit change in critical current (in A) when varying heat treatment duration.

Evaluating these derivatives and electromechanical trade-off at the three investigated heat treatment durations (with CTD-101K® resin, $\xi_r = 1.0$) using the parameters $J_{c,max}(12\,\text{T}) = 727\,\text{A}$, $n = 0.035$, $\tau_{ref} = 75\,\text{h}$, $\sigma_0 = 140\,\text{MPa}$, $\alpha = 0.4$, $\tau_{gr} = 135\,\text{h}$, $\tau_0 = 30\,\text{h}$, and $\tau_{RRR} = 60\,\text{h}$, is the sensitivity analysis of the performance metrics and is shown in Table 3.22.

The sensitivity analysis reveals the diffusion-controlled kinetics governing the performance metrics. Positive J_c' values quantify the decelerating improvement in the ampacity from 0.8 to $0.3\,\text{A/h}$. The negative σ_{th}' and RRR' derivatives signify the mechanical degradation and deterioriation in the quality of stabilizer with extended processing. The diminishing magnitudes reflect the parabolic diffusion kinetics where the barrier consumption and grain coarsening rates decelerate with time. The trade-off parameter, Λ ranges from -3.1 to $-2.1\,\text{MPa/A}$, with the negative values indicating that the electromagnetic gains are invariably accompanied by mechanical losses. Over the investigated range from 30 to 75 hours, the integrated effect yields the experimentally

Table 3.22: Sensitivity analysis of performance metrics to heat treatment duration

Parameter	**Unit**	**Value at**		
		$\tau = 30\,\mathrm{h}$	$\tau = 50\,\mathrm{h}$	$\tau = 75\,\mathrm{h}$
J_c'	A/h	$+0.8$	$+0.5$	$+0.3$
σ_{th}'	MPa/h	-2.4	-1.2	-0.7
RRR'	h^{-1}	-8.6	-6.2	-4.1
Mechanical-Electromagnetic Trade-off				
Λ	MPa/A	-3.1	-2.3	-2.1

Prime notation (') denotes $\partial/\partial\tau$

observed relationship: $60\,\mathrm{MPa}$ mechanical improvement requires accepting a 3.4% reduction in J_c, corresponding to an average of approximately $2.5\,\mathrm{MPa/A}$ change in critical current at $12\,\mathrm{T}$.

Combining the composite performance index and sensitivity analysis from Tables 3.21 and 3.22 enables strategising of optimal heat treatment durations based on application-specific priorities:

1. **Electromagnetically dominated** ($w_1 > 0.5$): An extended heat treatment is justified despite mechanical penalties. The diminishing returns on the current-carrying capacity ($\partial J_c/\partial\tau < 0.4\,\mathrm{A/h}$ above $60\,\mathrm{h}$) establish $45 - 75\,\mathrm{h}$ as an optimal duration. In this regime, A15 layer growth approaches completion while σ_{th} retains $55 - 75\%$ of maximum strength, which is sufficient for applications such as high-field solenoids where electromagnetic design margins dominate structural requirements.

2. **Mechanically constrained** ($w_2 > 0.5$): An abbreviated heat treatment is recommended for high-stress environments such as accelerator magnets. The steep degradation in the thresholds for onset of damage ($|\partial\sigma_{th}/\partial\tau| > 2\,\mathrm{MPa/h}$ below $30\,\mathrm{h}$) bounds the optimal range at $30 - 40\,\mathrm{h}$ while still retaining 97% of maximum J_c. This strategy preserves thicker Nb barriers and finer grain structures, maximizing crack initiation thresholds where mechanical failure modes govern magnet lifetime. The modest electromagnetic sacrifice proves negligible compared to avoiding premature degradation under Lorentz loading, particularly in training-sensitive configurations.

3. **Balanced optimization** ($w_1 \approx w_2 \approx 0.3$): Next-generation magnets requiring both high fields and mechanical resilience achieve optimal performance near $35 - 45\,\mathrm{h}$. At $\tau \approx 40\,\mathrm{h}$, the configuration delivers 98% of maximum J_c while maintaining 85% of peak mechanical

threshold. This reflects the compromise where incremental electromagnetic gains balance mechanical losses for equally-weighted applications.

Resin selection introduces multiplicative enhancement factors (ξ_r) that translate performance curves without altering their functional form. For example, POLAB Mix provides up to 5% electrical performance improvement, effectively shifting the parameter optimization window while preserving the fundamental trade-off structure. This orthogonal optimization pathway is proven with the combined strategy ($30\,\mathrm{h}$ + POLAB Mix, CPI = 1.29) surpassing individual parameter optimizations.

This chapter has systematically characterized the electromechanical behavior of impregnated Nb_3Sn Rutherford-type cables through a comprehensive experimental investigation spanning electrical performance evaluation and mechanical damage assessment. The five case studies establish quantitative relationships between two chosen processing parameters, viz. reaction heat treatment duration and impregnation resin selection and their effects on electrical performance and mechanical resilience. The critical thresholds for damage onset and evolution under transverse compression stress have been identified and correlated with microstructural features. The consequences of inadequate mechanical support during operation have been demonstrated through controlled experimentation. The investigation culminates in a multidimensional optimization framework that enables balancing of current-carrying capacity against structural integrity across the parameter space, providing essential guidance for next-generation accelerator magnet design.

4 Conclusion

This thesis has presented an investigation of electromechanical degradation mechanisms in Nb_3Sn Rutherford-type cables for high-field accelerator magnets. The work addressed critical knowledge gaps between mechanical damage onset and electrical performance degradation through parallel electromagnetic and metallographic characterization. The findings establish quantitative relationships between the reaction heat treatment duration, impregnation resin selection and the fundamental limits of conductor performance under transverse compression stress. These relationships provide essential engineering data for optimizing Nb_3Sn conductor processing while maintaining the mechanical integrity required for next-generation accelerator magnets targeting fields beyond 15 T.

The purpose of this concluding chapter is to synthesize the key results, assess their implications for magnet engineering, and identify pathways for future development. The discussion examines how the established damage thresholds and processing optimizations address the original research questions while acknowledging remaining challenges in pushing Nb_3Sn technology toward its fundamental limits.

Summary of Key Results

- **Quantification of true damage onset thresholds:** The systematic metallographic analysis established that mechanical damage in the A15 phase of Nb_3Sn subelements initiates at transverse pressures substantially below those causing measurable electrical degradation. This critical finding reveals an operational window where undetected mechanical damage accumulates despite stable electrical performance. The damage classification methodology developed in this work transformed qualitative crack observations into quantitative threshold metrics applicable to design specifications, leading to implementation of refined assembly limits for MQXF quadrupole production at CERN.
- **Demonstration of prestress criticality:** The cables tested without adequate external mechanical support or prestress exhibited severe performance degradation through interfacial

debonding at pressures well below the direct Nb_3Sn damage threshold. The substantial reduction in current-carrying capacity and negative operating margins confirm that prestress application represents a fundamental requirement for operation of Nb_3Sn cos-theta magnets. The progressive debonding mechanism explains extended training behavior observed in operational magnets and validates mechanical support specifications.

- **Heat treatment duration as dominant parameter:** The processing time at the A15 formation plateau of the RHT cycle proved the most influential factor governing electromechanical behavior. Abbreviated heat treatments preserved the niobium barrier integrity and limited grain coarsening, yielding significantly enhanced mechanical resilience with only modest penalties in the electrical performance. Conversely, extended treatments accelerated barrier consumption and grain growth, precipitating mechanical degradation at much lower transverse compressive stress while providing diminishing returns in critical current enhancement.
- **Resin system enhancement effects:** The elastic modulus and fracture toughness of the impregnation resin represent viable optimization parameters for mechanically-constrained applications. A lower elastic modulus elevates the onset of damage, while a higher fracture toughness reduces the damage evolution rate. The enhanced resin systems effectively redistribute localized stresses, reducing both damage initiation rates and crack propagation through the hierarchical conductor structure. This is consequently reflected in the current-carrying capacity and training behaviour of the impregnated conductor cables.
- **Complementary optimization strategy:** A combined process modification targeting both the intrinsic conductor properties (through heat treatment) and extrinsic mechanical environment (through resin selection) demonstrated complementary benefits. This combined approach creates a hierarchical defense against electromechanical degradation spanning multiple structural scales, from grain boundaries to the macroscopic cable composite, providing a pathway for reliable operation at the stress levels required for future high-field accelerator magnets.

Implications for Nb_3Sn Magnet Engineering

The systematic characterization presented in this thesis establishes engineering guidelines that directly address the mechanical constraints limiting next-generation accelerator magnets. The quantified damage thresholds provide essential data for stress management strategies as electromagnetic forces approach material limits. For current technology operating at $10 - 12\,\mathrm{T}$, the validated $100\,\mathrm{MPa}$ assembly limit with standard processing provides adequate margins. The reference configuration achieves reliable performance through established manufacturing procedures while accommodating typical stress concentrations and measurement uncertainties. The modest training behavior and operational stability of MQXF magnets confirm the viability of this approach. For future magnets targeting $14 - 16\,\mathrm{T}$ operation, the quadratic azimuthal stress scaling with field will reach $150 - 200\,\mathrm{MPa}$, exceeding damage thresholds obtained with the current protocols for processing the Nb_3Sn conductor cables. Reduction in the duration for A15 phase formation of the RHT cycle emerges as essential, providing improved resistance to damage due to tranverse compression. When combined with enhanced resins, this configuration achieves higher mechanical margins. The thresholds obtained in this work are based on controlled laboratory measurements with $\pm 10\,\mathrm{MPa}$ uncertainty. Real magnet assemblies should incorporate additional safety factors to account for manufacturing variability and stress concentration effects.

The offset between mechanical damage initiation and electrical degradation presents both opportunity and risk. While conductors maintain functionality despite localized cracking, this apparent resilience masks progressive deterioration that could manifest catastrophically under cyclic loading. Design margins must account for damage accumulation over operational lifetimes spanning decades and hundreds of thermal cycles. The demonstrated trade-offs between electromagnetic enhancement and mechanical vulnerability through extended processing challenge conventional approaches prioritizing maximum critical current. For stress-limited applications, accepting minor electromagnetic penalties yields substantial reliability improvements.

Recommendations for Future Development

The quantitative relationships established in this thesis between processing parameters and electromechanical performance point to specific research priorities that build directly on the experimental findings:

- **Process optimization within established parameters:** The abbreviated heat treatment combined with enhanced resin systems demonstrated sufficient damage thresholds for next-generation applications. Near-term optimizations should include fine-tuning the A15 formation plateau duration to maximize the mechanical resilience while maintaining acceptable electromagnetic performance. Development of rapid screening methodologies based on the established microstructure-property correlations would accelerate this optimization process without requiring full-scale magnet testing.
- **Bridging damage onset and electrical degradation:** This thesis revealed mechanical damage at stress levels significantly below those causing measurable electrical degradation. Future work should investigate how this subsurface damage evolves under cyclic loading

conditions typical of accelerator operations, particularly focusing on damage accumulation mechanisms that may manifest as performance deterioration over extended operational periods. Such studies would establish more precise lifetime predictions for magnets operating with stresses in this critical intermediate range.

- **Hybrid conductor architectures:** The microstructural analysis demonstrated how grain coarsening and niobium barrier consumption limits mechanical resilience in RRP® conductors. Investigation of modified architectures with reinforced barriers or strategic grain refinement additives could potentially extend damage thresholds beyond those achievable through process optimization alone. Preliminary development could focus on targeted modifications to proven designs rather than radical architectural changes requiring extensive requalification.
- **Integrated multiscale modeling:** The experimental data presented in this thesis provide essential validation benchmarks for developing integrated mechanical models spanning from crystal plasticity of the A15 phase through composite mechanics of the cable assembly. Such models would enable predictive optimization of processing parameters without extensive empirical testing, particularly for exploring parameter spaces beyond those experimentally investigated in this work.

Closing Perspectives

As accelerator magnets push toward fields exceeding $15\,\mathrm{T}$, the research landscape for Nb_3Sn conductors demands new perspectives. This thesis contributes to that ongoing effort by establishing quantitative relationships in the electromechanical behavior that guide optimization for increasingly demanding applications.

The findings challenge the paradigm of maximizing electromagnetic performance in the conductor without equal consideration of mechanical integrity. As next-generation accelerators approach stress levels comparable to material damage thresholds, this balance becomes not merely important but absolutely critical. The demonstrated ability to enhance mechanical resilience through targeted processing modifications by shortened heat treatment preserving microstructural integrity and enhanced resins improving damage tolerance and improved electrical behaviour provides essential tools for extending Nb_3Sn technology. Yet significant challenges remain. The fundamental strain sensitivity of the superconductor imposes ultimate limits that incremental optimization cannot overcome. Revolutionary advances may require departing from current architectures entirely, whether through alternative superconductors, hybrid conductor designs, or reconceptualization of how electromagnetic forces are managed in high-field magnets.

The interdisciplinary nature of these challenges spanning materials science, mechanical engineering, electromagnetics, and cryogenics demands continued collaboration across traditional boundaries. Just as this investigation benefited from parallel approaches combining electrical characterization with metallographic analysis, future progress requires integration of diverse expertise and methodologies. Ultimately, the pursuit of ever-higher magnetic fields for particle physics drives innovation that extends far beyond accelerator applications.

A Appendix

A.1 Phase Diagrams for Nb_3Sn Conductor Processing

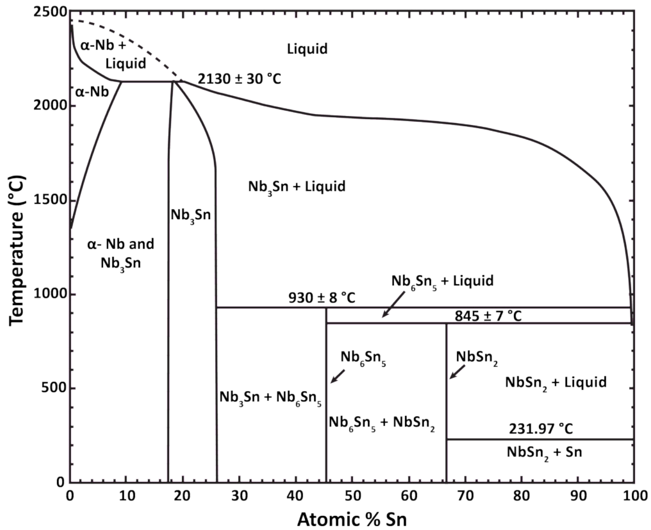

Figure A.1: Binary phase diagram of the Nb-Sn system showing the formation regions of various intermetallic compounds including the superconducting A15 phase (Nb_3Sn). Image by Charlie Sanabria, reproduced under Wikimedia Creative Commons by 4.0 license [177].

The reaction heat treatment of Nb_3Sn conductors involves solid-state diffusion processes governed by two primary binary phase systems: the Nb-Sn system that determines the formation of the superconducting A15 phase, and the Cu-Sn system that controls bronze formation and intermediate phase evolution.

The Nb-Sn Binary Phase Diagram

The Nb-Sn binary system [178], shown in Figure A.1, exhibits several intermetallic compounds relevant to Nb_3Sn conductor processing. The A15 phase (Nb_3Sn) exists over a composition range of approximately $18 - 25$ at.% Sn, with the stoichiometric composition at 25 at.% Sn exhibiting the highest critical temperature ($T_c \approx 18\,\mathrm{K}$) and upper critical field ($B_{c2} \approx 30\,\mathrm{T}$). The A15 phase forms peritectically at $2130\,^{\circ}\mathrm{C}$, though solid-state diffusion during practical heat treatment occurs at significantly lower temperatures ($650 - 700\,^{\circ}\mathrm{C}$). The presence of Nb_6Sn_5 as an intermediate phase can degrade superconducting properties if not properly controlled, while the limited solid solubility of Sn in Nb (< 1 at.% at processing temperatures) necessitates long-range diffusion for A15 formation. Off-stoichiometric Nb_3Sn with lower Sn content exhibits reduced T_c and B_{c2}, emphasizing the importance of maintaining adequate Sn supply during reaction.

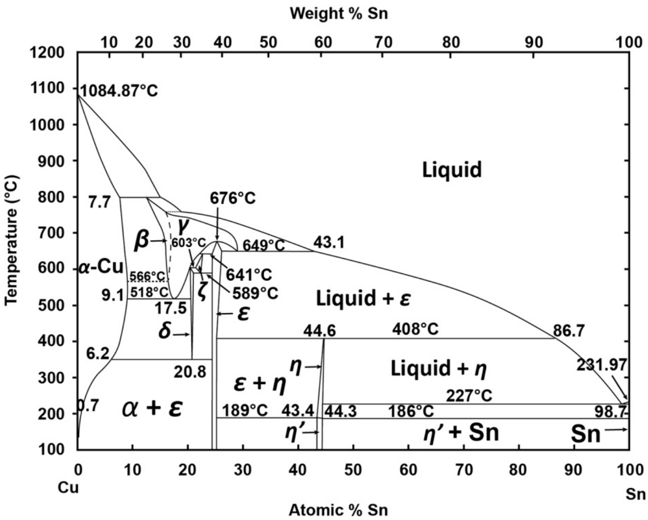

Figure A.2: Binary phase diagram of the Cu-Sn system showing the bronze region and Cu-Sn intermetallic compounds. Image by Charlie Sanabria, reproduced under Wikimedia Creative Commons by 4.0 license [179].

The Cu-Sn Binary Phase Diagram

The Cu-Sn system [180], illustrated in Figure A.2, governs the initial stages of the reaction heat treatment where bronze formation and Cu-Sn intermetallic development occur. This system is particularly important for understanding the formation of intermediate phases that act as Sn sources and diffusion mediators during Nb_3Sn growth. The α-bronze phase (fcc Cu with Sn in solid solution) exhibits limited Sn solubility with a maximum of 15.8 wt.% (9.1 at.%) at $520\,^{\circ}\mathrm{C}$. The ϵ-Cu_3Sn phase forms at bronze/Sn interfaces and plays a crucial role in controlling Sn diffusion rates, while the η-Cu_6Sn_5 phase appears first during low-temperature heat treatment stages and later decomposes to form ϵ-Cu_3Sn. Volume changes during phase transformations, particularly the $\eta \rightarrow \epsilon$ transition, contribute to Kirkendall void formation. The eutectoid transformation at $520\,^{\circ}\mathrm{C}$ limits the practical bronze composition in bronze-route conductors.

Ternary Cu-Nb-Sn Interactions

While the binary phase diagrams provide the foundation for understanding phase formation, the actual conductor system involves ternary interactions that significantly influence the reaction kinetics. The Nausite phase (nominally $(Nb_{0.75}Cu_{0.25})Sn_2$) forms at Cu-Nb-Sn interfaces and acts as an osmotic membrane that permits Cu diffusion from the filament region into the Sn-rich core while restricting Sn diffusion into the filament pack during early heat treatment stages. This phase controls the uniformity of subsequent Nb_3Sn layer formation and decomposes above $586\,^{\circ}C$ to enable final A15 phase growth.

A.2 Vacuum Pressure Impregnation Process Details

The vacuum pressure impregnation (VPI) process for Nb_3Sn accelerator magnets consists of three essential stages that must be carefully controlled to achieve the mechanical properties required for reliable magnet operation[95]. For MQXF magnets using the standard CTD-101K® resin system, the process proceeds as follows:

Stage 1: Vacuum Evacuation

The initial evacuation stage is essential to prevent void formation in the final impregnated structure. The composite coil assembly is susceptible to void spaces between strands, insulation materials within the cables, and at the interfaces with structural elements. Typical vacuum levels of $0.35\,\mathrm{mbar}$ are achieved after $24 - 48$ hours of pumping for MQXF-class magnets. This deep vacuum serves to remove not only air but also moisture that would otherwise create localized vaporization during the subsequent curing cycle, which would also lead to void formation. For large accelerator magnets, moisture content even at parts-per-million levels can expand dramatically during the $125°\mathrm{C}$ curing stage, creating bubbles that would compromise mechanical integrity.

Stage 2: Resin Introduction and Infiltration

The resin itself undergoes degassing prior to injection into the coil assembly. This serves to remove dissolved gases present in the uncured resin which will otherwise expand during curing, creating voids. This pre-degassing typically occurs at elevated temperatures ($60\,°\mathrm{C}$ for CTD-101K® systems) under vacuum, with stirring to promote bubble evolution and removal[124]. The resin injection phase leverages the pressure differential between the evacuated coil cavity and atmospheric pressure (or higher, when overpressure is applied) in the resin reservoir. This drives infiltration through the intricate network of spaces within the coils. Infiltration must overcome significant resistance from the compacted insulation structure, which typically exhibits permeability values that can vary by more than an order of magnitude within a single coil due to local compaction variations[124]. The injection duration provides a critical quality control parameter. For MQXF quadrupoles, typical injection times range from 60 minutes to 105 minutes for larger assemblies, with significant deviations indicating potential infiltration issues[95]. During this phase, the coil remains under vacuum to maintain the driving force for resin penetration into all accessible volumes.

Stage 3: Controlled Curing Cycle

The final stage is the controlled curing cycle to achieve optimal resin polymerization. The cycle must consider the differential thermal expansion behaviors of the composite system. The standard curing cycle of 5 hours at $110\,°\mathrm{C}$ followed by 16 hours at $125°\mathrm{C}$, represents a carefully optimized compromise between achieving complete crosslinking and minimizing thermal stress[95]. During the initial $110^{\circ}\mathrm{C}$ phase, the resin transitions through its gel point, where viscosity increases rapidly, effectively "locking in" the coil geometry. This prevents dimensional changes during the subsequent higher-temperature phase where final curing occurs. Crucially, the curing cycle must be completed before the assembly is allowed to cool, as premature cooling can lead to incomplete curing and inhomogeneous mechanical properties. Temperature monitoring throughout the coil cross-section ensures uniform heating in order to prevent localized under-curing.

The entire VPI process requires approximately 8 days for large accelerator magnets, with the bulk of this time allocated to the curing cycle. This extended timeline ensures the formation of a mechanically robust composite structure that provides essential support to the brittle Nb_3Sn conductors while maintaining the precise dimensions required for accelerator-quality field homogeneity [27].

A.3 Review of Studies on transverse compression on Nb_3Sn cables

This appendix provides a compilation of experimental studies investigating the response of Nb_3Sn cables to transverse compression over the past four decades. Table A.1 provides a chronological overview of experimental investigations.

Table A.1: Comprehensive review of transverse compression studies on Nb_3Sn conductors

Authors	**Sample Details**	**RHT & Impregnation Resin**	**Irreversible Damage Limit (MPa)**	**Key Findings on Damage Mechanism**
Jakob et al. [72]	28-strand Rutherford cable with 0.8 mm ∅ Bronze route wires	Not specified; Solder (Pb62Sn36Ag2)	∼200	• 5 % degradation at 200 MPa (cable face) and 15 % degradation at 200 MPa (cable edge) • Cable edge 2–3× more sensitive than cable face. Edge effects dominant in determining integral cable response
ten Kate et al. [145]	36-strand Rutherford cable with 0.9–1.0 mm ∅ PIT wires	650 °C/50 h; Stycast 2850FT	∼200	• 12 ± 2 % degradation at 200 MPa • Significant strand-to-strand variation observed • Voltage criteria affects degradation assessment
van Oort et al. [134]	48/26-strand keystoned Rutherford cables with 0.65–1.29 mm ∅ MJR wires	650 °C/48 h; Stycast 2850FT	20–50	• 63 % degradation at 150 MPa (48-strand cable) • Thin edge of keystoned cable most vulnerable • Number of subelements per strand (6 vs. 36) dramatically affects stress sensitivity • Higher subelement count improves stress tolerance
Pasztor et al. [146]	36-strand Rutherford cable with 0.92 mm ∅ Bronze process wires	Not specified; Solder vs. None	Solder-filled: ∼200 Unfilled: ∼160	• Solder-filled: 13 % degradation at 160 MPa • Unfilled: 25 % degradation at 160 MPa • Cable face shows 100 % higher degradation in unfilled cables • Stress distribution function of wire geometry • Cable edges are weak link determining integral response

Continued on next page

Table A.1 – continued from previous page

Authors	Sample Details	RHT & Impregnation Resin	Irreversible Damage Limit (MPa)	Key Findings on Damage Mechanism
Barzi et al.[73]	Single strand in dummy cable; 0.7–1.0 mm ∅ MJR, PIT, IT, RRP wires	Various cycles; None	PIT: ∼60 Others: ∼140–150	• 70–80 % degradation at 200 MPa (all architectures) • PIT conductors significantly more stress-sensitive than others • Stainless steel cores improved stress tolerance • Field-dependent degradation observed
Bordini et al.[149]	18-strand Rutherford cable with 1.0 mm ∅ PIT wires	650 °C/50 h; Epoxy resin	∼90	• 24 % degradation at 155 MPa • Degradation attributed to B_{c2} reduction • Suggests reversible strain effects rather than filament cracking • Lower stress tolerance compared to RRP architectures
Wolf et al.[84]	40-strand Rutherford cable with 0.7 mm ∅ RRP® 144/169 wires	Not specified; CTD-101K® vs Sn-Ag Solder	Not specified	• High-quality neutron diffraction data on elastic strain evolution • Epoxy vs. solder impregnation shows different mechanical responses • Differences attributed to yield stress of impregnation material • Provides fundamental understanding of load transfer mechanisms
Duvauchelle et al.[140]	40-strand Rutherford cable with 1.0 mm ∅ RRP® 132/169 wires with Ti bars	210 °C/72 h, 400 °C/72 h, 665 °C/50 h; CTD-101K®	∼120–140	• 11 % degradation at 160 MPa • Degradation attributed to B_{c2} reduction • Suggests reversible strain effects rather than filament cracking • Ti bars influence stress distribution
Ebermann et al.[76,141]	40-strand Rutherford cable with 0.7 mm ∅ RRP® 144/169 wires	210 °C/48 h, 400 °C/50 h, 650 °C/50 h; CTD-101K®	∼150–175	• Non-monotonic behavior with improvement up to 75 MPa • No observable degradation up to 150 MPa • 4 % degradation at 175 MPa • Strongly degraded at 200 MPa • Longitudinal cracks parallel to applied stress

Continued on next page

Table A.1 – continued from previous page

Authors	Sample Details	RHT & Impregnation Resin	Irreversible Damage Limit (MPa)	Key Findings on Damage Mechanism
Gao et al.[75,161]	18/40-strand Rutherford cables with 0.7–1.0 mm ∅ RRP®/PIT wires	Various; CTD-101K®	RRP®: ∼150–250 PIT: ∼70–150	• RRP®: 7 % degradation at 150 MPa • PIT: 10 % degradation at 150 MPa • Degradation attributed to B_{c2} reduction • No significant degradation after thermal cycling • Deviatoric strain decreases with increasing Young's modulus of epoxy • Glass reinforcement reduces strain by 5 %
Lenoir et al.[135]	40-strand Rutherford cable with 0.7 mm ∅ RRP® 108/127 wires	210 °C/48 h, 400 °C/50 h, 650 °C/50 h; CTD-101K®	∼170	• 2 % degradation at 170 MPa, 16 % after cycling • Mechanical damage in form of cracks appears before electrical degradation • I_c maximum at 140 MPa with cracks already present • Cracks form 45 ° X-shaped patterns • Cumulative loading more damaging than monotonic loading
Vallone et al.[147]	40-strand Rutherford cable (10-stack) with 0.85 mm ∅ RRP® 108/127 wires	Not specified; CTD-101K®	100–125 (uniaxial)	• Failure surface shows strong interaction between loading directions • Hydrostatic-like loading less damaging than deviatoric • 40 MPa radial prestress prevents cracks at 150 MPa azimuthal stress • Multiaxial stress state critical for damage assessment

The progression of transverse compression research over four decades reveals systematic advances in understanding electromechanical degradation mechanisms and establishing operational boundaries for Nb_3Sn conductors. Key insights include the hierarchy of mechanical resilience across architectures, and the critical knowledge gap on damage onset. These studies have employed various methodologies for applying transverse compression. Jakob and Pasztor[72] utilize flat anvils in a universal testing machine to compress solder-filled cables. Barzi et al.[73] develop a specialized fixture that places individual strands within a simulated cable environment to isolate strand-level effects. Development of a novel pressurised bladder-type sample holder at the FRESCA test facility enabled critical current measurements of Nb_3Sn Rutherford cables under in-situ transverse compression[140,149]. Another series of studies[135,141] at the same facility employed application of room-temperature compression to separate the effect of prestress application on irreversible degradation in the current carrying capacity of Nb_3Sn Rutherford-type cables. For neutron diffraction studies, Wolf et al.[83] incorporate pressure-sensitive films to characterize the stress distribution on cable stacks under compression. In studies involving multiple cable layers, such as the 10-stack measurements conducted by Vallone et al.[147], custom-designed compression fixtures with precisely machined surfaces are employed to ensure parallelism and uniform loading.

The systematic evolution of transverse compression research reveals a consistent pattern of degradation thresholds across different conductor architectures and experimental methodologies. Early studies on bronze-route and PIT conductors established damage thresholds in the range of $60 - 150\,\mathrm{MPa}$, while more recent investigations using advanced RRP® architectures demonstrate improved stress tolerance with irreversible degradation typically initiating between $150 - 175\,\mathrm{MPa}$. Notably, the transition from reversible strain effects to permanent structural damage occurs within a relatively narrow stress window of $20 - 40\,\mathrm{MPa}$ across all conductor types, emphasizing the critical importance of precise stress management in magnet design.

A.4 The HL-LHC low-β Quadrupole magnet, MQXF: an overview

The High-Luminosity Large Hadron Collider (HL-LHC) upgrade demanded a technological leap that would push superconducting magnet engineering to its absolute limits. The MQXF low-β quadrupole magnets, designed to replace the current LHC triplet quadrupoles, represent the first long superconducting accelerator magnets built with Nb_3Sn technology. With a $150\,\mathrm{mm}$ aperture, current of $16.23\,\mathrm{kA}$ and a peak field of $11.23\,\mathrm{T}$ these magnets exemplify the engineering challenges inherent in high-field Nb_3Sn applications [27]. Their development journey illustrates the multifaceted challenges in engineering practical Nb_3Sn accelerator magnets, where mechanical and electromagnetic constraints intertwine with materials properties across every phase from reaction heat treatment to operational performance.

The development program, spanning nearly a decade from 2015 to 2024, emerged from the US LHC Accelerator Research Program (LARP) collaboration between CERN and American institutions. Two variants define the MQXF family: MQXFA, fabricated by the US Accelerator Upgrade Program (AUP) with a length of $4.2\,\mathrm{m}$, and MQXFB, produced at CERN with a $7.15\,\mathrm{m}$ magnetic length. The cables are of Rutherford-type comprising 40 strands of $0.85\,\mathrm{mm}$ diameter using RRP® $108/127$ wires [79]. A critical decision involved reducing the reaction heat treatment duration from the manufacturer-recommended 75 hours at $665\,^{\circ}\mathrm{C}$ to 50 hours, accepting a performance trade-off to achieve the high residual resistivity ratio (RRR > 150) essential for thermal and electrical stability during magnet operation [59].

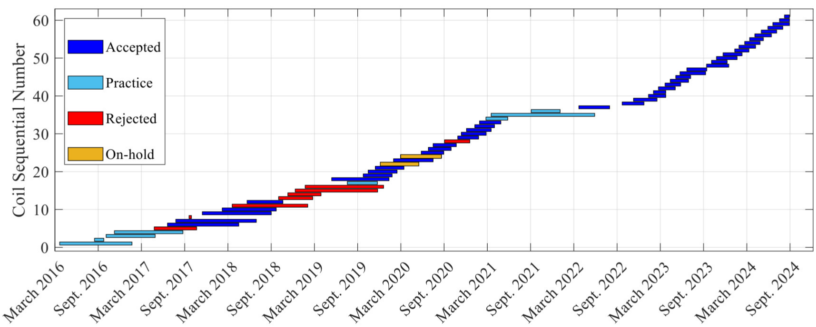

Figure A.3: Timeline of MQXF development program showing progression from short models through prototypes to series production magnets [28].

The engineering journey began with short model magnets ($1.5\,\mathrm{m}$) to validate fundamental design concepts. The first single-coil test conducted in May 2015 initiated a systematic development progression through MQXFS1, MQXFS3, MQXFS4, and MQXFS5, each iteration revealing critical insights about mechanical stress management and superconductor behavior [27]. MQXFS3 exhibited particularly concerning behavior, showing progressive degradation in quench performance after 19 thermal cycles, an early indication of the mechanical sensitivity challenges that would dominate the program.

The transition to full-length prototypes exposed fundamental manufacturing challenges unique to long Nb_3Sn magnets. MQXFB prototype 1 (MQXFBP1) achieved only $15.3\,\mathrm{kA}$ at $1.9\,\mathrm{K}$, falling short of the required $16.23\,\mathrm{kA}$ for $7\,\mathrm{TeV}$ operation. More troubling was its degraded performance at $4.5\,\mathrm{K}$, reaching just $13.9\,\mathrm{kA}$ at $100\,\mathrm{A/s}$ ramp rate and demonstrating significant ramp rate sensitivity. MQXFBP2 performed marginally better at $15.9\,\mathrm{kA}$ but similarly failed to meet the critical target of nominal current plus $300\,\mathrm{A}$ margin ($16.53\,\mathrm{kA}$) [28].

The breakdown in understanding these failures came through advanced metallographic examination [166], which combined high-energy linac X-ray CT scanning with detailed metallographic analysis. Their investigation revealed transverse cracks in Nb_3Sn filaments concentrated near titanium pole-to-pole transitions where stress concentrations were highest. In MQXFBP1, damaged strands with broken filaments appeared consistently at the inner layer pole turn cable facing the titanium pole, creating distinct crack fields spanning approximately $90\,\mathrm{mm}$ along the magnet length, precisely correlating with quench initiation sites. The systematic analysis of quench origins revealed patterns directly linked to mechanical stress: early prototypes showed quenches initiating in high-field regions of the straight section where electromagnetic forces were maximum, while improved magnets shifted quench locations to coil heads where residual stress concentrations proved less critical to performance.

The $7.2\,\mathrm{m}$ MQXFB magnets presented additional challenges. Systematic "humps" emerged after reaction heat treatment, with vertical displacements up to $1.5\,\mathrm{mm}$ toward the longitudinal center [92]. Post-impregnation "bellies" showed larger azimuthal dimensions in the coil's central region. Pressure-sensitive films revealed extreme stress concentrations at pole-to-pole transitions, with torque requirements for fixture closure nearly doubling at the coil's midpoint compared to the ends. These deformations traced to volume changes during Nb_3Sn formation, creating stored energy in the coil due to friction with the reaction fixture. The quality of resin impregnation emerged as a critical factor, complete epoxy infiltration proved essential for mechanical stability, though the process presented challenges in long magnets where pressure drops during resin flow could create voids in central regions. Thermal cycling behavior revealed additional degradation mechanisms, with early magnets showing cumulative performance degradation after multiple thermal cycles while improved designs maintained stable performance. The correlation between impregnation uniformity, thermal cycling tolerance, and training behavior demonstrated the interconnected nature of mechanical and electromagnetic performance in these systems.

A systematic three-stage improvement program emerged from this comprehensive failure analysis:

Stage 1: Mechanical decoupling between the outer stainless-steel shell and magnet structure, implemented in MQXFBP3.

Stage 2: Addressing coil overstress during bladder operations through innovative auxiliary bladder placement in the iron yoke cooling holes. This modified procedure shifted from quadrant-by-quadrant to simultaneous full-bladder pressurization, reducing peak stress from $140\,\mathrm{MPa}$ to $74\,\mathrm{MPa}$ and maintaining values below the newly established $100\,\mathrm{MPa}$ limit [51]. The stress limit evolution reflected growing understanding of Nb_3Sn degradation mechanisms, from initial values of $150 - 200\,\mathrm{MPa}$ based on conservative estimates to the more stringent $100\,\mathrm{MPa}$ threshold established through systematic metallographic analysis, which is an outcome of this thesis work.

Stage 3: Critical modifications to coil fabrication processes, including increased pole gaps (from $2.0\,\mathrm{mm/m}$ to $2.5\,\mathrm{mm/m}$), removal of ceramic binder from the outer layer (which carbonized during heat treatment), and modified fixtures allowing longitudinal coil movement during reaction [92].

MQXFB02, implementing stages 1 and 2, met HL-LHC requirements at $1.9\,\mathrm{K}$ but remained limited at $4.5\,\mathrm{K}$. MQXFB03, incorporating all three improvement stages, achieved the target current of $16.53\,\mathrm{kA}$ at $1.9\,\mathrm{K}$ after eight training quenches and demonstrated no performance limitation at $4.5\,\mathrm{K}$, sustaining target currents at $100\,\mathrm{A/s}$ without quenching. The shift in quench locations from straight sections to coil heads signaled the successful mitigation of stress-related issues. MQXFB04 further validated these improvements, reaching target current after just three training quenches, a dramatic reduction from early prototypes that required extensive training and often detraining [28]. The training behavior correlation with mechanical stress management provides empirical evidence for the importance of precise stress control in Nb_3Sn magnet performance.

Contemporary research has provided crucial context for these mechanical limits. Mangiarotti et al. systematically evaluated MQXFS7 across azimuthal pre-load stresses from $90 - 190\,\mathrm{MPa}$, demonstrating that RRP Nb_3Sn conductors maintain performance up to $84 - 85\%$ of their short sample limit up to $190\,\mathrm{MPa}$ [56]. Höll et al.'s thermal contraction measurements revealed anisotropic behavior (-2.9×10^{-3} longitudinal, -2.32 to -2.87×10^{-3} azimuthal, -1.55 to -1.75×10^{-3} radial) that fundamentally influences stress development during cooldown [181].

As of early 2025, the MQXFB program approaches series production readiness. Six full-length magnets have undergone testing, with MQXFB05 ready for evaluation and MQXFB06-07 in final assembly stages. Two-thirds of required coils have been completed with a production rate approaching one coil per month. Of the 10 MQXFB series magnets required for HL-LHC (8 operational plus 2 spares), substantial progress toward completion has been achieved[28].

The MQXF development exemplifies the complex interplay between fundamental materials science and practical engineering. The program's progression from partial failures to complete success illuminates the critical nature of mechanical stress management in Nb_3Sn superconductors. The decision to prioritize RRR over maximum critical current density through reduced heat treatment duration, the systematic refinement of assembly procedures to minimize stress concentrations, and the evolution of training behavior all demonstrate the multidimensional optimization required for practical high-field magnet implementation. Knowledge gained through systematic metallographic analysis, innovative assembly procedures, and iterative design improvements has not only enabled HL-LHC upgrade but established new paradigms for high-field magnet technology, demonstrating how material limitations drive engineering innovation in superconducting accelerator applications.

A.5 Kernel Density Estimation for Quench Current Analysis

The kernel density estimation method employed for analyzing quench current distributions provides a non-parametric approach to estimate the probability density function from discrete measurements. At each applied field for n quench currents $\{I_1, I_2, ..., I_n\}$, the probability density function is estimated as:

$$\hat{f}(I) = \frac{1}{nh} \sum_{i=1}^{n} K\left(\frac{I - I_i}{h}\right) \tag{A.1}$$

where:

- $\hat{f}(I)$ is the estimated probability density at current I in kA^{-1}
- I is the current value in kA at which the probability density is being evaluated
- n is the number of recorded quench events at the applied field
- h is the bandwidth parameter calculated using Scott's rule: $h = 1.06\sigma n^{-1/5}$
- σ is the standard deviation of the quench current dataset $\{I_1, I_2, ..., I_n\}$
- $K(u)$ is the Gaussian kernel function where $K(u) = (2\pi)^{-1/2} \exp(-u^2/2)$
- $u = \frac{I - I_i}{h}$ is the standardized distance between evaluation point and data point
- I_i are the individual measured quench currents in kA

This method smooths the discrete quench current measurements into a continuous probability distribution, enabling identification of the stable operating regime through percentile analysis while accounting for the natural variability in training behavior.

A.6 Damage distribution comparisons

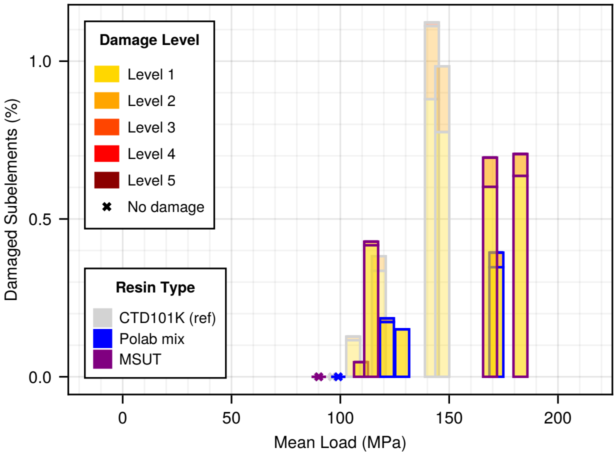

Figure A.4: Damage distribution across resin systems as a function of mechanical load. Comparison of three resin formulations (CTD-101K®, Polab mix, and MSUT) demonstrates varying damage susceptibility, with critical damage onset occurring above 150 MPa.

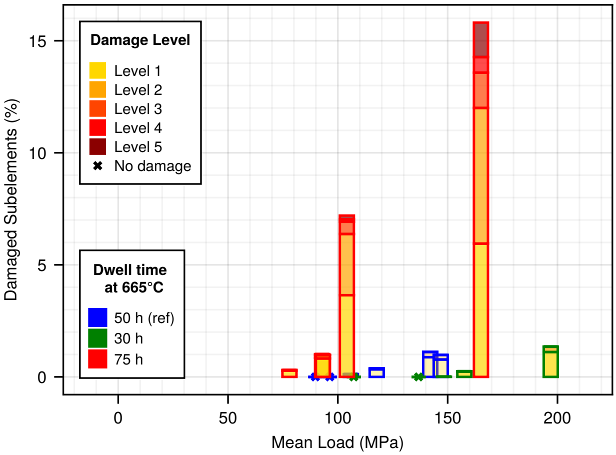

Figure A.5: Effect of thermal dwell time on damage accumulation at 665°C processing conditions. Extended dwell duration (75 h) significantly accelerates damage initiation compared to shorter treatments (30-50 h), demonstrating dwell time as a critical processing parameter.

List of Figures

List of Tables

List of Tools

This thesis employed various software tools for data acquisition, analysis, and document preparation. The following list details the primary software applications and their specific applications in this research:

Software	Purpose
Julia[182]	Data analysis and statistical plotting
LabVIEW[183]	Data acquisition and experimental control
COMSOL Multiphysics[184]	Finite element analysis
Zeiss SmartSEM[185]	SEM control and imaging
Olympus Stream[186]	Optical microscopy and analysis
Keyence VHX[187]	Digital microscopy and measurement
FPD-8010E Software[163]	Pressure distribution analysis
Claude (Anthropic)[188]	AI assistance
Inkscape[189]	Vector graphics and technical drawings
LaTeX[190]	Document preparation and typesetting

Bibliography

[1] Martin N Wilson. Superconducting magnets. 1983.

[2] Michael Tinkham. *Introduction to Superconductivity*. McGraw-Hill, New York, 2nd edition, 1996.

[3] JW Ekin. Strain effects in superconducting compounds. In *Advances in Cryogenic Engineering Materials: Volume 30*, pages 823–836. Springer, 1984.

[4] Arno Godeke. A review of the properties of Nb_3Sn and their variation with a15 composition, morphology and strain state. *Superconductor Science and Technology*, 19(8):R68, 2006.

[5] A Godeke, F Hellman, HHJ Ten Kate, and MGT Mentink. Fundamental origin of the large impact of strain on superconducting Nb_3Sn. *Superconductor Science and Technology*, 31(10):105011, 2018.

[6] Nobuya Banno. Low-temperature superconductors: Nb_3Sn, Nb_3Al, and NbTi. *Superconductivity*, 6:100047, 2023.

[7] CB Müller and EJ Saur. Influence of mechanical constraints on the superconducting transition of Nb_3Sn-coated niobium wires and ribbons. In *Advances in Cryogenic Engineering: Proceedings of the 1962 Cryogenic Engineering Conference University of California Los Angeles, California August 14–16, 1962*, pages 574–578. Springer, 1963.

[8] Gianluca De Marzi and Luigi Muzzi. Nb-based superconductors. In *Handbook of Superconductivity*, pages 132–165. CRC Press, 2022.

[9] A Godeke, Matthew C Jewell, Chad M Fischer, Alexander A Squitieri, Peter J Lee, and David C Larbalestier. The upper critical field of filamentary Nb_3Sn conductors. *Journal of applied physics*, 97(9), 2005.

[10] A Godeke, B Ten Haken, HHJ Ten Kate, and DC Larbalestier. A general scaling relation for the critical current density in Nb_3Sn. *Superconductor science and technology*, 19(10):R100, 2006.

[11] B Bordini, P Alknes, L Bottura, L Rossi, and D Valentinis. An exponential scaling law for the strain dependence of the Nb_3Sn critical current density. *Superconductor Science and Technology*, 26(7):075014, 2013.

[12] JW Ekin. Unified scaling law for flux pinning in practical superconductors: I. Separability postulate, raw scaling data and parameterization at moderate strains. *Superconductor Science and Technology*, 23(8):083001, 2010.

[13] Jack W Ekin, Najib Cheggour, Loren Goodrich, Jolene Splett, Bernardo Bordini, and David Richter. Unified scaling law for flux pinning in practical superconductors: II. parameter testing, scaling constants, and the extrapolative scaling expression. *Superconductor Science and Technology*, 29(12):123002, 2016.

[14] Jack W Ekin, Najib Cheggour, Loren Goodrich, and Jolene Splett. Unified scaling law for flux pinning in practical superconductors: III. minimum datasets, core parameters, and application of the extrapolative scaling expression. *Superconductor Science and Technology*, 30(3):033005, 2017.

[15] G Rupp. Parameters affecting prestrain and B_{c2} in multifilamentary Nb_3Sn conductors. In *Advances in Cryogenic Engineering Materials: Volume 26*, pages 522–529. Springer, 1980.

[16] B Ten Haken, A Godeke, and HHJ Ten Kate. The strain dependence of the critical properties of Nb_3Sn conductors. *Journal of applied physics*, 85(6):3247–3253, 1999.

[17] Matthew C Jewell, Peter J Lee, and David C Larbalestier. The influence of Nb_3Sn strand geometry on filament breakage under bend strain as revealed by metallography. *Superconductor Science and Technology*, 16(9):1005, 2003.

[18] Arend Nijhuis, Y Miyoshi, MC Jewell, Wouter Abbas, and Wilhelm AJ Wessel. Systematic study on filament fracture distribution in ITER Nb_3Sn strands. *IEEE transactions on applied superconductivity*, 19(3):2628–2632, 2009.

[19] Yuhu Zhai, Ciro Calzolaio, and Carmine Senatore. Understanding irreversible degradation of Nb_3Sn wires with fundamental fracture mechanics. 2014.

[20] Y Miyoshi, EPA Van Lanen, Marc MJ Dhalle, and Arend Nijhuis. Distinct voltage–current characteristics of Nb_3Sn strands with dispersed and collective crack distributions. *Superconductor Science and Technology*, 22(8):085009, 2009.

[21] Loren F Goodrich, Najib Cheggour, XF Lu, Jolene D Splett, Theodore C Stauffer, and Bernard J Filla. Method for determining the irreversible strain limit of Nb_3Sn wires. *Superconductor Science and Technology*, 24(7):075022, 2011.

[22] C Scheuerlein, M Di Michiel, F Buta, B Seeber, C Senatore, R Flükiger, T Siegrist, Tiglet Besara, J Kadar, B Bordini, et al. Stress distribution and lattice distortions in Nb_3Sn multifilament wires under uniaxial tensile loading at 4.2 k. *Superconductor Science and Technology*, 27(4):044021, 2014.

[23] Y Iwasa. Mechanical disturbances in superconducting magnets—a review. *IEEE Transactions on Magnetics*, 28(1):113–120, 1992.

[24] Luca Bottura, Gijs De Rijk, Lucio Rossi, and Ezio Todesco. Advanced accelerator magnets for upgrading the LHC. *IEEE Transactions on Applied Superconductivity*, 22(3):4002008–4002008, 2012.

[25] Ezio Todesco, H Bajas, M Bajko, A Ballarino, S Izquierdo Bermudez, B Bordini, L Bottura, G De Rijk, A Devred, D Duarte Ramos, et al. The high luminosity LHC interaction region magnets towards series production. *Superconductor Science and Technology*, 34(5):053001, 2021.

[26] P Ferracin. LARP Nb_3Sn quadrupole magnets for the LHC luminosity upgrade. In *AIP Conference Proceedings*, volume 1218, pages 1291–1300. American Institute of Physics, 2010.

[27] Paolo Ferracin, Giorgio Ambrosio, Michael Anerella, Hugues Bajas, Marta Bajko, Bernardo Bordini, Rodger Bossert, Nicolas Bourcey, Daniel W Cheng, Guram Chlachidze, et al. The HL-LHC low-β quadrupole magnet MQXF: From short models to long prototypes. *IEEE Transactions on applied superconductivity*, 29(5):1–9, 2019.

[28] Susana Izquierdo Bermudez, Giorgio Ambrosio, Jerome Axensalva, Amalia Ballarino, Lucie Baudin, Christian Barth, Nicolas Bourcey, Thierry Boutboul, Delio Duarte Ramos, Arnaud Devred, et al. Status and challenges in the MQXFB Nb_3Sn quadrupoles for the HL-LHC. *IEEE Transactions on Applied Superconductivity*, 2025.

[29] E Todesco and P Ferracin. Limits to high field magnets for particle accelerators. *IEEE transactions on applied superconductivity*, 22(3):4003106–4003106, 2012.

[30] F Bordry, L Bottura, A Milanese, D Tommasini, E Jensen, Ph Lebrun, L Tavian, JP Burnet, M Cerqueira Bastos, V Baglin, et al. Accelerator engineering and technology: Accelerator technology. In *Particle Physics Reference Library: Volume 3: Accelerators and Colliders*, pages 337–517. Springer, 2020.

[31] L Bottura. High field accelerator magnets for next generation colliders—motivation, goals, challenges and R&D drivers. In *THE HIGH LUMINOSITY LARGE HADRON COLLIDER: New Machine for Illuminating the Mysteries of the Universe*, pages 615–641. World Scientific, 2024.

[32] Ezio Todesco. Status and perspectives of high field magnets for particle accelerators. *IEEE Transactions on Applied Superconductivity*, 2025.

[33] Lucio Rossi and Luca Bottura. Superconducting magnets for particle accelerators. *Reviews of accelerator science and technology*, 5:51–89, 2012.

[34] E Todesco. Magnetic design of superconducting magnets. Technical report, CERN, 2014.

[35] A Devred, J-M Jimenez, H Prin, I Aviles Santillana, R Principe, J Fernandez, F Savary, P Rogacki, S Russenschuck, D Larbalestier, et al. submitter: Status and challenges of Nb_3Sn accelerator magnets at CERN: Lessons learned from ITER to HL-LHC. *CERN Monographs*, 2025.

[36] Amalia Ballarino and Luca Bottura. Targets for R&D on Nb_3Sn conductor for high energy physics. *IEEE Transactions on applied superconductivity*, 25(3):1–6, 2015.

[37] Michael B Field, Youzhu Zhang, Hanping Miao, Michael Gerace, and Jeffery A Parrell. Optimizing Nb_3Sn conductors for high field applications. *IEEE transactions on applied superconductivity*, 24(3):1–5, 2013.

[38] Luca Bottura and Arno Godeke. Superconducting materials and conductors: fabrication and limiting parameters. *Reviews of accelerator science and technology*, 5:25–50, 2012.

[39] P Ferracin, G Ambrosio, M Anerella, F Borgnolutti, R Bossert, D Cheng, DR Dietderich, H Felice, A Ghosh, A Godeke, et al. Magnet design of the 150 mm aperture low-β quadrupoles for the high luminosity LHC. *IEEE Transactions on Applied Superconductivity*, 24(3):1–6, 2013.

[40] O Aberle, C Adorisio, A Adraktas, M Ady, J Albertone, L Alberty, M Alcaide Leon, A Alekou, D Alesini, B Almeida Ferreira, et al. High-luminosity large hadron collider (HL-LHC): Technical design report. 2020.

[41] Fernando Toral. Mechanical design of superconducting accelerator magnets. Technical report, CERN, 2015.

[42] Paolo Ferracin, Scott E Bartlett, Shlomo Caspi, Daniel R Dietderich, Steve A Gourlay, Charles R Hannaford, Aurelio R Hafalia, Alan F Lietzke, Sara Mattafirri, Alfred D McInturff, et al. Development of a large aperture Nb_3Sn racetrack quadrupole magnet. *IEEE transactions on applied superconductivity*, 15(2):1132–1135, 2005.

[43] Patricia Borges de Sousa, Kirtana Puthran, Marta Sabaté-Gilarte, Francesco Cerutti, Susana Izquierdo Bermudez, Ezio Todesco, and Rob van Weelderen. Numerical assessment of

the inhomogeneous temperature field and the quality of heat extraction of Nb_3Sn impregnated magnets for the high luminosity upgrade of the LHC. *IEEE Transactions on Applied Superconductivity*, 33(5):1–5, 2023.

[44] Paolo Fessia, Federico Regis, and Ezio Todesco. Parametric analysis of forces and stresses in superconducting quadrupole sector windings. *IEEE transactions on applied superconductivity*, 17(2):1269–1272, 2007.

[45] S Prestemon, S Gourlay, P Ferracin, and E Todesco. Electro-magnetic forces and stresses in superconducting accelerator magnets. *USPAS, Michigan State University*, 2018.

[46] AV Tollestrup. Care and training of superconducting magnets. *IEEE Transactions on magnetics*, 17:863–872, 1981.

[47] Giorgio Vallone, Giorgio Ambrosio, Nicolas Bourcey, E Anderssen, Daniel W Cheng, Paolo Ferracin, Philippe Grosclaude, Michael Guinchard, Susana Izquierdo Bermudez, Mariusz Juchno, et al. Mechanical design analysis of MQXFB, the 7.2-m-long low-β quadrupole for the high-luminosity LHC upgrade. *IEEE Transactions on applied superconductivity*, 28(3):1–5, 2017.

[48] Eelis Takala, L Bianchi, F Lackner, P Ferracin, S Izquierdo Bermudez, and D Pulikowski. On the mechanics of MQXFB—the low-beta quadrupole for the HL-LHC. *Superconductor Science and Technology*, 34(9):095002, 2021.

[49] P Ferracin, G Ambrosio, DW Cheng, J Ferradas Troitino, L Garcia Fajardo, S Izquierdo Bermudez, S Prestemon, KL Ray, MJ Solis, E Todesco, et al. Assembly and pre-loading specifications for the series production of the Nb_3Sn MQXFA quadrupole magnets for the HL-LHC. *IEEE Transactions on Applied Superconductivity*, 32(6):1–6, 2022.

[50] R Ortwein, JC Perez, and D Pszenny. Loss of pre-stress in impregnated superconducting magnets, experimental results and numerical analysis. *Cryogenics*, 141:103893, 2024.

[51] J Ferradas Troitino, G Ambrosio, N Bourcey, D Cheng, A Devred, H Felice, P Ferracin, M Guinchard, S Izquierdo Bermudez, K Kandemir, et al. Optimizing the use of pressurized bladders for the assembly of HL-LHC MQXFB magnets. *Superconductor Science and Technology*, 36(6):065002, 2023.

[52] MJ Lamm, J Carson, S Gourlay, R Hanft, K Koepke, P Mantsch, AD Mclnturff, A Riddiford, and J Strait. Tests of high gradient superconducting quadrupole magnets for the tevatron. In *Advances in Cryogenic Engineering: Part A & B*, pages 609–616. Springer, 1989.

[53] Susana Izquierdo Bermudez, Giorgio Ambrosio, Giorgio Apollinari, Marta Bajko, Bernardo Bordini, Nicolas Bourcey, Delio Duarte Ramos, Paolo Ferracin, Lucio Fiscarelli, Sandor

Feher, et al. Progress in the development of the Nb_3Sn MQXFB quadrupole for the hilumi upgrade of the lhc. *IEEE Transactions on Applied Superconductivity*, 31(5):1–7, 2021.

[54] Michael Benedikt, Volker Mertens, Francesco Cerutti, Werner Riegler, Thomas Otto, Davide Tommasini, Laurent Jean Tavian, Johannes Gutleber, Frank Zimmermann, Michelangelo Mangano, et al. FCC-hh: The hadron collider: future circular collider conceptual design report volume 3. *Eur. Phys. J. Spec. Top.*, 228(CERN-ACC-2018-0058):755–1107, 2018.

[55] Giorgio Vallone, Eric Anderssen, Bernardo Bordini, Paolo Ferracin, J Ferradas Troitino, and Soren Prestemon. A methodology to compute the critical current limit in Nb_3Sn magnets. *Superconductor Science and Technology*, 34(2):025002, 2020.

[56] FJ Mangiarotti, S Izquierdo Bermudez, A Devred, R Diaz Vez, J Ferradas Troitino, S Ferradas Troitino, J Feuvrier, M Guinchard, A Haziot, A Milanese, et al. Performance of a HL-LHC Nb_3Sn quadrupole magnet in the 100-200 MPa range of azimuthal stress. *IEEE Transactions on Applied Superconductivity*, 2024.

[57] VI Dotsenko and IF Kislyak. Effect of epoxy debonding and cracking on stability of superconducting composites. *Cryogenics*, 31(10):906–912, 1991.

[58] JW Ekin. Effect of transverse compressive stress on the critical current and upper critical field of Nb_3Sn. *Journal of Applied Physics*, 62(12):4829–4834, 1987.

[59] Susana Izquierdo Bermudez, Giorgio Ambrosio, Bernardo Bordini, Nicolas Bourcey, Arnaud Devred, Paolo Ferracin, Jose Ferradas Troitino, Salvador Ferradas Troitino, Lucio Fiscarelli, Jerome Fleiter, et al. Performance of a MQXF Nb_3Sn quadrupole magnet under different stress level. *IEEE Transactions on Applied Superconductivity*, 32(6):1–6, 2022.

[60] D Larbalestier, P Madsen, J Lee, M Wilson, and J Charlesworth. Multifilamentary niobium tin magnet conductors. *IEEE Transactions on Magnetics*, 11(2):247–250, 1975.

[61] Ian Pong. Processing of low T_C conductors: The compound Nb_3Sn. In *Handbook of Superconductivity*, pages 213–275. CRC Press, 2022.

[62] Michael Field, Robert Hentges, Jeff Parrell, Youzhu Zhang, and Seungok Hong. Progress with Nb_3Sn conductors at oxford instruments, superconducting technology. *IEEE transactions on applied superconductivity*, 11(1):3692–3695, 2001.

[63] B Bordini, L Bottura, L Oberli, L Rossi, and E Takala. Impact of the residual resistivity ratio on the stability of Nb_3Sn magnets. *IEEE transactions on applied superconductivity*, 22(3):4705804–4705804, 2011.

[64] R Schwall, G Ozeryansky, D Hazelton, S Cogan, and R Rose. Properties and performance of high current density Sn-core process MF Nb_3Sn. *IEEE Transactions on Magnetics*, 19(3):1135–1138, 1983.

[65] Emanuela Barzi, Eric Gregory, and Tae Pyon. Heat treatment optimization of internal tin Nb_3Sn strands. *IEEE transactions on applied superconductivity*, 11(1):3573–3576, 2001.

[66] M Durante, P Bredy, A Devred, R Otmani, M Reytier, T Schild, and F Trillaud. Development of a Nb_3Sn multifilamentary wire for accelerator magnet applications. *Physica C: Superconductivity*, 354(1-4):449–453, 2001.

[67] Taeyoung Pyon and Hem Kanithi. Development of Nb_3Sn conductors for fusion and high energy physics. *IEEE transactions on applied superconductivity*, 13(2):3474–3477, 2003.

[68] Irina Deryagina, Elena Popova, and Evgeny Patrakov. Effect of diameter of Nb_3Sn-based internal-tin wires on the structure of superconducting layers. *IEEE Transactions on Applied Superconductivity*, 32(4):1–5, 2022.

[69] Thierry Boutboul, Luc Oberli, Andries den Ouden, Danilo Pedrini, Bernd Seeber, and Giovanni Volpini. Heat treatment optimization studies on PIT Nb_3Sn strand for the NED project. *IEEE transactions on applied superconductivity*, 19(3):2564–2567, 2009.

[70] Peter J Lee and David C Larbalestier. Compositional and microstructural profiles across Nb_3Sn filaments produced by different fabrication methods. *IEEE transactions on applied superconductivity*, 11(1):3671–3674, 2001.

[71] Jeffrey A Parrell, Youzhu Zhang, Michael B Field, Paul Cisek, and Seung Hong. High field Nb_3Sn conductor development at oxford superconducting technology. *IEEE transactions on applied superconductivity*, 13(2):3470–3473, 2003.

[72] B Jakob and G Pasztor. Effect of transverse compressive stress on the critical current of cabled Nb_3Sn conductor. *IEEE transactions on magnetics*, 25(2):2379–2381, 1989.

[73] E Barzi, T Wokas, and AV Zlobin. Sensitivity of Nb_3Sn rutherford-type cables to transverse pressure. *IEEE transactions on applied superconductivity*, 15(2):1541–1544, 2005.

[74] L Gämperle, Jose Ferradas, Christian Barth, Bernardo Bordini, Davide Tommasini, and Carmine Senatore. Determination of the electromechanical limits of high-performance Nb_3Sn rutherford cables under transverse stress from a single-wire experiment. *Physical Review Research*, 2(1):013211, 2020.

[75] P Gao, M Dhallé, B Bordini, A Ballarino, and HHJ Ten Kate. Transverse-pressure susceptibility of high-J_c RRP and PIT types of Nb_3Sn rutherford cables for accelerator magnets. *Superconductor Science and Technology*, 33(12):125005, 2020.

[76] P Ebermann, T Baumgartner, J Behnsen, M Daly, A Gallifa Terricabras, T Koettig, F Lackner, C Scheuerlein, and M Eisterer. Influence of transverse stress exerted at room temperature on the superconducting properties of Nb_3Sn wires. *Superconductor Science and Technology*, 32(9):095010, 2019.

[77] Tommaso Bagni, Diego Mauro, Marta Majkut, Alexander Rack, and Carmine Senatore. Formation and propagation of cracks in RRP Nb_3Sn wires studied by deep learning applied to x-ray tomography. *Superconductor Science and Technology*, 35(10):104003, 2022.

[78] Emanuela Barzi, Rodger Bossert, Shlomo Caspi, Daniel R Dietderich, Paolo Ferracin, Arup Ghosh, and Daniele Turrioni. RRP Nb_3Sn strand studies for LARP. *IEEE transactions on applied superconductivity*, 17(2):2607–2610, 2007.

[79] LD Cooley, AK Ghosh, DR Dietderich, and I Pong. Conductor specification and validation for high-luminosity LHC quadrupole magnets. *IEEE Transactions on Applied Superconductivity*, 27(4):1–5, 2017.

[80] SC Hopkins, B Medina-Clavijo, C Barth, J Fleiter, and A Ballarino. Design optimization, cabling and stability of large-diameter high J_c Nb_3Sn wires. *IEEE Transactions on Applied Superconductivity*, 33(5):1–9, 2023.

[81] Chiara Tarantini, Fumitake Kametani, Shreyas Balachandran, Steve M Heald, Laura Wheatley, Chris RM Grovenor, Michael P Moody, Yi-Feng Su, Peter J Lee, and David C Larbalestier. Origin of the enhanced Nb_3Sn performance by combined Hf and Ta doping. *Scientific reports*, 11(1):17845, 2021.

[82] Najib Cheggour, Loren F Goodrich, Theodore C Stauffer, Jolene D Splett, XF Lu, AK Ghosh, and G Ambrosio. Influence of Ti and Ta doping on the irreversible strain limit of ternary Nb_3Sn superconducting wires made by the restacked-rod process. *Superconductor Science and Technology*, 23(5):052002, 2010.

[83] Felix Wolf, Patrick Ebermann, Friedrich Lackner, Dennis Mosbach, Christian Scheuerlein, Katja Schladitz, and Daniel Schoerling. Characterization of the stress distribution on Nb_3Sn rutherford cables under transverse compression. *IEEE Transactions on Applied Superconductivity*, 28(3):1–6, 2017.

[84] Felix Wolf, Christian Scheuerlein, Marcus Lorentzon, Balduin Katzer, Michael Hofmann, Weimin Gan, Friedrich Lackner, Daniel Schoerling, Davide Tommasini, Frederic Savary, et al. Effect of applied compressive stress and impregnation material on internal strain and stress state in Nb_3Sn rutherford cable stacks. *IEEE Transactions on Applied Superconductivity*, 29(5):1–5, 2019.

[85] MN Wilson. Rate dependent magnetization in flat twisted superconducting cables. Technical report, 1972.

[86] Osami Tsukamoto and Y Iwasa. Mechanical disturbances in rutherford-type and braid conductors. *IEEE Transactions on Magnetics*, 19(3):443–445, 1983.

[87] Maximilien Brice. The first cable for the HL-LHC produced at CERN. 2016. General Photo.

[88] Jerome Fleiter, Amalia Ballarino, Angelo Bonasia, Bernardo Bordini, and David Richter. Optimization of Nb_3Sn rutherford cables geometry for the high-luminosity LHC. *IEEE Transactions on Applied Superconductivity*, 27(4):1–5, 2017.

[89] Maximilien Brice. Superconducting Nb_3Sn cable. 2020. General Photo.

[90] Tommaso Bagni, C Calzolaio, G Bovone, J Ferradas-Troitino, C Barth, A Ballarino, and C Senatore. Investigating the effect of rolling deformation on the electro-mechanical limits of Nb_3Sn wires produced by RRP® and PIT technologies. *Superconductor Science and Technology*, 37(9):095013, 2024.

[91] AV Zlobin, G Ambrosio, N Andreev, E Barzi, B Bordini, R Bossert, R Carcagno, DR Chichili, J DiMarco, L Elementi, et al. R&D of Nb_3Sn accelerator magnets at fermilab. *IEEE transactions on applied superconductivity*, 15(2):1113–1118, 2005.

[92] Nicholas Lusa, Arnaud Devred, José Ferradas Troitino, Susana Izquierdo Bermudez, Attilio Milanese, Penelope Matilde Quassolo, Simon Straarup, and Ezio Todesco. Towards MQXFB series coils. *IEEE Transactions on Applied Superconductivity*, 34(5):1–8, 2024.

[93] Arnaud Devred. Insulation systems for Nb_3Sn accelerator magnet coils manufactured by the wind & react technique. *IEEE transactions on applied superconductivity*, 12(1):1232–1237, 2002.

[94] Sree Shankhachur Roy, Prasad Potluri, Simon Canfer, and George Ellwood. Braiding ultrathin layer for insulation of superconducting rutherford cables. *Journal of Industrial Textiles*, 48(5):827–847, 2018.

[95] Jerome Axensalva, Friedrich Lackner, and Remy Gauthier. Vacuum pressure impregnation setup at CERN for Nb_3Sn coils. *IEEE Transactions on Applied Superconductivity*, 30(4):1–4, 2020.

[96] Friedrich Lackner, Paolo Ferracin, Ezio Todesco, Stephan Triquet, Marc Pozzobon, S Luzieux, Juan Carlos Perez, Christian Scheuerlein, Eugenio Cavanna, Timm Ohnweiler, et al. Status of the long mqxfb Nb_3Sn coil prototype production for the HiLumi LHC. *IEEE Transactions on Applied Superconductivity*, 27(4):1–5, 2017.

[97] DR Dietderich, JR Litty, and RM Scanlan. Dimensional changes of Nb_3Sn, Nb_3Al and $Bi_2Sr_2CaCu_2O_8$ conductors during heat treatment and their implication for coil design. *Advances in Cryogenic Engineering Materials*, pages 1013–1020, 1998.

[98] N Andreev, E Barzi, DR Chichili, S Mattafirri, and AV Zlobin. Volume expansion of Nb-Sn strands and cables during heat treatment. In *AIP Conference Proceedings*, volume 614, pages 941–948. American Institute of Physics, 2002.

[99] D Bocian, G Ambrosio, and GM Whitson. Measurements of Nb_3Sn conductor dimension changes during heat treatment. In *AIP Conference Proceedings*, volume 1435, pages 193–200. American Institute of Physics, 2012.

[100] E Rochepault, P Ferracin, G Ambrosio, M Anerella, A Ballarino, A Bonasia, B Bordini, D Cheng, DR Dietderich, H Felice, et al. Dimensional changes of Nb_3Sn rutherford cables during heat treatment. *IEEE Transactions on applied superconductivity*, 26(4):1–5, 2016.

[101] C Scheuerlein, F Lackner, F Savary, B Rehmer, M Finn, and C Meyer. Thermomechanical behavior of the HL-LHC 11 Tesla Nb_3Sn magnet coil constituents during reaction heat treatment. *IEEE Transactions on applied superconductivity*, 28(3):1–6, 2018.

[102] Matthias Michels, Friedrich Lackner, Christian Scheuerlein, Alejandro Carlon Zurita, Salvador Ferradas Troitino, Nicolas Bourcey, Frederic Savary, and Davide Tommasini. Length changes of unconfined Nb_3Sn rutherford cables during reaction heat treatment. *IEEE Transactions on applied superconductivity*, 29(5):1–5, 2019.

[103] Christian Scheuerlein, Jérôme Andrieux, Matthias Michels, Friedrich Lackner, Christian Meyer, Rodica Chiriac, François Toche, Matthias Hagner, and Marco Di Michiel. Effect of the fabrication route on the phase and volume changes during the reaction heat treatment of Nb_3Sn superconducting wires. *Superconductor Science and Technology*, 33(3):034004, 2020.

[104] Christian Scheuerlein, Marco Di Michiel, Gonzalo Arnau Izquierdo, and Florin Buta. Phase transformations during the reaction heat treatment of internal tin Nb_3Sn strands with high sn content. *IEEE transactions on applied superconductivity*, 18(4):1754–1760, 2008.

[105] Peter J Lee and David C Larbalestier. Microstructural factors important for the development of high critical current density Nb_3Sn strand. *Cryogenics*, 48(7-8):283–292, 2008.

[106] Charlie Sanabria, Michael Field, Peter J Lee, Hanping Miao, Jeff Parrell, and David C Larbalestier. Controlling Cu–Sn mixing so as to enable higher critical current densities in RRP® Nb_3Sn wires. *Superconductor Science and Technology*, 31(6):064001, 2018.

[107] Charlie Sanabria, Ian Pong, Luc Paul LaLonde, and Soren Prestemon. Further heat treatment optimizations for Nb_3Sn conductors: From wires to cables. *IEEE Transactions on Applied Superconductivity*, 29(5):1–4, 2019.

[108] Simon C Hopkins, Algirdas Baskys, Amalia Ballarino, Jonas Lachmann, and Andreas Leineweber. Phase evolution during heat treatment of Nb_3Sn wires under development for the FCC study. *IEEE Transactions on Applied Superconductivity*, 31(5):1–6, 2021.

[109] C Tarantini, PJ Lee, N Craig, A Ghosh, and DC Larbalestier. Examination of the trade-off between intrinsic and extrinsic properties in the optimization of a modern internal tin Nb_3Sn conductor. *Superconductor Science and Technology*, 27(6):065013, 2014.

[110] Arup K Ghosh, Edward A Sperry, Joseph D'Ambra, and Lance D Cooley. Systematic changes of the Nb-Sn reaction with time, temperature, and alloying in restacked-rod-process (RRP) Nb_3Sn strands. *IEEE Transactions on applied superconductivity*, 19(3):2580–2583, 2009.

[111] Michael T Naus, Peter J Lee, and David C Larbalestier. The interdiffusion of Cu and Sn in internal Sn Nb_3Sn superconductors. *IEEE transactions on applied superconductivity*, 10(1):983–987, 2002.

[112] Ian Pong, Luc-Rene Oberli, and Luca Bottura. Cu diffusion in Nb_3Sn internal tin superconductors during heat treatment. *Superconductor Science and Technology*, 26(10):105002, 2013.

[113] I Pong, SC Hopkins, X Fu, BA Glowacki, JA Elliott, and A Baldini. Microstructure development in Nb_3Sn (Ti) internal tin superconducting wire. *Journal of materials science*, 43(10):3522–3530, 2008.

[114] Najib Cheggour, Theodore C Stauffer, William Starch, Peter J Lee, Jolene D Splett, Loren F Goodrich, and Arup K Ghosh. Precipitous change of the irreversible strain limit with heat-treatment temperature in Nb_3Sn wires made by the restacked-rod process. *Scientific reports*, 8(1):13048, 2018.

[115] D Uglietti, V Abacherli, M Cantoni, and R Flukiger. Grain growth, morphology, and composition profiles in industrial Nb_3Sn wires. *IEEE transactions on applied superconductivity*, 17(2):2615–2618, 2007.

[116] David Broek. *Elementary Engineering Fracture Mechanics*. Martinus Nijhoff Publishers, Dordrecht, Netherlands, 4th edition, 1986.

[117] Daniel R Dietderich, Scott E Bartlett, Shlomo Caspi, Paolo Ferracin, Stephen A Gourlay, Hugh C Higley, Alan F Lietzke, Sara Mattafirri, Alfred D McInturff, GL Sabbi, et al.

Correlation between strand stability and magnet performance. *IEEE transactions on applied superconductivity*, 15(2):1524–1528, 2005.

[118] D Easton and D Kroeger. Kirkendall voids—a detriment to Nb_3Sn superconductors. *IEEE Transactions on Magnetics*, 15(1):178–181, 1979.

[119] Christian Barth, B Seeber, A Rack, C Calzolaio, Y Zhai, D Matera, and C Senatore. Quantitative correlation between the void morphology of niobium-tin wires and their irreversible critical current degradation upon mechanical loading. *Scientific reports*, 8(1):6589, 2018.

[120] C Scheuerlein, M Di Michiel, and A Haibel. On the formation of voids in internal tin Nb_3Sn superconductors. *Applied Physics Letters*, 90(13), 2007.

[121] Najib Cheggour, PJ Lee, LF Goodrich, ZH Sung, TC Stauffer, JD Splett, and Matthew C Jewell. Influence of the heat-treatment conditions, microchemistry, and microstructure on the irreversible strain limit of a selection of Ti-doped internal-tin Nb_3Sn ITER wires. *Superconductor Science and Technology*, 27(10):105004, 2014.

[122] Najib Cheggour, Theodore C Stauffer, William Starch, Loren F Goodrich, and Jolene D Splett. Implications of the strain irreversibility cliff on the fabrication of particle-accelerator magnets made of restacked-rod-process Nb_3Sn wires. *Scientific Reports*, 9(1):1–14, 2019.

[123] F Lackner, N Bourcey, P Ferracin, P Jozwiak, T Ohnweiler, P Revilak, F Savary, and S Triquet. Analysis of temperature uniformity during heat treatment of Nb_3Sn coils for the High-Luminosity LHC superconducting magnets. *IEEE Transactions on Applied Superconductivity*, 26(4):1–5, 2016.

[124] David Evans. Resins for superconducting magnet construction—an overview of requirements, processing and properties. In *IOP Conference Series: Materials Science and Engineering*, volume 756, page 012003. IOP Publishing, 2020.

[125] Shijian Yin, James Swanson, and Tengming Shen. Design of a high toughness epoxy for superconducting magnets and its key properties. *IEEE Transactions on Applied Superconductivity*, 30(4):1–5, 2020.

[126] Simon Otten, Anna Kario, WAJ Wessel, Jorick Leferink, Herman HJ Ten Kate, Michael Daly, Christoph Hug, Serguei Sidorov, André Brem, Bernhard Auchmann, et al. Training curves of Nb_3Sn rutherford cables with a wide range of impregnation materials measured in the BOX facility. *IEEE Transactions on Applied Superconductivity*, 33(5):1–5, 2023.

[127] Chris Reis, Tengming Shen, Soren Prestemon, Peter Hosemann, Mehul Nair, Tatsushi Nakamoto, and Toru Ogitsu. Investigating irradiated superconducting magnet insulation

materials for particle accelerators and other high-dose environments. *IEEE Transactions on Applied Superconductivity*, 33(5):1–7, 2023.

[128] Pascal B Studer, Alain Schwegler, and Theo A Tervoort. Tough epoxy resin systems for cryogenic applications. *Cryogenics*, 143:103923, 2024.

[129] André Brem, Barbara J Gold, Bernhard Auchmann, Davide Tommasini, and Theo A Tervoort. Elasticity, plasticity and fracture toughness at ambient and cryogenic temperatures of epoxy systems used for the impregnation of high-field superconducting magnets. *Cryogenics*, 115:103260, 2021.

[130] Anders Gaarud, Christian Scheuerlein, David Mate Parragh, Sébastien Clement, Jacob Bertsch, Cedric Urscheler, Roland Piccin, Federico Ravotti, Giuseppe Pezzullo, and Ralf Lach. Fracture toughness, radiation hardness, and processibility of polymers for superconducting magnets. *Polymers*, 16(9):1287, 2024.

[131] Emanuela Barzi, Claudio Franceschelli, Igor Novitski, Federico Sartori, and Alexander V Zlobin. Measurements and modeling of mechanical properties of nb 3 sn strands, cables, and coils. *IEEE Transactions on Applied Superconductivity*, 29(5):1–8, 2019.

[132] H Maeda and Y Iwasa. Heat generation from epoxy cracks and bond failures. *Cryogenics*, 22(9):473–476, 1982.

[133] Bharti Verma, Roland Piccin, Davide Tommasini, and Ignacio Avilles Santillana. Adhesion analysis of epoxy resin impregnation systems for Nb_3Sn superconducting magnets. In *IOP Conference Series: Materials Science and Engineering*, volume 1327, page 012208. IOP Publishing, 2025.

[134] JM Van Oort, RM Scanlan, HW Weijers, S Wessel, and Herman HJ ten Kate. The reduction of the critical current in Nb_3Sn cables under transverse loads. *IEEE transactions on applied superconductivity*, 3(1):559–562, 1993.

[135] Gilles Lenoir, Kirtana Puthran, Christian Barth, Jérôme Fleiter, and Amalia Ballarino. Effect of transverse compressive stress applied at room temperature on Nb_3Sn rutherford cables. *Superconductor Science and Technology*, 37(2):025013, 2024.

[136] Michael Daly, Bernhard Auchmann, André Brem, Christoph Hug, Serguei Sidorov, Simon Otten, Marc Dhallé, Zichuan Guo, Anna Kario, and Herman Ten Kate. Improved training in paraffin-wax impregnated Nb_3Sn rutherford cables demonstrated in BOX samples. *Superconductor science and technology*, 35(5):055014, 2022.

[137] H Bajas, G Ambrosio, M Anerella, M Bajko, R Bossert, S Caspi, A Chiuchiolo, G Chlachidze, D Dietderich, O Dunkel, et al. Cold test results of the LARP HQ

Nb_3Sn Quadrupole Magnet at 1.9 K. *IEEE Transactions on Applied Superconductivity*, 23(3):4002606–4002606, 2013.

[138] J Ferradas Troitino, T Bagni, C Barth, B Bordini, P Ferracin, L Gamperle, D Tommasini, D Zurmuehle, and C Senatore. Effects of the initial axial strain state on the response to transverse stress of high-performance RRP Nb_3Sn wires. *Superconductor Science and Technology*, 34(3):035008, 2021.

[139] C Senatore, T Bagni, J Ferradas-Troitino, B Bordini, and A Ballarino. Degradation of I_c due to residual stress in high-performance Nb_3Sn wires submitted to compressive transverse force. *Superconductor Science and Technology*, 36(7):075001, 2023.

[140] Jean-Eudes Duvauchelle, Bernardo Bordini, Jérôme Fleiter, and Amalia Ballarino. Critical current measurements under transverse pressure of a Nb_3Sn rutherford cable based on 1 mm RRP wires. *IEEE Transactions on Applied Superconductivity*, 28(4):1–5, 2018.

[141] Patrick Ebermann, Johannes Bernardi, Jerome Fleiter, Friedrich Lackner, Florian Meuter, Magdalena Pieler, Christian Scheuerlein, Daniel Schoerling, Felix Wolf, Amalia Ballarino, et al. Irreversible degradation of Nb_3Sn rutherford cables due to transverse compressive stress at room temperature. *Superconductor Science and Technology*, 31(6):065009, 2018.

[142] Patrick Ebermann. *Relevance of the irreversible degradation of superconducting Nb_3Sn wires and cables caused by transverse stress at room temperature within the FCC study at CERN*. PhD thesis, Technische Universität Wien, 2019.

[143] B Jakob, G Pasztor, M Bona, and A Asner. Reduced sensitivity of Nb_3Sn epoxy-impregnated cable to transverse stress. *Cryogenics*, 31(5):390–391, 1991.

[144] H Boschman, AP Verweij, S Wessel, H HJ ten Kate, and L JM van de Klundert. The effect of transverse loads up to 300 MPa on the critical currents of Nb_3Sn cables. *IEEE Transactions on Magnetics (Institute of Electrical and Electronics Engineers);(United States)*, 27(CONF-900944-), 1991.

[145] Herman HJ ten Kate, H Weijers, S Wessel, H Boschman, and LJM van de Klundert. The reduction of the critical current in Nb_3Sn cables under transverse forces. *IEEE transactions on magnetics*, 28(1):715–718, 1992.

[146] C Pasztor, A Anghel, B Jakob, and R Wesche. Transverse stress effects in Nb_3Sn cables. *IEEE transactions on magnetics*, 30(4):1938–1941, 1994.

[147] G Vallone, JF Croteau, E Anderssen, B Bordini, M D'Addazio, P Ferracin, and F Niccoli. Measurement and computation of Nb_3Sn rutherford cables strength under multi-axial loading conditions. *IEEE Transactions on Applied Superconductivity*, 34(5):1–5, 2023.

[148] Jean-Francois Croteau, Giorgio Vallone, Nandana Menon, Marika D'Addazio, Fabrizio Niccoli, Ian Pong, Paolo Ferracin, and Soren Prestemon. Crack identification and characterization in deformed Nb_3Sn rutherford cable stacks using machine learning. *IEEE Transactions on Applied Superconductivity*, 2024.

[149] B Bordini, P Alknes, A Ballarino, L Bottura, and L Oberli. Critical current measurements of high-J_c Nb_3Sn rutherford cables under transverse compression. *IEEE transactions on applied superconductivity*, 24(3):1–5, 2013.

[150] A Cattabiani, D Baffari, and B Bordini. A 3D finite element model of the reversible critical current reduction due to transverse load in Nb_3Sn wires. *IEEE Transactions on Applied Superconductivity*, 30(4):1–6, 2020.

[151] Gianluca De Marzi, Bernardo Bordini, and Dario Baffari. On the mechanisms governing the critical current reduction in Nb_3Sn rutherford cables under transverse stress. *Scientific Reports*, 11(1):7369, 2021.

[152] Loren F Goodrich and FR Fickett. Critical current measurements: a compendium of experimental results. *Cryogenics*, 22(5):225–241, 1982.

[153] H Wada, CR Walters, Loren F Goodrich, and K Tachikawa. VAMAS intercomparison of critical current measurements on Nb_3Sn superconductors: a summary report. *Cryogenics*, 34(11):899–908, 1994.

[154] Bernardo Bordini et al. Self-field correction in critical current measurements of superconducting wires tested on ITER VAMAS barrels. *CERN Internal Note*, 2010.

[155] AP Verweij, J Genest, A Knezovic, DF Leroy, J-P Marzolf, and LR Oberli. 1.9 K test facility for the reception of the superconducting cables for the LHC. *IEEE transactions on applied superconductivity*, 9(2):153–156, 1999.

[156] AP Verweij and AK Ghosh. Critical current measurements of the main LHC superconducting cables. *IEEE transactions on applied superconductivity*, 17(2):1454–1460, 2007.

[157] J Fleiter, B Bordini, A Ballarino, L Oberli, S Izquierdo, and L Bottura. Quench propagation in Nb_3Sn rutherford cables for the Hi-Lumi quadrupole magnets. *IEEE Transactions on applied superconductivity*, 25(3):1–4, 2014.

[158] G Ambrosio, S Bartlett, D Dietderich, L Elementi, K Ewald, A Nicolai, A Simmons, A Verweij, and O Vincent-Viry. Design of a sample holder for Nb_3Sn cable test at FRESCA. *Fermi National Accelerator Laboratory, Batavia, Il, USA, TD-04-022*, 2004.

[159] Jens Steckert, Reiner Denz, Surbhi Mundra, Tomasz Podzorny, Jelena Spasic, and Dragos-Gabriel Vancea. Application of the universal quench detection system to the protection of the high-luminosity LHC magnets at CERN. *IEEE Transactions on Applied Superconductivity*, 32(6):1–5, 2022.

[160] J Fleiter, A Bonasia, SC Hopkins, T Boutboul, and A Ballarino. Status of high-field rutherford cable production for the HL-LHC project. *IEEE Transactions on Applied Superconductivity*, 2025.

[161] P Gao, M Dhallé, and HHJ Ten Kate. Pressure-induced critical current reduction in impregnated Nb_3Sn rutherford cables for use in future accelerator magnets. In *IOP Conference Series: Materials Science and Engineering*, volume 756, page 012015. IOP Publishing, 2020.

[162] Fujifilm Corporation. Prescale - pressure measurement film, 2025.

[163] Fujifilm Corporation. Pressure distribution mapping system FPD-8010E, 2025.

[164] Y Zhai, L D'Hauthuille, C Barth, and C Senatore. Finite-element analysis of transverse compressive and thermal loads on Nb_3Sn wires with voids. *IEEE Transactions on Applied Superconductivity*, 26(4):1–5, 2016.

[165] Shreyas Balachandran, Jonathan Cooper, Orion B Van Oss, Peter J Lee, Luca Bottura, Arnaud Devred, Frederic Savary, Christian Scheuerlein, and Felix Wolf. Metallographic analysis of 11 T dipole coils for high luminosity-large hadron collider (HL-LHC). *Superconductor Science and Technology*, 34(2):025001, 2021.

[166] Alice Moros, Mickael Denis Crouvizier, Ignacio Aviles Santillana, Stefano Sgobba, Susana Izquierdo Bermudez, Nicholas Lusa, Jose Ferradas Troitino, Attilio Milanese, Ezio Todesco, Arnaud Devred, et al. A metallurgical inspection method to assess the damage in performance-limiting Nb_3Sn accelerator magnet coils. *IEEE Transactions on Applied Superconductivity*, 33(5):1–8, 2023.

[167] I Aviles Santillana, S Sgobba, MD Crouvizier, A Devred, G Arnau Izquierdo, B Bulat, A Moros, S Izquierdo Bermudez, A Milanese, F Savary, et al. Advanced examination of Nb_3Sn coils and conductors for the LHC luminosity upgrade: A methodology based on computed tomography and materialographic analyses. *Superconductor Science and Technology*, 37(8):085007, 2024.

[168] Struers. EpoxiCure 2, résine; 1,9 l - cold mounting compound, 2025.

[169] K. Puthran, C. Barth, A. Ballarino, A. Devred, and T. Arndt. Onset of mechanical degradation due to transverse compressive stress in Nb_3Sn Rutherford-type cables. *IEEE Transactions on Applied Superconductivity*, 33(5):1–6, 2023.

[170] Christian Scheuerlein, Friedrich Lackner, Frederic Savary, Birgit Rehmer, Monika Finn, and Patrick Uhlemann. Mechanical properties of the HL-LHC 11 T Nb_3Sn magnet constituent materials. *IEEE Transactions on Applied Superconductivity*, 27(4):1–7, 2016.

[171] Christopher Segal, Christian Barth, Iole Falorio, Alejandro Carlón Zurita, Amalia Ballarino, Xavier Chaud, Chiara Tarantini, Peter J Lee, and David C Larbalestier. Evidence of kramer extrapolation inaccuracy for predicting high field Nb_3Sn properties. In *Journal of Physics: Conference Series*, volume 1559, page 012062. IOP Publishing, 2020.

[172] Susana Izquierdo Bermudez, Giorgio Ambrosio, Giorgio Apollinari, Amalia Ballarino, Christian Barth, Mickael Denis Crouvizier, Delio Duarte Ramos, Arnaud Devred, Sandor Feher, Helene Felice, et al. Status of the MQXFB Nb_3Sn quadrupoles for the HL-LHC. *IEEE Transactions on Applied Superconductivity*, 33(5):1–9, 2023.

[173] M Hojo, T Matsuoka, M Hashimoto, M Tanaka, M Sugano, S Ochiai, and K Miyashita. Direct measurement of elastic modulus of Nb_3Sn using extracted filaments from superconducting composite wire and resin impregnation method. *Physica C: Superconductivity and its applications*, 445:814–818, 2006.

[174] Rui Zhang, Peifeng Gao, Xingzhe Wang, and Youhe Zhou. First-principles study on elastic and superconducting properties of Nb_3Sn and Nb_3Al under hydrostatic pressure. *AIP Advances*, 5(10), 2015.

[175] C Antoine, M Foley, and N Dhanaraj. Physical properties of niobium and specifications for fabrication of superconducting cavities. Technical report, Fermi National Accelerator Lab.(FNAL), Batavia, IL (United States), 2011.

[176] Reza Abbaschian, Lara Abbaschian, and Robert E. Reed-Hill. *Physical Metallurgy Principles*. Cengage Learning, Stamford, CT, 4 edition, 2009.

[177] Charlie Sanabria. Nb-Sn phase diagram. Wikimedia Commons, 2020. CC BY 4.0 license, `https://commons.wikimedia.org/wiki/File:Nb-Sn_phase_diagram.png`.

[178] JP Charlesworth, I Macphail, and PE Madsen. Experimental work on the niobium-tin constitution diagram and related studies. *Journal of Materials Science*, 5(7):580–603, 1970.

[179] Charlie Sanabria. Cu-Sn phase diagram. Wikimedia Commons, 2020. CC BY 4.0 license, `https://commons.wikimedia.org/wiki/File:Cu-Sn_phase_diagram.jpg`.

[180] Siegfried Fürtauer, Dajian Li, Damian Cupid, and Hans Flandorfer. The Cu–Sn phase diagram, part i: new experimental results. *Intermetallics*, 34:142–147, 2013.

[181] Stefan Holl, Michael Guinchard, Susana Izquierdo Bermudez, and Óscar Sacristán De Frutos. Study on the thermal contraction behavior of state-of-the-art Nb_3Sn superconducting magnet coils in the longitudinal, azimuthal, and radial direction. *IEEE Transactions on Applied Superconductivity*, 34(5):1–6, 2024.

[182] The Julia Programming Language,.

[183] National Instruments. Labview, 2024. Graphical programming environment for test and measurement.

[184] COMSOL Inc. Comsol multiphysics, 2024. Finite element analysis and multiphysics simulation software.

[185] Carl Zeiss Microscopy GmbH. Zeiss smartsem, 2024. SEM control and imaging software.

[186] Olympus Corporation. Olympus stream, 2019. Image analysis software for materials science applications.

[187] Keyence Corporation. Vhx series digital microscope, 2024. Digital microscopy system for inspection and measurement.

[188] Anthropic. Claude, 2024. AI assistant for analysis and writing.

[189] Inkscape Contributors. Inkscape, 2024. Free and open-source vector graphics editor.

[190] The LaTeX Project. Latex – a document preparation system, 2024. Document typesetting system.